A dual species MOT of Yb and Cs

BUTLER, KIRSTEEN,LOUISA

A dual species MOT of Yb and Cs

Kirsteen Louisa Butler

A thesis submitted in partial fulfilment
of the requirements for the degree of
Doctor of Philosophy

Department of Physics
Durham University

July 2, 2014

A dual species MOT of Yb and Cs

Kirsteen Louisa Butler

Abstract

This thesis describes the design and construction of a new apparatus to laser cool and trap Yb and Cs atoms with the ultimate aim of creating ultracold molecules with both an electric and magnetic dipole moment, which are of great interest in a range of fields.

The Yb and Cs atomic beams are first generated and overlapped in a dual species oven. A collimated atomic beam of the two species is formed by the use of an array of capillary tubes at the exit of the oven. At this stage the atoms have an average velocity of $311\,\mathrm{m\,s^{-1}}$ or $264\,\mathrm{m\,s^{-1}}$ for Yb and Cs respectively, therefore it is necessary to reduce their velocity before they can be trapped in a magneto-optical trap (MOT).
This initial stage of slowing is carried out with a Zeeman slower. Due to their atomic properties, Yb and Cs atoms are unable to be slowed by the same magnetic field profile therefore they cannot be loaded simultaneously, however, the Zeeman slower can load the atoms into a MOT sequentially. Once their velocities have been reduced to approximately $48\,\mathrm{m\,s^{-1}}$ ($10\,\mathrm{m\,s^{-1}}$) the Cs (Yb) atoms can be captured in a MOT.

The laser systems for cooling Yb and Cs are also presented. Laser cooling of Cs is achieved on the D_2 transition at 852.3 nm whereas Yb can either be cooled on the ${}^1S_0 \rightarrow {}^1P_1$ or ${}^1S_0 \rightarrow {}^3P_1$ transitions at 398.9 nm or 555.8 nm respectively. Due to the relative linewidths of these transitions ($2\pi \times 28.0\,\mathrm{MHz}$ and $2\pi \times 182.2\,\mathrm{kHz}$), Zeeman slowing is performed for Yb on the ${}^1S_0 \rightarrow {}^1P_1$ transition and magneto-optical trapping on the ${}^1S_0 \rightarrow {}^3P_1$ transition.

A Cs MOT with 1×10^8 atoms and an Yb MOT with the order of 10^8 atoms on the narrow 556 nm transition are demonstrated. The mixture can be sequentially loaded into a dual species MOT, paving the way for many further experiments exploring this novel mixture.

Declaration

I confirm that no part of the material offered has previously been submitted by myself for a degree in this or any other University. Where material has been generated through joint work, the work of others has been indicated.

Kirsteen Louisa Butler
Durham, July 2, 2014

For Mum and Dad,
for everything.

Acknowledgements

There are many people whose help goes into creating a new experiment and getting it to a point where a thesis can be written; it is never the accomplishment of just one person so I would like to thank everyone who has helped me on my way. There are doubtless too many people to list, so I apologise to anyone I forget. Firstly, I give my thanks to my supervisor, Simon Cornish, without whom this thesis would not exist.

I would like to thank Team YbCs not just for all of their hard work on the project but also for making the lab a better place to be. Special thanks must go to Steve Hopkins for all of his help and advice: a true font of all knowledge and an electronics wizard, his novel solutions to problems often saved the day - the mains circuit in a cardboard box was a particular favourite!

I could not have asked for a better lab-mate than Stefan Kemp, his dedication and hard work cannot be easily matched and being almost as crazy as I am made for many entertaining hours in the lab. I thank him for all of the Madness, the Friday chocolate and joining in with the crazy hand gestures and dancing. And who knew the many uses we could find for mylar, blue tack and araldite! I've enjoyed working with him and I know the experiment will go on to bigger and better things in his very capable hands. I would also like to thank him for an amazing thesis hat, the best one yet!

My thanks also go to Ruben Freytag for all of his work on the Yb laser systems and for introducing Spotify to the lab. I know it must have been hard coming up from Imperial to Durham half way through his PhD, but I've enjoyed working with him. I would also like to thank Phil Gregory for his painstaking and patient measurements of the Zeeman slower field one summer and for his brilliant addition to the time-lapse!

From Mixtures, I would first like to thank Michael Köppinger for all of his help and advice over the years. My first friend in AtMol, our chats in the corridor and lab were always good fun, although editing out the many, many time-lapse images with him leant against our table did make that job more difficult! I particularly enjoyed our jaunts to Krakow and Innsbruck; he taught me that a poster session must have beer, talks must be followed by cake and that no nation is safe from being invaded by him! Also from Mixtures, thanks have to go to Danny McCarron, Dan Jenkin and Hung Wen

Cho for teaching me the ropes in my first year.

From Solitons, I would like to thank Tim Wiles and Manfred Yu: Tim for being a LabVIEW guru and Manfred for making me laugh. I have enjoyed and appreciated the many physics and non-physics related conversations I've had with both of them over the years.

The Mechanical Workshop have done a great job throughout my PhD and I could not have achieved what I did without their hard work. I would especially like to thank Steve Lishman for showing me how to make better designs, Malcolm Robertshaw for teaching me most of what I now know about materials and Kevin Ring for his infinite patience with my complicated designs, teaching me how to drill and tap and for always moving the drill table up for me! I would also like to thank John Dobson for all of his help, both during my PhD and in my fourth year project.

Lastly, I would like to thank the rest of AtMol, especially the class of 2010 for their friendship and conversation on my rare trips to the office and tearoom. Thank you to Ifan Hughes for being my second supervisor and for finding my viva room for me! Also thank you to Matt Jones, Simon Gardiner, Kevin Weatherill, David Carty, Charles Adams and Robert Potvliege for their helpful conversations and advice.

On a more personal note, a great many thanks go to my lovely James; true to his word he kept me together throughout this and I really would not have been able to finish this work without his love and support. He has been so patient with all of my whinging about broken lasers, lab accidents and everything else that he deserves a medal! I want to thank him for always being there when I need him; never mind what day I've had, coming home to him never fails to wash away my worries and make me smile.

And last but certainly not least, my greatest thanks go to my family; my wonderful parents, grandparents and sister. To try and list all the ways in which they've helped and loved me over the years would be futile, but I hope they know that I am forever grateful. Everything I have ever achieved is due to them, they have always been there to believe in me, support me and to push me to be the best that I can be. No words could ever thank them enough; simply put, I would not be where I am were it not for them.

Contents

List of Figures

List of Tables

Chapter 1

Introduction

This thesis describes the design and construction of a new apparatus to laser cool caesium and ytterbium atoms with the ultimate aim of creating ultracold CsYb molecules in the ro-vibrational ground state. This introduction outlines the motivation for this project and presents a précis of the field of cold molecules.

1.1 Introduction to cold molecules

The importance of ultracold atomic gases has been recognised by two Nobel prizes in Physics; the 1997 prize for laser cooling [1–3] and the 2001 prize for the first realisation of Bose-Einstein condensation in atomic gases [4, 5]. Just as ultracold atoms opened up many new and novel areas of physics, it is expected that ultracold molecules could have many potential uses as well, the main areas of which are summarised in [6]. These include areas such as fundamental physics research [7–10], cold chemistry [11, 12], modelling condensed matter systems [13–15] and quantum simulation and computation [16, 17].

1.1.1 Uses for ultracold molecules

The addition of vibrational and rotational degrees of freedom within a molecule and the presence of a permanent electric dipole moment in heteronuclear dimers allow different quantities to be measured with molecules that are inaccessible with simple atoms. For example, electronic transitions within a molecule depend upon the properties of the electron, whereas vibrational transitions depend upon the properties of the two nuclei (in dimer molecules), therefore transitions within a molecule can allow the electron-proton mass ratio to be precisely measured [8, 9]. High resolution molecular spectroscopy can also be used to measure the time dependence of other funda-

mental constants, such as the fine structure constant [7]. If the measurements from a terrestrial laboratory are compared to astronomical data, discrepancies between the values may be found. Molecules are also being used to put limits on the electric dipole moment of the electron to help eliminate rival super-symmetric extensions to the Standard Model of particle physics [10, 18].

Observing and, through the use of external static and dynamic fields, controlling the reactions of ultracold molecules is expected to allow a better understanding of chemical reactions taking place in interstellar gas clouds, although the temperatures achievable in the lab will ultimately be lower than those in space. As the molecules will have such a low velocity, their de Broglie wavelength will be longer than the typical intermolecular forces and as such the reactions will be dominated by quantum mechanical effects [11].

In a direct comparison to the breakthroughs in atomic physics with the advent of the BEC, novel quantum phases could be achieved with ultracold molecules such as Bose-Einstein condensation or Fermi degeneracy of molecules. As heteronuclear molecules are dipolar, this opens the possibility of creating and studying dipolar BECs. The first dipolar BEC observed was in ^{52}Cr atoms [14] and recently in ^{164}Dy [19], which both have a magnetic dipole moment. However, the electric dipole moment of ground state heteronuclear molecules will be much greater and so the dipole-dipole interactions between particles will be larger. The properties of dipolar BECs (e.g. stability) are strongly influenced by the dipole-dipole interaction and so, in conjunction with the trapping geometry, a large degree of control over the quantum state is offered [13]. For example, if the molecules were trapped in a 2D pancake trap then phase transitions between crystalline and superfluid phases could be observed [20].

If heteronuclear diatomic molecules were trapped in an optical lattice where each site could be individually addressed, then each electric dipole moment of the molecules could be treated as a qubit and quantum information processing implemented [17]. In such a system an external electric field would orientate the electric dipole moments of the molecules either with or against the field, creating the necessary $|0\rangle$ and $|1\rangle$ states. If an electric field gradient is applied across the lattice, each site could be individually addressed with microwave transitions and neighbouring qubits coupled via the dipole-dipole interaction.

In an expansion to this, paramagnetic diatomic molecules, such as CsYb, allow extra control over the molecules by the addition of a magnetic dipole moment due to the unpaired electron from the Yb atom as well as the electric dipole moment in the ground state. This additional dipole moment allows the engineering of spin dependent interactions to simulate lattice-spin models if the molecules are loaded into an optical lattice [16, 21].

1.1.2 Methods for cooling molecules

The very properties that make molecules interesting to study - their vibrational and rotational degrees of freedom - also make molecules harder to cool than atoms as simple laser cooling schemes with relatively closed optical transitions are generally absent. Most molecular transitions are able to decay to multiple vibrational and rotational levels which would require an impractical number of repump lasers. There are some molecules where fairly simple laser cooling schemes have been found, but these are the exception to the rule and even for these molecules there are still many repumping levels that must be closed in order for efficient cooling to occur [22, 23].

Therefore other methods for cooling molecules have had to be found. These break down into two general categories referred to as direct and indirect cooling methods [24]. Direct cooling methods involve cooling a beam of pre-existing molecules, whereas indirect methods involve cooling the constituent atoms before forming molecules with them. Each of these categories has its advantages and disadvantages. Direct cooling offers the use of a wider range of molecules but, at the current time, cannot cool molecules to temperatures as low as laser cooled atoms. On the other hand, indirect cooling allows lower temperatures to be achieved (determined by the temperature of the constituent atoms at the time of molecule formation) but only with combinations of atoms that can be laser cooled.

Direct cooling

Some examples of direct cooling include Stark deceleration [25, 26], magnetic deceleration [27, 28], buffer gas cooling [29, 30] and direct laser cooling [22, 23]. Once a sample of cold molecules has been created, these methods can then be combined with sympathetic cooling between atoms and molecules [31] or cooling in microwave traps [32] to lower the temperature further.

Buffer gas cooling often includes a laser-ablated source of molecules that undergo initial cooling by thermalisation with a buffer gas of helium [30]. The buffer gas is swept past the ablation target and so carries the target molecules along with it, producing molecular beams that can then be cooled using further techniques.

Stark deceleration is where a time-varying electric field is applied to a beam of dipolar molecules [25, 26]. If the molecules possess an electric dipole moment the Stark effect will act on them when they move into a region of electric field. The Stark energy gained by the molecules accompanies a loss of kinetic energy so if the electric field is turned off at the appropriate time the molecule will lose energy. Repeating this process can theoretically decelerate a packet of molecules to zero velocity. Stark deceleration merely decelerates a packet of atoms, i.e., shifts their velocity distribution to a lower average

value, rather than cooling the atoms (narrowing their velocity distribution) which is often done in an initial stage such as supersonic expansion [33].

Conversely, magnetic deceleration of paramagnetic molecules can be achieved through the use of a travelling magnetic trap with a controllable velocity [27, 28]. As the trap velocity slows, the molecules will be slowed along with it. For both electric and magnetic deceleration the limiting factor is often the large distance required to cool the molecules to low temperatures.

Indirect cooling

There are two main methods for the formation of ultracold molecules from their constituent atoms: photoassociation [34, 35] and magnetoassociation [36].

Photoassociation is the process by which two free atoms absorb a photon and form a molecule in an excited electronic state. This highly excited molecule can then decay into the ground electronic state, although in general the molecule will not decay into the lowest vibrational state. However, once in the ground electronic state other methods such as Stimulated Raman Adiabatic Passage (STIRAP) [37] could be utilised to create ro-vibrational ground state molecules.

Magnetoassociation makes use of magnetically tunable Feshbach resonances [36] to create loosely bound 'Feshbach molecules' from the two constituent atoms. The same process of STIRAP can then be used to transfer these Feshbach molecules to their ro-vibrational ground state. If Feshbach resonances occur at readily accessible magnetic fields for the system under study, magnetoassociation is a good method to create ultracold molecules as the process is relatively simple.

To the author's knowledge at the time of writing, Feshbach molecules have been made from ^{6}Li^{40}K [38, 39], ^{23}Na^{40}K [40] and ^{23}Na^{6}Li [41], whereas ground state molecules have been formed from $^{133}Cs_2$ [42], $^{87}Rb_2$ [43], ^{40}K^{87}Rb [44] and ^{87}Rb^{133}Cs [45]. Other mixtures currently being worked on are ^{6}Li-^{133}Cs [46], Rb-Sr [47], Yb-Rb [48], Yb-Li [49, 50] and Yb-^{133}Cs (this work). (Specific isotopes are only given where a definite mixture has been settled on and is known to the author).

1.2 CsYb molecules

The aim of this experiment will be to use ultracold caesium and ytterbium atoms to form ro-vibrational ground state dipolar molecules for use as a quantum simulator. However, as a first generation experiment the apparatus does not have the ability to generate an optical lattice for quantum simulation but will act as a proof of principle and pave the way for further experiments.

1.3 Thesis overview

This thesis begins with the general background theory relevant to the project in Chapter 2. Chapter 3 introduces the vacuum system designed and constructed specifically for the Yb-Cs project. Chapter 4 gives details about the laser systems used to cool ytterbium and caesium as well as some background theory on laser cooling. Chapter 5 describes the dual species Zeeman slower that is used to sequentially load Cs and Yb atoms into their respective MOTs. Chapter 6 gives results of optimising the Zeeman slower and single species MOT for Cs with similar results for Yb presented in Chapter 7. Chapter 8 looks towards operating the system as a dual species experiment and gives an overview of the next steps for the experiment.

This thesis ends with some details of the work the author carried out on a different experiment (the Rb-Cs mixture experiment) during 2010-2011 in Appendix A, with code for calculating the electric dipole moment in Appendix B and various vacuum details and engineering drawings in Appendices C-E.

The author would like to thank Michael Tarbutt for providing the original Mathematica code for the Zeeman simulations in Chapter 5 and Stephen Hopkins for doing the majority of the work on these. The author would also like to thank Stefan Kemp for winding and testing the Zeeman slower and MOT coils. Finally, the author would like to thank Ruben Freytag for his work on the Yb laser systems whilst at Imperial College London.

Chapter 2

Background Theory

The field of ultracold atoms is a well established one, with readily available reference material detailing the theory behind the field. Therefore, this chapter only outlines the processes directly relevant to the Yb-Cs experiment, starting with introducing the properties of the ytterbium and caesium atoms before describing the Feshbach resonance mechanism which can be used to associate the atoms into loosely bound Feshbach molecules. Next, detail is provided on how photoassociation spectroscopy can be used to determine the interspecies background scattering length, a value that is needed to pin-point the magnitude of magnetic field at which the Feshbach resonances are predicted to occur. Finally, the electric and magnetic dipole moments of the CsYb molecule in the ro-vibrational ground state is described.

Only brief introductions to these topics are presented here as there are many review articles that can be consulted for further details, for example, [12, 15, 16, 34–36].

2.1 The atoms: caesium and ytterbium

The experimental apparatus described in this thesis was designed to laser cool and co-trap Cs and Yb atoms with the aim to form ro-vibrational ground state CsYb molecules. Therefore, a logical place to start is to examine these atoms and their properties and so understand why they have been chosen.

2.1.1 Caesium

Caesium (Cs) is an alkali metal with an atomic number of 55. It is highly reactive with water and has only one stable isotope: ^{133}Cs. Since 1967 the transition between the two hyperfine levels in the ground state of Cs has been used to define the SI second, which is defined as being equal to 9,192,631,770 periods of radiation [51, 52], see figure 2.1(a).

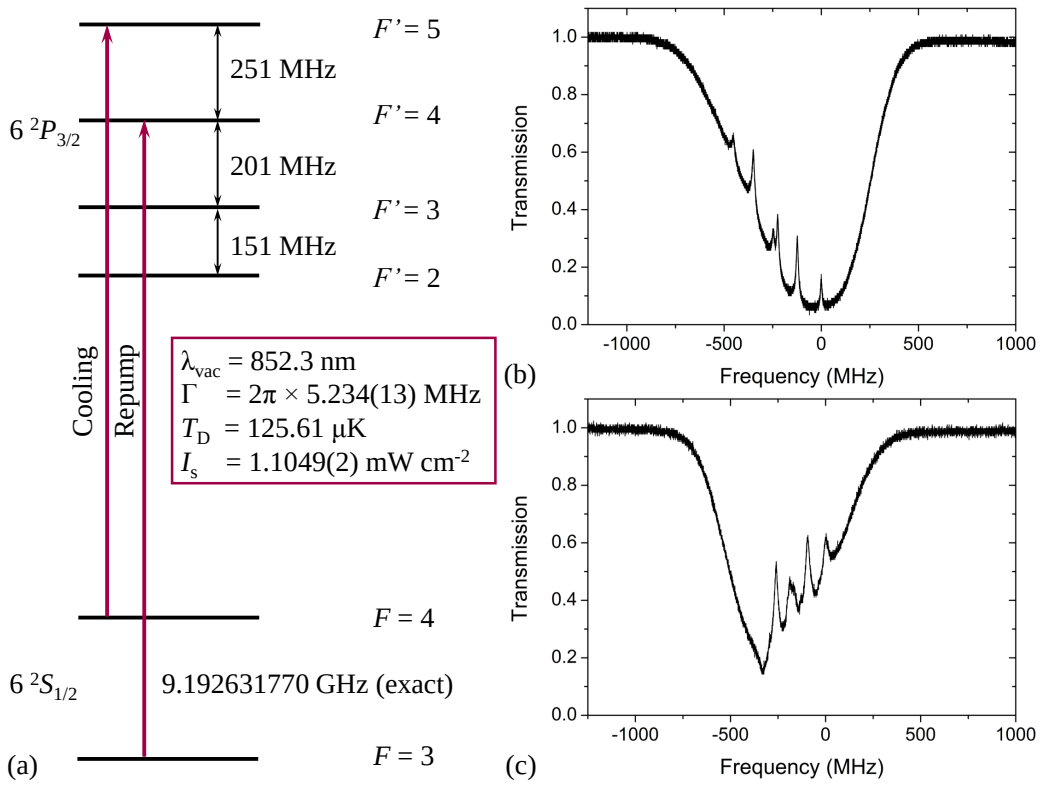

Figure 2.1: (a) The relevant atomic transitions for caesium. Laser cooling is achieved on the $F = 4 \rightarrow F' = 5$ transition, which requires repumping light on the $F = 3 \rightarrow F; = 4$ transition. The wavelength of the $6\ ^2S_{1/2} \rightarrow 6\ ^2P_{3/2}$ transition, λ_{vac}, linewidth, Γ, Doppler temperature, T_{D} and saturation intensity, I_{s} are shown in the box (atomic properties taken from [53]). The spectra for (b) the $F = 4 \rightarrow F'$ transition and (c) $F = 3 \rightarrow F'$ transition are also shown.

Isotope	Abundance (%)	Nuclear spin	Scattering length (nm)
168	0.13	0	13.33(18)
170	3.05	0	3.38(11)
171	14.3	$^1/_2$	-0.15(19)
172	21.9	0	-31.7(3.4)
173	16.12	$^5/_2$	10.55(11)
174	31.8	0	5.55(8)
176	12.7	0	-1.28(23)

Table 2.1: The isotopes of ytterbium and their natural abundances. Scattering lengths are also given as these indicate which bosonic isotopes are most readily condensed. Data taken from [64].

Due to its favourable energy level structure, in common with the rest of the alkali metals, Cs atoms are able to be laser cooled and indeed to date three groups world wide have achieved Bose-Einstein condensation of Cs [54–56]. Figure 2.1 shows the relevant energy levels for laser cooling along with the spectra for each group of transitions; $F = 4 \rightarrow F'$ and $F = 3 \rightarrow F'$ (discussed in depth in Section 4.1). The required wavelength for cooling Cs is 852.3 nm, which is easily achievable with diode lasers.

2.1.2 Ytterbium

Ytterbium (Yb) is a rare earth metal in the lanthanide series of the periodic table with an atomic number of 70. Yb has seven stable isotopes, 5 bosons and 2 fermions, the abundances of which can be seen in table 2.1. Like Cs, Yb also has readily accessible transitions that allow for laser cooling: one going from the ground state, $^1S_0$, to the $^1P_1$ excited state with a wavelength of 398.9 nm and the other from $^1S_0$ to $^3P_1$ at 555.8 nm. All but one bosonic isotope of Yb has been cooled to low enough temperatures to form a Bose-Einstein condensate [57–61] and the two fermionic isotopes have been made to form quantum degenerate Fermi gases [62, 63]. The boson that has not been condensed is ^{172}Yb as it has a relatively large, negative scattering length (see table 2.1).

Figure 2.2 shows the relevant transitions for laser cooling Yb. The $^1S_0 \rightarrow {}^1P_1$ transition has a relatively large linewidth and so is used in this experiment for Zeeman slowing (explained in Section 5.1) whilst the $^1S_0 \rightarrow {}^3P_1$ intercombination transition has a narrow linewidth and is therefore used for the magneto-optical trap (MOT) as it has a correspondingly low Doppler temperature of 4.4 μK. According to the electric dipole transition selections rules the $^1S_0 \rightarrow {}^3P_1$ transition should be forbidden as $\Delta S = 1$, however, higher order electric and magnetic multipole effects mean that this transitions is weakly allowed, which accounts for its narrow linewidth.

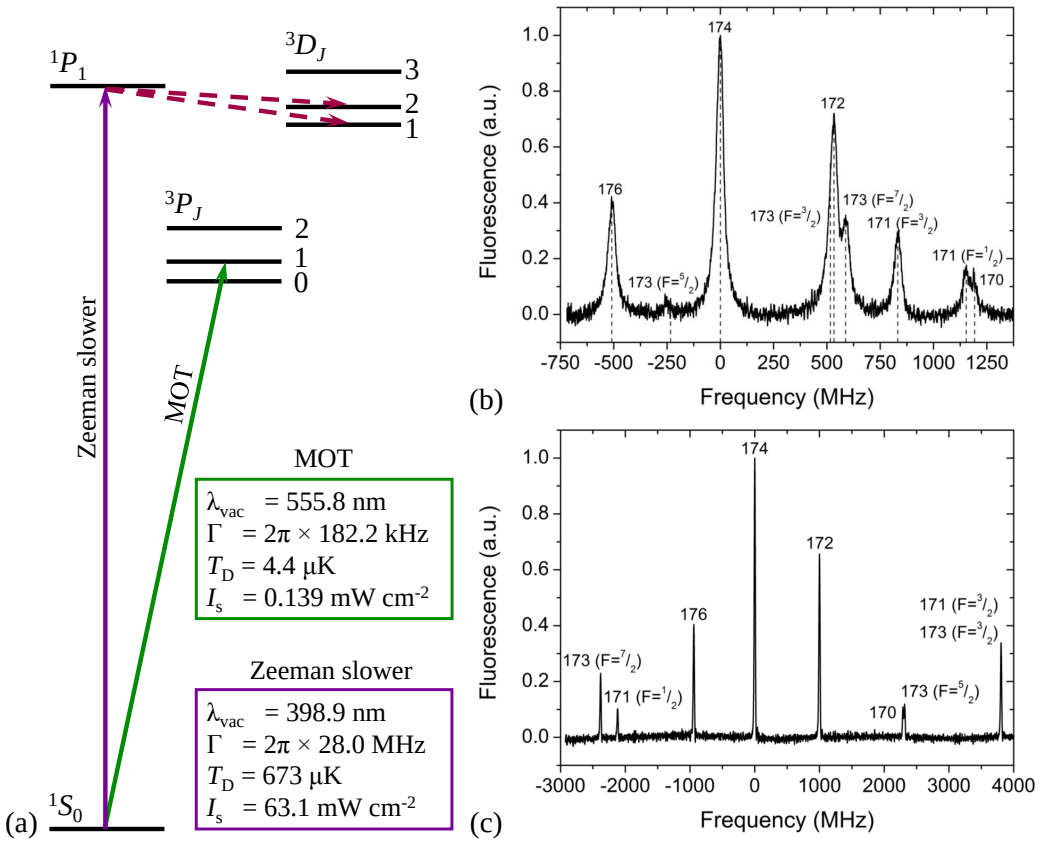

Figure 2.2: (a) The main transitions in ytterbium used for laser cooling. Zeeman slowing is accomplished on the $^1S_0 \rightarrow {}^1P_1$ line; the fluorescence spectrum for this line can be seen in (b). The MOT is achieved with the $^1S_0 \rightarrow {}^3P_1$ transition as this is a perfect two level system with no losses to other states; the spectrum for this transition can be seen in (c). The wavelength, λ_{vac}, linewidth, Γ, Doppler temperature, T_{D} and saturation intensity, I_{s}, are shown for each transition. The wavelengths are taken from the wavenumber in [65] and the linewidths from [60].

Isotope	Shift from ^{174}Yb (MHz)	
	$^1S_0$ to $^1P_1$ [70]	$^1S_0$ to $^3P_1$ [71]
168	1887.400(50)	3655.128(100)
170	1192.393(66)	2286.345(85)
171 ($F = 1/2$)	1153.696(61)	-2132.063(85)
171 ($F = 3/2$)	832.436(50)	3804.608(100)
172	533.309(53)	1000.020(85)
173 ($F = 3/2$)	515.975(200)	3807.278(134)
173 ($F = 5/2$)	-253.418(50)	2311.411(85)
173 ($F = 7/2$)	587.986(56)	-2386.704(85)
174	0	0
176	-509.310(50)	-954.832(60)

Table 2.2: The isotope shifts from ^{174}Yb for both the $^1S_0 \rightarrow {}^1P_1$ and $^1S_0 \rightarrow {}^3P_1$ lines. The data for the $^1S_0 \rightarrow {}^3P_1$ line has been shifted from that in [71] as that data was centred on ^{176}Yb. The errors have therefore also been corrected to account for the uncertainty in the quoted position of ^{174}Yb relative to ^{176}Yb.

Laser cooling and trapping can be accomplished with the 399 nm transition ([66] for example) but the $^1P_1$ state can decay to other states ($^3D_2$ and $^3D_1$) that will not necessarily decay back into the ground state and so atom losses occur. The lower limit of the branching ratio for this decay is 1.2×10^{-7} [67, 68]. The 556 nm transition is a perfect two level system and so no losses to other states occur.

Table 2.2 shows the isotope shifts from the most abundant isotope, ^{174}Yb, for both the 399 nm and 556 nm transitions. There are two effects that produce an isotope shift; mass effects and the volume shift, both of which are explained in detail in [69].

2.1.3 Ytterbium - caesium mixture

There are several reasons why the specific mixture of Yb and Cs was chosen: the presence of an extra valence electron in Yb, the range of Yb isotopes available and the effect these isotopes have on the predicted Feshbach resonances (discussed further in Section 2.2).

Valence electron

The electronic structure of Yb is [Xe] $4f^{14}$ $6s^2$. This makes it a 'closed shell' atom but the two s-electrons can act as valence electrons. These valence electrons mean that the CsYb ro-vibrational ground state molecule will have not just an electric dipole moment but also a magnetic dipole moment as one

of the electrons will not be involved in bonding (see Section 2.4.1 for a more detailed discussion of molecular dipole moments).

Yb isotopes

As described in table 2.1, Yb has seven stable isotopes; five of which are bosonic and two fermionic. This in itself opens up some interesting physics to study with Bose-Bose and Bose-Fermi mixtures, such as phase separation and miscibility studies [72, 73].

The range of isotopes also give a greater probability that one mixture of ^{x}Yb-Cs will have a favourable interspecies scattering length and Feshbach spectrum.

Reduced mass tuning

The positions and widths of Feshbach resonances can be tuned by changing the reduced mass of the system (see Section 2.2):

$$m_{\mathrm{r}} = \frac{M_{\mathrm{Cs}} M_{\mathrm{Yb}}}{M_{\mathrm{Cs}} + M_{\mathrm{Yb}}} \tag{2.1}$$

where M_{Cs} and M_{Yb} are the masses of the Cs and Yb atoms respectively. As Cs is the heaviest alkali-metal atom, the reduced mass can be tuned over a fairly large range on changing the Yb isotope. This helps when trying to find a Feshbach resonance at a reasonable magnetic field as both the positions and widths of the resonances scale with the reduced mass of the molecule.

2.2 Feshbach resonances

Feshbach resonances were first predicted in 1958 by Herman Feshbach [74] in nuclear systems. The first experimental observation of one in a dilute atomic gas was in 1998 in a sodium BEC [75]. In atomic physics they have become a useful tool for varying the background scattering length of a system and also in the formation of ultracold loosely bound Feshbach molecules [76–85], which are a precursor to forming molecules in the ro-vibrational ground state.

2.2.1 The origin of Feshbach resonances

A Feshbach resonance occurs when the energy of a molecular state (the closed channel) crosses that of a continuum scattering state of a pair of free atoms (the open channel) [86], as illustrated in figure 2.3(d). When this happens atoms in the free potential can be made to resonantly couple to the bound

state and Feshbach molecules can be created. The energy difference between the bound and free states can be tuned with a magnetic field if the corresponding magnetic moments of the free atoms and the molecule they form are different. This tuning allows free atoms in a trap to be swept over a Feshbach resonance by applying a smoothly varying magnetic field, creating Feshbach molecules.

Using this magnetic tuning, the s-wave scattering length varies with magnetic field as [36]:

$$a\left(B\right) = a_{\mathrm{bg}}\left(1 - \frac{\Delta}{B - B_{\mathrm{res}}}\right), \tag{2.2}$$

where a_{bg} is the background scattering length and B_{res} is the magnetic field at which the resonance is located. The scattering length becomes infinite at B_{res} and changes sign to either side of it as can be seen diagrammatically in figure 2.3(e).

In general, the scattering length changes sign depending on the position of a bound state with respect to the molecular potential [87]: a negative scattering length occurs when the potential is not deep enough to support a bound state (figure 2.3(a)), whereas the scattering length is infinite in the special case where the bound state lies on the dissociation limit (dashed line in figure 2.3(b)). When the potential supports a bound state below the threshold then the scattering length is positive (figure 2.3(c)). When applied to Feshbach resonances the bound state is that of the closed channel, $\mathrm{E_c}$.

The width of the resonance is defined as:

$$\Delta = B_0 - B_{\mathrm{res}}, \tag{2.3}$$

where B_0 is the magnetic field closest to the resonance at which $a = 0$.

2.2.2 Alkali - alkali metal mixtures

In the field of atomic physics, Feshbach resonances are usually observed in homo- or heteronuclear alkali metal systems [76–85]. For a Feshbach resonance to occur, the two potentials (open and closed channels) must have both coupling between the states and an avoided crossing in energy.

Alkali metals have a non-zero nuclear spin (i) and an electron spin of $s = 1/2$ giving each atom a ground state of ^2S. Therefore, when two alkali metal atoms are brought together, they can form either a singlet ($\mathrm{S} = |s_{\mathrm{a}} - s_{\mathrm{b}}| = 0$) or a triplet ($\mathrm{S} = s_{\mathrm{a}} + s_{\mathrm{b}} = 1$) potential curve. These potentials have different characteristics, which give rise to the coupling between states necessary for Feshbach resonances when the molecular levels cross the atomic thresholds.

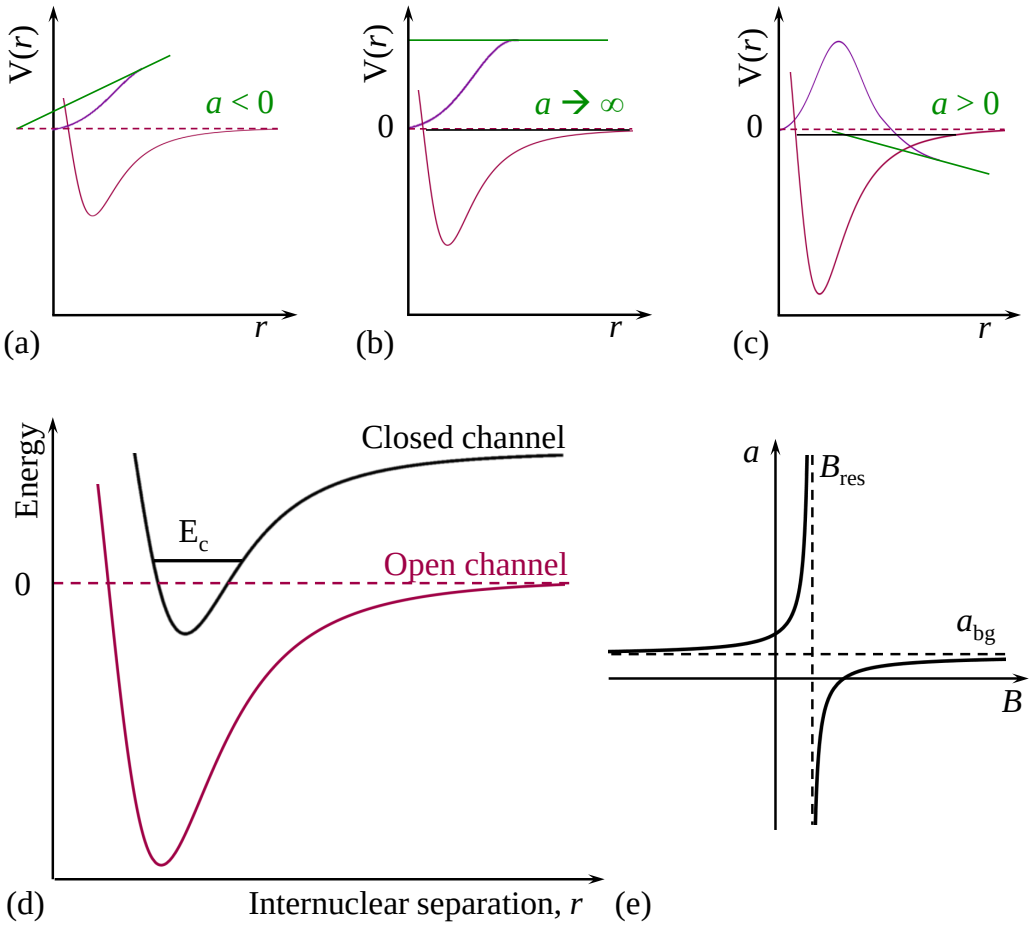

Figure 2.3: The value of the scattering length changes as the position of the bound state (shown as a black line in (b) and (c)) moves with respect to the molecular potential. (a) The scattering length is negative when the potential does not support a bound state, (b) goes to infinity when the bound state is at the threshold of the potential and (c) is negative when the potential supports a bound state. In these figures the radial wavefunction is shown in purple whilst its asymptotic behaviour is shown in green. It is the zero crossing of this asymptote that determines the sign of the scattering length. (d) A Feshbach resonance therefore occurs when a bound state, E_c, in the closed channel crosses in energy a continuum state (the open channel) of a pair of free atoms (shown by the dashed line). This can be achieved by magnetically tuning the states such that E_c is brought close to the continuum state. (e) The scattering length $a \to \pm\infty$ at the magnetic field at which the resonance occurs, B_{res}.

Therefore, resonances only occur when a triplet molecular state crosses a singlet atomic state and vice versa.

Therefore, in these systems the coupling between the continuum and molecular states is given by the difference between the singlet ($^1\Sigma$) and triplet ($^3\Sigma$) potential curves. The molecular states have different spin characteristics to the atomic states, giving different magnetic moments and this provides the avoided crossings between the atomic and molecular potentials.

For the purpose of this discussion, the notation used for molecular states is $^{2S+1}\Lambda$, where S is the total spin of the mixture and Λ is the rotational state of the molecule with $\Lambda = 0, 1, 2...$ being denoted by $\Sigma, \Pi, \Delta...$

2.2.3 Alkali - closed shell atom mixtures

Doublet molecular potential

The mechanism for producing Feshbach resonances as described in the section above is absent for a mixture of an alkali metal atom, such as Cs, with a closed shell atom such as Yb. This is because the ground state of the Cs atom is ^2S, but the Yb atom has a ^1S ground state (as $s = 0$). As such, when the atoms are brought together, there is only one molecular electronic state: the doublet, $^2\Sigma$. Therefore, the potential curves for different atomic hyperfine or Zeeman states are parallel to each other in energy. In principle, crossings do still occur for molecular states that increase in energy with magnetic field and atomic states that decrease in energy, i.e., crossings between states with $f = i + 1/2$ and $f = i - 1/2$. However, crossings alone are not enough to form Feshbach resonances; coupling is also required.

To describe why there is no coupling between the different states in a $^2S + ^1S$ system it is necessary to look at the molecular Hamiltonian [88]:

$$H = T + V(R) + \zeta \hat{i}.\hat{s} + H_{\text{Zeeman}}, \tag{2.4}$$

where T is a kinetic energy term, $V(R)$ is the molecular potential, H_{Zeeman} is the Zeeman Hamiltonian and $\zeta \hat{i}.\hat{s}$ is an atomic hyperfine term, with ζ being the atomic hyperfine coupling constant. Only the ^2S atom (the alkali metal) has nuclear spin so $\zeta \hat{i}.\hat{s}$ is zero for Yb and therefore nothing in the above Hamiltonian couples the molecular states to the atomic state.

Therefore, although there are crossings between states, because there is no coupling between them they do not form Feshbach resonances, or they form Feshbach resonances but with zero width.

Internuclear distance dependence of ζ

The above reasoning is only true when the hyperfine coupling constant, ζ, is independent of the distance between two atoms. Fortunately this is not the case, however. It has been predicted [86] that ζ varies significantly when a second atom (in this case the ^1S atom) is brought close to the ^2S atom. The ζ of one atom changes when another is brought close due to the perturbing effect of the second atom's electrons. This internuclear distance dependence of ζ introduces coupling that mixes the atomic and molecular states, giving width to the Feshbach resonances at the crossings described above.

Crossings and coupling: Feshbach resonances

Theoretically, now that there are both crossings and coupling between the atomic and molecular states, Feshbach resonances could be detected in an experiment using an alkali-closed shell atomic mixture. Potentials for the Cs-Yb system have been calculated [86] and the widths of these resonances are given by:

$$\Delta = \frac{\pi I_{\mathrm{m_{f,a}}}^2 I_{\mathrm{nk}}^2}{k a_{\mathrm{bg}} \delta\mu_{\mathrm{res}}}, \tag{2.5}$$

where $I_{\mathrm{m_{f,a}}}$ is the atomic matrix element of $\hat{\imath}.\hat{s}$, i.e., the hyperfine coupling between two atomic states; I_{nk} is the radial matrix element of $\Delta\zeta(R)$ between the bound and continuum states with $\Delta\zeta(R)$ being the distance dependence of the hyperfine coupling constant for Cs; $\delta\mu_{\mathrm{res}}$ is the difference in magnetic moments of the molecular bound state and that of the free atom pair, which gives the rate at which the bound state crosses the atomic threshold and k is the wave vector.

From an experimental point of view, each of these factors have an impact on either the width or the position of the Feshbach resonances:

- At zero magnetic field, $I_{\mathrm{m_{f,a}}}$ is equal to zero as the atomic states are eigenfunctions of $\hat{\imath}.\hat{s}$. However, at low but finite fields (up to approximately 2000 G), $I_{\mathrm{m_{f,a}}}$ increases linearly with B and so the width, $\Delta \propto B^2$. This means that resonances at larger magnetic field values will be wider. Practically, this causes some problems as an apparatus will not only have to be able to produce large but also very stable magnetic fields. Another aspect of this factor is that alkali atoms with larger nuclear spin (generally heavier alkalis like Cs) will have intrinsic advantages as $I_{\mathrm{m_{f,a}}}$ will be larger.

- I_{nk} depends on $\Delta\zeta(R)$ which is larger for larger ζ and so, again, heavier alkali metals will be better and form wider Feshbach resonances.

- The dependence of Δ on $1/\delta\mu_{\rm res}$ means that if the difference between the magnetic moment of the molecular and atomic states happens to be low then the states may have a 'glancing blow' and the resulting Feshbach resonance will be wider. Whether this will happen depends on the choice of Yb isotope; there is a possibility that one isotope might have this happen at a low field, which would give a good candidate to associate the CsYb Feshbach molecules.
- The $a_{\rm bg}$ factor in the denominator of equation (2.5) on the surface appears to suggest that broader resonances will occur for smaller background scattering lengths, however, the strength of the Feshbach resonance actually depends on $a_{\rm bg}\Delta$ (equation (2.2)) so smaller values of $a_{\rm bg}$ are not actually advantageous.

Therefore, in brief, the broadest Feshbach resonances will occur with heavier alkali atoms at large magnetic fields.

Fermionic isotopes of ytterbium

The fermionic isotopes of Yb have nuclear spin and so another mechanism to create additional Feshbach resonances comes into play. When the alkali atom is brought close to a fermionic Yb atom, a new type of hyperfine interaction coupling between the electron spin of the alkali and the nuclear magnetic moment of the Yb occurs. This can give rise to increased widths of the Feshbach resonances, which may occur in slightly different places to the bosonic isotopes. However, for most alkali atoms the resonances are not expected to be significantly broader; the only system where the widths of the Feshbach resonances created from this mechanism are expected to be significantly wider are for Li-Yb [89].

Theoretical predictions for the locations of the Feshbach resonances

The molecular states cannot be calculated completely accurately *ab initio* and require experimental measurements of the interspecies scattering length to feed into the theory. The method by which this can be achieved is discussed in more detail in Section 2.3. However, these measurements need only be done for one isotope combination as mass scaling can then be used to extrapolate for the other isotopes.

The scattering length is given by [90]:

$$a = -\lim_{k\to 0}\frac{\tan\delta(k)}{k}, \tag{2.6}$$

where $k = \sqrt{2m_{\rm r}E/\hbar^2}$ is the wave vector and $\delta(k)$ is the phase shift. From

this it can be seen that changing the reduced mass of the system has an affect on the scattering length in a predictable way.

Generally speaking, increasing the reduced mass shifts the molecular states down in energy, resulting in lighter isotope combinations having atomic and molecular state crossings at lower magnetic fields.

Why CsYb?

Cs is the highest mass alkali so gives greater mass scaling when combined with the different isotopes of Yb (see equation (2.1)), which means that there is more of a chance that a wide Feshbach resonance will be found at an experimentally feasible magnetic field. The larger mass also means that there are a higher density of molecular bound states near the threshold and so a better chance of finding resonances at lower magnetic fields.

Cs also has a relatively large change in hyperfine coupling when another atom is brought close [86], which increases I_{nk} and so the width of the resonance (equation (2.5)).

Both of these considerations mean that Yb-Cs is one of the more promising mixtures for trying to find this type of Feshbach resonance.

2.3 Finding the background scattering length

The background interspecies scattering length or binding energy of the highest bound state in the molecular electronic ground state (which itself gives information on the scattering length) can be fed into the Feshbach resonance calculations to give the positions and widths of the Feshbach resonances for CsYb. There are two methods by which the interspecies scattering length can be found: using the thermalisation between the two atomic species in the same trap or by photoassociation.

2.3.1 Thermalisation

As derived in [90], the scattering cross section for two atoms of different species, such as Cs and Yb, is:

$$\sigma = \frac{4\pi}{k^2} \sum_l (2l+1) \sin^2 \delta_l(k), \tag{2.7}$$

where k and $\delta_l(k)$ are as defined for equation (2.6). If the atoms were indistinguishable bosons (fermions) the above equation would be doubled but the sum would only be taken over the even (odd) l.

In order to use the cross section to determine the interspecies scattering length, only s-wave ($l = 0$) scattering should be considered. If this is the case the scattering cross section simplifies to:

$$\sigma_0 = \frac{4\pi}{k^2} \sin^2 \delta(k), \tag{2.8}$$

(again, this would be doubled for indistinguishable particles). Substituting the definition of the scattering length (equation (2.6)) into the above equaiton gives

$$\sigma_0 = \frac{4\pi a^2}{k^2 a^2 + 1}. \tag{2.9}$$

It is only for atoms at very low temperatures where s-wave scattering occurs exclusively. This is because as the temperature decreases, fewer partial waves contribute to the scattering process until a temperature is reached where only s-waves contributes. For $l > 0$ a modification to the molecular potential arises where a centrifugal barrier is superimposed on the long range part of the molecular potential ($-C_6/r^6$), such that the effective potential becomes:

$$V_{\text{eff}} = -\frac{C_6}{r^6} + \frac{\hbar^2 l(l+1)}{2m_{\text{r}} r^2}, \tag{2.10}$$

where the second term is the additional centrifugal barrier with m_{r} being the reduced mass of equation (2.1). This barrier can be seen in figure 2.4, where both the long range tail of the molecular potential (purple) and the centrifugal barrier (red) can be seen contributing to the overall potential (black). This example was calculated using two colliding Cs atoms.

The C_6 coefficient for the Yb-Cs mixture is unknown, however, for Cs-Cs it is $(6890.48 \pm 0.08)\, E_{\text{h}} a_0^6$ [91] and $(1932 \pm 30)\, E_{\text{h}} a_0^6$ for Yb-Yb [64] (both given in atomic units where $E_{\text{h}} = \hbar^2/m_{\text{e}} a_0^2$ is the Hartree energy and a_0 is the Bohr radius). For indistinguishable bosons only even partial waves contribute to the scattering cross section, so the first centrifugal barrier for Cs (^{174}Yb) occurs for $l = 2$ and gives a barrier height of $180\,\mu$K ($228\,\mu$K), therefore if the temperature is below this only s-wave ($l = 0$) scattering takes place.

These low temperatures are best achieved in an optical dipole trap where any rethermalisation measurements in this experiment would be carried out. An optical dipole trap not only allows low temperatures to be reached but also provides a conservative trap for the atoms so any change in the trapping potential translates directly into kinetic energy of the atoms. The rethermalisation rate, γ_{therm}, can be measured by introducing a small deviation from equilibrium to the trap, such as changing the trap aspect ratio, before letting the atoms relax back into the original trap geometry. Plotting the time taken for the temperature of the trapped atoms to return to the equilibrium

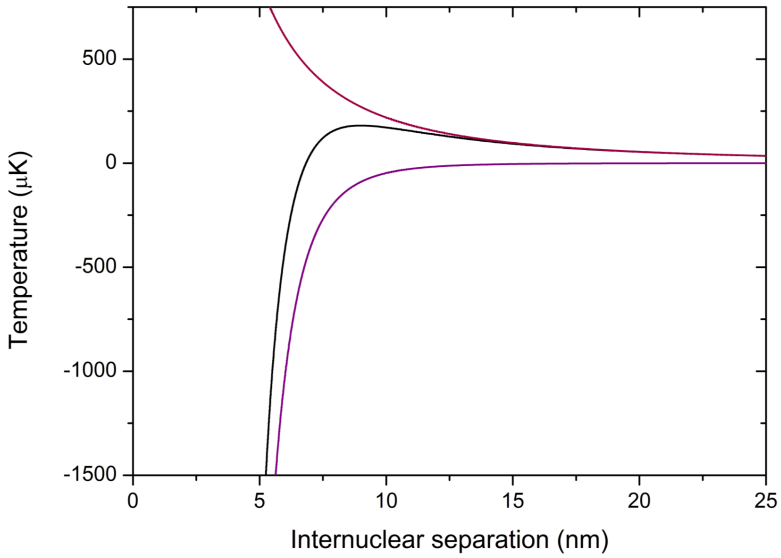

Figure 2.4: The contributions to the total scatting potential (black) from the centrifugal term for $l > 1$ (red) and the long range part of the molecular potential (purple) can be seen. The height of the centrifugal barrier increases as l increases and determines which partial waves contribute to the scattering.

temperature gives γ_{therm}. The cross section is then directly proportional to the rethermalisation rate, $\gamma_{\text{therm}} = \bar{n}\bar{v}\sigma$, where $\bar{n}$ is the mean number density and $\bar{v}$ is the average relative collision velocity. Therefore measuring this rate allows the scattering length to be calculated [90, 92].

However, as can be seen in equation (2.9) above, this method only gives a^2, so there will be no information on the sign of the scattering length. There will also be a larger uncertainty associated with the scattering length value calculated from thermalisation measurements compared to using photoassociation spectroscopy (discussed in the next section). This is because other effects, such as shape resonances [90], may mean that partial waves with $l > 0$ still contribute to the scattering even at temperatures where only s-wave scattering would be expected. The preferred method to determine the interspecies scattering length is therefore photoassociation.

2.3.2 1-photon photoassociation

In general, either 1-photon or 2-photon photoassociation can be used to obtain the background scattering length. If 1-photon photoassociation spectroscopy is coupled with knowledge about the shape of the ground-state potential at internuclear separations larger than the separation at which the photoassociation spectrum is being investigated, the scattering length can be calculated. The second method uses 2-photon photoassociation to directly

measure the binding energy of the highest few bound levels of the electronic ground state, which, when coupled with knowledge about the long-range potential shape gives the scattering length. More in-depth information about photoassociation can be found in several review articles, such as [34, 35].

Photoassociation is the process by which two colliding free atoms (A and B) are bound together into an electronically excited molecule ($(AB)^*$) by the absorption of a photon of a specific frequency:

$$A + B + \gamma \rightarrow (AB)^*, \tag{2.11}$$

where the asterisk indicates an electronically excited state. The energy of the photon, $\mathrm{E_{PA}}$, must equal the energy difference between the colliding atoms and the electronically excited bound state.

Once in the excited state the molecule can either decay into two free atoms again or into a bound state in the electronic ground potential, in each case the molecule emits another photon which is not necessarily of the same frequency as the absorbed photon in (2.11),

$$\begin{aligned} (AB)^* &\rightarrow A + B + \gamma_\mathrm{d} \\ (AB)^* &\rightarrow AB + \gamma_\mathrm{d}. \end{aligned} \tag{2.12}$$

As the time scale for electronic transitions is much faster than that for nuclear vibration, the internuclear separation between the two free atoms and the molecule they form stays the same during an electronic transition. This is illustrated by the vertical arrows in figure 2.5(a). Therefore, the probability of a transition occurring depends upon the overlap between the ground and excited state wavefunctions at a particular internuclear distance. Collectively, this is known as the Franck-Condon principle [6, 93]. A molecular wavefunction has the largest amplitude at the turning point of the molecular potential as this is where the kinetic energy of the molecule is the least, therefore transitions are most likely to occur at these internuclear distances, as demonstrated diagrammatically in figure 2.5(b).

Experimentally, the Franck-Condon principle means that when the molecule $(AB)^*$ decays it is unlikely to produce a molecule in a low-lying vibrational level but instead in one of the highest bound states, if not two free atoms. This is because the turning points of the highly excited vibrational level in the electronically excited state and the low-lying vibrational levels in the ground state do not generally occur at the same internuclear distance and so their Franck-Condon overlap will be negligible. This is especially true for photoassociation within a MOT as the typical internuclear distance might be expected to be of the order of microns, producing molecules with a very high vibrational quantum number.

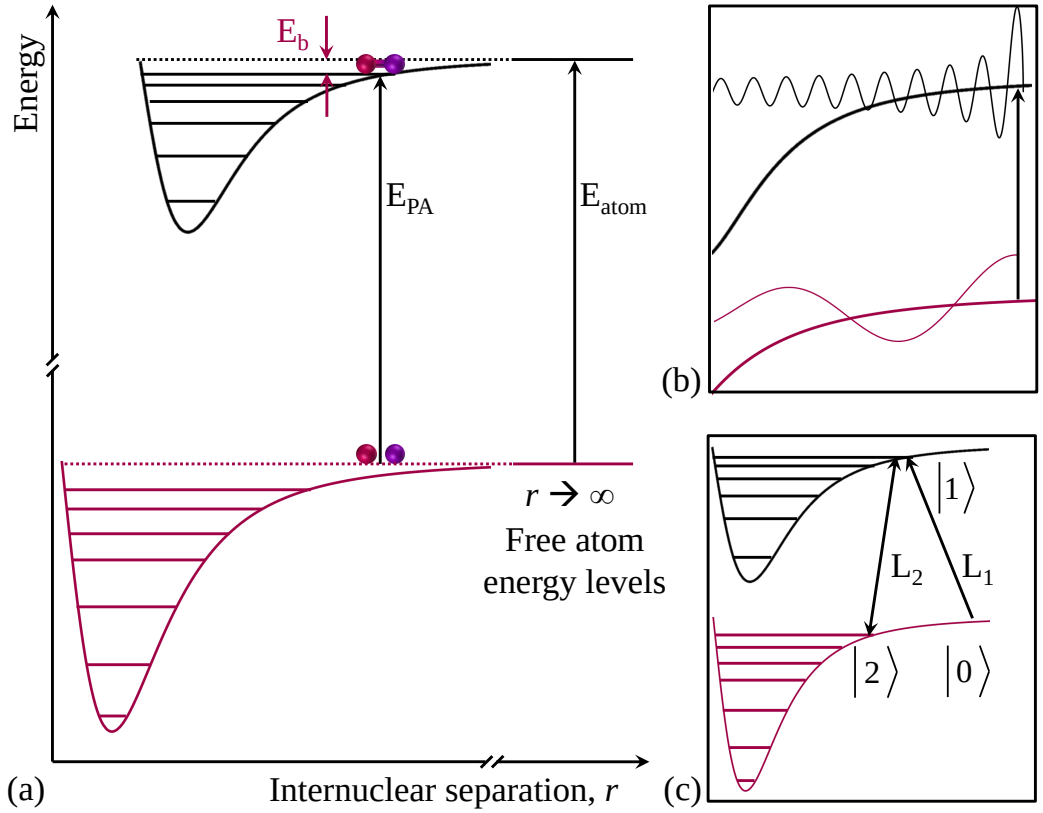

Figure 2.5: (a) A schematic of photoassociation showing the atomic transition at the limit of $r \rightarrow \infty$. The energy of the photoassociation transition, E_{PA}, is less than that of the atomic transition, E_{atom}. The energy difference is the binding energy, E_b, of the electronically excited state. (b) An illustrative example of the Franck-Condon overlap where the transition probability is greatest when the excited and ground state wavefunctions are largest, marked by the position of the arrow in the figure. (c) 2-photon photoassociation, or Autler-Townes spectroscopy, where the laser frequency, L_1, drives the same single photon photoassociation transition as in (a) and the second laser, L_2, dresses states $|1\rangle$ and $|2\rangle$ leading to a smaller loss rate when observing photoassociation within a continuously loaded MOT.

Finding the scattering length

The scattering length of a system can be found by mapping out the location of a node in the free atom wavefunction by locating several photoassociation resonances and comparing their relative linestrengths. Due to the Franck-Condon overlap, when the free atom wavefunction is near a node (i.e., close to zero), then the probability of a transition is very small, thus the linestrengths of photoassociation features reduce near a node. Once located, the scattering length can be calculated provided the shape of the potential is known for internuclear distances greater than the nodal position. This has been done with, for example, ^{86}Sr and ^{88}Sr [94].

Heteronuclear systems

The above discussion is true for homonuclear systems, however, when there is a mixture of atomic species then this is no longer the case. The method of mapping where the node in the free atom wavefunction is cannot be done as simply for heteronuclear systems, as the long range part of the potential has a different dependence on the internuclear distance and so some assumptions needed to calculate the scattering length break down [35].

Therefore, in a dual species experiment 2-photon photoassociation spectroscopy must be used in order to obtain the background scattering length.

2.3.3 2-photon photoassociation

2-photon photoassociation is demonstrated in figure 2.5(c). As for 1-photon photoassociation the laser frequency, L_1, is tuned to the photoassociation resonance creating a steady population in state $|1\rangle$ if the number of atoms being probed by the laser is in a steady state (for example, a magneto-optical trap being continuously loaded). The second laser, L_2, then disrupts this photoassociation process resulting in fewer atoms being lost from the trap. This happens if the $|1\rangle \rightarrow |2\rangle$ transition is strongly driven, as this mixes the levels so L_1 no longer produces molecules in state $|1\rangle$. This is the same idea as Autler-Townes spectroscopy [95]. The binding energies of the states in the electronic ground state potential can then be easily calculated as the energy difference between L_1 and L_2.

As before, the probability of a transition occurring, or in other words the linewidth of the transition, depends on the overlap between the excited and ground state wavefunctions. This is why only the few highest levels in the ground state can normally be probed as the value of the Franck-Condon overlap to lower-lying states is negligible.

Finding the scattering length

Once the binding energy of the last bound state has been found it can be used to calculate the scattering length numerically from the molecular potential [35]. This is done using the following equation [64, 96, 97]:

$$a = \bar{a}\left[1 - \tan\left(\Phi - \frac{\pi}{8}\right)\right], \tag{2.13}$$

where Φ is a semiclassical phase calculated from the classical turning point of the potential where $V(r_0) = 0$ to infinity:

$$\Phi = \frac{\sqrt{2m_\mathrm{r}}}{\hbar}\int_{r_0}^{\infty}\sqrt{-V(r)}\mathrm{dr}, \tag{2.14}$$

and $\bar{a}$ is the mean scattering length given by:

$$\bar{a} = 2^{-\frac{3}{2}}\left(\frac{2m_\mathrm{r}C_6}{\hbar^2}\right)^{\frac{1}{4}}\frac{\Gamma\left(\frac{3}{4}\right)}{\Gamma\left(\frac{5}{4}\right)}, \tag{2.15}$$

where the Γ terms are gamma-functions.

In order to use these equations to calculate the scattering length, the C_6 coefficient for Cs-Yb needs to be found, as recently achieved in a similar mixture of Rb-Yb [48]. This was done by finding the binding energies of the last few bound states with 2-photon photoassociation as described above and fitting the values with the LeRoy-Bernstein formula [98] for the positions of the vibrational levels:

$$\Delta_b = -\frac{1}{hc}\left(\frac{2\hbar}{3}\left(\frac{2\pi}{m_\mathrm{r}}\right)^{\frac{1}{2}}\frac{\Gamma\left(\frac{7}{6}\right)}{\Gamma\left(\frac{2}{3}\right)}\frac{6}{\mathrm{C}_6^{1/6}}(v_\mathrm{D} - \Delta v)\right)^3, \tag{2.16}$$

using C_6 and v_D as fitting parameters, where v_D is the non-integer value of the vibrational quantum number at the dissociation limit.

Once the C_6 value is known, numerical analysis of the Schrödinger equation can be used to find the following approximation to the long range part of the molecular potential:

$$V(r) = -\left(\frac{C_{12}}{r^{12}} + \frac{C_6}{r^6}\right), \tag{2.17}$$

where C_{12} is used as a fitting parameter. Once a good approximation to $V(r)$ has been found that matches the experimental data well, the phase, Φ, can be calculated and equation (2.13) used to find the scattering length.

Once a is known for one isotopic combination, the mass scaling of Φ can be used to determine a for the remaining isotopes. This method gives a more precise measurement of the scattering length than that described for 1-photon photoassociation and also works for heteronuclear mixtures.

2.4 Electric and magnetic dipole moments

Once Feshbach molecules have been created they can be transferred into the absolute ro-vibrational ground state using a process called STIRAP (Stimulated Raman Adiabatic Passage) which will not be discussed here but detailed descriptions of the process can be found in, for example, [37, 99].

It is in the ground state that the molecules have an electric dipole moment, which, along with the permanent magnetic dipole moment of the CsYb molecule can be used for many interesting experiments, such as engineering spin dependent interactions once the molecules have been loaded into an optical lattice. These can be used for investigating lattice-spin models [16].

Dipolar molecules are interesting due to their long-range, anisotropic dipole-dipole interaction. The maximum energy for this interaction when all of the dipoles are aligned is given by:

$$U_{\mathrm{dd}} = \frac{C_{\mathrm{dd}}}{4\pi}\frac{1-3\cos^2\theta}{r^3}, \tag{2.18}$$

where C_{dd} is a coupling constant. This takes on different values depending on whether the dipole is an electric dipole, d_0 ($C_{\mathrm{dd}} = d_0^2/\epsilon_0$) or a magnetic dipole, μ ($C_{\mathrm{dd}} = \mu^2\mu_0$) [15]. The long-range character of the dipole-dipole interaction can be seen from the r^{-3} term, contrasting with the r^{-6} dependence of the contact interaction for neutral atoms. The anisotropic behaviour is evident from the $1-3\cos^2\theta$ term.

A characteristic length, a_{dd}, can be defined as:

$$a_{\mathrm{dd}} = \frac{C_{\mathrm{dd}}m}{12\pi\hbar^2}, \tag{2.19}$$

with m as the mass of the molecule. This can be used to compare the dipole-dipole interaction with the contact interaction (which depends on the s-wave scattering length, a) by the ratio:

$$\epsilon_{\mathrm{dd}} = \frac{a_{\mathrm{dd}}}{a}. \tag{2.20}$$

2.4.1 Electric dipole moment of molecules in the ro-vibrational ground state

Diatomic molecules only show a significant permanent electric dipole moment when in the ro-vibrational ground state (where rotation and vibration quantum numbers are all zero and the internuclear distances are the smallest). This is because the dipole moment is proportional to r^{-7} and so is vanishingly small for molecules with larger internuclear distances [100].

When vibration within the molecule is ignored, a diatomic molecule can be modelled as a rigid rotator with each atom treated as a point mass at a distance r away from the other. The eigenfunctions of such a system can be shown to be [101]:

$$\psi_r = N_r P_J^{|m_J|}(\cos\theta)\mathrm{e}^{im_J\phi}, \tag{2.21}$$

where N_r is a normalisation constant, ϕ is the azimuthal angle between the line connecting the two atoms and the origin about the z-axis, θ is the angle between this line and the z-axis and $P_J^{|m_J|}(\cos\theta)$ is the associated Legendre function. The probability distribution is then given by $\psi^*\psi$ and some of these can be seen in figure 2.6. These plots show that the molecule will only start to show 'direction' when higher order rotational states start to be mixed in; specifically as J increases the $m_J = J$ state starts to look like a classical rigid rod rotating about the z-axis. When there is no rotation ($J = 0$), there is no preferred direction for the molecule and the probability distribution is spatially symmetric.

For diatomic molecules that have two different atoms, such as CsYb or RbCs, a permanent electric dipole moment will be associated with the molecule as the centres of positive and negative charges do not overlap as they would within a homonuclear molecule. However, the dipole moment will not start to manifest until there is rotation associated with the molecule. This is because, as for the $J = 0, m_J = 0$ state in figure 2.6, the charge is evenly distributed over the molecule and there is no preferred direction.

Therefore, in order to measure the electric dipole moment the molecule must not only be in the ro-vibrational ground state, but must also have a direction imposed on it by the addition of an external electric field, which acts to mix in states with a higher rotational quantum number. This comes about from the Hamiltonian of a rigid rotator with a permanent electric dipole moment, d_0, interacting with an external electric field, E, [102]:

$$\begin{aligned}\langle Jm_J|\, H\, |J'm'_J\rangle &= B_{\mathrm{rot}} J\,(J+1)\,\delta_{JJ'm_Jm'_J} \\ &- d_0 E\sqrt{(2J+1)\,(2J'+1)}\,(-1)^{m_J}\begin{pmatrix} J & 1 & J' \\ -m_J & 0 & m'_J \end{pmatrix}\begin{pmatrix} J & 1 & J' \\ 0 & 0 & 0 \end{pmatrix}.\end{aligned} \tag{2.22}$$

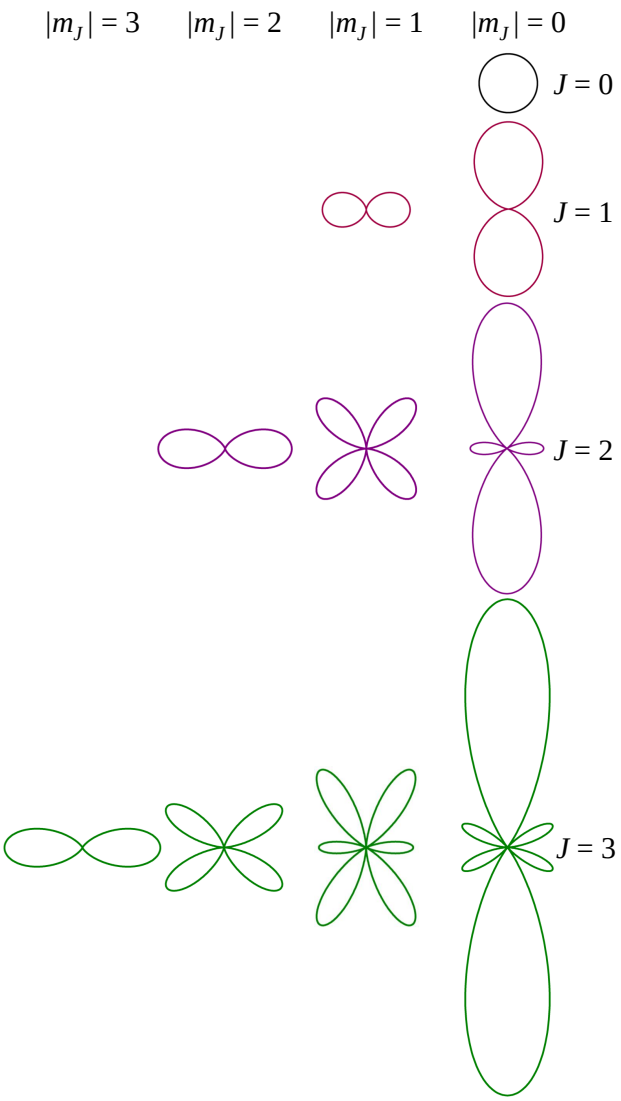

Figure 2.6: The probability distributions for different values of J and m_J for a diatomic molecule when modelled as a rigid rotator (all plotted on the same scale). The plots are plane sections through what would in reality be a 3-dimensional probability distribution. 'Direction' only starts to manifest at higher rotational quantum numbers, specifically for $m_J = J$.

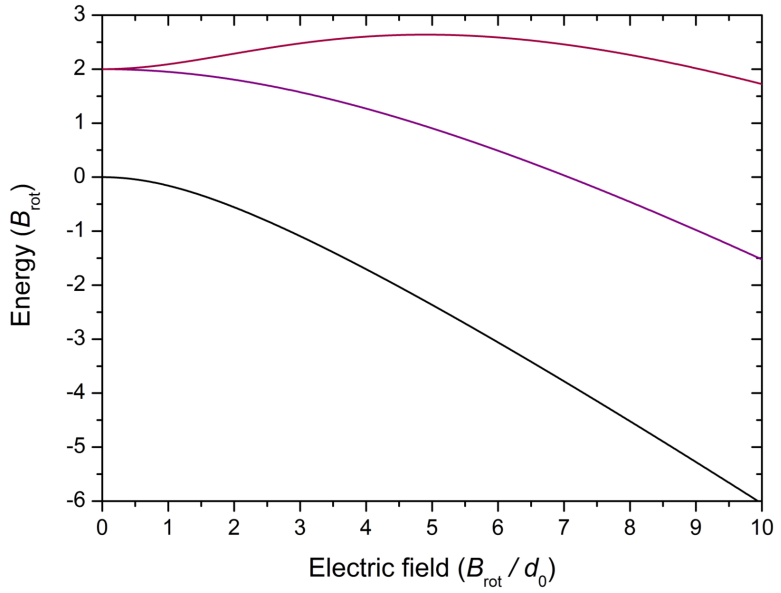

Figure 2.7: The Stark shift for the $J = 0, m_J = 0$ (black), $J = 1, m_J = 0$ (red) and $J = 1, m_J = 1$ (purple) states for any diatomic molecule. Specific values can be calculated by substituting in the relevant rotational constant (B_{rot}) and dipole moment (d_0).

The first term is simply the rotational energy which does not depend on the electric field, whilst the second term describes the Stark effect. The factors in brackets are the Wigner 3-j coefficients and B_{rot} is the rotational constant of the particular molecule. The Stark shift of a diatomic molecule with applied electric field for the $J = 0$ and $J = 1$ states can be seen in figure 2.7.

The dipole moment of the ground state molecule can be calculated by taking the gradient of the black line ($J = 0$) in figure 2.7. The dipole moment is plotted in the main graph in figure 2.8 in terms of d_0 and B_{rot}. It can be seen that the dipole moment never reaches d_0 and it would only reach that value at an infinitely large electric field. The inset in figure 2.8 shows how the dipole moment calculated at an electric field of $100E_{\text{crit}}$ (where E_{crit} is defined as B_{rot}/d_0) changes depending on the number of levels included in the calculation. As a compromise between accuracy and computation time for the graphs presented here 6 levels were used (i.e., $0 \leq J \leq 5$).

A useful parameter to calculate when comparing different dimers is the critical electric field, $E_{\text{crit}} = B_{\text{rot}}/d_0$. At E_{crit} the dipole moment will be equal to $d_0/3$, so it gives a good estimation of the magnitude of electric field that will need to be applied to the molecules when designing an experiment. Values of E_{crit} for some different diatomic molecules are listed in table 2.3 along with their d_0 and B_{rot} values. It can be seen that CsYb has a relatively small dipole moment, however, it does have the advantage that it also has a permanent magnetic dipole moment (see Section 2.4.2).

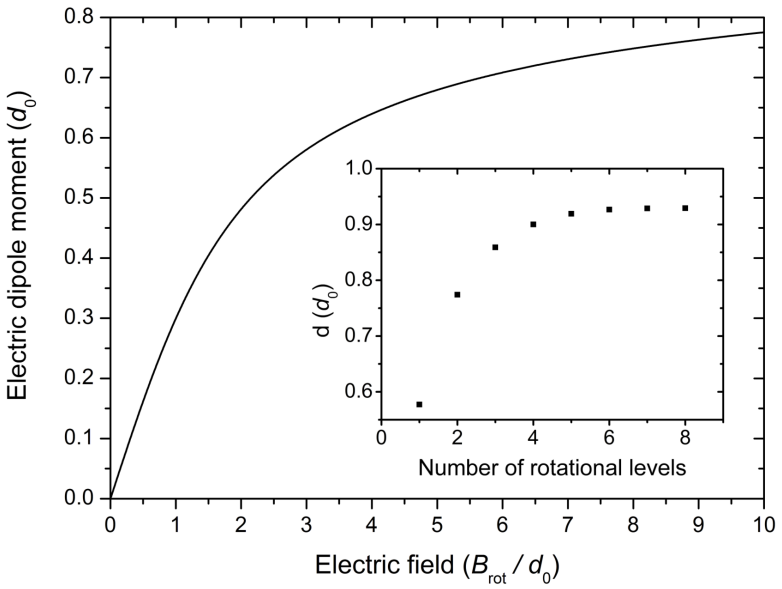

Figure 2.8: The electric dipole moment of a diatomic molecule with applied electric field. Specific values can be calculated by substituting in the relevant values of B_{rot} and d_0 for a particular molecule. Inset: how the number of rotational levels included in the calculation influences the value of the dipole moment calculated. The dipole moment only reaches d_0 at infinitely large electric fields.

Additional information on the electric dipole moment of ro-vibrational ground state molecules can be found in [15, 16].

2.4.2 Magnetic dipole moment

Bi-alklai dimers, such as RbCs, do not have a magnetic dipole moment as both Cs and Rb have just one valence electron, both of which are involved in forming the bond within the RbCs molecule. However, when a rare earth atom, such as Yb, is bonded to an alkali atom, one valence electron is left free after the bond has formed, due to Yb possessing two valence electrons.

Molecule	B_{rot} (GHz)	d_0 (D)	E_{crit} (kV cm^{-1})
CsYb	0.21	0.24	1.71
RbCs	0.51	1.26	0.80
KRb	1.16	0.566(17)	3.74

Table 2.3: The rotational constant, B_{rot}, dipole moment, d_0, and critical electric field, E_{crit} (as described in the text) for a selection of diatomic molecules. Data taken from [44].

Therefore, the CsYb molecule has both an electric and a magnetic dipole moment in the ro-vibrational ground state.

The main difference between the magnetic and electric dipole moments is that the magnetic dipole moment is present in all states; the CsYb molecule does not have to be in the ro-vibrational ground state to measure a significant magnetic dipole. However, the magnetic dipole moment is much weaker than the electric dipole moment. Taking the ratio between the coupling constants, C_{dd}, for the electric and magnetic dipole moments for CsYb demonstrates this, as $\frac{\mu^2\mu_0}{d_0^2/\epsilon_0} = 1.5 \times 10^{-3}$.

Even though the magnetic dipole moment is quite weak, it does allow the molecules to be controlled via both magnetic and electric fields. This gives both dipole-dipole interactions and the ability to engineer spin-rotation coupling between molecules [16].

2.5 Summary

To summarise, it is advantageous to study a closed shell-alkali metal mixture because of the availability of both a magnetic and electric dipole moment. The specific mixture of Yb-Cs was chosen as Feshbach resonances have been predicted to occur for mixtures such as this due to the internuclear distance dependent change in the hyperfine coupling constant of the alkali atom. These Feshbach resonances could be used for magnetoassociation to form molecules from the atoms. Cs in particular was chosen as it is the highest mass alkali that can be readily laser cooled and thus has more promising characteristics that may make the predicted Yb-Cs Feshbach resonances wider at lower magnetic fields.

Chapter 3

Experimental apparatus: Vacuum system

The simultaneous laser cooling and trapping of Cs and Yb required a complex vacuum system to be constructed. An overview of the vacuum system can be seen in figure 3.1 and this chapter will detail the design, construction and testing of each section labelled. The vacuum system was designed to have five main sections; a dual species oven (Section 3.2), a region where spectroscopy can be carried out on the beam (Section 3.3), a Zeeman slower (Section 3.4) connected to an ultra high vacuum science chamber (Section 3.5) pumped out by the final pumping station section (Section 3.6).

3.1 Overview of the vacuum system

Each section of the vacuum system labelled in figure 3.1 has a specific purpose and therefore a specific vacuum requirement.

The Cs and Yb atomic beams are formed and spatially overlapped at the oven, which naturally has a higher pressure due to the temperatures required to produce the beams. This higher pressure region must be isolated by differential pumping from the UHV science chamber so that the pressure there remains constant and low. The narrow Zeeman slower tube physically separates the two ends of the completed vacuum system, which can be seen in figure 3.2. Spectroscopy can be performed on the atomic beams at the six-way cross before the Zeeman slower.

3.2 Dual species oven

The first element of the vacuum system to be considered was the dual species oven. This needed to produce a similar flux of each atomic species in a single

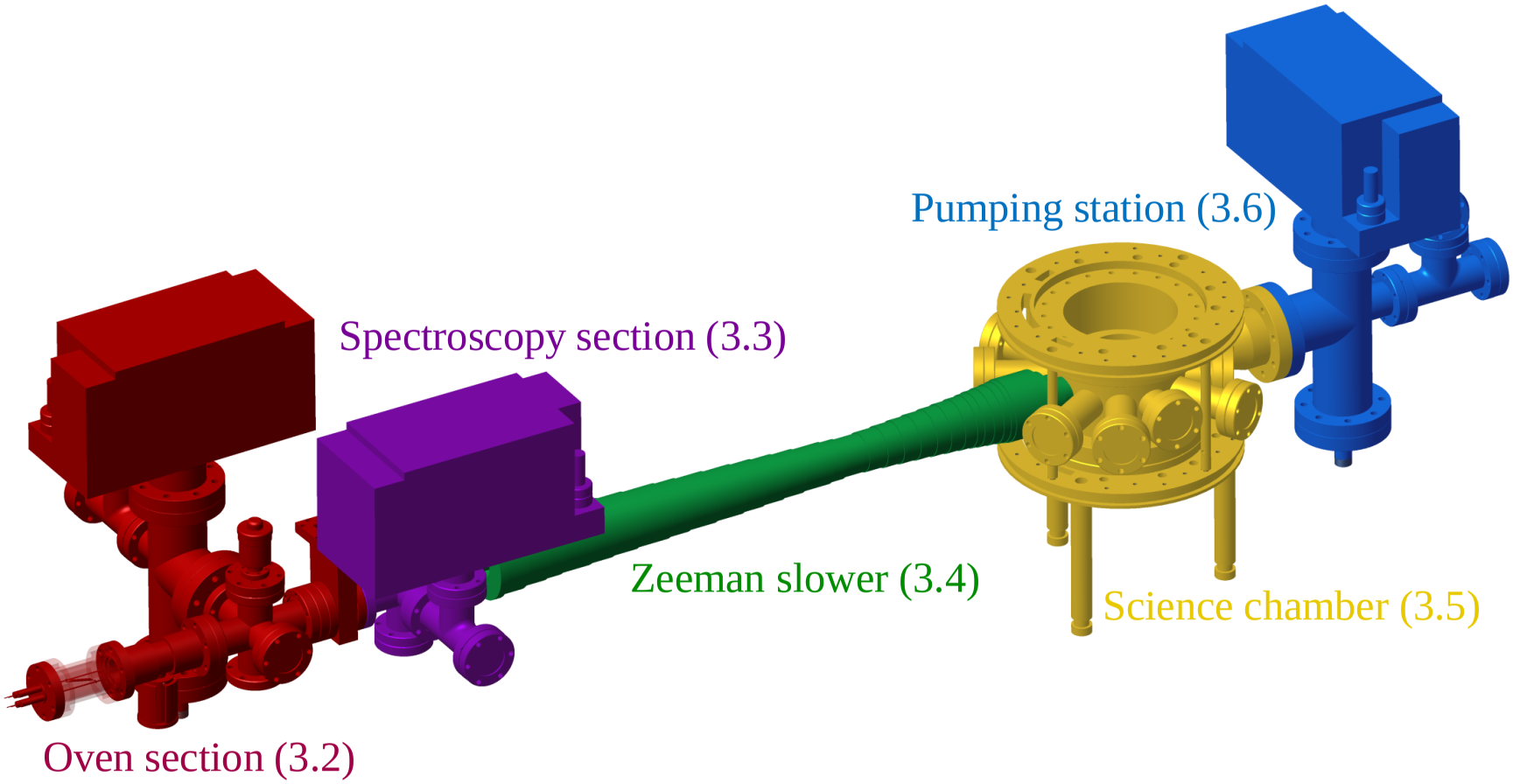

Figure 3.1: An overview of the Yb-Cs vacuum system. The coloured sections represent distinct areas of the vacuum system used for specific purposes; the dual species oven (red), spectroscopy section (purple), Zeeman slower (green), science chamber (yellow) and pumping station (blue). The numbers in brackets show the sections in this chapter that describe each area.

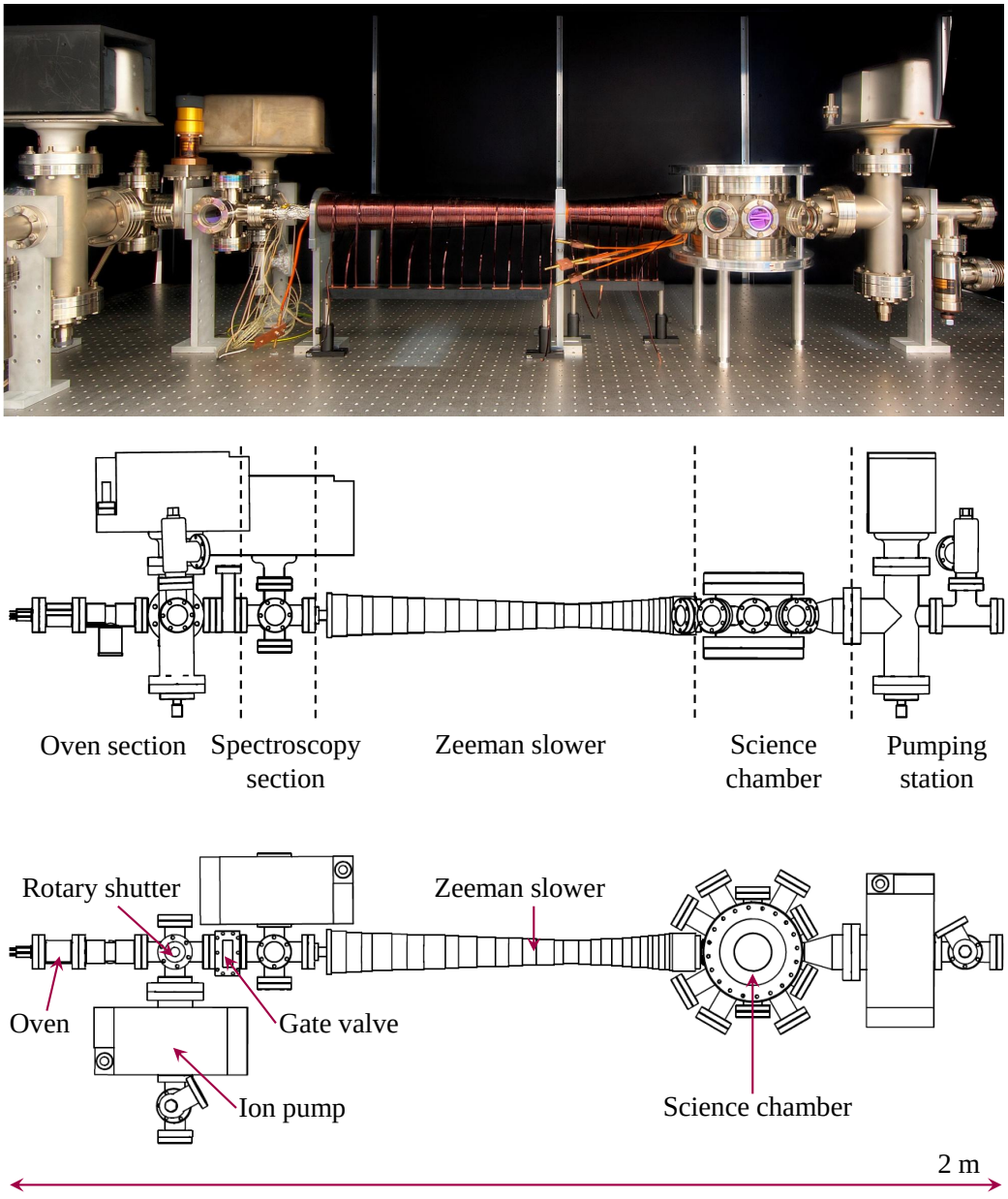

Figure 3.2: Top: the vacuum system shortly before the final bake-out on the optical table in the lab. The magnets are not on the ion pumps at this point as the bake is about to begin. Middle and bottom: a side and top view schematic of the vacuum system showing the five sections and the locations of specific components such as the rotary shutter and gate valve.

overlapped beam. Therefore, it was necessary to first consider how atomic beams are formed in an oven before the dual species oven for Cs and Yb could be designed.

3.2.1 Theoretical considerations

In this section a brief overview of molecular beams effusing from both a thin-walled aperture and longer tubes will be given, however, greater detail can be found in many textbooks, for example, [103–105].

The first design parameter that needed to be considered is what temperatures are required to provide approximately the same flux for each metal. For a first approximation, equalising the vapour pressures for each species will give the same flux of atoms.

Vapour pressure

The vapour pressure for Yb can be calculated using [106]:

$$\log(P) = 2.881 + 9.111 - \frac{8111}{T} - 1.0849\log(T), \tag{3.1}$$

where the pressure, P, has been converted to units of Torr and where $298 \leq T \leq 900\,\mathrm{K}$. In a similar manner, the vapour pressure can be calculated for Cs using the equations below, where the pressure is again in Torr [106]:

$$\log(P) = \begin{cases} 2.881 + 4.711 - \frac{3999}{T}, & 298 < T < \text{m.p.} \\ 2.881 + 4.165 - \frac{3830}{T}, & \text{m.p.} < T < 550. \end{cases} \tag{3.2}$$

Here the top equation is for the solid phase of Cs and the bottom for the liquid phase. The melting point (m.p.) of Cs is 301.65 K [107].

Figure 3.3 compares the calculated vapour pressures for Cs and Yb, plotted on a log scale. It can be seen that only a small change in the temperature of the oven can result in a large change in the pressure (and so atom flux). The dual species oven is run such that the vapour pressures of Cs and Yb are approximately equal, with the Cs chamber being heated to 100 °C (373 K) compared to the 400 °C (673 K) required for Yb. This gives vapour pressures of 6.0×10^{-4} Torr and 7.4×10^{-4} Torr respectively.

The number density, n, of the atoms in the oven can be easily calculated by approximating the atoms as an ideal gas (assuming the number of atoms leaving the oven through the aperture is negligible compared to the total number),

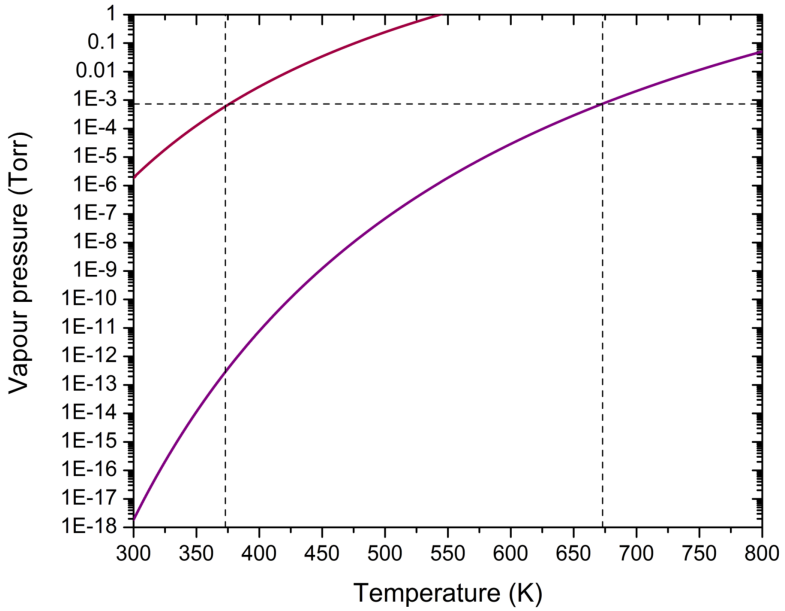

Figure 3.3: The vapour pressure for Cs (red) and Yb (purple). It can be seen that the Cs has a much larger vapour pressure at any given temperature. The dashed lines show the temperatures at which Yb and Cs have a vapour pressure appropriate for the oven. This impacts on the design of the oven in that two areas with very different temperatures need to be created and the temperature gradient between them carefully managed.

$$n = \frac{P}{k_{\mathrm{B}}T}. \tag{3.3}$$

The number densities for Cs and Yb at the temperatures and pressures above are $(1.6 \times 10^{19})\,\mathrm{atoms\,m^{-3}}$ and $(1.1 \times 10^{19})\,\mathrm{atoms\,m^{-3}}$ respectively.

Effusion from a thin-walled aperture

Once the atoms have been heated to the appropriate temperature in the oven a beam can be formed by letting some of the atoms effuse out of the oven chamber. The simplest choice of exit from the oven is a thin-walled aperture. In general, if the area of the aperture is small compared to the total area of the oven and if the mean free path, Λ, is large compared to the aperture diameter then the beam will be fairly well collimated. The mean free path is the average distance an atom travels before it collides with another atom and it can be calculated from [104]

$$\Lambda = \frac{1}{\sqrt{2}\pi\sigma n}, \tag{3.4}$$

where σ is the cross sectional area for collision and n is the number density of the atoms. If the velocity of the atoms follows the Maxwell-Boltzmann distribution and the gas is at a certain pressure, P, then the mean free path can be estimated as

$$\Lambda = \frac{k_{\mathrm{B}}T}{\sqrt{2}\pi d^2 P}, \tag{3.5}$$

where the collision cross section has been approximated to be the diameter of an atom, d, squared.

Velocity distribution

The velocity distribution of the atoms within the oven is described by the Maxwell-Boltzmann distribution [105],

$$f(x) = \frac{4}{\sqrt{\pi}} x^2 \mathrm{e}^{x^2}, \tag{3.6}$$

with $x = v/v_{\mathrm{g}}$ where v_{g} is the most probable velocity for an atom in the oven:

$$v_{\mathrm{g}} = \sqrt{\frac{2k_{\mathrm{B}}T}{m}}. \tag{3.7}$$

However, for an atomic beam the most probable velocity is [108]

$$v_{\mathrm{b}} = \sqrt{\frac{3k_{\mathrm{B}}T}{m}}. \tag{3.8}$$

The most probable velocities for the Cs and Yb atomic beams with the above oven temperatures are $264\,\mathrm{m\,s^{-1}}$ and $311\,\mathrm{m\,s^{-1}}$ respectively. The Maxwell-Boltzmann distributions for Yb and Cs at oven temperatures of 400 °C and 100 °C are shown in figure 3.4.

Atomic flux

At a large distance from the aperture the atomic intensity or flux (atoms in a certain solid angle per unit time) will be given by

$$I(\theta)\mathrm{d}\omega = \frac{n v_{\mathrm{g}}}{2\pi^{3/2}} A \cos(\theta)\mathrm{d}\omega, \tag{3.9}$$

where $\mathrm{d}\omega$ is a solid angle element ($\mathrm{d}\omega = \sin(\theta)\mathrm{d}\theta\mathrm{d}\phi$), θ is the angle from the axis normal to the aperture, A is the aperture area, n is the number density

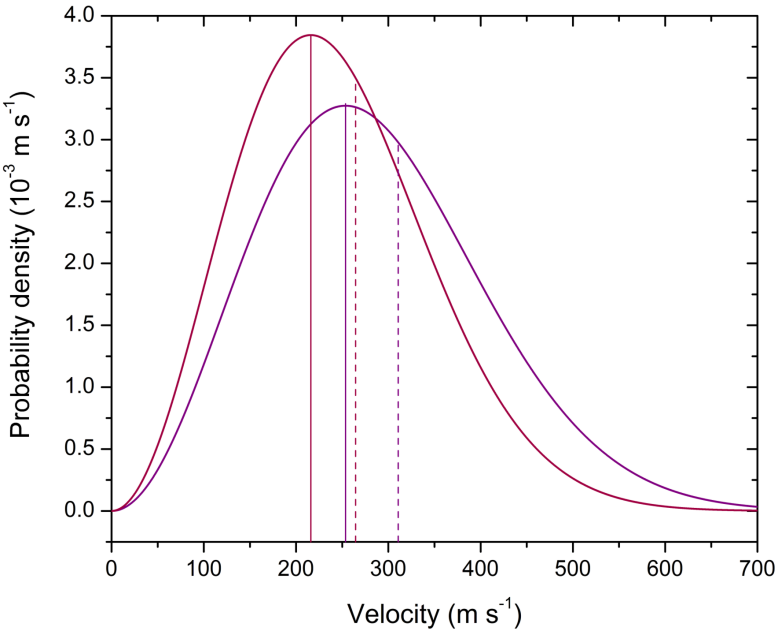

Figure 3.4: The Maxwell-Boltzmann distribution for Cs at a temperature of 100 °C (red) and Yb at 400 °C (purple). The solid red (purple) line shows the average velocity for a gas, v_g, in the oven, whilst the dashed red (purple) line shows the average velocity in the atomic beam, v_b, for Cs (Yb).

in the oven (calculated in the previous section with equation (3.3)) and v_g is as given in equation (3.7). This result is derived in full in [105].

Following from this, the total intensity of atoms leaving the aperture is:

$$I_A = \int_0^{2\pi} \int_0^{\frac{\pi}{2}} \frac{n v_g A}{2\pi^{3/2}} \cos(\theta) \sin(\theta) \mathrm{d}\theta \mathrm{d}\phi = \frac{n v_g A}{2\sqrt{\pi}} \tag{3.10}$$

and the intensity in the forward direction (i.e., for $\theta = 0$) is:

$$I_0 = \frac{n v_g A}{2\pi^{3/2}}. \tag{3.11}$$

Effusion from a tube: collimating a beam

The atomic beam can be made to be collimated by using a tube with radius r and length L (rather than a plain aperture of area πr^2) as the exit from the oven. If the number density is kept low enough such that the mean free path is large compared to L then only atom-wall collisions take place (rather than atom-atom collisions), i.e., the atoms will still be in the molecular flow regime rather than the opaque (viscous) regime where atom-atom collisions dominate.

When considering a tube rather than an aperture it is useful to define a new variable, q, [105] such that

$$q = \frac{L}{2r}\tan\theta. \tag{3.12}$$

For $q \leq 1$ we have both contributions to the atomic beam intensity from the source where atoms do not strike the wall and also contributions from atoms that have struck the wall and bounced off. For $q \geq 1$ there are only contributions from atoms that have rebounded from the wall.

Therefore, it can be shown (see [105] and the references therein) that the angular variation of the intensity is modified from equation (3.9) to the following form:

$$I(\theta) = \frac{n v_{\mathrm{g}} A}{2\pi^{3/2}} j(\theta), \tag{3.13}$$

where $j(\theta)$ is the angular variation given by

$$j(\theta) = \begin{cases} \alpha\cos(\theta) + \frac{2}{\pi}\cos(\theta)\left[(1-\alpha)R(q) + \frac{2}{3q}(1-2\alpha)(1-(1-q^2)^{\frac{3}{2}})\right] & q \leq 1 \\ \alpha\cos(\theta) + \frac{4}{3\pi q}(1-2\alpha)\cos(\theta) & q \geq 1 \end{cases} \tag{3.14}$$

Here α and β are geometric factors,

$$\beta = \frac{2r}{L}, \tag{3.15}$$

$$\alpha = \frac{1}{2} - \frac{1}{3\beta^2}\left(\frac{1 - 2\beta^3 + (2\beta^2 - 1)\sqrt{1+\beta^2}}{\sqrt{1+\beta^2} - \beta^2 \sinh^{-1}(1/\beta)}\right), \tag{3.16}$$

whilst $R(q)$ is the radial movement of the atom,

$$R(q) = \cos^{-1}(q) - q\sqrt{1-q^2}. \tag{3.17}$$

If $\beta \to \infty$ then equation (3.13) simplifies down to the solution for a thin-walled aperture (equation (3.9)).

The total intensity over all angles for a tube follows

$$I = W I_{\mathrm{A}}, \tag{3.18}$$

where I_{A} is as given in equation (3.10) and where the transmission probability of the tube is,

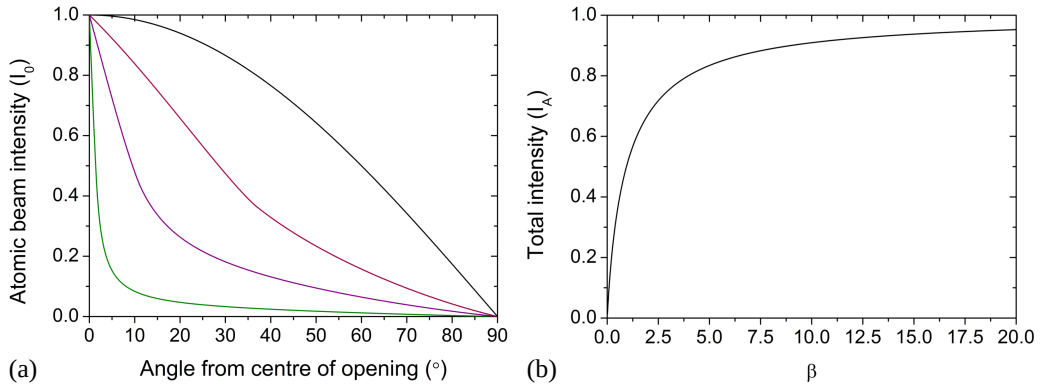

Figure 3.5: (a) The atomic beam intensity as a function of angle from the opening (either aperture or tube) for β values of ∞ (black), 0.75 (red), 0.2 (purple) and 0.029 (green). Collimation of the beam increases as β decreases, however, as can be seen in (b) a smaller β value also reduces the total intensity in the beam as there is now less intensity in the wings.

$$W = 1 + \frac{2}{3}(1 - 2\alpha)(\beta - \sqrt{1 + \beta^2}) + \frac{2}{3\beta^2}(1 + \alpha)(1 - \sqrt{1 + \beta^2}). \qquad (3.19)$$

The intensity profiles for various values of β have been plotted in figure 3.5(a) normalised to the forward intensity, I_0. The case where $\beta = \infty$ (black line) shows the intensity profile for a simple thin-walled aperture of area πr^2, as discussed in Section 3.2.1. The green line shows the intensity profile for a β value of 0.029 which characterises the atomic beam from one of the capillary tubes used in the vacuum system ($r = 0.29\,\text{mm}$ and $L = 20\,\text{mm}$, see Section 3.2.2). The red and purple lines give an idea of how changing the radius and length of the tube can help collimate the atomic beam.

For the same oven pressure and number density, the forward intensity in each case is equal to equation (3.11) for both a thin-walled aperture and a tube, but as the total intensity decreases for a tube (as $W < 1$), it follows that there will be less intensity in the wings and so fewer atoms are wasted. The total intensity, $I = WI_\text{A}$, as a function of β can be seen in figure 3.5(b); as would be expected the total intensity in the beam decreases as the diameter of the opening decreases (or the length of the tube increases).

Tube array

The results above are for a single tube, however, using an array of tubes can give a greater forward intensity but without loss of collimation. This is because any interference between atomic beams coming from individual tubes can be neglected therefore the forward intensity scales linearly with

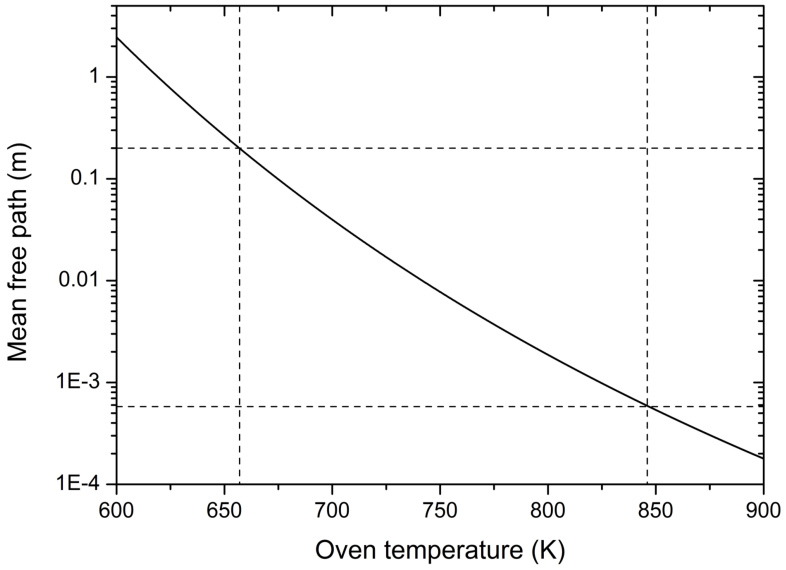

Figure 3.6: The mean free path for Yb in the oven. The two horizontal lines represent where $\Lambda = \beta L$ or $10L$ (the two limits where the flow starts to become opaque (see text).

the number of tubes in the array. Each atomic beam from each tube has the same intensity distribution and so the same collimation.

Molecular versus opaque flow

Molecular flow occurs when the mean free path of an atom is larger than a characteristic length scale: either the diameter of an aperture or the length of a tube that it is travelling through, i.e., $\Lambda > L, 2r$. However, if the pressure increases the mean free path decreases (as seen in equation (3.5)) and atom collisions become more probable. This results in the atom flow becoming 'opaque' (also referred to as viscous flow) with the main drawback being that the angular distribution of the intensity spreads and so collimation of the beam is lost.

Up to a certain point, the atomic flux can be increased by raising the temperature of the oven (and so the pressure or number density), however this does not hold forever. Past a certain pressure the flow will no longer be in the molecular regime and so atoms will start to be lost from the beam. The region at which this starts to occur is when the Knudsen number, $K_{\mathrm{nL}} = \Lambda/L$ is between $\beta \leq K_{\mathrm{nL}} \leq 10$ [105].

Encroaching on this regime is more likely for Yb as higher atomic fluxes (and so higher temperatures) are required to perform spectroscopy on the 556 nm transition. Therefore the vapour pressure for Yb (equation (3.1)) was substituted into the equation for the mean free path (equation (3.5))

with the radius of an Yb atom as $d/2 = 175\,\text{pm}$ [109]) and the dependence of the mean free path on the oven temperature was plotted to see the range at which flow begins to become opaque. The resulting graph can be seen in figure 3.6; the two horizontal lines show where $\Lambda = \beta L$ and $\Lambda = 10L$, giving a temperature range of approximately $669 \leq T \leq 867\,\text{K}$ ($396 \leq T \leq 594\,^\circ\text{C}$).

Empirically speaking, this temperature range fits the observations we have seen in the Yb spectroscopy beam machine (see Section 4.4.3). When running the oven at 560 °C a coating of Yb was seen forming a disc around the first aperture after the oven in an early version of the beam machine, suggesting that the Yb beam was no longer collimated. The lower end of this temperature range is less than the Yb oven temperature in the main vacuum system and, indeed, a thin coating of Yb is seen on the rotary shutter suggesting that even at 400 °C we are starting to enter this regime. This is not in itself a problem as we still get sufficient flux at the science chamber even if collimation of the Yb beam is compromised. Collimation could be regained by running the Yb oven at a lower temperature, however, the total atomic flux seen in the science chamber would be less.

Further increases in pressure above this point ($K_{\text{nL}} < \beta L$) lead to hydrodynamic effects becoming dominant and all collimation is lost. Operation of an oven then becomes inefficient as most atoms do not travel down the system.

3.2.2 Design and construction of the dual species oven

From Section 3.2.1, the design requirements for the dual species oven are that two separate sections with different temperatures are needed to get the correct vapour pressures for the two metals; 100 °C for Cs and 400 °C for Yb, and that the two atomic beams need to be overlapped and collimated using an array of capillary tubes to increase the forward intensity whilst keeping a high directivity. The place where this occurs should be the hottest part of the oven to avoid clogging the capillaries.

The Yb source is three ingots of Yb totalling 5 g (Sigma-Aldrich, 261300-5G) heated by a nozzle heater (Watlow, MB1J2AN1-X56, 450 W) clamped over a copper block to increase the thermal contact with the oven (see figure 3.7(b)). The flux of atoms going down the vacuum chamber can then be directly controlled by changing the temperature of the Yb oven separately.

A nickel gasket was chosen for use in the DN16 blank flange forming the bottom of this oven section as ytterbium often reacts in similar ways to strontium and work with this metal [110] suggested that copper gaskets would very readily react with the Yb. However, subsequently we found that a group in Washington [111] had found that the opposite was true and that Yb reacted with nickel and their vacuum system was subsequently compromised. To eliminate doubt over this, samples of different gasket materials (nickel, copper and silver-plated copper) were placed in the beam machine used for

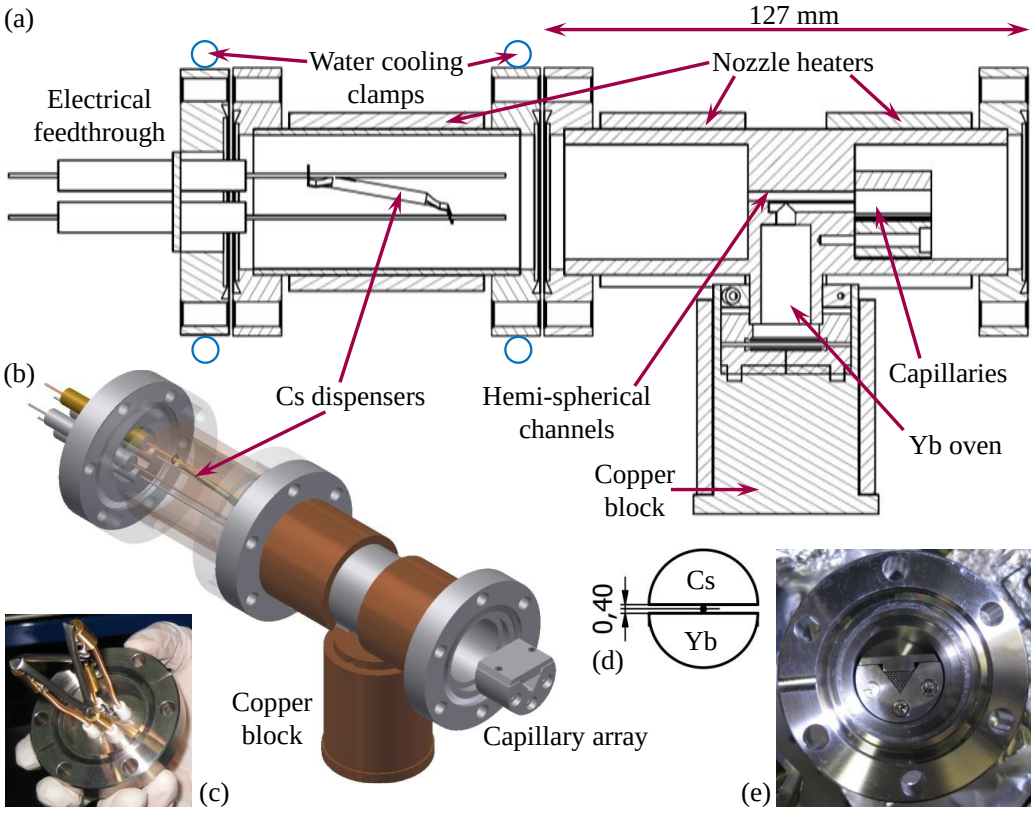

Figure 3.7: The dual species oven. (a) The Cs comes from three dispensers whilst the Yb source is three ingots. The atoms travel along hemi-spherical channels cut into the main oven section before passing through an array of capillary tubes. (b) Four nozzle heaters control the temperature gradient of the oven in conjunction with water-cooled clamps on some of the flanges. The location of two are shown in the diagram as blue circles whilst another two are clamped onto the six way cross immediately adjoining the oven to bring the temperature of the vacuum system back to room temperature in as short a distance as possible. (c) The Cs dispensers are arranged in such a way as to spray the inside walls of the oven with Cs, which will then act as a reservoir to be heated with the nozzle heaters. (d) The two hemi-spherical channels are separated by 0.4 mm allowing the atomic beams to overlap when they exit the oven. (e) The capillary array containing 55 tubes is bolted over the channels to collimate the atomic beams.

spectroscopy. Some pitting on the surface of the nickel gasket was found, appearing to confirm the findings of [111] but there was no change to the surfaces of the copper and silver-plated copper samples. At the time of writing, micro-leaks had started to develop in the oven section which meant that the oven had to be brought up to air for the nickel gasket to be replaced with a non-reactive copper one.

As can be seen in figure 3.7(c), the source for the Cs is an array of three 250 mg dispensers (Alvatec, AS-3-Cs-250-S) that can be individually addressed via the feedthrough flange (MDC Vacuum, HV5-30C-4-C40). The wiring diagram for these dispensers can be found in Appendix D. The Cs oven itself is simply a DN40 nipple (MDC Vacuum, CST40) that the dispenser array slides into. The dispensers are positioned in the oven such that they spray the Cs onto the walls of the tube so the vapour pressure, and therefore the atomic flux, can be controlled using another nozzle heater clamped over the body of the oven (see figure 3.7(a)).

Unfortunately, as mentioned above, after several months of running the oven at the temperatures required to produce both Cs and Yb atomic beams the vacuum in the oven section started to degrade. During the process of bringing the oven up to air the Cs dispensers oxidised, so they were replaced with six smaller 3.9 mg dispensers from SAES Getters (Cs/NF/3.9/12 FT10+10). Therefore, Chapter 6 contains results obtained from both sets of dispensers, however it is made clear on the text which set of dispensers were used.

The Cs oven was placed the furthest away from the capillaries as it needs to be the coolest part of the dual species oven to maintain the correct vapour pressure. A constant temperature of 100 °C is maintained across this oven section using a combination of a nozzle heater and water-cooled clamps on the two flanges of the nipple.

Once the Cs atoms have been heated they exit the oven through a hemi-spherical channel wire-eroded into the main oven (figures 3.7(a) and (c)). A similar channel is cut to provide a route for the Yb atoms to leave their oven section. The two channels are separated by 0.4 mm and this allows the atomic beams to be spatially overlapped. This main part of the oven was made by the mechanical workshop at Imperial College London and the technical drawing for it can also be seen in Appendix D.

An array of 55 capillary tubes (figure 3.7(e)) is clamped in a triangular mount (see Appendix D) and bolted over the hemi-spherical channels to collimate the atomic beams. Each 20 mm long capillary tube (Coopers Needleworks) is made of 304 stainless steel and has an inner diameter of 0.58 mm and an outer diameter of 0.89 mm.

A final nozzle heater (Watlow, MB1J1JN4-X36, 600 W) is placed over the location of the capillaries and this maintains the highest temperature in order to avoid clogging. The nozzle heater temperatures are given in table 3.1 along with the corresponding measured temperatures. Several thermistors have

Nozzle heater	T_{set} (°C)	T_{meas} (°C)
Cs oven	100	83
Middle	390	238, 267
Yb oven	400	434
Capillaries	570	478

Table 3.1: The temperature set points and corresponding measured temperatures along the dual species oven. Two measured temperatures are quoted for the middle nozzle heater; the lowest near the water-cooled flange next to the Cs oven and the highest closer to the capillaries.

been placed at various parts of the oven to monitor temperatures and ensure that the correct temperature gradients are being achieved. There is only a 40 °C difference between the Yb oven and the capillaries, which is not ideal, however, to date it has not caused a problem. In a second generation design, the tube forming the Yb oven may be lengthened, allowing independent cooling of the Yb oven and a greater temperature gradient to be achieved.

The whole oven section

Whilst the most critical part of this region of the vacuum system to design is the dual species oven itself, there are other considerations to address with respect to the design of the rest of the oven section. These include ensuring that there is adequate pumping to remove the hydrogen that will be baked out of the metal of the oven chamber when it is operational, as if the pressure becomes too high no atomic beam will form as there will be too many collisions between atoms in the beam and background gas. This pumping is achieved with a $55\,\text{l}\,\text{s}^{-1}$ ion pump in combination with a Non-Evaporable Getter (NEG) pump. These will be discussed in more detail in Section 3.6 but their location in the oven section can be seen in figures 3.8(a) and (b).

The six-way cross (MDC Vacuum, CX6-40) after the oven, visible in figure 3.8(b), has further water-cooling clamps around it (seen as pairs of blue circles in the figure), decreasing the temperature of the metal back to room temperature in as short a distance as possible, thus decreasing the pressure due to out-gassing of hydrogen from the metal. This cross also houses a rotary shutter for blocking the atomic beams.

It is advantageous to be able to block the atomic beam after loading the MOT as this prevents hot atoms from colliding with the trapped atoms in the MOT. Therefore, in the six-way cross immediately after the oven a shutter has been attached to a motorised rotary motion feedthrough (MDC Vacuum, BRM-275-03) (see Appendix D for the technical drawing of the shutter), allowing the atomic beams to be blocked with a command from the LabVIEW control program (described in Section 4.6).

(a)

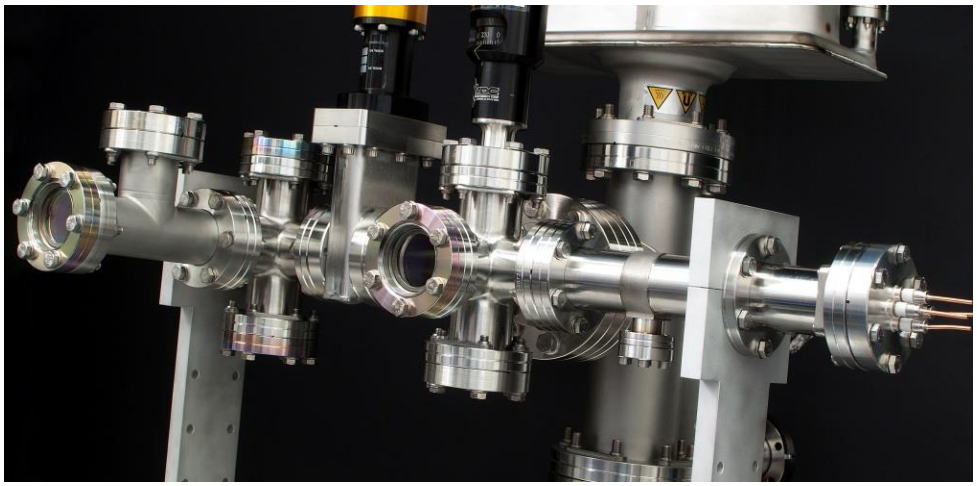

(b)

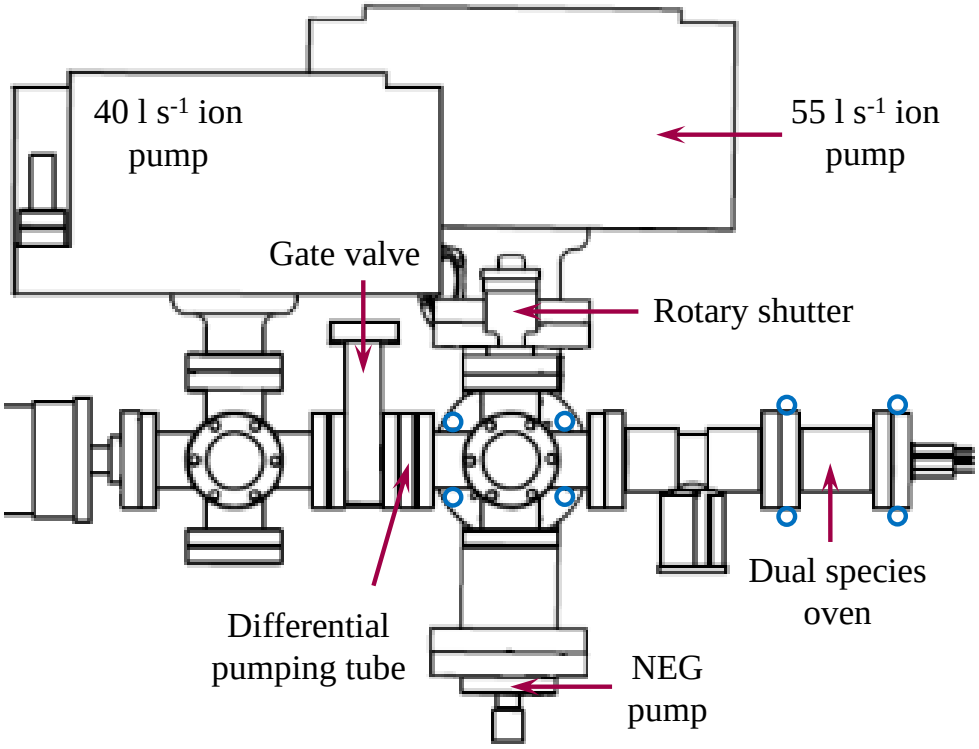

Figure 3.8: (a) A photograph taken of the oven and spectroscopy sections before their first bake. At this time the $40\,\mathrm{l\,s^{-1}}$ ion pump was still on an old vacuum system and wasn't added until the final bake out of the entire vacuum system, however the tee for it to be attached to can be seen towards the left of the photograph. (b) A schematic of the oven and spectroscopy sections, with key components such as the gate valve, differential pumping tube and pumps labelled. The locations of the water cooled clamps are shown as pairs of blue circles.

(a) 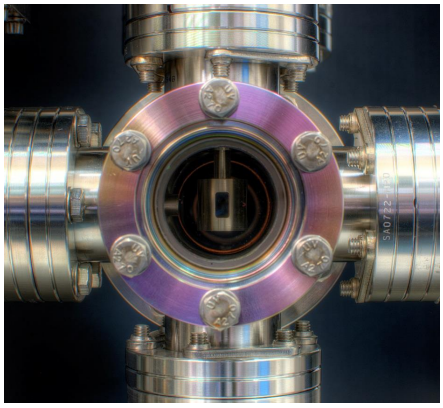 (b) 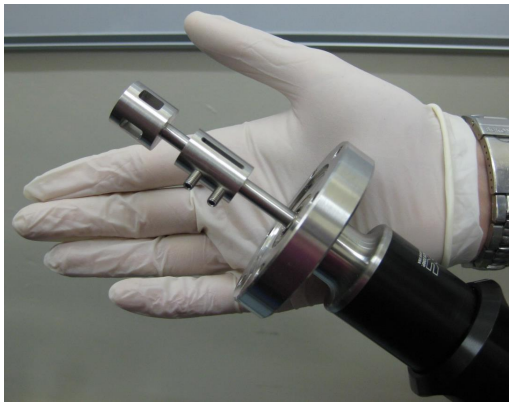

Figure 3.9: (a) The rotary shutter is centred on the atomic beam position and allows the atomic beam to be blocked when not in use. The differential pumping tube can be seen in the left of the viewport. (b) Two of the apertures in the shutter can be seen along with the grub screws holding the shutter on to the motarised feedthrough. The two longs slots allow trapped gas from the threads of the grub screws to escape.

The rotary shutter can be seen in figure 3.9. The shutter has two 5 mm notches cut through it at 90° to each other (figure 3.9(b)) such that one full revolution gives four pulses of atoms. This allows spectroscopy to be performed on the atomic beam when the shutter is open as light can be shone through perpendicular to the atomic beam.

The shutter is clamped to the rotary feedthrough with two grub screws. Two thin slots have then been machined into the top of the shutter which allows trapped gas to be released from the grub screw threads (see figure 3.9(b)).

A gate valve (MDC Vacuum, E-GV-1500M-11) separates the oven from the rest of the vacuum system, allowing the Cs dispensers or Yb ingots to be replaced without breaking vacuum in the science chamber. In a future second generation oven a further valve would be introduced between the Cs and Yb oven sections allowing the Cs dispensers to be replaced without disturbing the Yb oven. This gate valve would also stop Cs atoms escaping the oven, which they will do even at room temperature due to the relatively high vapour pressure of Cs; this will therefore increase the lifetime of the Cs source.

3.2.3 Testing the atomic beams

The first test that needed to be performed on the vacuum system oven was to see whether the capillaries were working as expected and were forming a collimated Cs atomic beam. The Yb beam was tested at a later date as the lasers for this species were still being developed at Imperial College London.

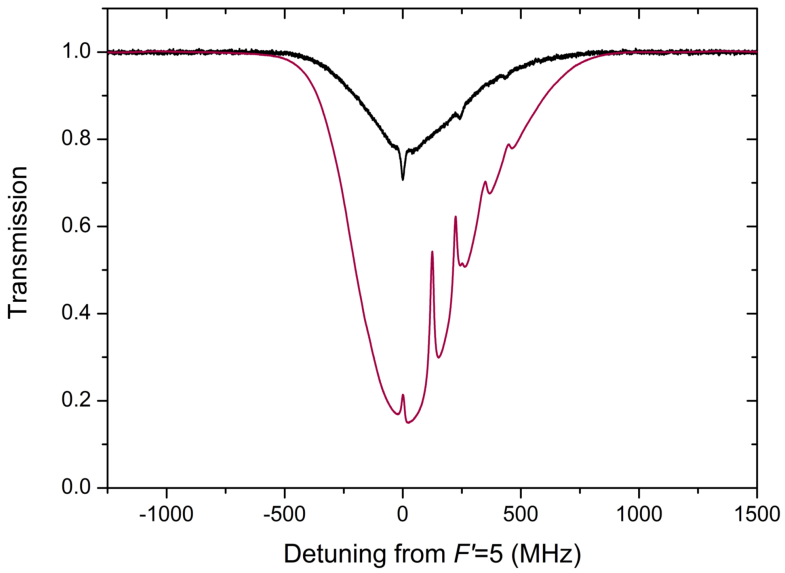

Figure 3.10: A comparison between Cs spectroscopy on the atomic beam (black trace) and in a vapour cell (red trace) as a reference. In the black data the absorption dips due to the atomic beam can be seen overlaid on a small Doppler background.

Caesium

To get the first signal from the Cs atomic beam in the vacuum system the Cs nozzle heater was run at 200 °C with the capillaries at 300 °C. Cs dispenser 1 (see wiring diagram in Appendix D) was run at the minimum activation current of 4 A for 3 hours and then at 6 A for a short time in order to boost the amount of Cs available on the walls of the oven to form a beam.

Beam profile

The absorption recorded from the Cs atomic beam can be seen in figure 3.10 along with a reference spectroscopy signal. The absorption dips from the $F' = 5$, $F' = 4$ and $F' = 3$ lines can clearly be seen on top of a Doppler background. The Doppler background is thought to be due to Cs depositing either on or nearby the capillaries as it was found that the Doppler profile could be reduced by increasing the temperature of the capillaries.

With the atomic beam detected, the Cs oven temperature could be turned down to 100 °C in order to preserve the amount of Cs and so the lifetime of the oven. The capillary nozzle heater was then at 150 °C, the middle heater at 100 °C and the Yb oven heater was not turned on. These oven settings were routinely run whenever Cs was being used alone in order to not deplete the Yb unnecessarily.

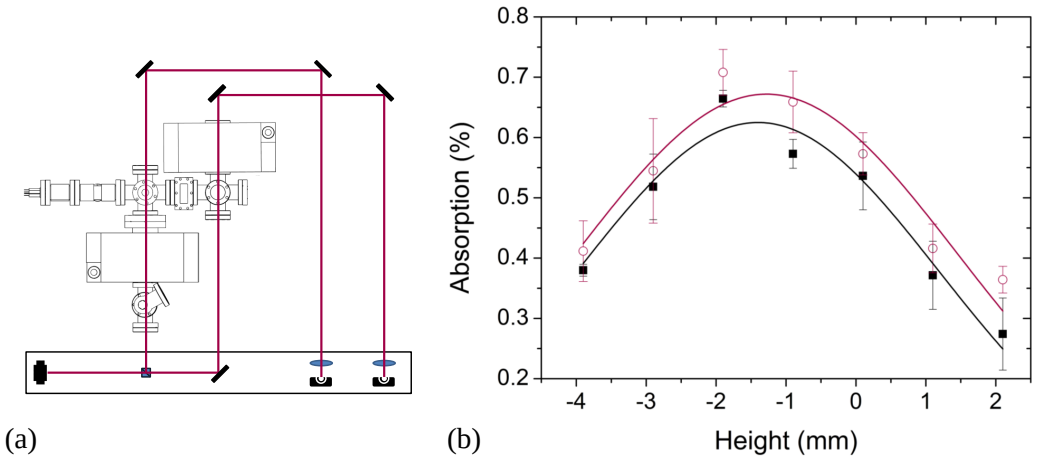

Figure 3.11: (a) The probe laser beams were set up on a breadboard which was translated vertically with respect to the viewports. The mirrors on the opposite side of the vacuum system had a large diameter so the probe beams did not need to be realigned each time. (b) The black squares are from the first set of viewports, through the rotary shutter. The red circles are data taken through the spectroscopy section six-way cross. The black and red lines are Gaussian fits to the data that have been constrained to be zero in the wings.

The atomic beam profile for Cs was measured at two places; through the rotary shutter straight after the oven and through the second six-way cross before the Zeeman slower (at (127 ± 5) mm and (361 ± 5) mm from the capillaries in the oven respectively). The measurements were taken by collimating two probe beams on an optical breadboard and translating the breadboard vertically with respect to the oven viewports (figure 3.11(a)). The probe beams both had the same $1/e^2$ diameter; (0.75 ± 0.06) mm horizontally and (0.82 ± 0.06) mm vertically. The beam through the first set of viewports had a power of $(1.37 \pm 0.05)\,\mu$W, whilst that through the second set was $(1.34 \pm 0.05)\,\mu$W. The absorption of each probe due to the Cs atomic beam was measured for different heights and the results can be seen in figure 3.11(b).

A Gaussian of the form,

$$y = \frac{A}{\sigma\sqrt{\frac{\pi}{2}}} \exp\left(-2\left(\frac{\mathrm{x} - \mathrm{x_c}}{\sigma}\right)^2\right), \tag{3.20}$$

was used to fit the data, where A is an amplitude and σ is the standard deviation. This Gaussian has been constrained to equal zero in the wings as where there is no atomic beam there will be no absorption of the light. The FWHM (denoted w here) of the beam at the two locations can be cal-

culated from this Gaussian as $2\sqrt{0.5\ln 2}\sigma$ giving $w_1 = (6.1 \pm 0.5)\,\mathrm{mm}$ and $w_2 = (6.5 \pm 0.6)\,\mathrm{mm}$ at $(127 \pm 5)\,\mathrm{mm}$ and $(361 \pm 5)\,\mathrm{mm}$ from the capillaries. Therefore, it can be concluded that the capillaries are working as expected and give a well collimated Cs atomic beam as the two measured widths were equal to within error. The half angle of divergence can be calculated to be $(0.05 \pm 0.08)^\circ$ using the small angle approximation with the known distances, L_1 and L_2, between the two width measurements:

$$\theta = \frac{w_2 - w_1}{2\,(L_2 - L_1)}. \tag{3.21}$$

The error on the divergence angle is larger than the angle itself as the two widths are equal to within error.

Atomic velocity

The velocity of the Cs atoms was determined by probing the atomic beam at a slight angle, 6°, from perpendicular to the atomic beam and measuring the shift in the frequency of the absorption peak. This gives information on the velocity as:

$$\omega = \omega_0 - kv, \tag{3.22}$$

where

$$\delta = kv = \frac{2\pi v}{\lambda}. \tag{3.23}$$

So, converting out of angular units, the frequency shift due to the component of the atomic velocity along the direction of the probe beam is,

$$\delta_{\parallel} = \frac{v \sin\theta}{\lambda}. \tag{3.24}$$

The measured value of $\delta_{\parallel} = (31 \pm 1)\,\mathrm{MHz}$ for an angle of $\theta = 6^\circ$. Therefore, rearranging the above equation gives $v = (260 \pm 10)\,\mathrm{m\,s^{-1}}$. This agrees to within error with the velocity calculated using equation (3.8) for a Cs beam.

Ytterbium

Beam profile

The width of the Yb atomic beam was also measured at two different locations to get an idea of how well collimated the beam is. This time the measurements were taken at the second six-way cross and at the science

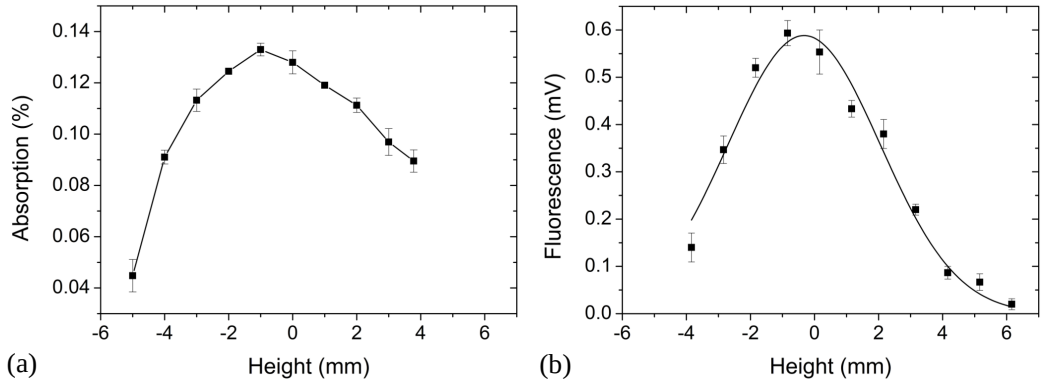

Figure 3.12: The Yb atomic beam profile at (a) the six-way cross near the oven and (b) the science chamber. The atomic beam appears to be smaller at the science chamber, however, this could be an artefact of the small signals recorded. The line in (a) is purely to guide the eye.

chamber using the $^1S_0 \rightarrow ^1P_1$ transition at 399 nm. Absorption data could only be taken near the oven and fluorescence had to be used at the science chamber as the atomic beam was too diffuse to detect absorption.

Unlike for Cs where narrow probe laser beams were used, for measuring the Yb atomic beam profile the probe beam was expanded to a large diameter and a 2 mm aperture translated vertically across it. At the six-way cross (figure 3.12(a)), the depth of the absorption feature for ^{174}Yb (the most abundant isotope) was measured on an oscilloscope (Tektronix, DPO 4034B) with the signal from the photodiode being AC coupled. A percentage absorption was then calculated by measuring the constant background on the photodiode when DC coupled.

The FWHM at the cross, figure 3.12(a), is (9 ± 2) mm, although, as the data were taken by translating a 2 mm aperture across the beam, this may be a convolution of the atomic beam width with that of a 2 mm aperture, giving an approximate FWHM of (7 ± 2) mm.

Figure 3.12(b) shows the fluorescence data taken at the science chamber and this gives a Gaussian width of (4.7 ± 0.4) mm. Again, this data may also be a convolution of the aperture and the atomic beam, however, the fluorescence signal was very small and close to indistinguishable from noise at the edges of the beam so the actual width may be larger. It is therefore not sensible to try and calculate a divergence angle for Yb as was done for Cs. When a large probe beam was shone on the atomic beam, the widths at the two ends of the vacuum system appear approximately equal by eye.

Transverse velocity

A complete fluorescence spectrum was taken at the science chamber, with every Yb isotope apart from the least abundant ^{168}Yb being detected, see figure 3.13(a). In order to obtain this spectrum, fluorescence from the atomic beam was collected onto a Thorlabs DET110 photodiode and compared to some etalon peaks from the same laser. The scan of the laser was not linear in frequency so the data had to first be linearised.

This was done by using two etalon peaks to convert the horizontal axis from time (as recorded on the oscilloscope trace) to frequency. The spectrum was then centred on the largest signal (from ^{174}Yb). The frequency shifts from ^{174}Yb to the rest of the distinguishable isotope peaks were then measured and compared to a reference (table 2.2, [71]). The differences were plotted versus the measured frequencies that the peaks occurred at and a high order polynomial was fitted to the data. This polynomial was then subtracted from the frequency axis, thus making the peaks from the various isotopes occur at the correct frequencies.

Some peaks in the spectra in figure 3.13(a) arise from multiple isotopes whose isotope shifts are similar, however, the widths of the peaks formed from a single isotope can be used to estimate the transverse velocity of the atoms. This was done by fitting a Voigt profile to the peaks with any Gaussian broadening from the fixed Lorentzian natural linewidth ($\Gamma = 2\pi \times 30.6\,\mathrm{MHz}$) indicating Doppler broadening due to the transverse velocity of the atoms.

The Voigt profiles fitted to each of the three peaks (^{176}Yb, ^{174}Yb and ^{171}Yb, $F = 3/2$) gave Gaussian widths of $(26.8 \pm 0.7)\,\mathrm{MHz}$, $(22.5 \pm 0.4)\,\mathrm{MHz}$ and $(21 \pm 1)\,\mathrm{MHz}$ respectively. These peaks can be seen in figures 3.13(b), (c) and (d).

The Gaussian width, σ, relates to the temperature, T, of the beam as

$$\sigma = \sqrt{\frac{k_\mathrm{B}T}{mc^2}} f_0 \tag{3.25}$$

where f_0 is the frequency of the transition. Re-arranging this gives a transverse 'temperature' of

$$T = \left(\frac{\sigma}{f_0}\right)^2 \frac{mc^2}{k_\mathrm{B}}. \tag{3.26}$$

The rms velocity is then given by the following formula:

$$v_\mathrm{rms} = \sqrt{\frac{3k_\mathrm{B}T}{m}} = \frac{\sqrt{3}\sigma c}{f_0}. \tag{3.27}$$

Calculating this velocity for the three peaks gives $(17.6 \pm 0.5)\,\mathrm{m\,s^{-1}}$,

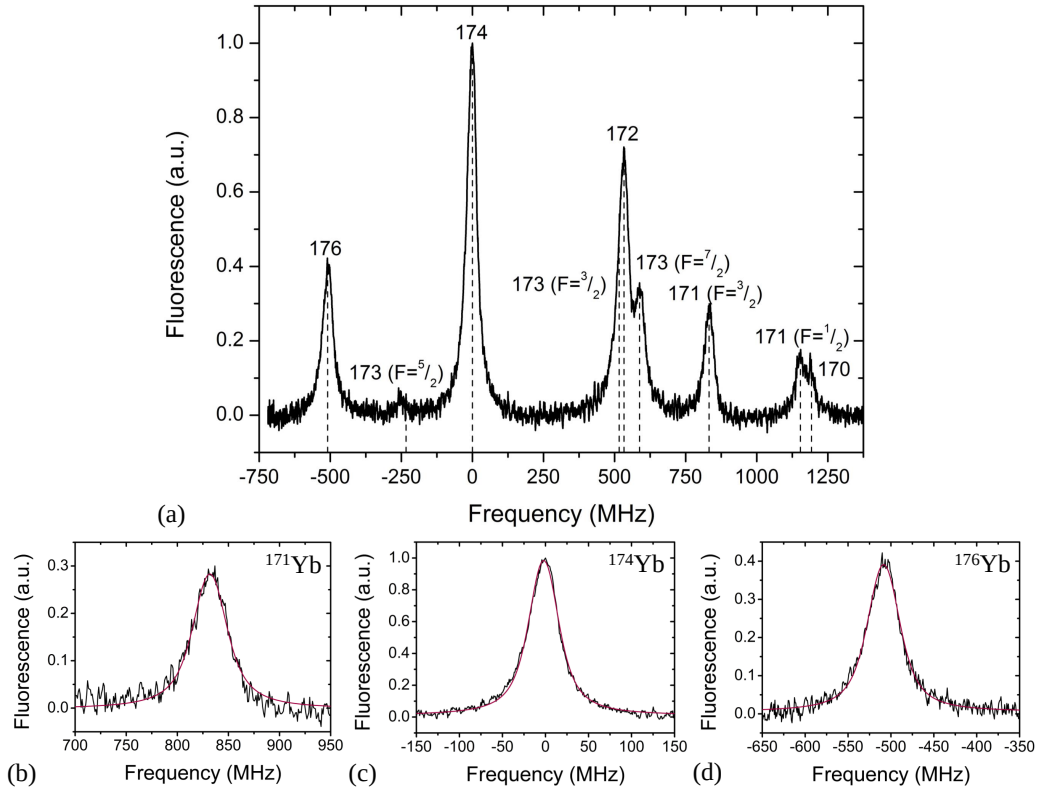

Figure 3.13: (a) The full Yb fluorescence spectrum recorded in the science chamber where signals from every isotope apart from the least abundant ^{168}Yb can be seen. Each of the single isotope peaks for (b) ^{171}Yb, $F = 3/2$, (c) ^{174}Yb and (d) ^{176}Yb were fitted with Voigt profiles (red lines) to calculate the transverse velocity (see text).

$(15.1 \pm 0.3)\,\mathrm{m\,s^{-1}}$ and $(13.1 \pm 0.7)\,\mathrm{m\,s^{-1}}$ for ^{176}Yb, ^{174}Yb and ^{171}Yb respectively, or a weighted average (using the method in [112]) of $(15.4 \pm 0.2)\,\mathrm{m\,s^{-1}}$. Whilst this is larger than the Yb MOT capture velocity, either power or artificial broadening of the MOT beams would allow atoms with this velocity to be captured (see Sections 4.2.2 and 4.2.3).

Using the average transverse velocity, the divergence of an atom travelling at the average beam velocity, v_b, can be calculated. This yields a value of $(61.9 \pm 0.8)\,\mathrm{mm}$ (or a half-angle of $(1.41 \pm 0.04)^\circ$). This seems like quite a large divergence but considering that the Yb beam may not be very well collimated in the temperature regime in which the oven is operating this may not be unreasonable.

3.3 Spectroscopy section

The main purpose for the spectroscopy section is to allow access to the atomic beams for spectroscopy (or potentially transverse cooling). However, this section has other uses in terms of the level of vacuum as a connection between the oven and the rest of the vacuum system.

The oven runs at relatively high pressures due to the temperatures involved and so an extra pumping stage is advantageous before the atomic beam is sent down the Zeeman slower due to vacuum conductance considerations.

3.3.1 Vacuum conductance and differential pumping

Ultra high vacuum is required in the science chamber so that trap lifetimes will be as long as possible. Therefore, the high pressure oven must be isolated from the science chamber and this is achieved using a series of differential pumping tubes.

Differential pumping arises as a consequence of the conductance of molecules in a vacuum going through tubes of different dimensions. In the molecular flow regime, as in high vacuum, the conductance of a tube in $\mathrm{l\,s^{-1}}$ is [113]:

$$C = 12\frac{D^3}{L}, \tag{3.28}$$

where D is the diameter of the tube and L is its length (both in centimetres). This formula is for air at 20 °C but gives a good indication of what the conductance of a high vacuum system will be. It can be seen that the conductance depends heavily on the diameter of the tube, therefore, using a tube with a smaller diameter decreases the conductance, allowing areas with different pressures to be isolated as much as possible.

In the vacuum system, there is a differential pumping tube after the rotary shutter (which can be seen at the left edge of the viewport in figure 3.9(a)). It has an inner diameter of 5 mm and a length of 60 mm. This gives a conductance of $0.25\,\mathrm{l\,s^{-1}}$, which is orders of magnitude smaller than the conductance of a DN40 tube of the same length, $124\,\mathrm{l\,s^{-1}}$. In addition to this, the Zeeman slower tube also acts as a second differential pumping stage with a conductance of $0.64\,\mathrm{l\,s^{-1}}$, although this stage is less effective as the diameter is larger, which isn't quite compensated for by its increased length. For two tubes in series the conductances add as:

$$C_{\mathrm{tot}} = \left(\frac{1}{C_1} + \frac{1}{C_2}\right)^{-1}, \tag{3.29}$$

giving a combined differential pumping conductance from the oven to the science chamber of $0.18\,\mathrm{l\,s^{-1}}$.

3.3.2 Spectroscopy section design

The spectroscopy section can be seen in figure 3.8(b) and simply consists of a six-way cross (MDC Vacuum, CX6-40) with a $40\,\mathrm{l\,s^{-1}}$ ion pump connected to it via a DN40 tee (MDC Vacuum, ET40). The viewports on the cross and one end of the tee are anit-reflection coated for 399 nm, 556 nm and 852 nm so both the Cs and Yb transitions can be probed if necessary.

The $40\,\mathrm{l\,s^{-1}}$ ion pump is included as a by-product of the differential pumping described above; as the both the Zeeman slower and differential pumping tubes limit the conductance to the science end pumps and oven pumps respectively. The pressure achievable at the spectroscopy section would be limited without the additional ion pump. This is especially true overnight as the gate valve is shut every day during the time when the oven is cooling in an effort to delay Yb coating the Zeeman slower viewport at the other end of the vacuum system.

3.4 Zeeman slower tube

The Zeeman slower tube is simply a DN16 pipe with an inner diameter of 16 mm and a length of 770 mm with a short bellows section (MDC Vacuum, 075-X) connecting to the science chamber. This was the last connection made when the vacuum system was bolted together, allowing the flexible bellows to absorb any stresses due to misalignment of the two halves of the system. Perfect horizontal alignment could not be guaranteed before the final connection was made due to the large size of the system, therefore there had to be some flexibility built in. The final alignment was achieved by visually sighting along the system from the Zeeman slower viewport at one end and making sure that the apertures formed by the entrance and exit of the Zeeman slower tube were centred on each other and equidistant from the two welds from the science chamber viewports either side of the Zeeman slower (see figure 3.14(a)).

The Zeeman slower coils were wound on to a separate former which was manoeuvred over the tube before the final connection was made.

As mentioned in the previous section, the vacuum inside the Zeeman slower tube is maintained from both ends by the spectroscopy section ion pump and the science end pumps (see Section 3.6).

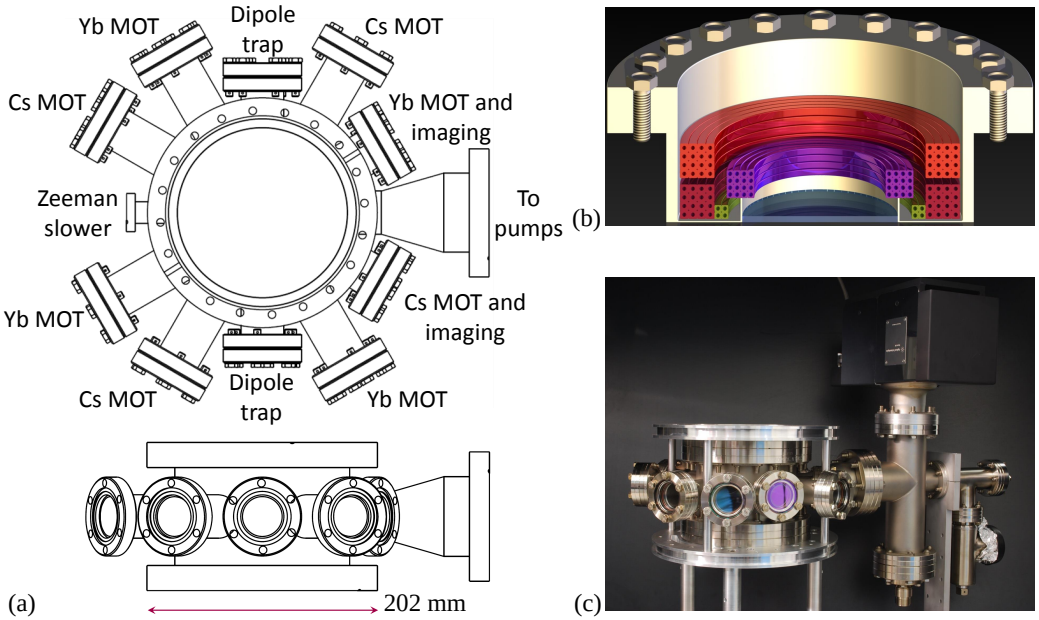

Figure 3.14: (a) A plan and side view of the science chamber, with each set of viewports labelled. (b) The top and bottom viewports are set in re-entrant flanges, which give room for multiple sets of coils to be placed close to the atoms. (c) A photograph of the science chamber and pumping station before connection to the rest of the vacuum system. The top and bottom plates of the science chamber stand have grooves running around their diameter for shim coils to be wound in place.

3.5 Science chamber

The most critical region in the vacuum system is the science chamber where the experiments take place. The design of this chamber had to balance good optical access with the ability to create large magnetic fields; requirements that led to a design where the chamber has ten horizontal viewports with various anti-reflection (AR) coatings and two re-entrant viewports on the top and bottom. The science chamber was a custom part made by VG Scienta and can be seen in figure 3.14(a) (with a more detailed engineering drawing given in Appendix D). The viewport coatings are given in table 3.2.

The re-entrant flanges (figure 3.14(b)) allow coils to be mounted as close to the position of the atoms as possible whilst maintaining optical access. These flanges were custom made by the UK Atomic Energy Authority (UKAEA) and the engineering drawing they supplied is given in Appendix D. The viewport substrates also came from UKAEA, however, they were AR coated by Vortex Optical Coatings to allow 399 nm, 556 nm and 852 nm light through.

There is a viewport at the end of the vacuum system that allows the two Zeeman slowing beams for Cs and Yb through. It is a fused silica Kovar, zero

Viewport	AR coating (nm)	Part number
Cs MOT	730 - 1064	VPZ38LABBAR-LN
Yb MOT	370 - 580	VPZ38LABBAR-LN
Dipole trap	532, 852, 1064	VPZ38LAWAR-LN
Re-entrant	399, 556, 852	Vortex
Zeeman slower	399, 556, 852	Vortex
Six-way cross	399, 556, 852	Vortex

Table 3.2: The viewport coatings for the vacuum system; the top three coatings were supplied by Torr Scientific, the bottom three by Vortex (no part number supplied).

length viewport (Torr Scientific, VPZ38LAQ) with a larger usable diameter, coated by Vortex with the same AR coating as the re-entrant viewports. Similarly, the viewports on the six-way crosses near the oven were bought from VG Scienta (ZVP38QU) but were coated by Vortex. This was done to allow spectroscopy of both Cs and Yb to be performed near the oven and also ensured that the viewports could be used for optical pumping or transverse cooling in the future, if needed.

3.6 Pumping station

After bake-out (detailed in Section 3.7) the vacuum is maintained with a combination of Non-Evaporable Getter (NEG) pumps (SAES Getters, Capacitorr C400-2 DSK) and $55\,\mathrm{l\,s^{-1}}$ ion pumps (Agilent, VacIon 55), both of which can be seen in figure 3.15 (as well as an additional $40\,\mathrm{l\,s^{-1}}$ ion pump (Varian (Agilent) VacIon 40) on the spectroscopy section).

NEG pumps are highly efficient at pumping hydrogen from a vacuum system, with pumping speeds of approximately $400\,\mathrm{l\,s^{-1}}$. Ion pumps on the other hand are better at pumping other molecules, so they clear any Cs that is not in the atomic beam (Yb would immediately adsorb onto the vacuum chamber rather than make it to the ion pumps due to its lower vapour pressure).

The pumping station section seen in figure 3.15 appears in two places on the vacuum system; one is attached to the oven section six-way cross and the other to the science chamber. The main component of the pumping station is a custom-made part (VG Scienta) and the engineering drawing supplied to the company can be seen in Appendix D. It is a modified four-way cross with three arms made from DN63 tubing (with an inner diameter of 63.8 mm) whilst the other is made from a DN40 tube (inner diameter 38.3 mm). The larger diameter of the DN63 tubes allows for a greater vacuum conductance (see equation (3.28)) leading to the ion and NEG pumps. The depth of the bottom DN63 arm is determined by the length of the NEG pump cartridge

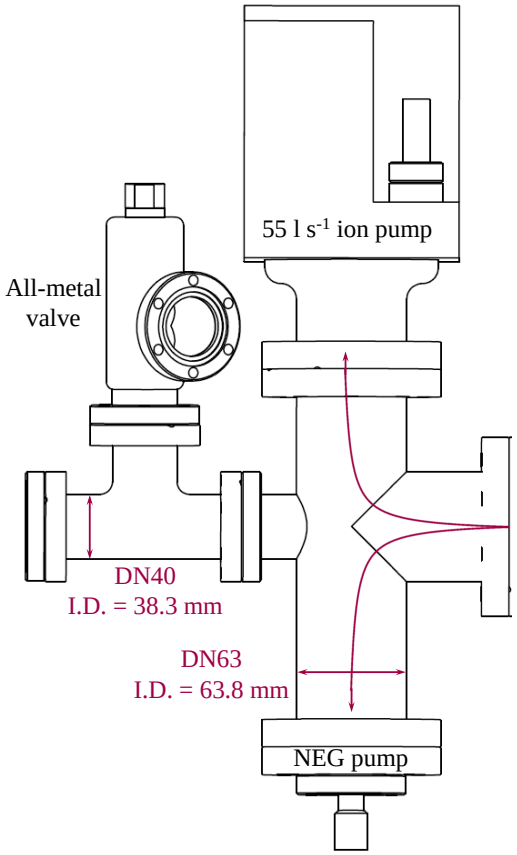

Figure 3.15: The pumping station was designed to maximise the vacuum conductance to the ion and NEG pumps by having sections of DN63 tubing with a larger diameter. The smaller DN40 section connects to the all-metal valves and viewport. The depth of the lower part of the pumping station exactly fits the length of the NEG pump used. The red arrows show the pumping routes for gas molecules within the vacuum system.

and puts a lower limit on the height the optics need to be at. The height of the upper DN63 arm is made as small as possible to minimise the overall height of the vacuum system. The DN40 arm allows connections to the all-metal valve and the DN40 viewports to be made.

When pumping down the vacuum system, all-metal valves (MDC Vacuum, MAV-150-T) provide the connection between the pump and the vacuum system. When complete, extra up-to-air valves (Swagelok, SS-4H-TW) are fitted onto the all-metal valves and then evacuated to provide an extra level of defence in case there are leaks within the all-metal valve.

The construction of the vacuum system was captured in a time-lapse sequence that can be viewed on the groups webpage [114].

3.7 Bake-out procedure

In order to create a vacuum system with a low final pressure, it was necessary to bake the system into a turbo pump. This removes any water, oxygen and other unwanted molecules from the system. The higher the temperature the bake is performed at the better, however, some components such as viewports have a maximum safe temperature so bake-outs are limited by these. A longer bake can compensate for using a lower temperature.

The vacuum system was baked in four steps: separate bakes for the oven, science chamber and Zeeman slower tube then a final bake out with everything connected. Individual bake-outs were done to ensure a better final pressure and so that the Cs atomic beam from the oven could be tested whilst the science end was still being baked.

3.7.1 Vacuum cleaning procedures

Before construction each component of the vacuum system made by the mechanical workshop had to be cleaned in order that no oil or grease would contaminate the vacuum. This involved following the procedure outlined in Appendix E.

3.7.2 Oven

The oven section of the vacuum system was baked in the prep room oven twice, before and after activation of the NEG pump. The first bake was at a temperature of 190 °C over 4 days. Immediately after the section had been cooled back down the NEG pump was activated. This was done by gradually increasing the voltage across the NEG cartridge over 2 hours until it was at 16 V, where is was left for 1 hour. This gradual increase was done so that

the cartridge did not overheat and damage any of the components near it. During this time the pressure measured by the ion gauge on the turbo pump increased by several orders of magnitude (similar to the behaviour seen in figure 3.17(b)).

Once the NEG pump had been activated the ion pump was also turned on. At this point the all-metal valve connecting the oven section to the turbo pump was closed and a second bake was performed into the ion pump. The pressure was then measured via the voltage readout on the ion pump controller which can be converted into pressure using the calibration curve supplied with the pumps. The temperature was left at 145 °C for 4 days for this second bake. The final pressure was at the accuracy limit of the readout on the ion pump.

3.7.3 Science chamber

Initially the science end underwent an air bake, where the chamber was at atmospheric pressure whilst the oven temperature was increased to 190 °C for 6 days. This might lead to a better final pressure as an oxide layer forms on the metal surfaces, preventing some out-gassing of hydrogen during the operational lifetime of the chamber.

After this, two bake-outs under vacuum were performed. In the first the oven temperature was increased to 190 °C over a period of 9 days, with the change in temperature of the oven never exceeding 1 °C/min, to ensure that the viewports were protected (as they cannot undergo temperature changes above 2-3 °C/min). Readouts from the Residual Gas Analyser (RGA) attached to the turbo pump before and after this bake are shown in figure 3.16. An RGA gives the partial pressures of gases according to their molecular weight. As can be seen, before the bake begins the pressure is dominated by water molecules from the atmosphere (molecular weight = 18) but afterwards the vacuum system is hydrogen dominated (molecular weight = 2) which indicates a clean environment where all other molecules have been baked away.

The initial pressure before the first bake was 9.0×10^{-5} Torr at room temperature. After 9 days of baking the final pressure reduced to 4.1×10^{-9} Torr (again, measured once the system was back to room temperature). The NEG pump was not activated on this section as it had to be let up to air again when the whole system was connected and this would reduce the lifetime of the NEG cartridge. However, the ion pump was turned on in order to keep the science section under vacuum whilst other sections were baked. The ion pump voltage measured at this time was 40 mV, corresponding to approximately 1.1×10^{-7} Torr.

A second vacuum bake was performed as there were doubts over the efficacy of the original all-metal valve after being baked in air so this part was replaced and the NEG cartridge inserted at the same time. During this bake the temperature was increased to 185 °C for 5 days. After cooling the ion pump

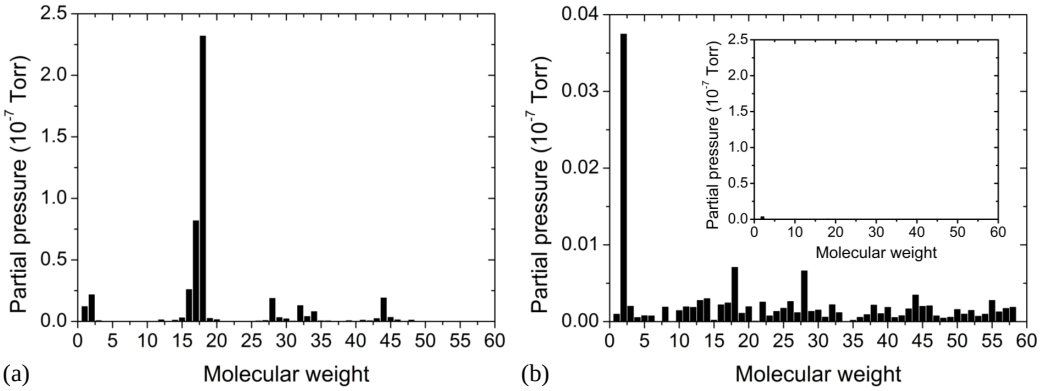

Figure 3.16: Residual gas analyser reading (a) before and (b) after the first vacuum bake of the science end. Water molecules (molecular weight = 18) dominate the readout before baking whilst hydrogen (molecular weight = 2) dominates afterwards. The inset in (b) shows the readout after the bake on the same scale as that before the bake showing a dramatic decrease in the partial pressure.

voltage was now down to 3.5 mV (1.2×10^{-8} Torr).

3.7.4 Zeeman slower tube

The Zeeman slower tube and bellows were also baked separately in order to remove any contaminants. They were wrapped in heater tape rather than put into an oven as the tube was too long. The temperature was increased to 200 °C for 4.5 days.

3.7.5 Complete bake-out

When the final connection between the Zeeman slower bellows and the science chamber was made, nitrogen gas was flushed through the system to ensure very little water vapour went back into the system. Whilst the connection was made the middle and science chamber ion pumps were turned off. The gate valve connecting the oven end to the rest of the system remained closed during the final connection and the ensuing bake as the Cs dispensers had already been activated and could not be brought up to air again.

Once the vacuum system was complete it underwent a final bake-out on the table in the lab, as by this point the system was too large to fit in the prep room oven. The bake-out was done by winding heater tapes around the system and insulating it with aluminium foil. Care was taken to make sure the heater tapes were not too close to any viewports so direct heat would not exceed the maximum temperature change rate. Temperatures

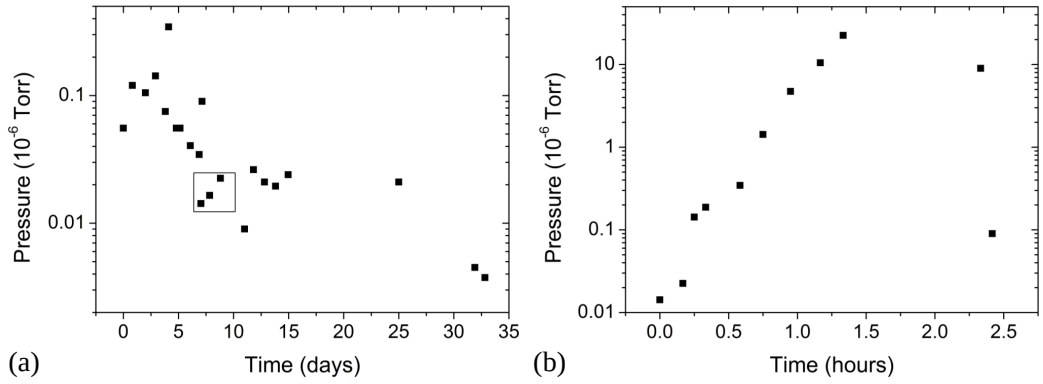

Figure 3.17: (a) Pressures during the bake out of the complete system. The highlighted area corresponds to the NEG pump activation, which can be seen in more detail in (b). During the activation process the pressure increases by several orders of magnitude before decreasing rapidly again. The last six points in (a) are readings from the ion pump controller as the bake was carried out into the ion pumps at this stage.

Ion pump	V_{ion} (mV)	Pressure (Torr)
Oven	90.0	7.5×10^{-8}
Spectroscopy	5.0	7.5×10^{-9}
Science chamber	1.9	3.8×10^{-9}

Table 3.3: The final voltage readouts from the ion pump controllers can be converted into known pressures inside the vacuum system.

were monitored with multiple thermocouples taped to the vacuum system underneath the insulation.

The vacuum system was baked at approximately 140 °C (temperatures varied slightly over the length of the vacuum system) for 4 days before the temperature was reduced in the vicinity of the NEG pump in order for it to be activated in the same way as for the oven section. The temperature was then increased to the same level again and left for a further 3 days. Once the system had been cooled down the valve to the turbo pump was closed and the ion pumps turned on. A final bake was then performed into the ion pumps, at a temperature of 110 °C for 19 days. A plot of the pressure measured at the turbo pump during the bake out is shown in figure 3.17 (the last six points are pressures read out from the ion pump controller).

After the end of the bake out, the pressure within the vacuum chamber was hydrogen limited and at the limit of the ion pump readouts. The pressures measured for the three ion pumps are given in table 3.3, however, the actual pressures may be lower than these readings as the voltages measured from the controllers are at their accuracy limit.

Chapter 4

Experimental apparatus: Laser systems

The 1997 Nobel Prize for Physics was awarded to Chu, Cohen-Tannoudji and Phillips for the first laser cooling of atoms [1–3] and ever since laser cooling has been common practice in atomic physics experiments world-wide. This chapter describes the laser systems used to cool Cs and Yb and by way of an introduction we start with the basic theory of laser cooling and so discuss the differences between Cs and Yb. More detailed descriptions of the theory of laser cooling can be obtained from various sources such as [69, 108, 115].

4.1 Laser cooling

The principle of laser cooling is quite simple; consider a simple atom with two energy levels separated by $E = hc/\lambda$. A photon of wavelength λ, if absorbed by this atom, will impart a momentum kick of $p = \hbar k$ in the direction of propagation of the photon (where $k = 2\pi/\lambda$ is the wavevector). Absorbing a photon will promote an electron in the atom to the higher energy level. The electron will eventually fall back down to the lower energy state, emitting another photon of the same wavelength. These photons will be emitted symmetrically and so the momentum change of the atom due to their emission will average to zero. This means that the overall momentum change for an atom absorbing N photons will be $-N\hbar k$ relative to the direction of propagation of the photons.

However, this simplistic view is not quite correct as it does not take into account the effect of the velocity of the atom in bringing the photon closer to or further from resonance. If an atom is travelling towards a photon, the frequency it will see will be $\omega' = \omega_{\mathrm{L}} + kv$, where ω_{L} is the angular laser frequency. In other words, the frequency will be Doppler shifted. Therefore, if the photons are red-detuned from the atomic resonance by some detuning,

δ, then an atom counter-propagating to the laser beam will be brought closer to resonance and so will be more likely to absorb the photon and be slowed. An atom moving in the same direction as the photon will be taken further from resonance and so will be less likely to absorb the photon.

The light force felt by the atom is therefore [69]

$$F = \hbar k \frac{\Gamma}{2} \frac{I/I_\mathrm{s}}{1 + I/I_\mathrm{s} + 4\left(\delta/\Gamma\right)^2}, \tag{4.1}$$

where Γ is the decay rate of the excited state (in $\mathrm{rad\,s^{-1}}$), I_s is the saturation intensity and $\delta = \omega_\mathrm{ge} - \omega_\mathrm{L}$ is 2π times the laser detuning in Hz (where ω_ge is the angular frequency on going from the ground to the excited energy level). If $I >> I_\mathrm{s}$ then the force tends to a limiting value of

$$F_\mathrm{max} = \frac{\hbar k \Gamma}{2} = a_\mathrm{max} m, \tag{4.2}$$

as the populations in both the upper and lower level of the atom tend to 1/2.

A single laser beam can slow atoms going in one direction only, however, in reality atoms can be moving in any direction. Therefore, to produce cooling in all directions, three orthogonal pairs of counter-propagating laser beams can be set up such as to slow the atoms' velocity in each direction. Only an atom at rest would feel no force from any beam, but a moving atom will feel a force imbalance acting against its movement due to the Doppler effect. This technique is called optical molasses and it results in a frictional force,

$$\begin{aligned} F_\mathrm{mol} &= F_+ - F_- \\ &= \frac{\hbar k \Gamma}{2} \left(\frac{I/I_\mathrm{s}}{1 + I/I_\mathrm{s} + 4\left(\frac{\delta - kv}{\Gamma}\right)^2} - \frac{I/I_\mathrm{s}}{1 + I/I_\mathrm{s} + 4\left(\frac{\delta + kv}{\Gamma}\right)^2} \right) \\ &\approx \frac{8\hbar k^2 \delta}{\Gamma} \frac{I/I_\mathrm{s}}{\left(1 + I/I_\mathrm{s} + 4\left(\frac{\delta}{\Gamma}\right)^2\right)^2} v = -\alpha v, \end{aligned} \tag{4.3}$$

where α is the frictional coefficient. As the velocity must be relatively small for the light to not be Doppler shifted completely off resonance, any terms including a v^2 term have been ignored. The overall force on an atom can be seen in figure 4.1; for an atom with a negative velocity the force is positive and vice versa so that the atom is slowed regardless of the direction it is moving. The maximum frictional force occurs when $\delta = \Gamma/2$.

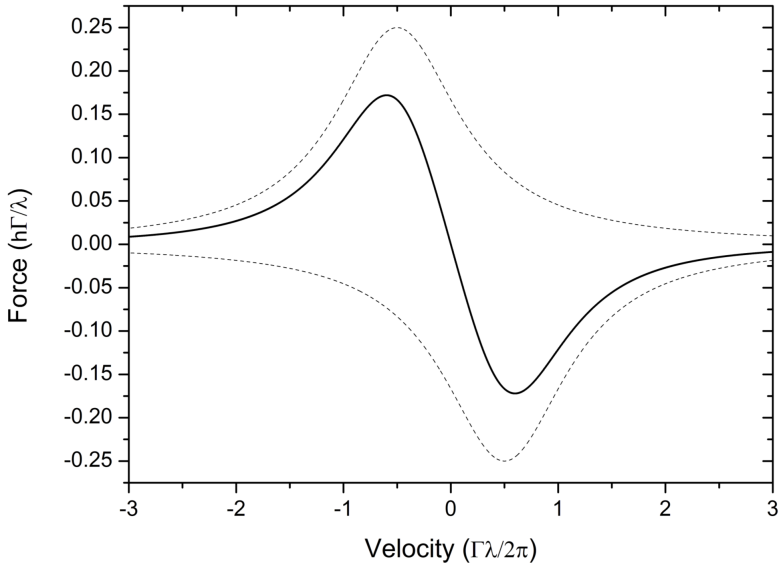

Figure 4.1: The optical molasses force as described in the text with $\delta = \Gamma/2$. The two dashed lines show the force on atoms with negative or positive velocities alone and the solid line is the combined force. An atom with a velocity in the positive direction will feel a force acting in the negative direction and vice versa, pushing the atom back into the centre.

4.1.1 Doppler cooling limit

Naïvely, it could be assumed that the optical molasses technique could cool the atoms to zero velocity, however, this is not true. In reality, the atoms are heated by the process of spontaneous emission which causes them to go on a random walk due to the momentum kicks imparted by each emitted photon. This random walk can be translated into a limiting temperature; the Doppler temperature,

$$T_{\mathrm{D}} = \frac{\hbar\Gamma}{2k_{\mathrm{B}}}. \tag{4.4}$$

A full derivation from this can be found in various textbooks, [69, 108].

The Doppler temperatures for Cs and Yb can be found in table 4.1. The Doppler temperature for the ${}^1S_0 \rightarrow {}^1P_1$ transition in Yb is two orders of magnitude greater than that for the ${}^1S_0 \rightarrow {}^3P_1$ transition due to the larger linewidth. However, the ${}^1S_0 \rightarrow {}^1P_1$ transition does have the advantage that a_{max} is large, making it a good choice for Zeeman slowing whereas the ${}^1S_0 \rightarrow {}^3P_1$ transition at 556 nm is a better choice for a magneto-optical trap because the Doppler temperature is smaller and there is no loss of atoms to other states. The Doppler temperature for Cs is also fairly large, however, Cs is able to access sub-Doppler cooling, as discussed in the next section.

Atom	Cooling transition	Γ (MHz)	T_{D} (μK)	a_{max} ($\mathrm{m\,s^2}$)
Cs	$6\ ^2S_{1/2} \rightarrow 6\ ^2P_{3/2}$	$2\pi \times 5.234(13)$	126	5.79×10^4
Yb	$^1S_0 \rightarrow\ ^1P_1$	$2\pi \times 28.0$	673	5.06×10^5
Yb	$^1S_0 \rightarrow\ ^3P_1$	$2\pi \times 0.1822$	4.4	2.36×10^3

Table 4.1: Some useful properties of Cs and Yb when discussing laser cooling. The linewidth, Γ, Doppler temperature, T_{D} and maximum acceleration, a_{max} are given for Cs and both transitions in Yb. ^{174}Yb was used as a representative example in the calculation of a_{max} for Yb. Linewidths were taken from [53, 60].

4.1.2 Sub-Doppler cooling

For many atomic systems, such as the alkali-metal atoms, cooling to temperatures below the Doppler limit has been observed [116]. There are two possible mechanisms that cause sub-Doppler cooling, both relying on the fact that counter-propagating laser beams cannot be treated independently. The first mechanism uses counter-propagating linearly polarised beams that interfere to produce gradients in the polarisation of the light field, which, when coupled with optical pumping between the Zeeman levels in the hyperfine ground state acts to cool the atoms beyond the Doppler limit.

The second mechanism arises when the two counter-propagating beams have opposite handedness of circularly polarised light. Here the beams interfere to produce linearly polarised light whose polarisation direction traces a helix in space. This rotation leads to a population imbalance among the magnetic sublevels which acts to cool the atoms. Both mechanisms are described in detail in [115].

lin $\perp$ lin configuration: Sisyphus cooling

When two laser beams with orthogonal linear polarisation are counter-propagating they form a standing wave in which the polarisation varies with position depending on the relative phase of the two beams. The polarisation of the resultant electric field goes from linear to left handed circularly polarised to linear to right handed circularly polarised and then back to linear over a distance of $\lambda/2$.

Consider an atom, such as Cs, with a ground state of $J = 1/2$ and an excited state of $J' = 3/2$. When right handed circularly polarised light is incident on the atom, optical pumping transfers the population to the $m_J = +1/2$ sublevel. This occurs because $\Delta m_J = +1$ transitions are driven and whilst spontaneous emission can occur with $\Delta m_J = \pm 1,0$, overall $\Delta m_J \geq 0$ for each scattering event. The opposite is true for left handed circularly polarised light, where Δm_J = -1 and $\Delta m_J \leq 0$ so the population is transferred to the

m_J = -1/2 sublevel. Therefore, when travelling through the standing wave described above, the population of the atoms is driven from $m_J = +1/2$ to m_J = -1/2 over a distance of $\lambda/4$, as shown in figure 4.2.

In the absence of a light field the $m_J = \pm 1/2$ sublevels are degenerate. However, when atom-light interactions are taken into account the sublevels experience a shift in energy relative to each other. In the low intensity limit of two laser beams of intensity I, the light shift for the ground state is,

$$\Delta E_{\mathrm{g}} = \frac{\hbar \Gamma^2 C_{\mathrm{ge}}^2}{4\delta} \frac{I}{I_{\mathrm{s}}}, \tag{4.5}$$

where C_{ge} is the Clebsch-Gordan coefficient that describes the coupling between the atoms and the light field [108], where g,e signifies the ground and excited states respectively. As these coefficients depend on the magnetic quantum number and the polarisation of the light they are different for each m_J sublevel and change over the course of moving through the standing wave.

Both m_J sublevels are shifted lower in energy due to atom-light interactions but their energy varies depending on the polarisation of the light. Therefore, as the polarisation cycles, the m_J sublevels become higher or lower in energy with respect to each other. Optical pumping causes more population to be in the state with the larger light shift so atoms at the top of the potential hills decay down into the troughs, for example, the atom in the $m_J = -1/2$ sublevel shown in the diagram absorbs a photon and subsequently decays down into the lower energy $m_J = +1/2$ sublevel at $\lambda/4$ when the polarisation is right hand circularly polarised (driving σ^+ transitions). Although there is a probability that the atom will decay back into the state it started in, over time $\Delta m_J \geq 0$ for right handed (σ^+) and $\Delta m_J \leq 0$ for left handed (σ^-) circularly polarised light so decaying to the troughs is more likely.

Each optical pumping event where an atom goes from a potential hill to a trough results in the absorption of light at a lower frequency than that emitted, dissipating energy to the light field. Atoms moving over the potential hills and troughs speed up or slow down, so if an optical pumping event occurs when the atom is on a hill then the kinetic energy lost climbing the hill is transformed into the light field, leading to cooling. Eventually the atoms will not have enough energy to climb the potential hills and will all reside in the troughs.

Therefore, combining optical pumping with the light shifts of the sublevels leads to Sisyphus cooling, shown pictorially in figure 4.2. Sisyphus cooling is named after the Greek legend of Sisyphus, who was punished by the gods to repeatedly push a rock up a hill only to watch it roll back down again.

Atoms must first be cooled using 'ordinary' Doppler cooling as Sisyphus cooling will only work over a small range of atomic velocities. This is because the optical pumping time scale is a lot longer than the natural linewidth of

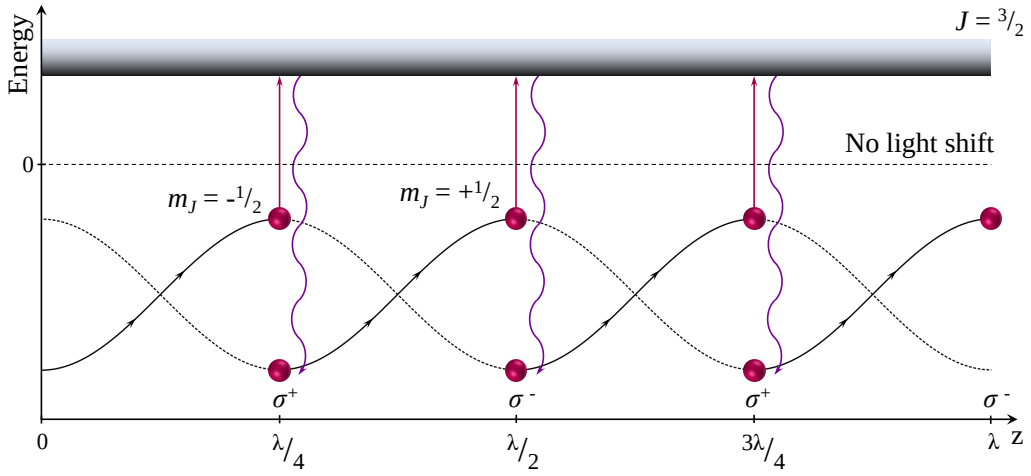

Figure 4.2: In Sisyphus cooling the energy of the magnetic sublevels changes depending on the polarisation of the light due to the light shift, so an atom pumped from one m_J state to the other loses energy if the scattering event happens when the atom is at the top of one of the potential hills.

the transition, $\tau_\mathrm{p} >> 1/\Gamma$, so the atoms must be moving slowly enough over the potential hills that there is a good probability that an optical pumping event will occur when the atom is at the top of a hill.

Recoil limit

The energy loss for each optical pumping event is equal to the energy difference between the top of the potential hill and the bottom of a trough. Therefore, as can be seen from equation (4.5), the amount of energy lost can be increased by either increasing the detuning, δ, or decreasing the light intensity, I. However, Sisyphus cooling does reach a limit when the energy lost in an optical pumping event is balanced by the recoil energy gained on emission of a photon. The equivalent temperature due to these recoils is

$$T_\mathrm{r} = \frac{\hbar^2 k^2}{m k_\mathrm{B}}, \tag{4.6}$$

where m is the mass of an atom.

For heavy atoms like Cs this recoil temperature is very low at $0.2\,\mu$K, although in practice the lowest temperatures reached would be several times this limit. One reason for this is due to perturbations of the magnetic sublevels due to stray magnetic fields, therefore the lowest temperatures are only reached when very good nulling of the ambient magnetic field in the lab is achieved.

With Sub-Doppler cooling, Cs can be cooled to approximately the same

temperature as Yb cooled on the $^1S_0 \rightarrow {}^3P_1$ transition which can only access Doppler cooling for most isotopes (approximately $4\,\mu$K).

$\sigma^+ - \sigma^-$ configuration

When a right handed (σ^+) circularly polarised laser beam counter-propagates with a left handed (σ^-) beam they form a light field with linear polarisation (assuming the two beams have equal amplitude), where the direction of polarisation traces a helix in space with pitch λ. As the polarisation is linear everywhere and the intensity of the light field does not change with position, the light shifts of the ground state sublevels are equal so there is no force like in the lin $\perp$ lin configuration. Instead it is an imbalance in population in the sublevels that causes sub-Doppler cooling for the $\sigma^+ - \sigma^-$ configuration.

Considering an atom where $J = 1$ and $J' = 2$, atoms at rest are optically pumped into the $m_J = 0$ state as this is the π transition being driven by the linearly polarised light. Moving atoms will experience a rotation of their quantisation axis as they move along the beam due to the rotation of the polarisation. However, as optical pumping takes a finite time the population in the $m_J = 0$ state lags behind the direction of polarisation. It can be shown [115] that this results in atoms travelling towards the σ^+ beam being more likely to be in the $m_J = +1$ state and so preferentially absorbing photons from this beam. The same is true for atoms travelling towards the σ^- beam. The preferential absorption of photons counter-propagating with the atoms leads to a frictional force pushing the atoms in the direction opposite to their motion, acting to reduce the velocity of the atoms.

As optical molasses are formed with three pairs of counter-propagating beams a complicated pattern of polarisation could be set up and so in reality a combination of sub-Doppler cooling mechanisms could exist in a MOT.

Sub-Doppler cooling in Yb

Sub-Doppler cooling has also been observed in non-alkali atoms [117–119] as Sisyphus cooling can be generalised for any atom where $J_\mathrm{e} = J_\mathrm{g} + 1$. For Yb, the odd isotopes, ^{171}Yb and ^{173}Yb, will be expected to have sub-Doppler cooling as reported in [117] as they have hyperfine structure in their ground states due to a non-zero nuclear spin.

4.2 Magneto-Optical Trapping

It is not just sufficient to cool the atoms, we also want to be able to trap them in a specific location for relatively long periods of time. In order to do this a Magneto-Optical Trap (MOT) is used.

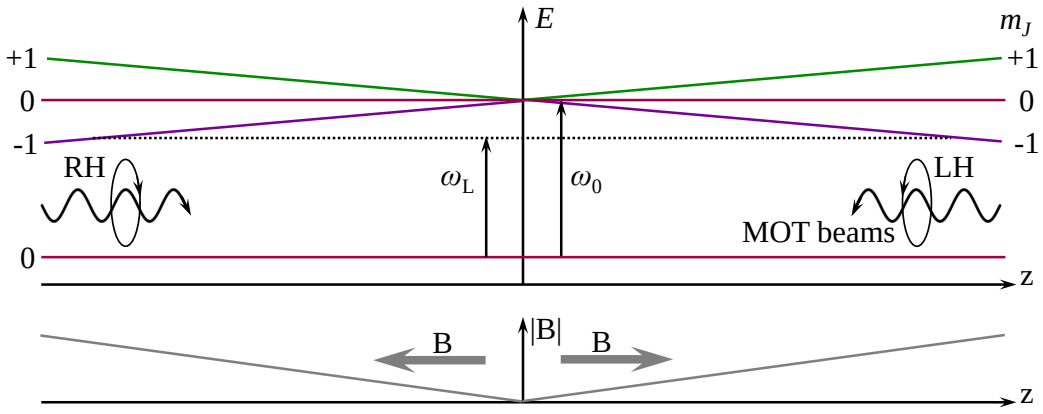

Figure 4.3: The magnetic sublevels of an atom are shifted in energy depending on their position within the magnetic field gradient with atoms in $m_J = -1$ shifted down in energy with increased magnetic field gradient. Therefore the left hand (LH) circularly polarised light drives $\Delta m_J = -1$ transitions for z > 0 but $\Delta m_J = +1$ for z < 0 and vice versa for the right hand (RH) circularly polarised light. Therefore the atoms preferentially absorb light that is counter-propagating to them, creating a restoring force. ω_L is the laser frequency detuned from the atomic resonance ω_0.

A MOT uses three pairs of counter-propagating laser beams with opposite handedness circularly polarised light. The light field is combined with a pair of coils in the anti-Helmholtz configuration, which gives a region at the centre where the magnetic field is zero and the gradient near this point is linear.

The magnetic field gradient causes the energy of the magnetic sublevels of the atom to vary linearly with distance and with the correct choice of polarisation a restoring force can be created that pushes the atoms back to the trap centre. For example, considering a simple $J = 0$ to $J = 1$ transition as in figure 4.3, if the atom is in a region where z > 0 then the $m_J = -1$ level will be brought closer to resonance and the left handed circularly polarised light will be preferentially absorbed, causing the atom to be pushed back into the trap centre. The opposite occurs for z < 0 with the right handed circularly polarised light now driving the $\Delta m_J = -1$ transition and so being more likely to be absorbed.

4.2.1 Choice of cooling transition

For Cs there is only one atomic transition that can be used for laser cooling and trapping; the $F = 4 \rightarrow F' = 5$ transition (see figure 2.1(a)). With this transition there is some finite probability that when light red-detuned from the transition is incident on an atom in the ground state it will drive the $F = 4 \rightarrow F' = 4$ transition instead. Once in the $F' = 4$ level the

atoms could either decay back into the $F = 4$ level or into the $F = 3$ level. Therefore, eventually all of the atoms would be lost into the $F = 3$ dark state if some way of transferring the population back into the $F = 4$ state was not implemented. Therefore, light resonant with the $F = 3 \rightarrow F' = 4$ transition is combined with the cooling light to close this loss route. This is referred to as the repumping light.

On the other hand Yb has a choice of two possible cooling transitions; ${}^1S_0 \rightarrow {}^1P_1$ or ${}^1S_0 \rightarrow {}^3P_1$ (see figure 2.2(a)). As summarised in table 4.1, the ${}^1S_0 \rightarrow {}^1P_1$ transition has a larger linewidth and $a_{\max}$ and so is ideal for Zeeman slowing as the cycle rate will be high and so more scattering events will occur in a given distance. However, it is less suited for use in a MOT as the larger linewidth will lead to a larger Doppler temperature and there is also a loss route for atoms into the triplet states, shown in figure 2.2(a), only some of which would decay back into the ground state (as discussed in Section 2.1.2). The small but finite branching ratio for atoms in the ${}^1P_1$ state to transfer into the triplet states is 1.2×10^{-7} [67, 68]. Any repumping scheme for this transition would be quite complicated so the simpler ${}^1S_0 \rightarrow {}^3P_1$ transition is often used for a MOT of Yb.

This transition is a perfect two level system so no repumping is required. It also has a small linewidth and so gives a low Doppler temperature, as shown in table 4.1.

4.2.2 Capture velocity

The capture velocity of a MOT can be estimated by considering the maximum force on an atom (equation (4.2)) and using it to calculate the maximum velocity that can be slowed to zero by this force in a distance D equal to the diameter of one of the MOT beams [108]. The capture velocity is then approximately

$$v_{\mathrm{c}} = \sqrt{\frac{h\Gamma D}{\lambda m}}. \tag{4.7}$$

Using typical values for a MOT beam diameter of 20 mm, this gives $48\,\mathrm{m\,s^{-1}}$ and $10\,\mathrm{m\,s^{-1}}$ for Cs and the ${}^1S_0 \rightarrow {}^3P_1$ transition in Yb respectively. This is the maximum velocity that the atoms should leave the Zeeman slower at in order to be captured by the MOT. The capture velocity of a MOT can be increased by increasing the linewidth, either by power broadening or frequency broadening. If the linewidth was power broadened then the Γ factor in the equation above would become $\Gamma = \Gamma_0\sqrt{1 + I/I_{\mathrm{s}}}$.

In reality, the capture velocity may be less than that quoted above as atom losses to different states (and so the time taken to repump the atoms into the desired state) is not taken into account.

4.2.3 Frequency broadening the MOT beams

The capture velocity for the 556 nm MOT for Yb is quite small, therefore, in order to increase the efficiency of capture from the Zeeman slower the MOT beams are artificially broadened in frequency, increasing the capture velocity as in equation (4.7). Several groups have already implemented this technique for capturing more Yb atoms in a MOT [66, 120].

This technique sacrifices a lower MOT temperature for a larger capture efficiency from the Zeeman slower, however, ramping down the sidebands once the atoms have been trapped will decrease the temperature again.

4.3 Laser system for caesium

As discussed in the previous section, to trap Cs we require not just cooling light ($F = 4 \rightarrow F' = 5$ transition) but also light resonant with the $F = 3 \rightarrow F' = 4$ transition to repump atoms lost into the $F = 3$ level via $F' = 4$. Therefore, two separate laser systems are needed to cool and trap Cs in a MOT and these are shown in figure 4.4. A Toptica DL 100 Pro extended cavity diode laser acts as a master laser and seeds a Toptica BoosTA tapered amplifier, which gives enough power for the MOT and Zeeman slower beams. The tapered amplifier potentially also gives adequate power to set up Degenerate Raman Sideband Cooling (DRSC) [121] at a later date if needed. The repump light is provided by a Toptica DL Pro extended cavity diode laser.

4.3.1 Lasers and their optical frequencies

The various frequencies needed to cool Cs are obtained by a combination of 10 acousto-optic modulators (AOMs), whose frequencies are given in table 4.2. The BoosTA AOM (AOM 1) changes the MOT and Zeeman slower detunings throughout the course of the experiment as it is double-passed so changes in the RF frequency will not effect beam pointing into subsequent fibres. The three frequency choices for AOM 1 are for different stages in the experiment: AB gives the correct detuning for operating the Zeeman slower, MOT and DRSC, AB for a compressed MOT (cMOT) stage and AB for a molasses stage. There is another channel (AB) that is not currently used and so is free if a further detuning is required at a later date. Figure 4.5 illustrates how the various detunings needed to cool Cs are achieved.

The AOMs (Crystal Technology 3080-122, 3110-120 and 3200-124 with centre frequencies of 80 MHz, 110 MHz and 200 MHz respectively) are driven by a voltage controlled oscillator (VCO) whose signal is amplified by a Mini-Circuits amplifier (ZHL-1-2W for the 200 MHz AOMs and ZHL-3A for the 80 MHz and 110 MHz AOMs).

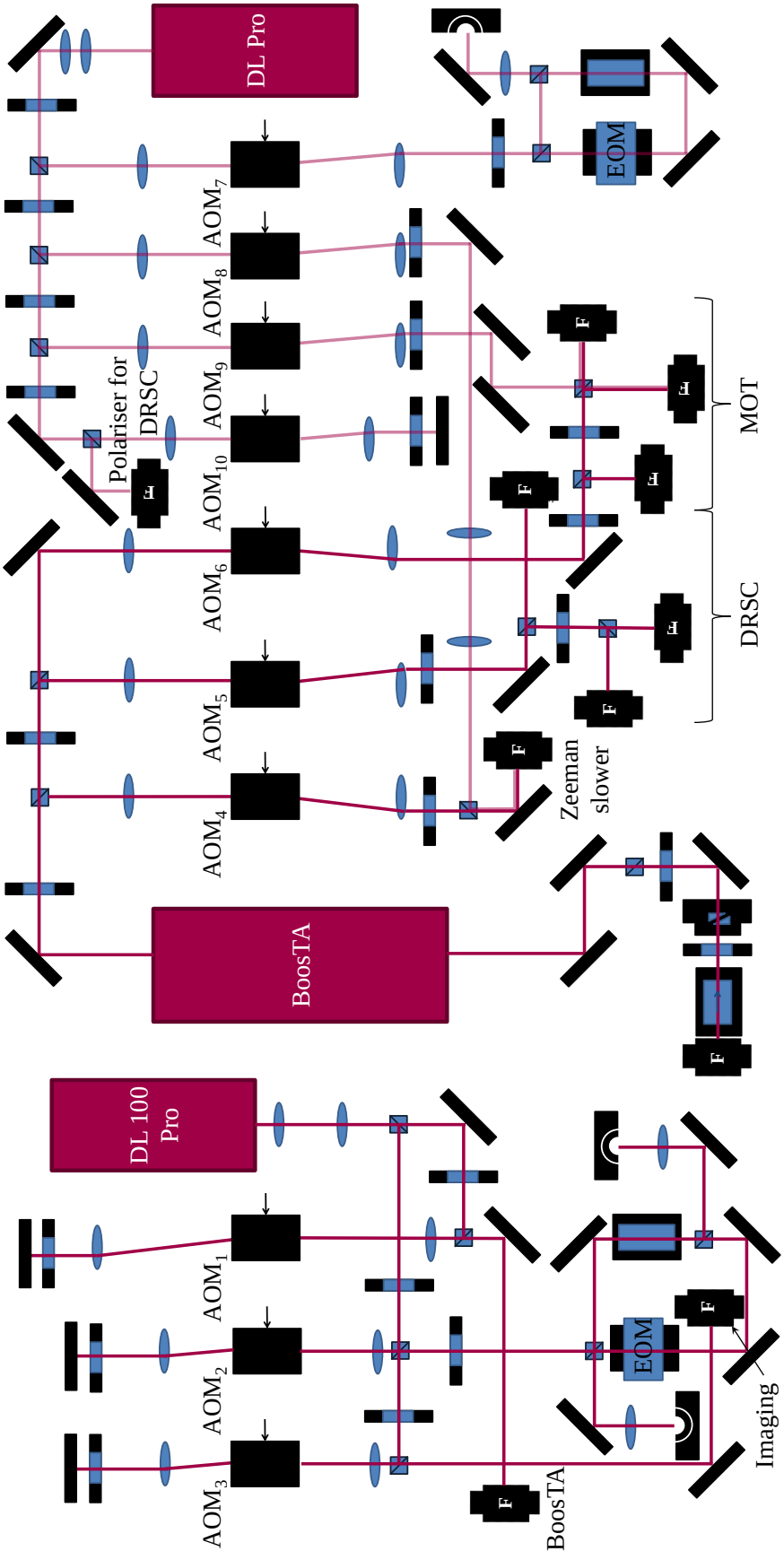

Figure 4.4: The laser system for caesium. Cooling light is provided by a Toptica DL 100 pro seeding a Toptica BoosTA tapered amplifier. The repump light is provided by a Toptica DL Pro laser. The positions of the 10 AOMs are shown as well as the spectroscopy set up for the cooling and repump lasers.

AOM	Destination	Frequency (MHz)	Detuning (MHz)	Transition
1	BoosTA	$\underline{\text{AB}} = 125$		
		$\text{A}\underline{\text{B}} = 119$		
		$\text{AB} = 103$		
2	Spectroscopy	192	0	$F = 4 \rightarrow F' = 5$
3	Imaging	192	0	$F = 4 \rightarrow F' = 5$
4	Zeeman slower	80	-55	$F = 4 \rightarrow F' = 5$
5	DRSC	116	1	$F = 4 \rightarrow F' = 4$
6	MOT	125	-9	$F = 4 \rightarrow F' = 5$
7	Repump spectroscopy	80	0	$F = 3 \rightarrow F' = 4$
8	Zeeman slower repump	130	-50	$F = 3 \rightarrow F' = 4$
9	MOT repump	85	-5	$F = 3 \rightarrow F' = 4$
10	DRSC polariser	216	0	$F = 3 \rightarrow F' = 2$

Table 4.2: The AOM frequencies for Cs, with AOMs 1-6 on the cooling laser and AOMs 7-10 on the repump laser. The detunings are referenced to the appropriate atomic line. The detunings for AOMs 1-6 are quoted for the $\underline{\text{AB}} = 125\,\text{MHz}$ case.

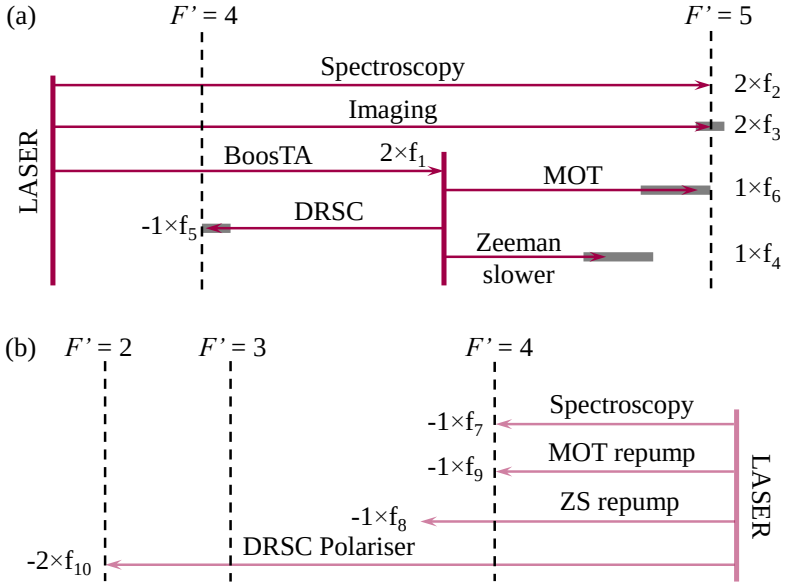

Figure 4.5: The frequencies of the laser beams required to cool and trap Cs are shown diagrammatically relative to the relevant atomic transitions for (a) the cooling light and (b) the repump light. The AOM frequencies (f_1 - f_{10}) in table 4.2 combine to provide the correct detuning for the MOT, Zeeman slower and potential DRSC beams and their respective repumping beams. The approximate range over which the frequencies can be detuned are shown by the grey shaded areas in the diagram.

4.3.2 Laser frequency stabilisation

To operate the lasers with a linewidth less than the natural linewidth they must be frequency stabilised, or 'locked', which can be done with an error signal derived from an atomic source. There are many methods available for locking lasers to an atomic signal, including polarisation spectroscopy [122], the dichroic atomic vapour laser lock (DAVLL) [123–125], frequency modulation spectroscopy [126] and modulation transfer spectroscopy [127, 128]. It is the last two methods that are used in this experiment; the laser used for the $F = 4 \rightarrow F' = 5$ cooling transition is locked using modulation transfer spectroscopy on a Cs vapour cell, whereas the repump laser on the $F = 3 \rightarrow F' = 4$ transition uses frequency modulation spectroscopy.

Modulation transfer spectroscopy

Modulation transfer (MT) spectroscopy is ideal for use with closed transitions, such as the cooling transition in Cs, as it gives a large signal on a zero background that is broadly independent of changes in temperature, polarisation and beam intensity.

As in saturation absorption spectroscopy [129], counter-propagating pump and probe beams are aligned collinearly through a Cs vapour cell (figure 4.6(a)). These beams have approximately equal powers but the pump beam has first been sent through an electro-optic modulator (EOM). An EOM consists of a lithium niobate ($LiNbO_3$) crystal (DÖHRER Elektrooptik) incorporated into an LCR circuit where the capacitance, C, is that of the crystal itself and L and R are the inductance and resistance of an inductor. The resonant frequency of the EOM is then given by:

$$\omega = \frac{1}{\sqrt{LC}}. \tag{4.8}$$

Therefore, changing the inductance of the circuit allows the resonant frequency of the EOM to be tailored to suit the requirements of the system, in this case we require the resonant frequency to be approximately one natural linewidth of the sub-Doppler transition, approximately 5 MHz.

Modulation frequency at the resonant frequency is then applied to the EOM and this acts to add two sidebands to the pump beam, each separated from the central carrier frequency by the modulation frequency [130].

If the pump and probe beams interact with the atomic vapour in a sufficiently non-linear way then a process of four-wave mixing [131] can occur and sidebands appear on the probe beam, i.e., the modulation is transferred. The central carrier frequency and the sidebands then beat together and this can be detected on a fast photodiode. This signal can then be turned into an error signal to lock the laser to.

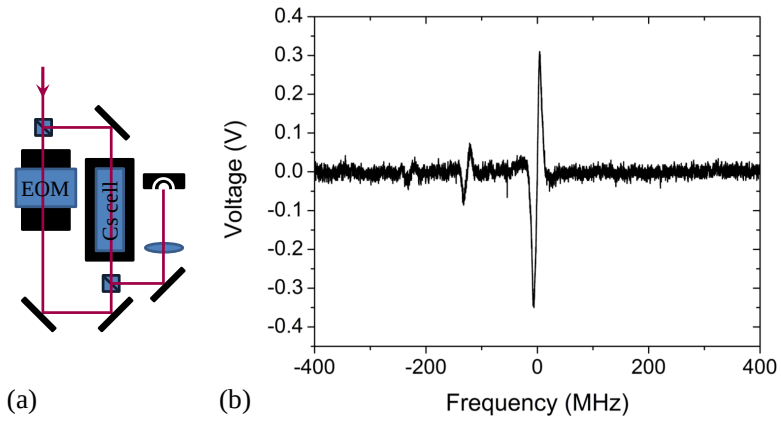

Figure 4.6: (a) The optical set up for modulation transfer spectroscopy and (b) the modulation transfer signal obtained on the $F = 4 \rightarrow F'$ transition in Cs. The largest dispersion signal arises from the closed $F = 4 \rightarrow F' = 5$ line whereas the smaller peaks are from two crossover resonances.

The process of four-wave mixing is most efficient for closed transitions as there are no other ground states the atoms can relax into, therefore the strongest signals for Cs are seen with the $F = 4 \rightarrow F' = 5$ transition. Signals are seen for other transitions or crossovers but they are much weaker (two crossover resonances can be seen in figure 4.6(b)).

To obtain the best locking signal, the pump and probe beams have approximately equal powers, $(310 \pm 1)\,\mu$W and $(210 \pm 1)\,\mu$W respectively. The EOMs resonant frequency is (5.907 ± 0.008) MHz which is driven by a GW Instek SFG-2120 signal generator. The amplitude of the output signal is 10 V peak to peak and is split by a coupler (Mini-Circuits, ZFDC-15-6+) which sends most of the signal to the EOM with some going to a frequency mixer (Mini-Circuits, ZAD-3+). The pump and probe beams are aligned though a 7 cm long Cs vapour cell before the probe light is incident on a Hamamatsu S5972 (15 MHz) photodiode. The signal from this goes to the frequency mixer, whose output is amplified by approximately 200× in a low pass gain filter. The filter acts to remove the high frequency signal from the mixer, leaving just the DC component which forms the error signal (figure 4.6(b)).

Frequency modulation spectroscopy

It would be ideal to use modulation transfer spectroscopy for locking both the cooling and repump transitions as it gives a zero background and is resistant to changes in temperature, polarisation and beam intensity, however, as the repump transition is not closed, the modulation transfer signal is relatively small and so frequency modulation (FM) spectroscopy is a better choice.

Unlike MT spectroscopy, in FM spectroscopy it is the probe beam that

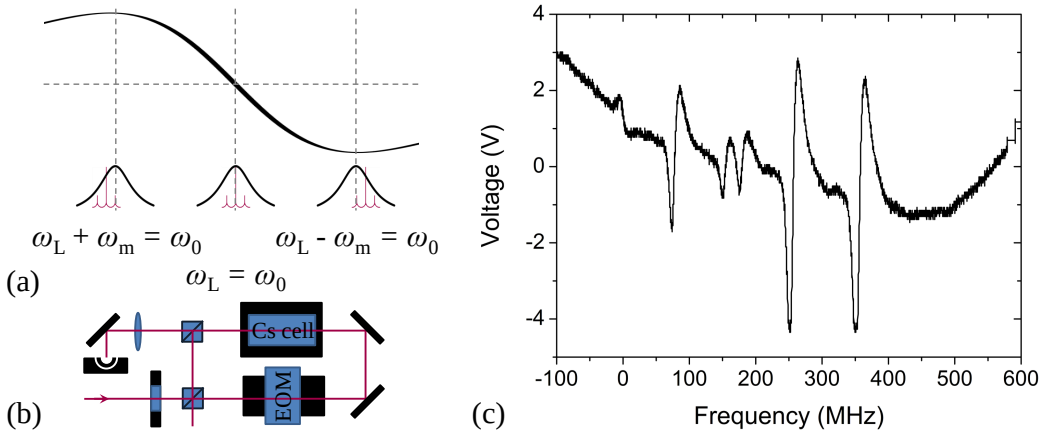

Figure 4.7: (a) As the laser scans over the atomic resonance, the two sidebands (smaller red lines) are absorbed by different amounts leading to the production of an error signal (top black line). (b) The optical set up for FM spectroscopy where sidebands are added to the probe beam by the EOM. (c) The FM signal for the $F = 3 \rightarrow F'$ transition in Cs. Signals from each of the lines and crossover resonances can be seen.

is phase-modulated with an EOM. This beam is then collinearly counter-propagated with the pump beam through a Cs vapour cell before being detected on a fast photodiode (figure 4.7(b)).

When the probe beam is incident on the photodiode each sideband beats with the carrier frequency at the modulation frequency, ω_m. When the light is off resonance with the atoms then the beat signals due to each sideband are equal in magnitude but opposite in phase and so exactly cancel. However, when the light is close to resonance with an atomic transition, one sideband may be absorbed more than the other, destroying the exact cancellation.

As the laser frequency, ω_L, is swept across the atomic resonance, ω_0, there are certain frequencies at which one sideband will be absorbed more than the other, giving rise to a beat frequency on the photodiode. For a symmetric lineshape, such as those in figure 4.7(a), the largest beat signal will occur when each sideband is on resonance with the atoms, i.e., at $\omega_L - \omega_m = \omega_0$ and $\omega_L + \omega_m = \omega_0$. However, if the laser is on resonance instead, i.e., $\omega_L = \omega_0$, then both sidebands will be absorbed by the same amount and the beat signals will cancel again leading to a zero-crossing on the error signal.

Therefore, as FM spectroscopy depends on the exact form of the atomic lineshape it is affected by the Doppler background which distorts the sub-Doppler features and so the centre of the dispersion-type signal is not always exactly at the centre of the sub-Doppler transition. There is also always a non-zero background which must be compensated for with an electronic offset when locking the laser (figure 4.7(c)). This means that FM spectroscopy is

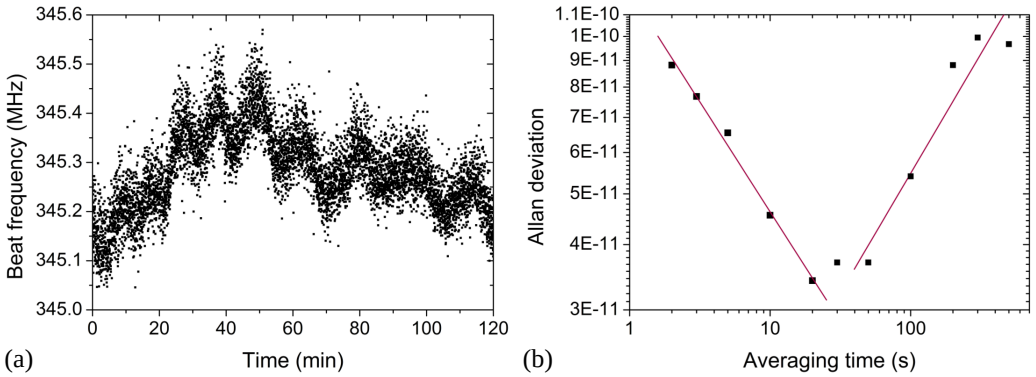

Figure 4.8: (a) Beat frequency measurements and (b) the associated Allan deviation between the master and repump lasers locked with MT and FM spectroscopy respectively. The oscillations in the beat frequency data arise due to changes in lab temperature from the air conditioning cycle.

more prone to changes in temperature than MT spectroscopy.

For FM spectroscopy the pump and probe beam powers are not equal; the pump beam has $(138 \pm 1)\,\mu$W whereas the probe beam has only $(57 \pm 1)\,\mu$W. The EOM is run at 8.6437 MHz, supplied by a GW Instek SFG-2120 signal generator. The error signal is derived in a similar way to MT locking; the signal from the fast photodiode (Hamamatsu avalanche photodiode, C5460) is sent to a frequency mixer (Mini-Circuts, ZAD-3+) where it is mixed with some of the modulation frequency signal by a coupler (Mini-Circuits ZFDC-15-6+). The output from the mixer is amplified and filtered and only the DC component forms the error signal the laser is locked to.

Frequency stability

In order to test the quality of the frequency stabilisation for the two 852 nm lasers, beat frequency measurements were carried out. Light from both lasers were coupled down the same fibre and focussed onto a fast photodiode (EOT, ET 2030A). The signal from this was sent to a frequency counter (Agilent, 53220A) and the beat frequency was sampled every 1 s using a LabVIEW program. The resulting data are plotted in figure 4.8.

Oscillations in the beat frequency with an approximate amplitude of 150 kHz and a period of 14 minutes can be seen in figure 4.8(a). These correlate with variations in laboratory temperature due to the cycle of the air conditioning unit. A larger variation of 300 kHz over the period the data were taken can also be seen, but both of these drifts are much smaller than the natural linewidth of $2\pi \times 5.234(13)$ MHz [53] for Cs, therefore the laser frequencies are stable enough for our purposes.

The Allan deviation is given by [132, 133],

$$\sigma_{\mathrm{y}}(\tau) = \sqrt{\frac{1}{2(n-1)} \sum_{i} \left(y(\tau)_{i+1} - y(\tau)_{i} \right)^{2}}, \tag{4.9}$$

where τ is the averaging time, y_i the averaged signal in bin i and n is the number of bins. The Allan deviation is a useful measure to compare frequency stability between systems and can inform the user whether a system is white noise limited (large Allan deviation at short τ) or long term drift limited (large Allan deviation at long τ). Figure 4.8(b) shows the Allan deviation for the two lasers in the Cs system and from this it can be seen that overall the frequency stability is very good with low Allan deviation across all time periods (some comparison systems are discussed in Appendix A). The oscillations due to temperature cause the higher Allan variance at long averaging times ($\tau = 600\,\mathrm{s}$).

4.3.3 Tapered amplifier

The DL 100 Pro alone would not provide enough power for all of the cooling beams required, and would certainly not give the option to use DRSC. Therefore, a tapered amplifier is required to boost the amount of power available. We use a commercially available Toptica BoosTA for this purpose.

A tapered amplifier contains a semiconductor chip that has a tapered gain region where the amplification of the seed light occurs. The gain region is tapered to avoid damaging the chip due to the high light intensities within it. The output light is of the same frequency and mode structure as the seed. When not seeded, the BoosTA outputs light from both the front and back of the tapered amplifier chip as both ends are AR-coated, so without a seed it acts as a single pass laser with output in both directions.

In order to get the most efficient amplification, the seed beam must be shaped with anamorphic prisms to match the beam from the back of the BoosTA. This will ensure that the seed beam will be perfectly matched into the tapered amplifier chip and so the whole of the gain region used. The guide beam was measured to have an aspect ratio of 2.33:1 (vertical:horizontal) and so a pair of anamorphic prisms (Thorlabs, PS871-B) were used to match this. The resulting seed beam had a corresponding aspect ratio of 2.31:1.

The BoosTA is injected by using the two mirrors before it (see figure 4.4) to walk the seed beam until it overlaps with the guide beam coming from the BoosTA itself. For fine adjustments of the injection, the power in the output beam from the BoosTA was monitored as small adjustments were made to the two mirrors.

The performance of the BoosTA was tested to see if it matched the specifications sheet supplied with it and to see if the performance was similar to another BoosTA used in the research group [134]. The first test was to

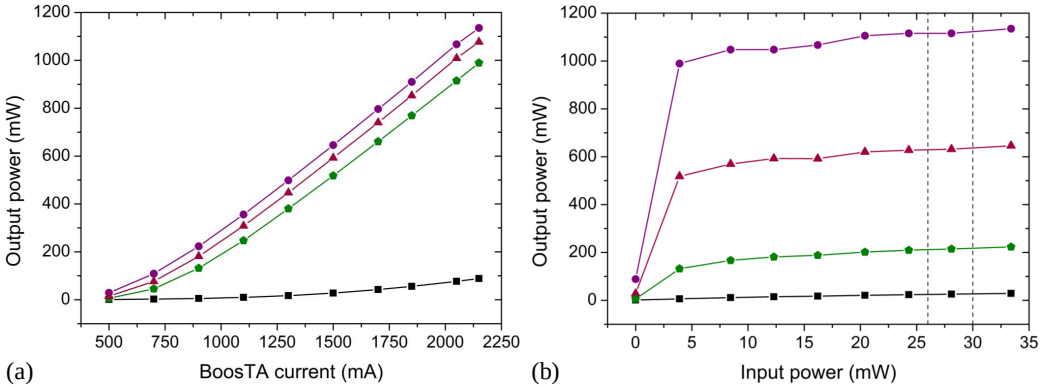

Figure 4.9: Injection performance of the tapered amplifier as (a) the current to the tapered amplifier or (b) the input power from the seed laser increases. (a) As the current increases the output power also increases. Different seed powers were used for each current set; 0 mW (black squares), 3.91 mW (green pentagons), 12.3 mW (red triangles) and 33.4 mW (purple circles). (b) The amount of output power varies only slightly with increased input seed power after the initial jump from no seed power. As seen, higher power is accessed by increasing the current; 500 mA (black squares), 900 mA (green pentagons), 1500 mA (red triangles) and 2150 mA (purple circles). The two dashed lines show the range of input powers used in the experiment as the frequency of the seed beam is varied by the AOM (as described in table 4.2).

see how the output power varies with the current supplied to the tapered amplifier. The results from this investigation can be seen in figure 4.9(a); as for all laser diodes, the output power increases as more current is applied. This figure also shows that there is a rapid increase in output power from the case with no seed power (black squares) to even a small amount of seed light, for example, the green pentagons in the figure are for an input seed power of only 3.91 mW.

Figure 4.9(b) shows the output power as a function of the seed power. It can be seen that the power does not increase appreciably with increased seed power after the first jump from no seed beam, i.e., each set of points has only a small gradient. This is ideal as the input power to the BoosTA inevitably varies slightly as the frequency of AOM 1 changes during different stages of the experiment (table 4.2). Each AOM is optimised for use at the centre frequency it is expected to run at for the majority of the experiment, but the efficiency changes as the RF frequency changes. Therefore, as the frequency differs the double passed diffraction efficiency also changes, as can be seen in figure 4.10. The efficiency of light coupling into the BoosTA fibre is also shown in red; the dashed lines show the frequency range used and no appreciable change in efficiency is seen.

Access to higher output powers from the BoosTA mainly comes from the

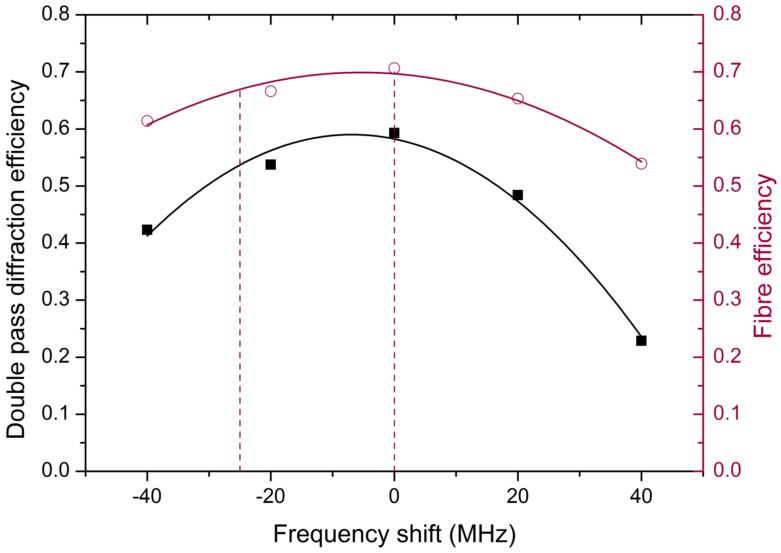

Figure 4.10: The double passed diffraction efficiency of AOM 1 (black) along with the associated fibre efficiency (red). The AOM is optimised at the frequency most often used in the experiment (case AB in table 4.2) and the frequency shift from that condition is plotted. The dashed lines indicate the total range of frequency required in the experiment and no significant change in efficiency (and so overall power) is seen.

choice of current supplied to it. With respect to this, as with any laser device, the lifetime of the semiconductor chip will be increased if it is not routinely run at full power, therefore, it was necessary to consider the power budget after the BoosTA and so consequently choose a sensible operating current. The BoosTA is normally run at 1450 mA, the maximum being 2150 mA.

Once the operating current has been chosen the injection into the BoosTA should be fine tuned as it has been observed that each current has a slightly different optimum injection to give the best power output. This also affects coupling into subsequent fibres as differing beam profiles have been observed out of the BoosTA when the injection of the input beam is not optimised for each current. This effect has not been extensively studied, but may possibly be due to the temperature of the chip changing between currents.

4.3.4 Matching polarisation into fibres

The light for the MOT and Zeeman slower beams is delivered to the main table using four 8 m long optical fibres (Oz Optics, LPC-02-850-5/125-P-1.3-6.2AS-40-3A-8). These are polarisation maintaining fibres where the polarisation going into the fibre has been matched to the fast axis of the fibre using the method described in [135]. Specifically this involves rotating the

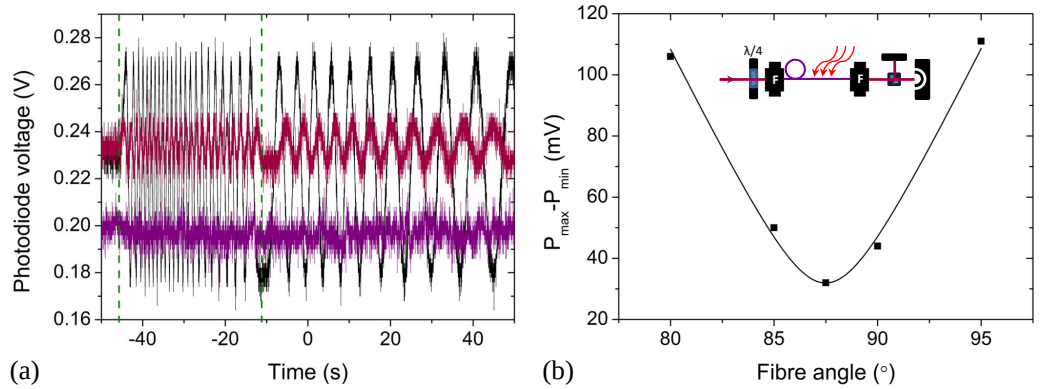

Figure 4.11: (a) The oscillations in power after the polarising beam splitter after the imaging fibre for a misaligned fibre (black), a fibre whose input coupler has been rotated to match the polarisation angle of the linearly polarised input light (red) and an aligned fibre with a quarter waveplate compensating for stresses within the fibre (purple). (b) Plotting the amplitude of the oscillations against the input coupler angle helps to locate the angle where the polarisation is matched into the fibre. The inset in (b) shows the optical set up for this process.

input of the fibre by small angle increments and heating a small section of fibre with a gentle source of heat such as a hair dryer for approximately 30 s at a time. The power after a polarising beam splitter cube at the output of the fibre is recorded for each angle (as can be seen diagrammatically in the inset of figure 4.11(b)).

If the polarisation is not well matched into the fibre then when the heat is applied the internal birefringence changes, giving a change in the output polarisation state. This causes oscillations in the transmitted power through a polarising beam splitter cube at the output of the fibre, as can be seen in figure 4.11(a). Therefore, minimising the oscillations in the polarisation after the fibre indicates that the fast axis of the fibre is well matched to the polarisation of the light at the input. An example of this process is demonstrated in figure 4.11(a) where the black line is the power oscillations before optimisation and the red line shows the reduction in the amplitude of oscillations after the fibre input has been turned to match the polarisation angle of the input light. Figure 4.11(b) shows an example of the data generated when optimising the fibre input where the amplitude of the oscillations (P_{max}-P_{min}) are plotted against the angle of the fibre in order to find the value where the oscillations will be minimised.

An additional level of polarisation stabilisation can be achieved by putting a quarter waveplate before the fibre to eliminate polarisation changes due to stresses within the fibre. If a fibre is under stress it can induce phase changes in the beam and so the polarisation at the output of the fibre becomes slightly

elliptical. Therefore, if the input light is made to have elliptical polarisation of the other handedness then the output light will have linear polarisation again. Therefore, optimising the angle of the waveplate can eliminate the oscillations in the polarisation completely as can be seen in the purple line in figure 4.11(a). Typically only very small amounts of ellipticity need to be compensated for.

4.3.5 MOT, Zeeman slower and imaging optics

The MOT beams are expanded and collimated to a $1/e^2$ diameter of (18.0 ± 0.1) mm using Thorlabs cage systems (figure 4.12) and have (29.9 ± 0.1) mW per MOT beam. The repump light is combined with the cooling light before the fibres and so delivered to the science chamber simultaneously. The repump light therefore travels down the slow axis of the fibre, which means that the polarisation isn't as well maintained, however, we have seen that any polarisation drifts in the repump light are not critical. The MOT has (13.5 ± 0.1) mW repump light in total, most of which goes down a single fibre.

Light for absorption imaging is also delivered to the table using a fibre and is combined with one of the horizontal MOT beams using a polarising beam splitter cube (Thorlabs, PBS252 620-1000 nm) and so co-propagates through the chamber before being split off again with another cube (see figure 4.12). This MOT beam does not include any repump light to avoid unwanted light incident on the CCD camera during the absorption imaging sequence.

The Zeeman slower has (6.0 ± 0.1) mW of light on the cooling transition and (2.76 ± 0.01) mW of repump power. The Zeeman slower beam is passed through a series of lenses (seen in figure 4.13) in order to expand the beam and focus it down the Zeeman slower. The first of these lenses has a focal length f = -25 mm (Thorlabs, LD2297-B) which expands the beam from the fibre output coupler (Thorlabs, CFC-8X-B) and the second lens has a focal length of $f = 300$ mm (Thorlabs, LA1256-B), which slowly focusses the light to a waist of $(89 \pm 1)\,\mu$m, (2.09 ± 0.01) m from the Zeeman slower viewport. The reason for focussing the light is discussed in more detail in Section 5.3.2.

The light is aligned down the Zeeman slower using a dichroic mirror (Thorlabs, DMSP805L) which reflects 852 nm light but transmits 399 nm light, thus allowing the two Zeeman slowing beams for Cs and Yb to be overlapped.

4.4 Laser system for ytterbium

The laser system for Yb consists of two parts; the 399 nm lasers that form the Zeeman slowing and imaging beams and the 556 nm laser which gives the MOT beams. The optical lay out for these lasers can be seen in figure 4.14.

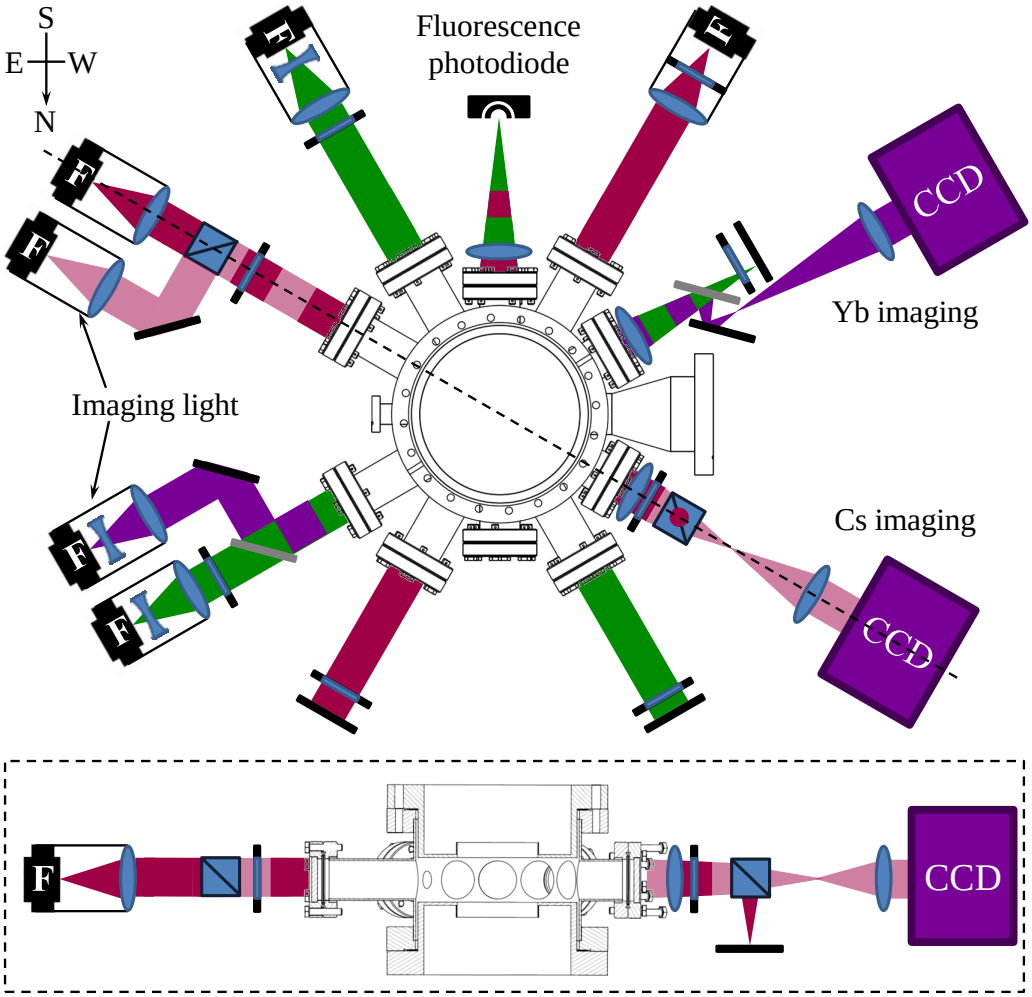

Figure 4.12: The optical set up for both the Yb and Cs MOTs relative to the science chamber. The MOT light is delivered through fibres and is collimated in cage systems. Another two cages systems launch the vertical MOT beams from beneath the chamber, where the 852 nm and 556 nm beams are combined on a dichroic mirror. A further dichroic mirror splits the beams above the chamber again so separate quarter waveplates for each wavelength can be used. Along the dashed line, the red circle after the North-West viewport indicates where Cs MOT light is sent downwards before retro-reflection to separate it from the imaging light. This is shown in detail in the dashed box.

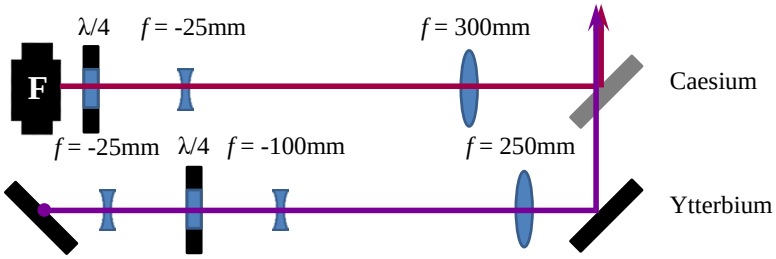

Figure 4.13: The optical set up for both the Yb and Cs Zeeman slower beams. The two wavelengths are combined on a dichroic mirror (grey rectangle). The purple circle indicates where the 399 nm beam comes down from an upper breadboard.

4.4.1 556 nm laser

The 556 nm laser is a MenloSystems 'orange one'; a doubled fibre laser at 1111.6 nm. During typical running conditions, this gives an output of 268 mW. Two single passed AOMs (Gooch and Housego, 46200-0.3-LTD) are used to get the required detuning of approximately 8 MHz for the MOT beams. As the detuning is small for Yb, it does not matter that the AOMs are only single passed as changing the detuning for the MOT will not result in any appreciable beam pointing changes and so the transmission efficiency of light down the MOT fibres will not be affected. We have found that a frequency shift of ±5 MHz from the centre frequency of the AOM causes a decrease in fibre coupling efficiency of approximately 2.5%.

The MOT light is delivered to the science chamber through three separate 8 m long optical fibres (Oz Optics, LPC-02-556-3.5/125-P-1.3-6.2AS-40-3A-3-8). As for Cs, the fibres are polarisation maintaining and the polarisation of the light going into the fibre has therefore been matched to the fast axis. At the output of the fibre Thorlabs cage systems are used to expand and collimate the beam, giving MOT beams with a $1/e^2$ diameter of (24.4 ± 0.2) mm and a power per beam of (20.0 ± 0.1) mW. As the ${}^1S_0 \rightarrow {}^3P_1$ transition is a perfect two level system, no repump light is required.

4.4.2 399 nm lasers

The 399 nm Zeeman slower laser system was initially developed at Imperial College London and comprises two Nichia diodes (NDV4314) in a master-slave arrangement. The master laser is an ECDL in a Littrow configuration with a Thorlabs GH13-36U (3600 lines/mm) grating providing the feedback to the diode. It has a maximum output of 52 mW but is typically run at 30 mW and is frequency stabilised by locking to a transfer cavity, which has itself been locked to the atomic signal for the 556 nm transition (discussed

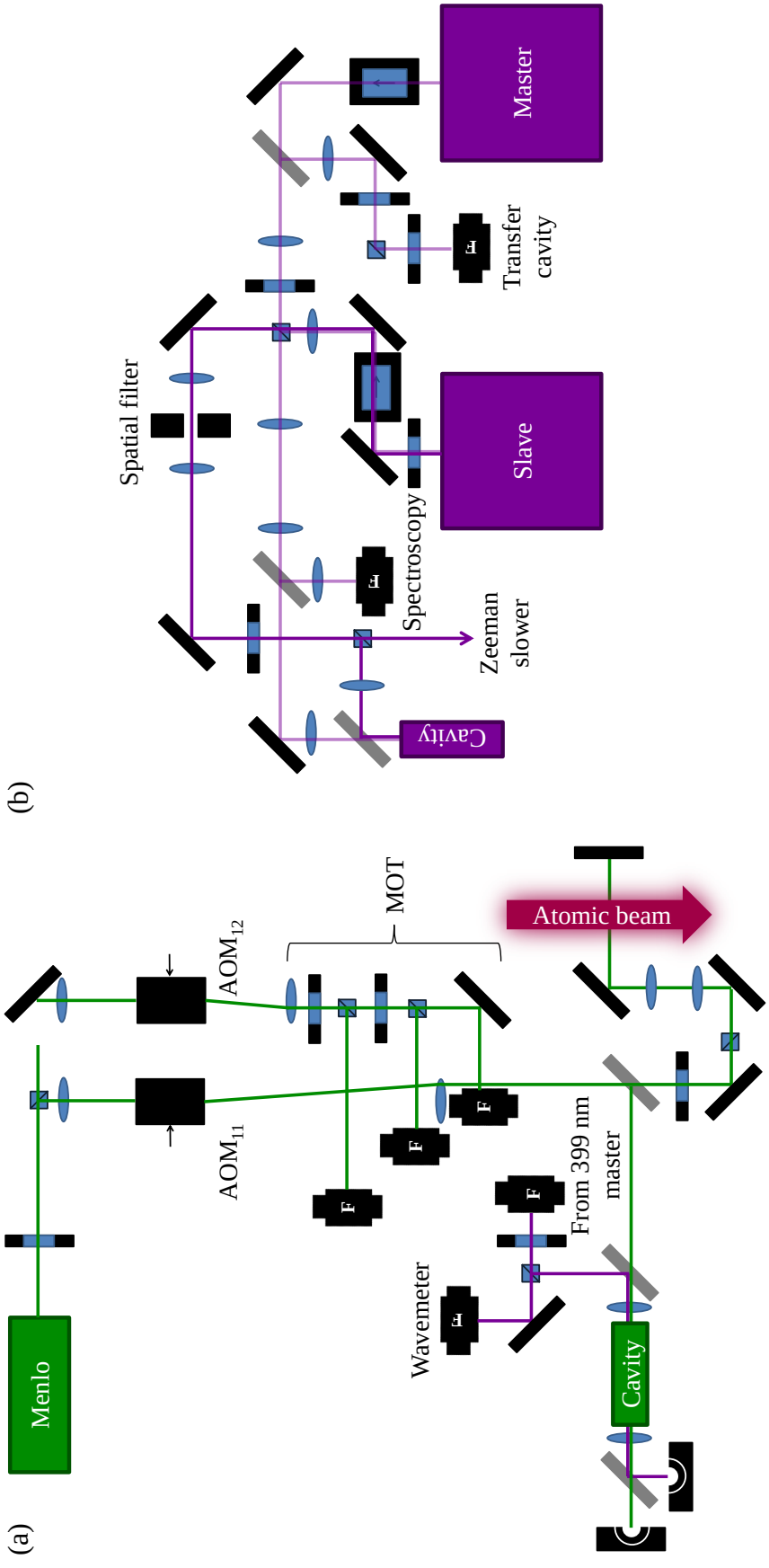

Figure 4.14: (a) The 556 nm laser system for ytterbium, including the transfer cavity that forms the lock for the 399 nm master laser. (b) The 399 nm laser system; a master laser is locked to the transfer cavity and seeds a slave laser which provides the power required in the Zeeman slower beam. An additional fibre provides light for spectroscopy if needed.

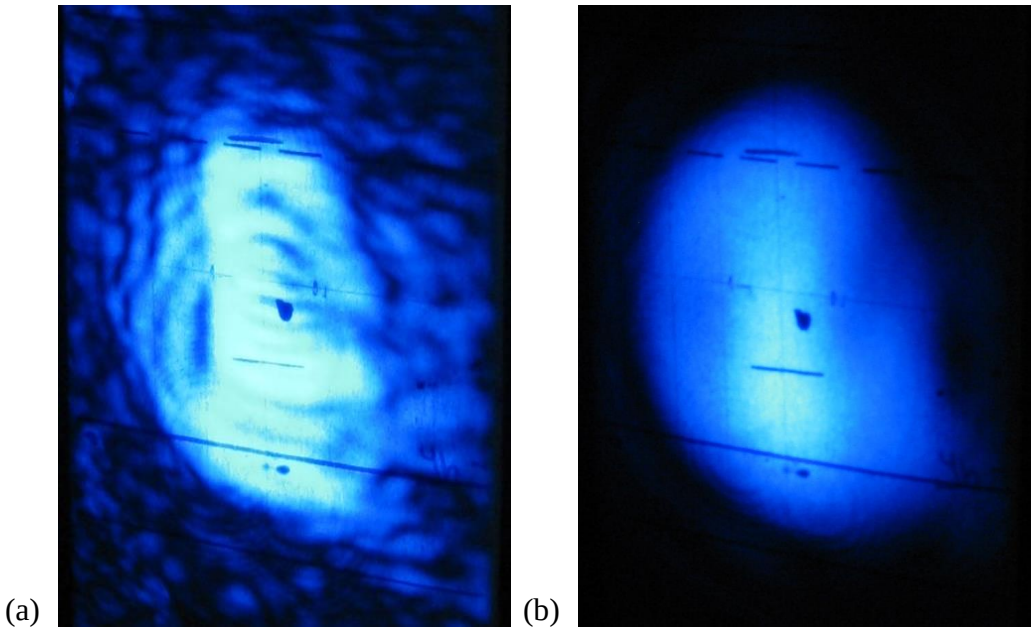

Figure 4.15: The 399 nm Zeeman slower beam (a) before and (b) after spatial filtering. The lines are markings on the beam dump used as a background. The interference in the beam before spatial filtering is thought to occur either due to imperfections in the optics or as a by-product of the type of diode.

later in Section 4.4.3). Approximately 1-2 mW from this laser is used to seed the second Nichia diode, which will then lase at the same frequency as the master laser. This slave laser gives up to 45 mW for the Zeeman slowing beam. As can be seen in figure 4.14, light from both lasers are sent into a cavity (Thorlabs, SM1D12) so that the injection of the slave can be monitored.

Unfortunately, possibly due to the nature of the laser diodes used, the beam from the slave laser is not a smooth Gaussian in appearance, but has many interference fringes across it (figure 4.15(a)). If expanded and sent down the Zeeman slower this may mean that there would be areas of the beam where the atoms would feel too much slowing or none at all, thus potentially reducing the number of atoms captured and slowed. To prevent this problem spatial filtering was performed on the Zeeman slowing beam by focussing the light onto a 50 μm pinhole (Thorlabs P50S); the resulting beam can be seen in figure 4.15(b). Spatially filtering the beam gives a power loss of 28%.

Spatial filtering uses the principle of Fourier optics to remove unwanted higher frequency modes from a laser beam. When light is focussed to a point it forms a diffraction pattern of concentric rings, where each ring is at a higher frequency than the one before. Therefore, to clean up a beam it is simply necessary to block all of the rings and let only the central portion of the beam through. The resulting beam will have a Gaussian distribution

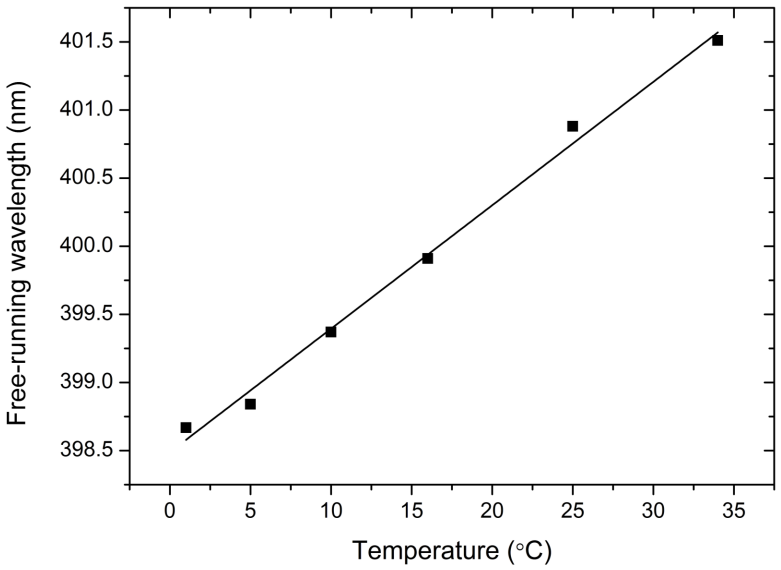

Figure 4.16: The free-running wavelength of the Mitsubishi ML320G2-11 401 nm diode as its temperature is changed. The wavelength was measured with a wavemeter. The desired wavelength of 398.9 nm is reached at a temperature of approximately 5°C.

across it. In reality, there is often a trade-off between power loss and complete removal of the high frequency noise on the beam. Empirically, the pinhole used should be approximately 30% of the diffraction limited spot size, D = $f\lambda/r$, where f is the focal length of the lens and r the $1/e^2$ radius of the input beam.

After the pinhole the Zeeman slower beam is expanded and subsequently focussed in a similar way to Cs (see figure 4.13). In this case, the beam passes through two divergent lenses with f = -25 mm and f = -100 mm (Thorlabs, LD2297-A and LD1613-A respectively) before being focussed down the Zeeman slower by a f = 250 mm lens (Thorlabs, LA1301-A). This gives a waist of $(307 \pm 8)\,\mu$m at (1.93 ± 0.01) m from the viewport.

A separate 399 nm laser has been developed at Durham and will be used for absorption imaging of the atoms. This laser housing was initially designed for use with a Mitsubishi ML320G2-11 401 nm diode, which required cooling to around 5 °C in order to lase at the correct wavelength, as can be seen in figure 4.16.

Therefore, as shown in figure 4.17, the compartment for the diode is capable of being hermetically sealed, with the collimating lens forming an air-tight window so desiccant packs can be placed around the diode to prevent condensation or ice build up. The diode itself is mounted in a small copper block which can be cooled using a thermo-electric cooler (TEC). The grating (Thorlabs, GH13-36U, 3600 lines/mm) is mounted in a separate housing,

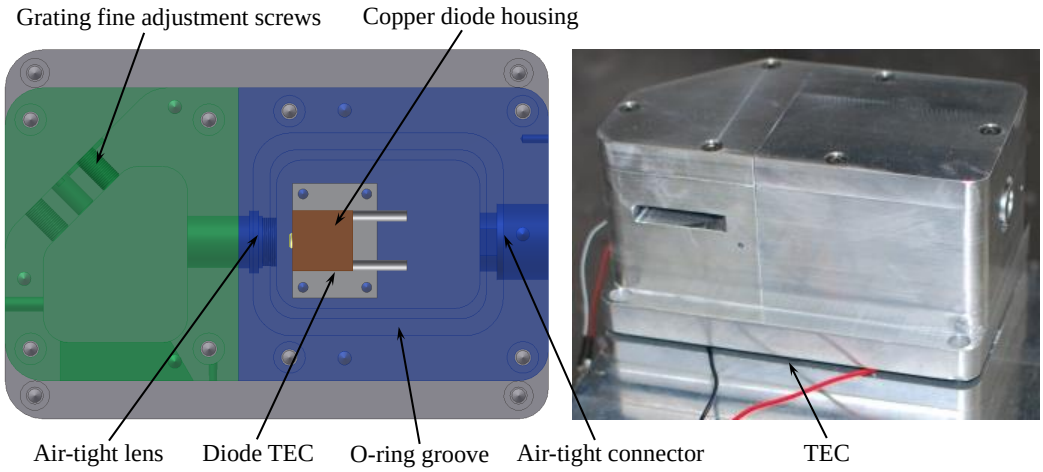

Figure 4.17: A diode housing capable of hermetically sealing the laser diode so cooling to below 0°C can occur without ice build-up. The diode is placed within a copper block which can be cooled separately and the compartment is sealed with an air-tight electrical connector with the collimating lens forming another seal. The lid forms the last seal with the use of an o-ring. The grating housing is separate but both halves are temperature stabilised using the same TEC.

but the whole assembly is thermally stabilised using a further TEC. However, the Mitsubishi diodes were found to not be very stable so the housing was then used for another Nichia NDV4314 diode, which does not require cooling. Technical drawings for the diode and grating housing can be seen in Appendix D.

With the Nichia diode, the laser typically outputs 9 mW when running single mode, however, due to the same interference-type patterns on the beam as seen in the slave laser, only ~3.5 mW of this is usable. This is still enough, however, for use in absorption imaging where only 500 μW [136] is typically required.

4.4.3 Laser frequency stabilisation

The two laser systems for Yb are locked relative to each other using a transfer cavity (Thorlabs SM1D12). The 556 nm laser is locked to an atomic signal, the cavity is then locked to this laser and the 399 nm master laser is locked to the cavity. This is shown schematically in figure 4.18.

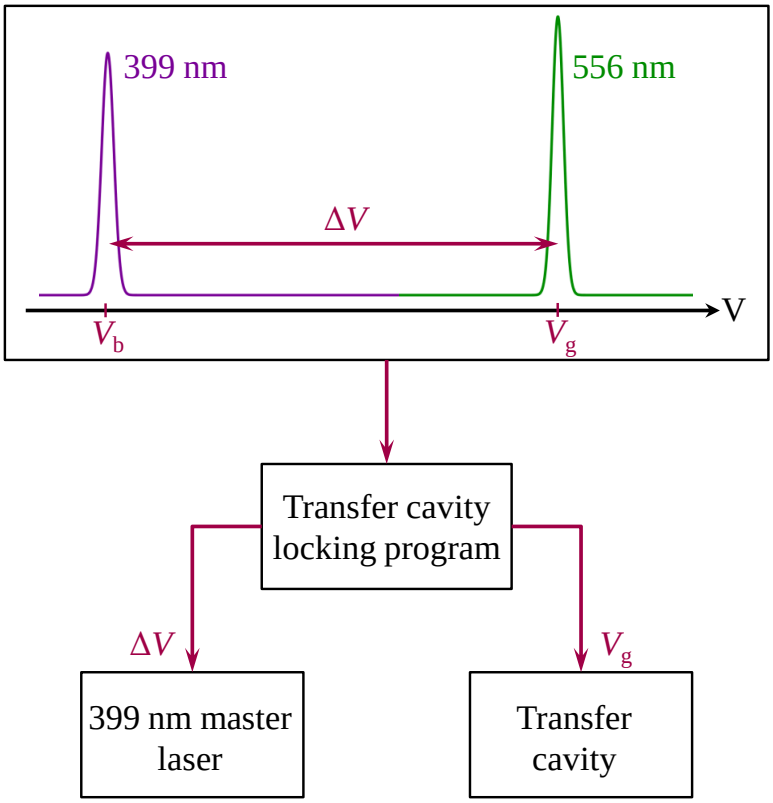

Figure 4.18: A simple schematic of the locking scheme for the 556 nm and 399 nm laser systems. The 556 nm laser is independently locked to an atomic signal before the cavity is stabilised to the cavity peak of the 556 nm light, V_g. The locked cavity then stabilises the frequency of the 399 nm master laser by keeping the offset voltage, $\Delta V = V_b - V_g$, between the cavity peaks constant.

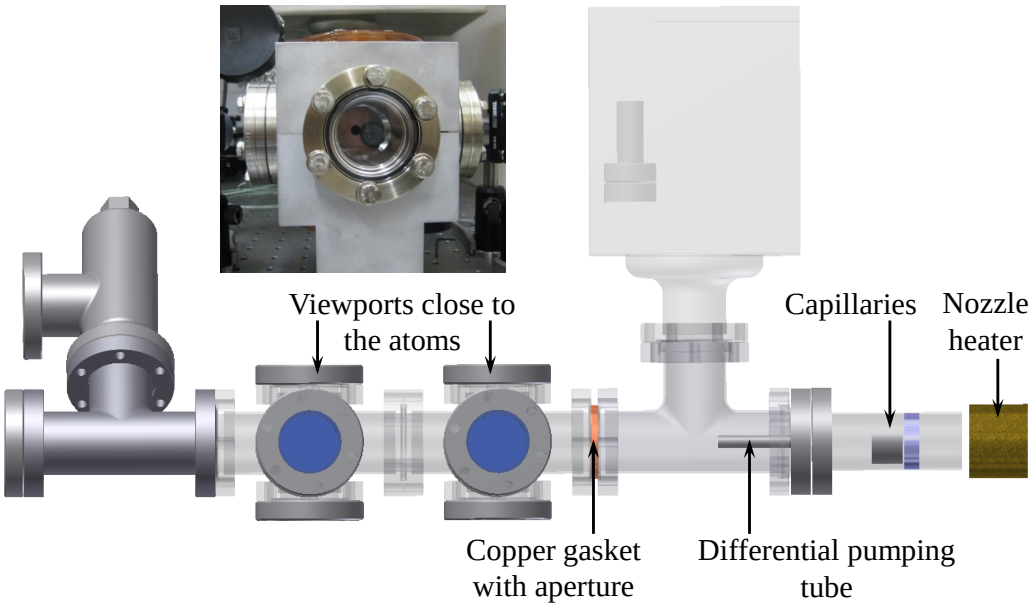

Figure 4.19: The current beam machine design with a similar oven to the main vacuum system where the Yb beam is collimated with an array of 55 capillary tubes. Both a differential pumping tube and an aperture before the viewports act to further collimate the beam. Two 6-way crosses provide access for spectroscopy on both the 556 nm and 399 nm lines. In the photographic inset; a black spot of Yb quickly develops on the end viewport.

556 nm laser frequency stabilisation

In order to lock the 556 nm laser an atomic signal is required and this is supplied by a beam machine; a simplified version of the oven used in the main vacuum system.

The beam machine is simply a nipple with the same arrangement of collimating capillaries as in the main oven, giving rise to an atomic beam. There is an 8 mm aperture drilled into a copper gasket at (171 ± 2) mm from the capillaries that acts to further collimate the beam. A $55\,\mathrm{l\,s^{-1}}$ ion pump (Varian (Agilent), VacIon Plus 55) maintains the vacuum inside; no NEG pump is used as a lower vacuum than the main chamber is acceptable and the beam machine will have to be brought up to atmosphere more often, which would eventually degrade a NEG pump. To avoid stray magnetic fields from the ion pump causing a Zeeman shift in the atoms a mu-metal shield is clamped around the ion pump magnets. Optical access to the atomic beam is through a six-way cross at the end of the beam machine, see figure 4.19.

Due to the narrow linewidth for the 556 nm transition of $2\pi \times 182.2$ kHz [137], to get a large enough spectroscopy signal the atomic flux needs to be higher than that used in the main vacuum system and so the beam machine oven

is run at a higher temperature of 480 °C. This means that the transmission of Yb atoms through the capillaries is no longer molecular and the mean free path is shorter than the capillary length. Yb is then not very well collimated coming out of the capillaries and a coating of the metal is found over a large angle within the beam machine, resulting in the Yb having to be replaced on a more regular basis. This was especially true in an earlier iteration of the beam machine where temperatures of 560 °C were regularly run. The uncollimated atomic beam accounts for the Doppler broadening of the fluorescence signal in figure 4.22(b).

Light from the laser is expanded to match the approximate diameter of the atomic beam and sent through the beam machine to interact with the atoms. As the fluorescence signals from the 556 nm transition are typically quite small, a fluorescence detection scheme has been designed that maximises the signal collected; this scheme can be seen in figure 4.20. The fluorescence emitted vertically upwards (green lines) is collected by a large diameter lens and focussed onto a photodiode (Centronics, OSD50-E). The fluorescence emitted downwards would normally be lost, however, in our scheme a concave mirror reflects it back upwards (purple lines), giving an increase in signal of approximately 2.8×.

Two shielded BNCs take the signal from the photodiode to the locking electronics. This limits the noise picked up through the wires. To further limit noise on the signal, the photodiode is battery powered (to avoid 50 Hz noise from the mains electricity supply) and housed in a metal can, which acts as a Faraday cage. With this set up we get typical fluorescence signals of the order of 10 V. This allowed the temperature of the beam machine to be lowered from the 560 °C we initially used to 480 °C.

To form the locking signal, the frequency of the light is dithered by applying a varying voltage to the spectroscopy AOM resulting in modulation appearing on the fluorescence signal. This is then detected by a lock-in amplifier (Stanford Research Systems, SR830DSP) and subsequently turned into an error signal to lock to. The dither frequency sent to the AOM is supplied by the lock-in amplifier itself.

Lock-in amplifiers have three main stages, illustrated in figure 4.21. The input signal (in this case fluorescence) and the reference (dither) signal are multiplied together in a frequency mixer, before the output of this is passed through a low-pass filter. The remaining DC terms are subsequently amplified and form the final output signal. This gives several variables that can be controlled, including the sensitivity, time constant and filter frequency.

As can be seen in figure 4.22(b), adding a dither frequency to the AOM means that when the laser is scanned a modulation is added on top of the atomic fluorescence which is larger on the flanks and zero off resonance. Modulation with twice the dither frequency but lower amplitude is created near the peak of the resonance as for one dither cycle the resonance is crossed over twice.

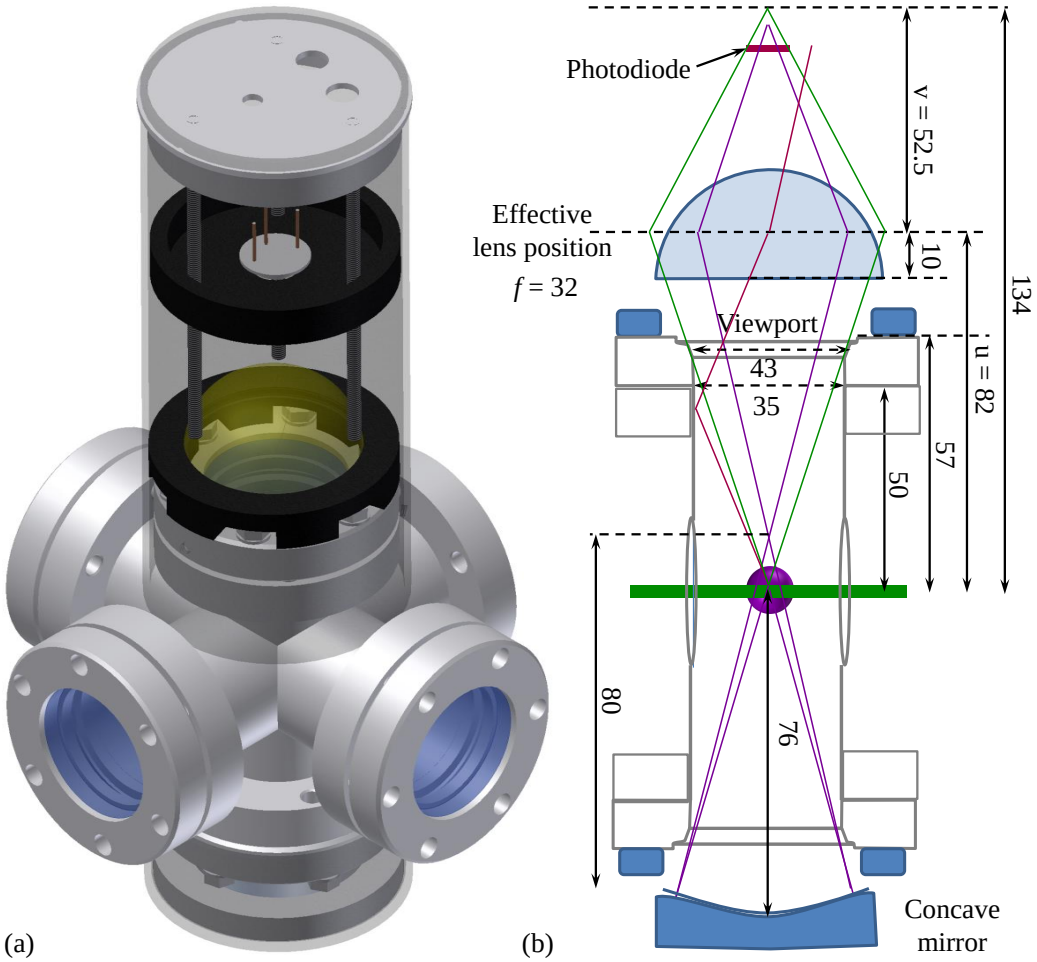

Figure 4.20: The fluorescence detection scheme. (a) The metal can the photodiode and lens are housed in is designed to fit snugly over the top viewport on the beam machine with the concave mirror fixed to the bottom viewport. Metal caps for the horizontal viewports have also been designed that only allow the laser beam through in order to minimise background light incident on the photodiode (not shown on the diagram). (b) The principle behind the fluorescence detection; the largest possible solid angle of fluorescence emitted vertically is collected onto the photodiode (green lines), although due to reflections within the beam machine there will always be some fluorescence which will miss the photodiode (red line). The concave mirror reflects light emitted downwards back up to the photodiode to increase the signal (purple lines).

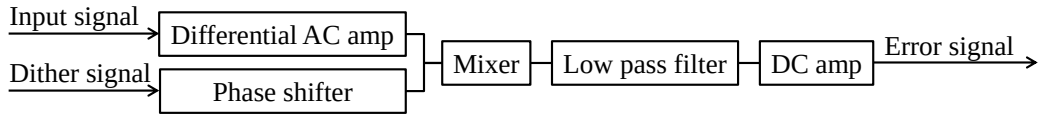

Figure 4.21: A schematic of a lock-in amplifier; the input and reference signals are phase-corrected before being mixed together. The mixed signal then goes through a low-pass filter before the remaining DC terms are amplified.

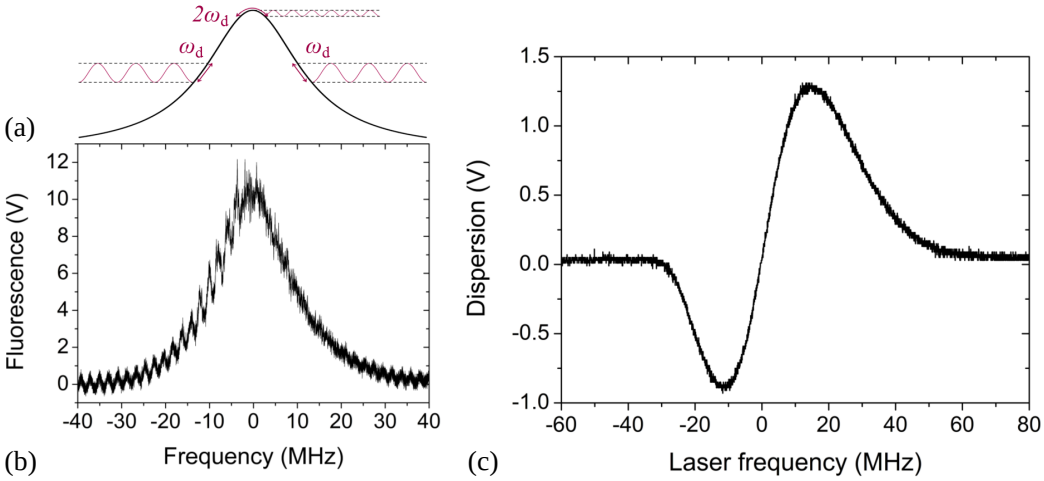

Figure 4.22: (a) As the laser scans over the atomic resonance the dither frequency adds modulation with frequency ω_d on the flanks and $2\omega_d$ at the peak. (b) An example of the modulation as it appears on the fluorescence peak of the 556 nm transition in Yb. Here $\omega_d = 100$ Hz in order to make the modulation easier to see. Uneven modulation can be seen on the flanks of the peak, although the reason behind this is unclear. Even with this apparently uneven modulation, a good error signal (c) is derived by the lock-in amplifier (the signal in (c) is not the matching dispersion signal for (b) but derived using the modulation frequency described in the text). The frequency scale on both (b) and (c) were calibrated by passing two beams through the beam machine with a known frequency offset (supplied by the AOMs).

This modulated fluorescence signal can be used to produce an error signal with the lock-in amplifier. In order to understand how the lock-in amplifier works it is necessary to consider only a small section of the modulated fluorescence signal at a time. In doing this the input signal can be approximated as a sine wave, $V_{\text{in}} = A\sin(\omega t)$ where A is the amplitude of the signal. The reference dither signal is also a sine function, $V_{\text{d}} = B\sin(\omega_{\text{d}} t)$, where B is the amplitude. The frequency mixer in the lock-in amplifier then multiplies these signals together to get

$$V_{\text{mix}} = AB\sin(\omega t)\sin(\omega_{\text{d}} t) = \frac{AB}{2}\left(\cos(\omega t - \omega_{\text{d}} t) - \cos(\omega t + \omega_{\text{d}} t)\right). \quad (4.10)$$

There are then three regions to consider in forming the error signal: off resonance, on the flanks of the resonance peak and exactly on resonance.

Off resonance there is no modulation on the input signal, i.e., $V_{\text{in}} = A$, so the mixed signal is merely $V_{\text{mix}} = AB\sin(\omega_{\text{d}} t)$. This signal is removed by the low-pass filter in the lock-in amplifier.

On the flanks of the resonance the modulation is at the dither frequency so

$$V_{\text{mix}} = \frac{AB}{2}\left(1 - \cos(2\omega_{\text{d}} t)\right); \quad (4.11)$$

the output from the mixer has both a DC and AC component. Again, the AC component is removed by the low-pass filter but this time the DC component remains.

The final case to consider is when the laser is exactly on resonance. Here $V_{\text{in}} = A\sin(2\omega_{\text{d}} t)$ so the output from the mixer is

$$V_{\text{mix}} = \frac{AB}{2}\left(\cos(\omega_{\text{d}} t) - \cos(3\omega_{\text{d}} t)\right). \quad (4.12)$$

Both of these components are subsequently removed by the filter so the output signal is zero.

In this way the error signal can be constructed as the laser scans over the atomic resonance; the output signal will initially be zero before increasing as the modulation starts to affect the fluorescence signal, only to become zero once again on resonance. On the other side of the resonance the phase of the modulation will have flipped relative to the reference signal so the sign of the DC output will also have changed. This is illustrated in figure 4.22(a).

The correct phase between the reference dither signal and the modulated fluorescence signal must be chosen in order to see this dispersion signal as if the phase is wrong then the mixer will not output a DC term. The phase of the reference signal can be changed to match that of the input signal before the two are mixed together (see figure 4.21).

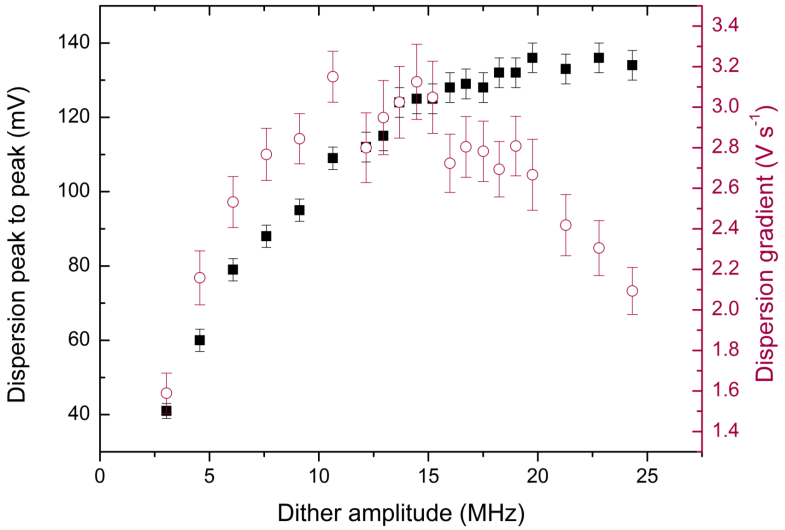

Figure 4.23: The peak to peak amplitude of the dispersion signal only saturates at large dither amplitudes (black axis), however, the dispersion gradient peaks at around 15 MHz amplitude before being washed out at larger dither amplitudes. Therefore, a compromise of 19.2 MHz was chosen giving both a large amplitude and gradient.

To lock the 556 nm laser (1.28 ± 0.02) mW of laser light was used with a dither frequency of 3 kHz; the final error signal can be seen in figure 4.22(c). This was optimised by varying the amplitude of the dither signal going to the AOM and recording the effects on both the gradient of the dispersion signal and its peak to peak amplitude. These results can be seen in figure 4.23. A final dither amplitude of 19.2 MHz was chosen as a good compromise between the two parameters. The gradient in the locking signal used in figure 4.22(c) is (0.1333 ± 0.0003) V/MHz, which gives of the order of tens of kHz stability.

Transfer cavity lock

Once the 556 nm laser is locked the transfer cavity can be locked to it, and the 399 nm laser to the cavity. A computer program, originally written by Sean Tokunaga at Imperial College London [138, 139], is used to lock lasers in this way and a screen shot of the control panel is shown in figure 4.24. The lasers are locked in this fashion in order to allow complete control over the frequency of the 399 nm laser when switching between isotopes; the 556 nm laser must simply be locked to a different atomic resonance and the frequency of the 399 nm laser can easily be shifted by the appropriate amount.

It is necessary to lock the cavity as its length can drift with temperature which will translate into frequency drifts in the blue laser as can be seen diagrammatically in figure 4.18. If V_g drifts but ΔV remains the same then

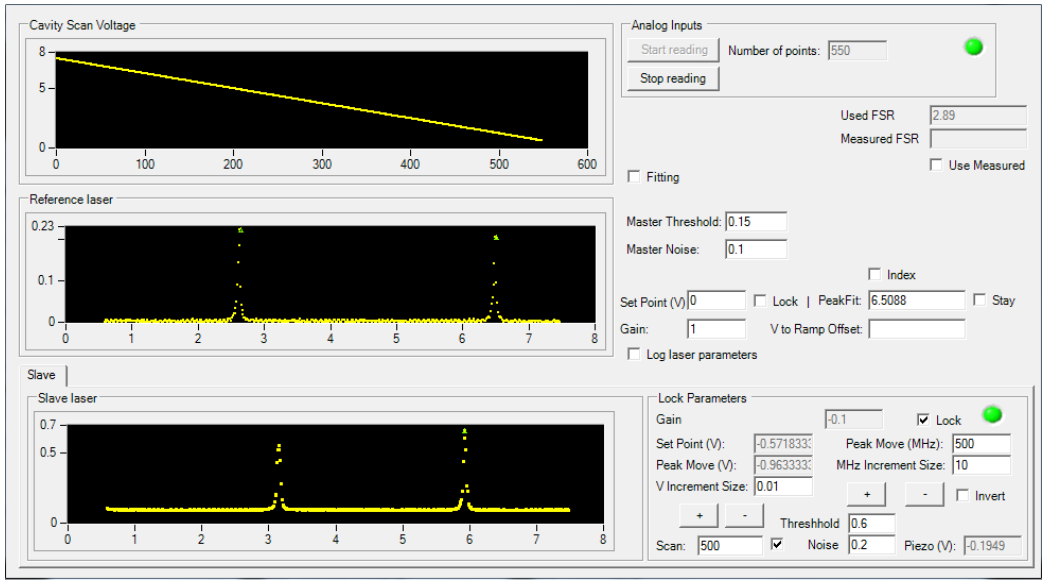

Figure 4.24: A screen shot of the transfer cavity locking program. The top plot is the cavity ramp, whilst the middle and bottom plots show the cavity peaks of the green and blue lasers respectively. The control inputs to lock the cavity and blue laser are to the right.

V_b will also drift. In the ideal case the cavity would always scan so that the length goes from $L + L_\mathrm{s}$ to $L + L_\mathrm{e}$ where L_s and L_e are determined by the start and end piezo voltages. However, in reality the cavity will drift with temperature, giving a length of $L + \mathrm{d}L$, so to make sure that the piezo is scanning over the right range the cavity length now needs to go from $L + L_\mathrm{s} - \mathrm{d}L$ to $L + L_\mathrm{e} - \mathrm{d}L$.

These lengths can be expressed as voltages using $V = \alpha L$, where α is a constant conversion factor. So $V_\mathrm{s,e} + \mathrm{d}V = \alpha(L_\mathrm{s,e} - \mathrm{d}L)$ and $\mathrm{d}V = \alpha \mathrm{d}L$. It is then this $\mathrm{d}V$ that needs to be corrected for. This is achieved by using a cavity peak for the green laser, located at some voltage V_g (see figure 4.18). If the cavity drifts with temperature this cavity peak will then occur at $V_\mathrm{g} + \mathrm{d}V$ so by monitoring the position of the peak the temperature drifts can be compensated for by adding an offset of $-\mathrm{d}V$ to the cavity piezo.

With the cavity stabilised, the cavity length at each transmission peak for the blue 399 nm (b) and green 556 nm lasers (g) are:

$$L + \Delta L_\mathrm{b} = m\frac{\lambda_\mathrm{b}}{2}, \tag{4.13}$$

$$L + \Delta L_\mathrm{g} = n\frac{\lambda_\mathrm{g}}{2}. \tag{4.14}$$

Subtracting equation (4.14) from equation (4.13) and converting both to voltages gives

$$\Delta V = V_{\mathrm{b}} - V_{\mathrm{g}} = \frac{\alpha}{2}\left(m\lambda_{\mathrm{b}} - n\lambda_{\mathrm{g}}\right), \tag{4.15}$$

with $V_{\mathrm{b}} = \alpha(L + \Delta L_{\mathrm{b}})$ and $V_{\mathrm{g}} = \alpha(L + \Delta L_{\mathrm{g}})$. By periodically scanning the voltage supplied to the piezo these voltages can be recorded.

In equation (4.15), λ_{g} is fixed as the green laser has been independently locked. A particular cavity peak has been chosen to reference the cavity to and so n is also a constant. That leaves m and λ_{b} to stabilise.

A wavemeter is used to bring the 399 nm laser frequency within 1.5 GHz (a free spectral range of the cavity) of the required frequency to ensure that the right m is selected by the program. This means that any drift in the blue laser frequency (in other words, λ_{b}) causes a change in ($\Delta V = V_{\mathrm{b}} - V_{\mathrm{g}}$). Therefore the following voltage feedback loop can be used to control the voltage, V_{out}, going to the piezo in the 399 nm master laser to bring the wavelength back to the correct value:

$$V_{\mathrm{out_n}} = V_{\mathrm{out_{n-1}}} + G\left(V_{\mathrm{set}} - (V_{\mathrm{b}} - V_{\mathrm{g}})\right), \tag{4.16}$$

where G is the gain and V_{set} is the initial (V_{b} - V_{g}) plus any voltage offset added later in the program to move the blue laser to the correct detuning. The gain has empirically been set to a value of -0.1 to give good stabilisation of the 399 nm laser.

4.4.4 Adding sidebands to the MOT beams

Sidebands were added onto the light going through the MOT AOM in order to broaden the linewidth of the light that the atoms interact with. This allowed atoms with a larger velocity to be captured from the Zeeman slower and so a greater efficiency achieved. The compromise to this situation is that the atoms will have a higher Doppler temperature in the MOT than if no sidebands were used, however, once captured the temperature of the atoms can be lowered by slowly ramping down the sidebands.

The sidebands were added by applying frequency modulation at 25 kHz to the usual RF signal driving the Yb MOT AOM (AOM 12). This was done using an Agilent E4421B ESG series signal generator set to a peak-peak amplitude of 50 mV. The amplitude determines how many sidebands were added to the light. This gave an overall linewidth of approximately 1.5 MHz. The detuning used was (8.0 ± 0.5) MHz from the atomic transition.

The sideband parameters mentioned here are merely a starting point for further optimisation with absorption imaging where both atom number and temperature will be measured to find an optimum.

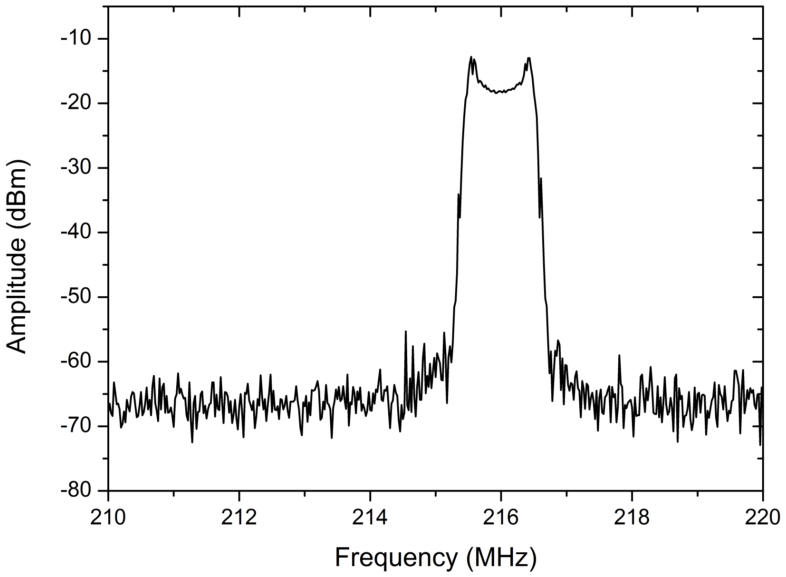

Figure 4.25: The frequency of the MOT beams is artificially broadened by the addition of many sidebands. The sideband separation is 25 kHz, which is supplied by with approximately 60 sidebands forming the broadened line.

4.5 Fluorescence detection

The number of atoms in a MOT can be inferred using fluorescence detection (figure 4.26). This is where light spontaneously emitted by the atoms trapped in the MOT is collected by a lens and focussed onto a photodiode. The lens should be as close to the atoms as possible so that a larger solid angle of emitted light can be collected.

In the experiment a lens with a focal length of 75 mm is used to focus the light onto a Thorlabs DET110 photodiode. An iris is placed before the lens to get a better measure of the solid angle of light collected- a factor that is needed when using fluorescence to calculate the number of atoms in the MOT. The iris helps to ensure all of the fluorescence from the MOT is collected whilst eliminating as much background light as possible. Figure 4.27 shows how the fluorescence signal from the MOT (the total signal recorded on the photodiode minus the level recorded when the MOT magnetic field is switched off) increases with iris diameter up to a certain point. After this diameter value the fluorescence signal from the MOT plateaus, therefore the iris should be set to this diameter as it allows the largest signal from the MOT to be collected whilst limiting the background signal.

To do this it is first necessary to consider the power, P, scattered by N atoms in a MOT [140],

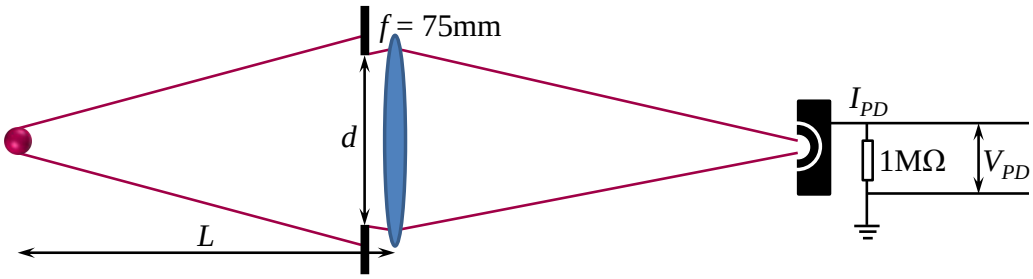

Figure 4.26: Light scattered by the atoms is collected onto a photodiode by a large diameter lens. The solid angle of light collected is calculated using an iris immediately before the lens. The fluorescence detection is currently set up in the position shown in figure 4.12.

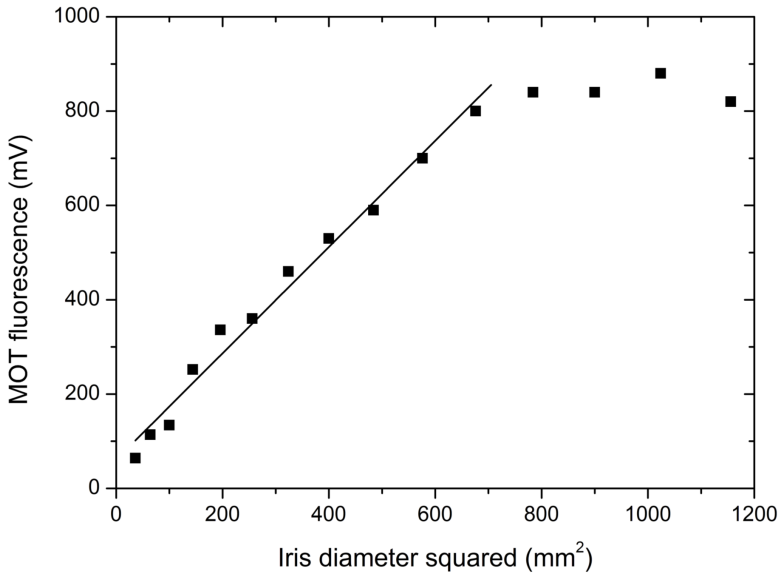

Figure 4.27: An iris is placed just before the fluorescence lens and its diameter varied. The fluorescence voltage recorded on the photodiode plateaus at a certain diameter when all of the possible light from the MOT has been collected. The iris is set at the diameter where the signal starts to plateau as this is where the best signal to noise ratio will be achieved.

$$P = \frac{Nhc}{\lambda}\frac{\Gamma}{2}\frac{I/I_\mathrm{s}}{1+4\left(\delta/\Gamma\right)^2+I/I_\mathrm{s}}, \tag{4.17}$$

where Γ is the decay rate of the excited state (in $\mathrm{rad\,s^{-1}}$), δ is 2π times the detuning in MHz and the saturation intensity is [108],

$$I_\mathrm{s} = \frac{\pi hc\Gamma}{3\lambda^3}. \tag{4.18}$$

This power is emitted symmetrically, so it is necessary to consider only the light emitted in the solid angle focussed onto the photodiode, $\Omega = d^2\pi/4L^2$, where d is the diameter of the iris and L is the atom-lens distance (illustrated in figure 4.26). Therefore the total power on the photodiode, P_PD, is

$$P_\mathrm{PD} = \frac{\Omega}{4\pi}P = \frac{d^2}{16L^2}P. \tag{4.19}$$

The photodiode is connected to an oscilloscope with a $1\,\mathrm{M\Omega}$ termination, so the corresponding voltage measured will be

$$V_\mathrm{PD} = I_\mathrm{PD}R = \mathcal{R}\left(\lambda\right)P_\mathrm{PD}R, \tag{4.20}$$

where I_PD is the photocurrent, R is the load resistance and $\mathcal{R}\left(\lambda\right)$ is the responsivity of the photodiode at the laser wavelength. The responsivity for the Thorlabs DET110 photodiode at 852 nm and 556 nm is $0.55\,\mathrm{A\,W^{-1}}$ and $0.34\,\mathrm{A\,W^{-1}}$ respectively.

Substituting in equations (4.17) and (4.19) and considering that $I >> I_\mathrm{s}$ gives the number of atoms in the MOT for Cs:

$$N = \frac{V_\mathrm{PD}}{\mathcal{R}\left(\lambda\right)R}\frac{16L^2}{d^2}\frac{\lambda}{hc}\frac{2}{\Gamma}. \tag{4.21}$$

However, this treatment does not take into account the various transitions between the Zeeman sub-levels in the ground and excited states. To take these into account the following correction needs to be made to equation (4.17):

$$P = \frac{Nhc}{\lambda}\frac{\Gamma}{2}\frac{C_1^2 I/I_\mathrm{s}}{1+4\left(\delta/\Gamma\right)^2+C_2^2 I/I_\mathrm{s}}, \tag{4.22}$$

where C_1 and C_2 are average Clebsch-Gordan co-efficients. These have experimentally been found to be $C_1 = C_2 = 0.73 \pm 0.1$ for Cs [140].

4.6 Experimental control

Experimental control is realised by using the National Instruments LabVIEW software in combination with a Field Programmable Gate Array (FPGA) board (National Instruments R-series PCI FPGA card, NI PCI-7833R) to generate both analogue and digital inputs and outputs [141].

There are 56 'fast' digital outputs which can give pulses as short as 0.9 μs and 16 'slow' digital outputs (8.2 μs). Likewise, there are 16 'slow' analogue outputs, with a response time of 44 μs and 8 'fast' analogue outputs (1.7 μs). The 16 digital inputs can act as triggers for the program to wait for an action in the experiment to occur before moving on to the next step, for example, waiting for a camera to fire. There are also 8 analogue inputs. The program is also capable of controlling devices using a GPIB connection.

4.7 Outlook: Polarisability and the optical dipole trap

Once the atoms have been captured in a MOT the next step will be to transfer them into an optical dipole trap. When an electric field, $\boldsymbol{E}$, is incident on an atom it induces a dipole moment, $\boldsymbol{d} = \alpha(\omega)\boldsymbol{E}$, where $\alpha(\omega)$ is the wavelength dependent complex polarisability of the atom. The interaction potential between the incident electric field and the dipole moment is then

$$U_{\mathrm{dip}} = -\frac{1}{2\epsilon_0 c}\mathrm{Re}(\alpha)I(\mathrm{r}), \tag{4.23}$$

where $I(r)$ is the intensity of the electric field and $\mathrm{Re}(\alpha)$ is the real part of the atomic polarisability.

In an optical dipole trap the applied electric field comes from a far off resonance laser beam. As the laser intensity varies across the diameter of the Gaussian beam, the atoms feel a force equal to the gradient of the interaction potential, which traps them within the most intense part of the beam. The depth of the trap for the atoms can be calculated from equation (4.23) by inputting the maximum intensity, I_0, of the laser,

$$I_0 = \frac{2P}{\pi\omega_0^2}, \tag{4.24}$$

where P is the laser power and ω_0 is the waist.

Therefore, in order to prepare for the next step in the experiment of trapping the atoms optically and to ensure that the correct lasers were bought, the polarisabilities of Cs and Yb were calculated and used to calculate the respective optical trap depths.

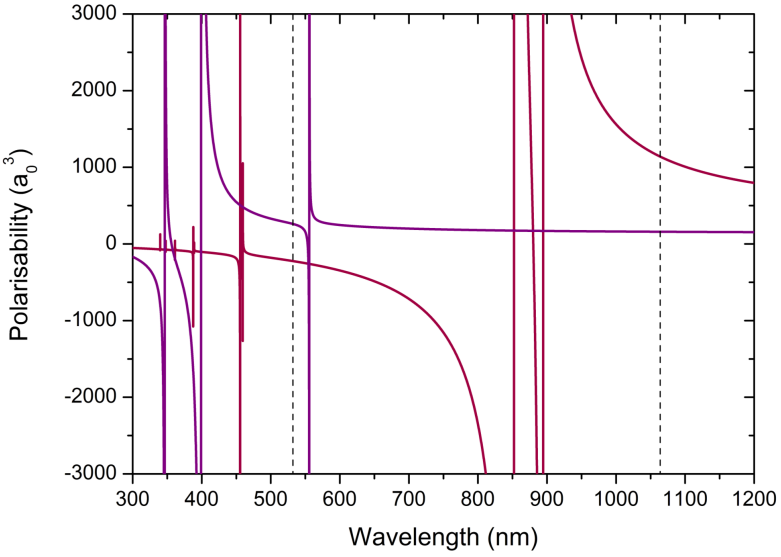

Figure 4.28: The polarisability of Cs (red) and Yb (purple). The wavelengths of the possible dipole trap lasers (532 nm and 1064 nm) are shown as dashed lines. The polarisability of Cs is negative at 532 nm indicating that a barrier rather than a potential well would be created by a laser beam of this wavelength. This may help to balance the trap depths for Cs and Yb if both wavelengths were used.

4.7.1 Polarisability

The polarisability of an atom can be thought of as the amount by which the electronic charge distribution is distorted by an applied electromagnetic field. It can be calculated using the following formula [142]:

$$\alpha_\nu^{ns} = \frac{1}{3}\sum_{n'}\left(\frac{\delta E_{n'p_{1/2}}\left\langle n'p_{1/2}\left\|D\right\|ns\right\rangle^2}{\delta E_{n'p_{1/2}}^2-\omega_0^2}+\frac{\delta E_{n'p_{3/2}}\left\langle n'p_{3/2}\left\|D\right\|ns\right\rangle^2}{\delta E_{n'p_{3/2}}^2-\omega_0^2}\right) \quad (4.25)$$

where $\left\langle n'p_{1/2}\left\|D\right\|ns\right\rangle$ and $\left\langle n'p_{3/2}\left\|D\right\|ns\right\rangle$ are the matrix elements for the transition from an s state to a p state, ω_0 is the frequency of this transition and E_{np} its energy. In practice, a good approximation for the real part of the polarisability can be calculated by summing over the light shifts for several atomic levels,

$$\mathrm{Re}(\alpha) = \sum_{\mathrm{i}}\frac{3\pi\epsilon_0 \mathrm{c}^3}{\omega_{0,\mathrm{i}}^3}\left(\frac{\mathrm{A_i}}{\omega_{0,\mathrm{i}}-\omega}+\frac{\mathrm{A_i}}{\omega_{0,1}+\omega}\right), \quad (4.26)$$

where ω is the laser frequency and A_i is the Einstein A-coefficient for transition, i. When summing over energy levels that have fine structure splitting

Transition	λ_{vac} (nm)	A-coefficient (s^{-1})
6s $^2S_{1/2} \rightarrow$ 6p $^2P_{1/2}$	894.5929600	2.862×10^7
6s $^2S_{1/2} \rightarrow$ 6p $^2P_{3/2}$	852.3472759	3.279×10^7
6s $^2S_{1/2} \rightarrow$ 7p $^2P_{1/2}$	459.44880	7.93×10^5
6s $^2S_{1/2} \rightarrow$ 7p $^2P_{3/2}$	455.65844	1.84×10^6
6s $^2S_{1/2} \rightarrow$ 8p $^2P_{1/2}$	388.9710415	8.99×10^4
6s $^2S_{1/2} \rightarrow$ 8p $^2P_{3/2}$	387.72473	3.86×10^5
6s $^2S_{1/2} \rightarrow$ 9p $^2P_{1/2}$	361.83400	2.23×10^4
6s $^2S_{1/2} \rightarrow$ 9p $^2P_{3/2}$	361.25014	1.43×10^5
6s $^2S_{1/2} \rightarrow$ 10p $^2P_{1/2}$	348.1057	6.33×10^3
6s $^2S_{1/2} \rightarrow$ 10p $^2P_{3/2}$	347.7805	6.27×10^4
6s $^2S_{1/2} \rightarrow$ 11p $^2P_{1/2}$	340.0955	2.36×10^3
6s $^2S_{1/2} \rightarrow$ 11p $^2P_{3/2}$	339.8941	3.61×10^4

Table 4.3: The transitions from the ground state in Cs used to calculate the polarisability. All values are taken from [143]. The wavelengths above have been calculated from the wavenumbers stated in the paper as the wavelengths given are in air.

Transition	λ_{vac} (nm)	A-coefficient (s^{-1})
$4f^{14}6s^2\ ^1S_0 \rightarrow 4f^{14}6s6p\ ^3P_1$	555.80236	1.15×10^6
$4f^{14}6s^2\ ^1S_0 \rightarrow 4f^{14}6s6p\ ^1P_1$	398.91142	1.92×10^8
$4f^{14}6s^2\ ^1S_0 \rightarrow 4f^{13}5d6s^2\ (7/2, 5/2)_1$	346.53620	6.83×10^7
$4f^{14}6s^2\ ^1S_0 \rightarrow 4f^{13}5d^26s$	267.2754	1.43×10^7
$4f^{14}6s^2\ ^1S_0 \rightarrow 4f^{14}6s7p\ ^1P_1$	246.5242	1.00×10^8

Table 4.4: The transitions from the ground state in Yb used to calculate the polarisability. All values and state assignments have been taken from [65], although the wavelengths are calculated from the wavenumber as the stated wavelengths in this reference are for air.

the A-coefficients should be weighted according to their angular momentum.

The polarisability for Yb and Cs can be seen in figure 4.28. The atomic levels used for these calculations are summarised in tables 4.3 and 4.4.

4.7.2 Optical dipole trap depth

Once the wavelength dependent polarisability is known, the maximum potential created by a laser beam can be calculated from equation (4.23). The two wavelengths that are routinely used to create an optical dipole trap for Yb are 532 nm and 1064 nm. However, as this is a dual-species experiment the same laser needs to be able to trap both species. As can be seen in figure 4.28, at 532 nm the polarisability for Yb is positive, giving a negative

Wavelength (nm)	Polarisability (a_0^3)	
	Cs	Yb
532	-223.9	261.2
1064	1139.1	158.2

Table 4.5: The polarisabilities for Cs and Yb at the two possible dipole trap wavelengths.

U_{dip} and so a potential well (in other words the Yb atoms would be trapped). However, the polarisability of Cs at this wavelength is negative, producing a potential barrier. Therefore, a 532 nm laser alone would not be able to trap both species.

On the other hand, the polarisabilities for both Yb and Cs are positive at 1064 nm, meaning that both can be trapped with a laser at this wavelength. However, as can be seen in table 4.5, the polarisability for Cs at this wavelength is much larger than that for Yb. This would give a trap depth approximately 7 times deeper for Cs. Therefore, to give the ability to modify the trap depths for Cs and Yb relative to each other a combination of 532 nm and 1064 nm light could be used; the 532 nm light would decrease the trap depth for Cs but increase it for Yb.

A similar method is used at the University of Düsseldorf in the RbYb experiment [136], although in this scheme the Rb is in a purely magnetic trap whereas Yb is trapped optically. This would not be an option for the Yb-Cs experiment as Cs cannot be condensed in a purely magnetic trap (although reaching BEC is not a pre-requisite for forming ultracold molecules).

Chapter 5

Experimental apparatus: Zeeman slower

This chapter gives a summary of the theory behind Zeeman slowing and then details how the dual species Zeeman slower for Cs and Yb was designed, constructed and simulated. More in-depth explanations of Zeeman slowing can be found in many atomic physics textbooks and review articles, for example, [69, 108, 144].

5.1 Basic principles

Zeeman slowers use the same basic principle of laser cooling described in Chapter 4. Atoms exiting the oven travel at velocities hundreds of times greater than the capture velocity of a MOT and so need to be slowed before they can be trapped. This cannot just be done with laser cooling as any appreciable change in their velocity will Doppler shift the atoms off resonance with the cooling light, therefore some way needs to be found to keep the atoms on resonance with the laser as the atoms are decelerated to rest.

Historically two methods have been used to achieve this; frequency chirping [145] and Zeeman slowing [144]. Chirp cooling sweeps the laser frequency to keep pace with the changing Doppler shift of the slowing atoms, whereas in a Zeeman slower a varying magnetic field is applied to perturb the energy levels of the atoms and so keep them on transition for the length of the slower. Chirp cooling is relatively simple, however it will only cool a small subset of atoms within a certain velocity range from the oven, giving a pulse of cooled atoms. Zeeman slowing will give a constant stream of cooled atoms and a larger velocity class of atoms can be slowed.

If an atom with initial velocity, v_0, is under a constant deceleration, a, then its velocity, v, at any point, z, along the Zeeman slower will follow

$$v_0^2 = v^2 + 2az. \tag{5.1}$$

The deceleration is provided by the radiation force discussed in Section 4.1 and the maximum deceleration is $a_{\max} = \hbar k\Gamma/2m$ from equation (4.2). In general, the deceleration provided by the Zeeman slower will be $a = \eta a_{\max}$ where η is a design parameter such that $0 < \eta < 1$. The stopping length for an atom to come to rest under this deceleration is $L_0 = v_0^2/a_{\max}$. Combining these gives the velocity profile under constant deceleration by the radiation force of

$$v = v_0\sqrt{\left(1 - \frac{2\eta z}{L_0}\right)}. \tag{5.2}$$

To keep the atoms on resonance the frequency shift produced by the Zeeman effect needs to obey

$$\omega_0 \pm \frac{\mu B(z)}{\hbar} = \omega + kv, \tag{5.3}$$

where ω_0 is the atomic resonance frequency, ω the laser frequency and $\mu = (g_e m_e - g_g m_g)\mu_B$ is the effective magnetic moment of the atom. Substituting in equation (5.2) and re-arranging gives the magnetic field profile required,

$$\begin{aligned} B(z) &= \frac{\hbar\Delta\omega}{\mu} \pm \frac{k\hbar v_0}{\mu}\sqrt{1 - \frac{2\eta z}{L_0}} \\ &= B_0 \pm \Delta B\sqrt{1 - \frac{z}{L}}, \end{aligned} \tag{5.4}$$

where $\Delta\omega = \omega - \omega_0 = \delta$ is the laser detuning from resonance. The $\pm$ sign is due to being able to drive either σ^- or σ^+ transitions depending on how the energy levels are shifted by the magnetic field (see Section 5.1.1). The effective length of the Zeeman slower can be defined as

$$L = \frac{L_0}{2\eta} = \frac{v_0^2 m}{\eta\hbar k\Gamma}. \tag{5.5}$$

Typically Zeeman slowers are designed so $1/3 < \eta < 2/3$. The upper limit on η gives headroom for fluctuations in magnetic field, detuning and laser intensity without causing atoms to be lost from the Zeeman slower. If $\eta > 1$ then an non-physical deceleration $a > a_{\max}$ is needed. The lower limit is merely to ensure that the Zeeman slower is not too long - a lower design parameter means that the length of the slower needs to increase to get the same level of slowing. Conversely, if there is limited laser power available

then the design parameter can be decreased in order to decelerate the atoms over a greater distance.

All atoms with initial velocities in the range v_0 to v_f (the final velocity at the end of the slower) will come into resonance with the laser somewhere along the length of the slower and so the capture efficiency is high compared to the chirp cooling method. The final exit velocity should be equal to or slower than the capture velocity of the MOT (calculated for Yb and Cs in Section 4.2.2).

5.1.1 Magnitude of the magnetic field

As can be seen in equation (5.4), there are two basic choices of magnetic field profile for a Zeeman slower; one with an increasing magnetic field magnitude and the other with a decreasing field following from the minus or plus sign in the equation respectively. These two profiles are shown in figure 5.1(a). An offset could be added to each of these field profiles which would affect the detuning of light required to slow the atoms and, if the field changed sign part way along the slower, would mean that the magnetic field would be decreasing in magnitude in one part and increasing in the other, for example, the field shown in figure 5.1(b). Different atomic transitions are driven (by the same handedness of circularly polarised light) in these two regimes.

Considering a simple example of an atom with $F = 0$ and $F' = 1$, the Zeeman effect causes a shift in energy of

$$E = m_F g_F \mu_\mathrm{B} B \tag{5.6}$$

for each magnetic sublevel, m_F, where the effective magnetic moment $\mu = m_F g_F$. As illustrated in figure 5.1(d), when an atom slows, the laser frequency, ω, required to keep the atoms on resonance decreases until it matches the resonance frequency for atoms at rest, ω_0. At the end of the slower when the velocity of the atoms is close to zero, the Doppler shift (kv) is also zero so $\hbar\Delta\omega = \mu B_0$ as in equation (5.4). Therefore, to keep track of the reducing Doppler shift, the energy of the sublevel must also decrease.

In an example where the magnitude of the magnetic field decreases, a state must be found whose energy decreases with decreasing field and that state is $m_F = +1$, see figure 5.1(c). This means that the energy of the sublevel is decreasing along the length of the slower to keep track of the slowing velocity. The same can be done for an increasing field Zeeman slower, where a state must be found whose energy decreases as the field increases, in other words $m_F = -1$. More generally, decreasing field Zeeman slowers use $\Delta m_F = +1$ transitions (σ^+) whilst increasing field Zeeman slowers use $\Delta m_F = -1$ transitions (σ^-).

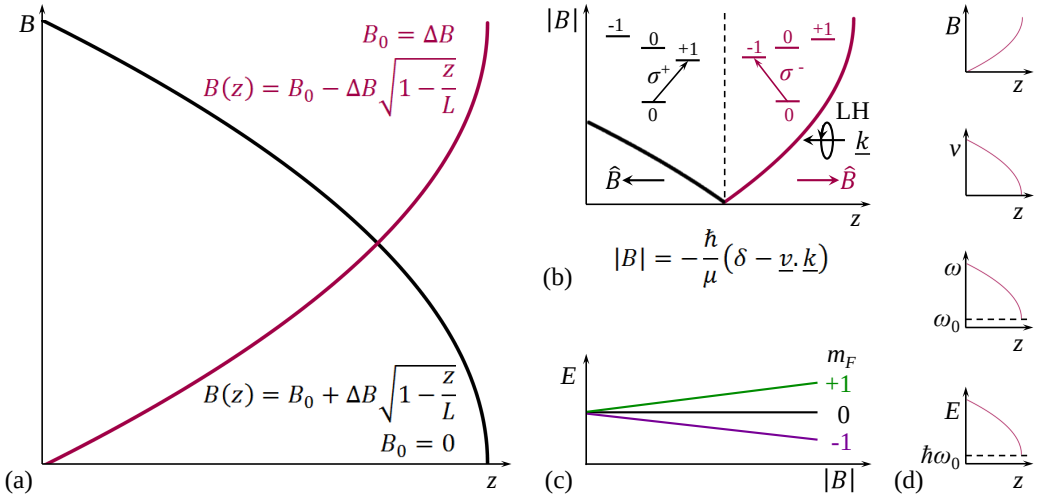

Figure 5.1: (a) The magnetic field magnitude of a Zeeman slower can either increase or decrease, depending on the choice of sign in equation (5.4). The two fields here are plotted such that the sign of the field does not change along the slower. However, if, as in (b), the magnetic field does change direction along the slower, the first part will be a decreasing field Zeeman slower whilst in the second half the magnitude will increase again. This means that σ^+ transitions will be driven at first and then σ^- for the same handedness of light. (c) A state is needed whose energy decreases as the magnitude of the field either decreases ($m_F = +1$) or increases ($m_F = -1$). (d) Whether the field increases or decreases, the velocity always decreases along the slower meaning that the required laser frequency also decreases and therefore the energy of the state must decrease to keep track of the changing Doppler shift.

5.2 Zeeman slowing multiple atomic species

Bearing in mind that for an efficient Zeeman slower η should be somewhere in the range $1/3 < \eta < 2/3$ this puts limits on which atomic species can be slowed simultaneously in the same magnetic field profile. For two species, a and b, to be slowed by the same magnetic field profile then $B_{0,\mathrm{a}}/L_{0,\mathrm{a}} = B_{0,\mathrm{b}}/L_{0,\mathrm{b}}$. Using equation (5.5), the following ratio can then be derived,

$$\frac{\eta_{\mathrm{a}}}{\eta_{\mathrm{b}}} = \frac{\mu_{\mathrm{a}}^2 m_{\mathrm{a}} k_{\mathrm{b}}^3 \Gamma_{\mathrm{b}}}{\mu_{\mathrm{b}}^2 m_{\mathrm{b}} k_{\mathrm{a}}^3 \Gamma_{\mathrm{a}}}. \tag{5.7}$$

For both species to be efficiently slowed, this ratio should be in the range $1/2 < \eta_{\mathrm{a}}/\eta_{\mathrm{b}} < 2$ so that the individual η can still be in the normal range of $1/3 < \eta < 2/3$. For the relevant transitions for ^{133}Cs and ^{174}Yb, $\mu_{\mathrm{Cs}} = \mu_{\mathrm{Yb}} = \mu_{\mathrm{B}}$ and so this ratio equals 0.015, which is outside of the range. Therefore Cs and Yb cannot be simultaneously and efficiently slowed in the same Zeeman slower. However, the same set of coils can be run at different currents to produce distinct magnetic field profiles for sequential loading.

$\eta_{\mathrm{a}}/\eta_{\mathrm{b}}$ values for various combinations of atomic species are listed in [146].

5.3 Design of the Yb-Cs Zeeman slower

When designing a Zeeman slower many considerations can come into play, such as available space in the lab dictating the total length of the slower, ensuring the Zeeman slower light has a sufficient detuning from resonance so that atoms in the MOT are not affected by it and making certain that the magnetic field at the end of the slower is properly nulled before the MOT region. An added complication is that the same Zeeman slower coils must be able to give a suitable magnetic field profile for both Cs and Yb, so a certain degree of flexibility must be built into them.

There are three main areas that were considered in the design of the Yb-Cs Zeeman slower; the magnetic field profile, the laser beam properties and whether repumping transitions were needed.

5.3.1 Magnetic field profile

For clarity in the following discussion equation (5.4) is repeated again:

$$\begin{aligned} B(z) &= \frac{\hbar\Delta\omega}{\mu} \pm \frac{k\hbar v_0}{\mu}\sqrt{1 - \frac{2\eta z}{L_0}} \\ &= B_0 \pm \Delta B\sqrt{1 - \frac{z}{L}}, \end{aligned}$$

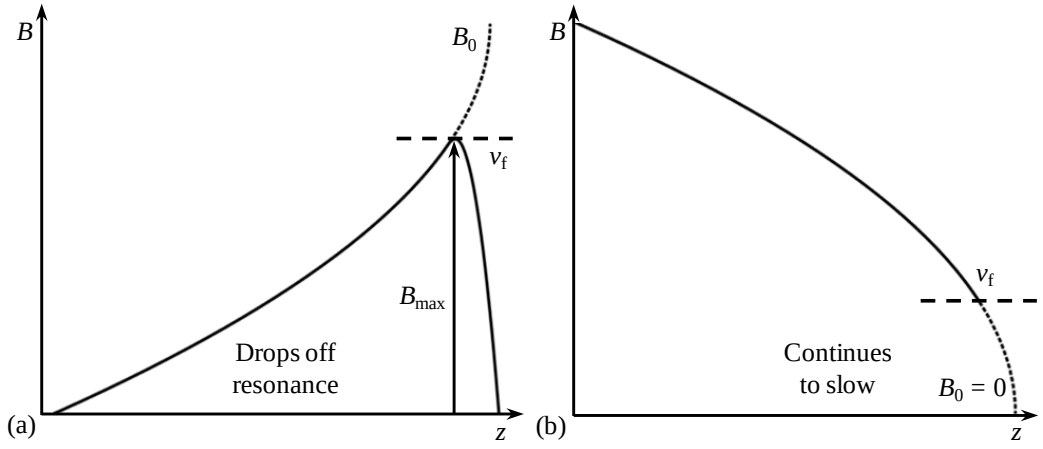

Figure 5.2: (a) If the magnitude of the magnetic field is increasing at the end of the Zeeman slower the atoms have a well defined final velocity, v_f, as their Zeeman sublevels are no longer being shifted by the field to be on resonance with the laser beam and so they are released from the slower cleanly. (b) On the other hand, if the magnetic field is decreasing then the desired final velocity is unlikely to be achieved as the atoms are on resonance with the laser beam with very little or no magnetic field and so they continue to interact with the light and are potentially slowed too much.

The relevant parameters to consider here are the total change in magnitude of the magnetic field, ΔB, the ideal field at the end of the slower, B_0, the actual field at the end of the slower, $B_{\max}$ and the length of the slower L.

Detuning, $\delta \rightarrow B_0$

The first decision to make when designing a Zeeman slower is how the atoms should be de-coupled from the magnetic field at the end of the slower. If the magnitude of the field is increasing at the end then the atoms rapidly come out of resonance with the laser and so there is greater control of the release velocity, v_f. However, if the magnitude of the field is decreasing to zero at the end the atoms will remain on resonance with the laser beam (whose detuning $\delta = 0$) and so there is a greater risk of the atoms being slowed too much and turned back down the slower. This is demonstrated in figure 5.2. Therefore, it was chosen to have an increasing field at the end of the Zeeman slower, such that σ^- transitions are driven, to give a clean release velocity.

Broadly speaking, a Zeeman slower can be designed for any possible detuning; it is merely a matter of shifting the entire magnetic field profile up or down in magnitude, in other words changing the B_0 value in the equation above. However, the Zeeman slower cannot just be considered in isolation; there is a dynamic interplay between the slower and the MOT, not just in terms of the magnetic fields of the two but also in terms of laser cooling.

The MOT is formed of three pairs of counter-propagating laser beams, as can be seen in figure 4.12. In the Yb-Cs system, the Zeeman slower beam passes through the centre of the MOT region at 30° to one of the horizontal MOT beams for both Cs and Yb and as such, it will contribute to the radiation force felt by the atoms in the MOT. Therefore, the Zeeman slowing beam should be detuned far enough away from resonance that it has a negligible effect on the MOT. However, at least in the case of Cs, if the detuning is too great the Zeeman slower light could start pumping significant numbers of atoms into the $F' = 4$ state as there is only 251 MHz separation between the $F' = 5$ and $F' = 4$ states (figure 2.1). Whilst this would not be disastrous due to the repumping beam already in place, it would at least mean that a larger power in the MOT repumping beam would be required.

In other experiments [147, 148] it has been found that the range of detuning for a Zeeman slower for Cs should be approximately 50 to 60 MHz. Therefore, we chose to use approximately 60 MHz (see table 5.1). The detuning required for a 399 nm Yb Zeeman slower feeding a 556 nm MOT has been experimentally found to be best from 500 MHz to 660 MHz [120, 136, 149]. This is quite a large detuning and comes about as the 399 nm light interferes with the 556 nm MOT [120].

Capture velocity, $v_0 \rightarrow \Delta B$

Whilst the theory behind equation (5.4) uses a single capture velocity to inform the shape of the magnetic field, in reality the oven will produce atoms with a range of velocities according to the Maxwell-Boltzmann distribution (as discussed in Section 3.2.1). A Zeeman slower can be designed to capture a large proportion of the atoms from the oven if the capture velocity is near the peak of the distribution. Figure 3.4 shows the Maxwell-Boltzmann distributions for both Cs and Yb atoms from the dual species oven running at temperatures of 100 °C and Yb at 400 °C respectively. From this figure it can be seen that the capture velocities of 200 m s^{-1} and 300 m s^{-1} for Cs and Yb cover close to half of the individual distributions.

However, if the capture velocity is too high then the Zeeman slower has to become longer in order to be able to slow the atoms if the same efficiency parameter is kept (see equation (5.5)).

Atoms with velocities below the design capture velocity will come into resonance with the magnetic field of the Zeeman slower at some point further along the length and so will start to be slowed from that point. On the other hand, atoms with velocities above the capture velocity will not be slowed at all and will travel down the vacuum system unhindered.

Design parameter, $\eta \rightarrow L$

As explained in Section 5.2, it is not possible to use the same magnetic field profile to slow Cs and Yb simultaneously. Therefore the same set of coils must be able to be run at different currents to sequentially load the atoms. This impacts the desired design parameters for the two species as compromises must be made to use the same coil set for both.

The maximum deceleration is smaller for Cs owing to its smaller scattering rate and smaller photon energy ($a_{\max}$ values for both Cs and Yb can be found in table 4.1). Thus it is Cs that dictates the minimum length of the Zeeman slower, being 0.70 m for a higher end efficiency of 0.5. Yb can easily be slowed in such a long Zeeman slower with a correspondingly low design parameter of 0.128. If Yb alone was being slowed by a Zeeman slower with the same design parameter as for Cs above (i.e., 0.5) the slower would have to be just 0.18 m.

The chosen value of η cannot be too high as if local magnetic field or laser intensity fluctuations require it to go above 1 then atoms will be lost as an non-physical deceleration greater than $a_{\max}$ would be required. Therefore the logical step to take when designing the Zeeman slower was to lower η_{Yb} but keep η_{Cs} at a sensible value. Therefore, the design efficiency parameters for Cs and Yb are 0.5 and 0.128 respectively.

Final velocity, $v_{\mathrm{f}} \rightarrow B_{\max}$

The idealised final velocity for a Zeeman slower is zero, however, in reality this is impractical as the end of the Zeeman slower cannot coincide exactly with the MOT position. Therefore, the atom has to have a non-zero final velocity in order to be captured in the MOT. However, the final velocity should not exceed the capture velocity of the MOT.

The MOT capture velocity for Yb is relatively small at $10\,\mathrm{m\,s^{-1}}$ (see Section 4.2.2), so the atoms need to be released from the Zeeman slower at a correspondingly low velocity. This impacts on the design of the Zeeman slower in two ways; firstly, the end of the magnetic field profile must be able to be precisely tailored to release the atoms at exactly the right velocity and secondly the distance between the release point of the Zeeman slower and the MOT location must be as short as possible. If the atoms are released too soon they will be too fast to capture in the MOT and if they are released too late they might be slowed too much and be turned back down the slower or else will have too little residual velocity to reach the MOT location before dropping under gravity. This is why the MOT must be as close as possible to the end of the Zeeman slower. The latter consideration had an impact on the choice of science chamber whereas the first point was a concern when designing the Zeeman slower coils.

In the ideal case shown in figure 5.2(a) (dashed line) the magnetic field makes a sudden drop off at $z = L$ which would theoretically slow the atoms to rest. This is neither desirable, in that the atoms would not make it to the MOT location, nor practical, in that so sharp a drop in magnetic field is not achievable. On a practical level, the release velocity of the Zeeman slower is adjusted by rounding off the field profile at the end of the slower. The smaller the magnitude of the magnetic field at the end of the slower, $B_{\max}$, the higher the release velocity as the atoms are decoupled from the slowing beam earlier.

However, as the capture velocity of the Yb MOT is so small, the Zeeman slower must have a relatively sharp drop off that is able to be precisely controlled to optimise the loading into the MOT. The field for Cs is much more flexible in that the MOT capture velocity is higher at $48\,\mathrm{m\,s^{-1}}$. To create the sudden drop in field a pair of high current, thin coils are used at the end of the slower, producing large, opposing magnetic fields. The first coil has a positive current to produce the fast upturn in field seen in figure 5.1 whilst the second coil has a current applied in the opposing direction, giving a large field orientated opposite to the first coil, producing the sharp drop off in field. The currents going to each coil can be varied to modify the exact release point.

Careful tailoring of the Zeeman slower magnetic field profile can limit the impact on the magnetic field magnitude and gradient at the MOT position. Fine tuning of the residual magnetic fields at the MOT location can be achieved with shim and compensation coils.

Producing the magnetic field

Once the magnetic field profile has been designed there are a number of methods for producing the required magnetic field; a single helical coil with varying pitch [150], permanent magnet arrangements [151], individual coils with varying numbers of turns able to be moved horizontally and coils wound the length of the slower. The most versatile of these is the last as it allows the whole field profile to be shifted up and down to match different detunings. If a solenoid is wound along the length of the slower this allows multiple atomic species to be slowed with the same coil set. Therefore, it was this method that was chosen for the Yb-Cs Zeeman slower.

5.3.2 Laser properties

Beam profile

The upper limit imposed on the efficiency parameter (typically $\eta < 2/3$) gives room for local fluctuations in magnetic field strength and random photon

scattering events that might cause atoms to be lost from the slower. This is the most critical at the end of the Zeeman slower where the atoms should be released at a specific velocity.

The Zeeman slower beam will have a Gaussian profile where the intensity varies across the cross-sectional area of the beam. It was found in simulations (see Section 5.5) that the best results were obtained when the beam was focussed towards the oven as this ensures that the beam intensities are larger than the nominal on-axis design intensity everywhere except at the very end of the slower. Thus the bulk of the atoms that are travelling on trajectories transversely displaced from the main slower axis are efficiently slowed.

Conversely, increasing the power can compensate for other parameters being sub-optimal in the Zeeman slower. Efficient slowing of atoms in a Zeeman slower depends on having the correct scattering rate which depends both on detuning and beam intensity, so each can compensate for the other.

Deceleration, a

The deceleration in the Zeeman slower is assumed to be constant in equation (5.4), however, in reality it is quantised as each photon absorbed gives the atom a distinct momentum kick. The random nature of the momentum changes could also cause some atoms to be lost from the Zeeman slower, however, the probability of this occurring is limited by setting η to an appropriately low value (i.e., no higher than 2/3).

5.3.3 Repumping transitions

Caesium

Just as for the MOT, Cs requires a repumping beam to close loss routes arising from off-resonant pumping into unwanted states. The Zeeman slower designed for Yb-Cs uses left handed circularly polarised light which primarily drives the $|4,+4\rangle \rightarrow |5,+5\rangle$ transition for the majority of the Zeeman slower (where the states have been labelled $|F, m_{\mathrm{F}}\rangle$). At the end of the slower the same light drives the $|4,-4\rangle \rightarrow |5,-5\rangle$ transition as the magnetic field starts to increase rather than decrease. This is illustrated in figure 5.3 by the dashed arrows. The following discussion will concentrate on the σ^+ transitions, however, the same treatment could also be applied to the σ^- transitions.

The same polarisation of light that drives the $|4,+4\rangle \rightarrow |5,+5\rangle$ transition could also drive the $|4,+3\rangle \rightarrow |5,+4\rangle$ transition, although the detuning for this line will be slightly different as the Zeeman shifts between the two states are different (g_{F} takes a different value in equation (5.6)). This may just increase the number of atoms that can be slowed by the Zeeman slower and is not a problem.

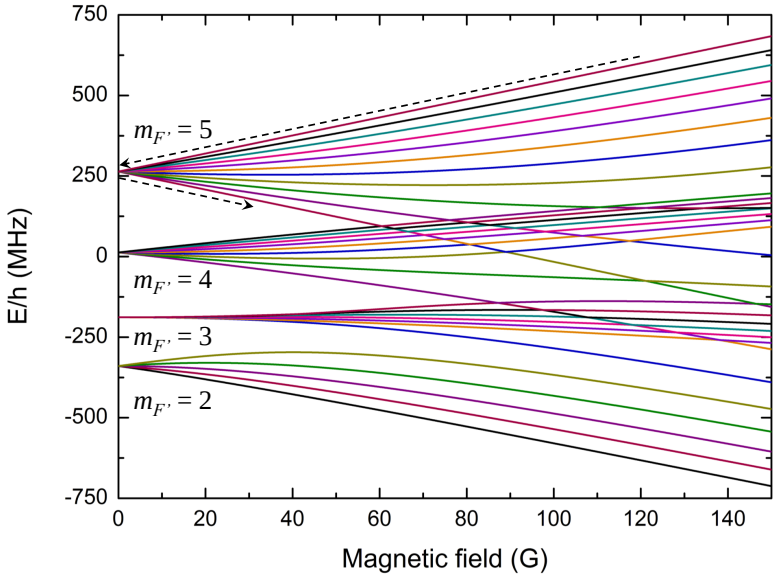

Figure 5.3: The Briet Rabi diagram for the $^2P_{3/2}$ state of Cs. The dashed arrows indicate the states used in the Zeeman slower; $|5, +5\rangle$ for the majority of the slower where the magnitude of the Zeeman slower field is decreasing and $|5, -5\rangle$ for the end section where the field increases.

In practice the Zeeman slowing laser beam will never have pure circular polarisation, a small percentage will have linear polarisation, which could drive the $|4, +4\rangle \rightarrow |5, +4\rangle$ transition. However, there is also a finite probability that some atoms will be pumped from the ground $|4, +4\rangle$ to the excited $|4, +4\rangle$ state by this linearly polarised light, in the same way that some atoms in a MOT will also be lost into the $F = 3$ state via the $F' = 4$ state. Therefore, repumping light on the $|3, +3\rangle$ to $|4, +4\rangle$ transition is required as otherwise atoms would eventually be lost into the $F = 3$ state. Furthermore, reflections and scattering within the vacuum tube can also lead to a small but significant percentage of ill-defined polarisation.

Another reason for using a repumping beam is that the Cs atoms effusing from the oven will be uniformly distributed over 16 possible m_F states (9 in $F = 4$ and 7 in $F = 3$). Although we have not yet carried out a detailed numerical simulation of the effect of this, we have identified many possible routes whereby atoms in non-target m_F states can come into resonance with the repumping and slowing beams at different positions along the slower and be optically pumped into the target state. This could account for the significant enhancement in number seen when the repumping beam is unblocked when loading a MOT (see Section 6.1.1).

Parameter	Cs	Yb
v_0 ($\mathrm{m\,s^{-1}}$)	200	300
δ (MHz)	58.7	609.2
η	0.500	0.128
L (m)	0.70	0.70
B_0 (G)	41.8	435
ΔB (G)	166.8	537
B_{max} (G)	13.1	378

Table 5.1: The design parameters for the Yb-Cs Zeeman slower.

Ytterbium

The Zeeman slowing beam for Yb uses the ${}^1S_0 \rightarrow {}^1P_1$ transition at 399 nm. As the branching ratio from the ${}^1P_1$ state into the triplet ${}^3D_2$ and ${}^3D_1$ states is fairly small there is no need to use repumping light for the Yb Zeeman slower beam. The branching ratio would be a problem in a MOT where atoms would undergo many more scattering events when trapped for an appreciable time, whereas atom losses to the dark states in a Zeeman slower are negligible. Any repumping scheme for this transition would also be fairly involved for little net gain.

5.3.4 Design conclusions

From the above discussion of each of the factors that need to be considered to design a Zeeman slower it can be seen that each parameter is intimately linked to the others and making a change to one impacts on all of them. Therefore, designing and optimising a Zeeman slower is quite a 'soft' process in that several combinations of parameters could be found that would produce the same effect. The most important parameters for a Zeeman slower for Cs and Yb are summarised in table 5.1.

The designed coil set

Bearing in mind the need for precise control of the magnetic field profile, the Yb-Cs Zeeman slower was designed to have five coils, as can be seen in figure 5.4; a solenoid running the whole length of the slower, the field-profile coils (in two parts) and two small, high current coils at the end of the slower.

The majority of the field profile is created by the two coils wound directly on top of the solenoid (coils 1 and 2 in figure 5.4(b)). These coils were wound in two sections so that the current direction could be switched between the two halves. This meant that the total number of turns required could be reduced and lower currents used as the magnetic field profile is kept as small

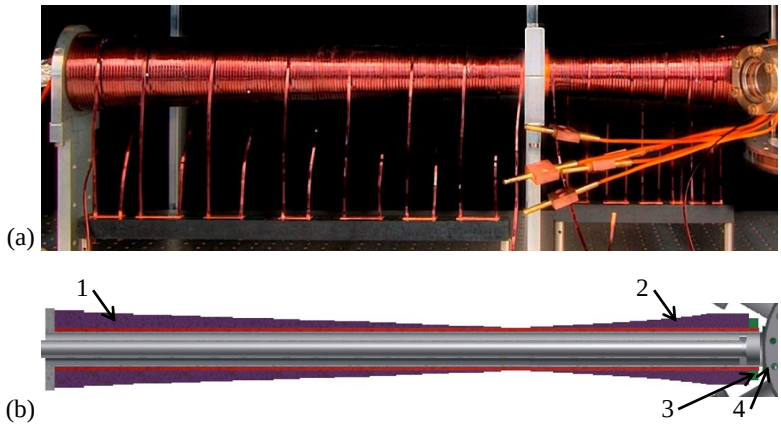

Figure 5.4: (a) The completed Zeeman slower; the connectors on the right allow water to flow through the coils, although in this photograph they have not been bent into their final positions yet. (b) A cut-away of the Zeeman slower; the red coil is the solenoid, the purple coils (1 and 2) produce the majority of the field profile and the green coils (3 and 4) give a sharp drop in field.

as possible by including a zero-crossing half way down the slower. The whole profile can then be shifted up or down with the solenoid to change the laser detuning required.

The purpose of the final two coils (3 and 4) was to create the large field with a sharp drop off at the end of the slower. As mentioned before, this method gives the flexibility to change the release velocity of the atoms, however, it does create some problems. Because the magnitudes of the magnetic fields associated with each coil are large, residual fields will radiate out from the coils and potentially affect the magnetic field magnitude and gradient at the MOT position. Trying to minimise this using the currents in the coils will change the release velocity at the same time. Therefore, a method needs to be implemented to have separate control of the magnetic field at the MOT position. This can be achieved with a combination of shim coils and a compensation coil mounted on the science chamber flange opposite the Zeeman slower. The shim coil pairs can increase or decrease the bias field at the MOT, whereas the compensation coil could reduce some of the gradient.

The designed coil windings are summarised in figure 5.5 including the number of turns per layer for each coil. The tapered profile of coils 1 and 2 generate the shape of the magnetic field but the addition of the solenoid means that fewer layers are needed overall.

The contributions of each of the five coils can be seen in figures 5.6 and 5.7 for Yb and Cs respectively. In the idealised theory, the magnetic field would have two discontinuities at the start and end of the slower and would be zero for $z > L$ and $z < 0$. Obviously this in non-physical and the magnetic field

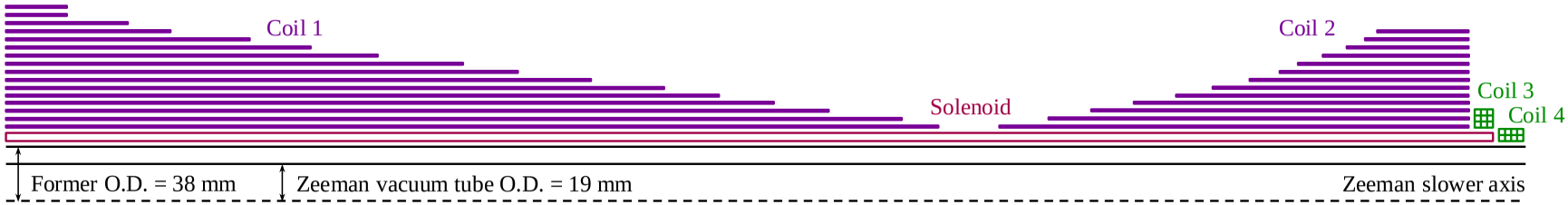

Coil 1

Layer	1	2	3	4	5	6	7	8	9	10	11	12	13	14	15	16
Turns	153	147	135	126	117	108	96	84	75	61	50	40	27	20	10	10

Coil 2

Layer	1	2	3	4	5	6	7	8	9	10	11	12	13
Turns	77	69	62	55	48	42	36	31	28	24	20	17	15

Coil 3

Layer	1	2	3
Turns	3	3	3

Coil 4

Layer	1	2
Turns	4	4

Solenoid

Layer	1
Turns	183

Coils 1 and 2 wound with 3 × 1 mm wire
Coils 3 and 4 wound with 3.4 × 3.4 mm wire
Solenoid wound with 4.3 × 4.3 mm wire

Figure 5.5: The discrete coil windings and positions of each layer for the Zeeman slower are shown with coils 1 and 2 in purple, the solenoid in red and coils 3 and 4 in green. The number of layers and turns per layer are summarised in the tables for each coil.

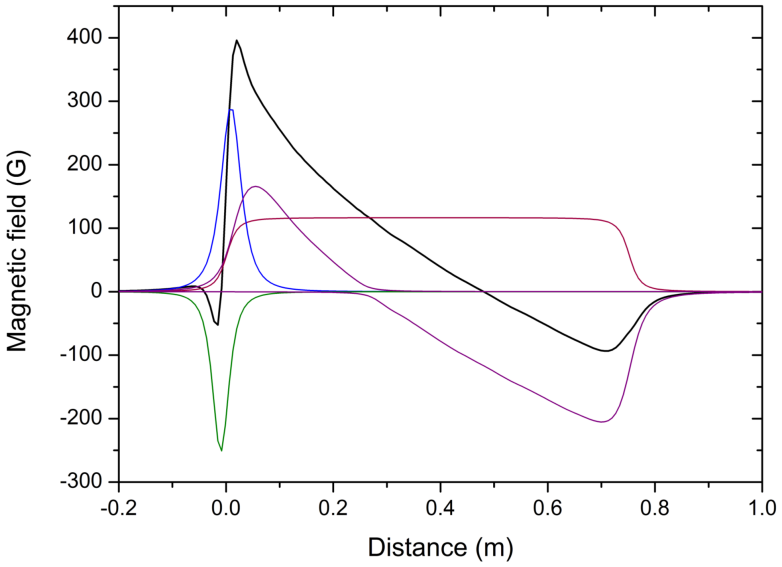

Figure 5.6: The individual contributions from each coil to the total magnetic field profile (black) for Yb. The solenoid is shown in red, coils 1 and 2 in purple, coil 3 in blue and coil 4 in green. The location of the MOT is -0.075 m on this scale.

profile instead has a gentle rise and fall and has some small corrugations along its length due to the discrete coil windings.

Any small imperfections in the magnetic field profile can largely be compensated for by the power in the Zeeman slower beam and the atoms are tolerant of some variations from the ideal field due to the choice of η. If η was closer to 1 then atoms would start to be lost from the slower if the magnetic field varied from the ideal case.

The gradual rise and fall at the ends of the Zeeman slower magnetic field profile mean that atoms can be on resonance with the laser beam for longer and so experience additional slowing. As discussed earlier, this can be compensated for by the choice of an increasing field at the end of the Zeeman slower as the atoms are only on resonance with the laser at high fields and so once the field has dropped by a certain amount, the atoms will no longer be slowed.

5.4 Construction of the Zeeman slower

The Zeeman slower was designed to work for both Yb and Cs but with different magnetic field profiles for each for sequential loading.

The solenoid effectively allows the field profile to be matched to the detuning of the light. It was wound with 4.3 $\times$ 4.3 mm hollow square copper wire

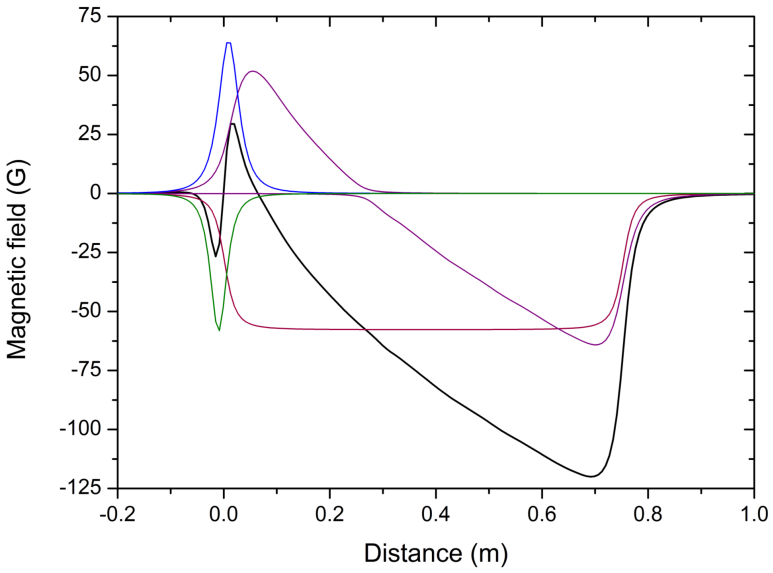

Figure 5.7: The individual contributions from each coil to the total magnetic field profile (black) for Cs. The solenoid is shown in red, coils 1 and 2 in purple, coil 3 in blue and coil 4 in green. The location of the MOT is -0.075 m on this scale.

wrapped in kapton tape. A central bore of 2.75 mm diameter allows cooling water to run through the coil, which avoids overheating when large currents are applied.

Most of the magnetic field profile is created by the coils wound directly on top of the solenoid. As the Zeeman slower has been designed such that the bulk of the magnetic field magnitude is provided by the solenoid, very little current need be supplied to the profile coils and so there is no need for direct water cooling. Therefore, these coils were wound with 3×1 mm rectangular wire (from Hi-Wire) with no central bore.

Coils 3 and 4 are run at high currents so also require water cooling in the same way as the solenoid. They were wound with 3.4×3.4 mm copper wire with a central bore of diameter 2 mm for water cooling.

Once wound, to test the coils were working as expected and had no shorts, the field profile was measured with the design currents running through them before the vacuum system was completed, the results of which can be seen in figure 5.8. The residuals from the ideal field are also shown and it can be seen that the field profile is consistently slightly lower than ideal for Yb (purple in the graph) but this can be corrected for by applying a higher solenoid current.

Figure 5.8 also shows the measured design parameter,

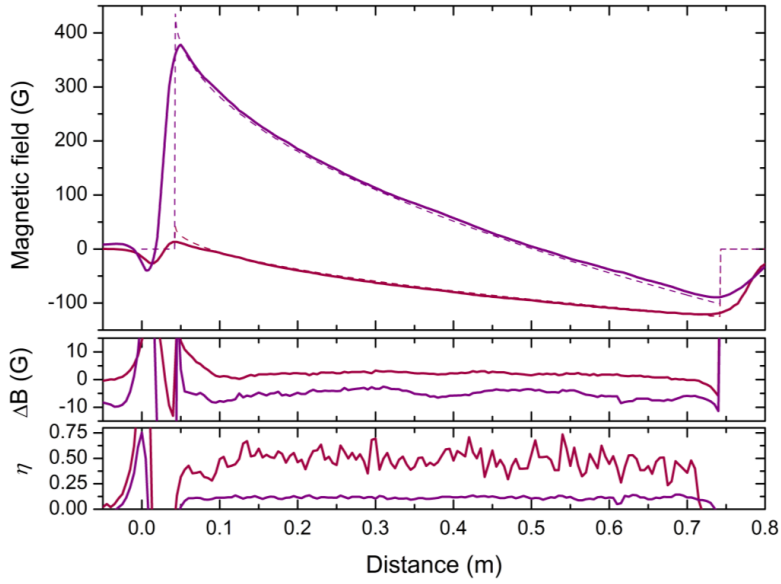

Figure 5.8: The measured magnetic field profiles for Yb (purple) and Cs (red). Residuals from the ideal field profile are also shown. 0 m is the end of the former tube which means that the MOT location is at -0.075 m. The measured efficiency parameter η is also shown in the bottom plot. This matches the design values of 0.128 and 0.5 well for Yb and Cs respectively.

$$\eta = \frac{2m\mu}{\hbar^2 k^3 \Gamma} \frac{\mathrm{d}B}{\mathrm{d}z} \left(\frac{\mu B}{\hbar} - \delta \right), \tag{5.8}$$

with $\delta = \mu B_0/\hbar$ and where $\mathrm{d}B/\mathrm{d}z$ has been numerically estimated from the measurements. This is a locally defined η which assumes constant laser intensity and that all of the atoms are on the axis of the Zeeman slower. Clearly this is not true, however, it does give a valuable insight into whether the fluctuations in the magnetic field are too high. Therefore, these measurements should match the design parameters for Cs and Yb of 0.5 and 0.128 respectively and this is shown to be true for most of the length of the slower; η only deviates from these values at the very end of the Zeeman slower when the atoms have already dropped out of resonance with the laser beam.

Both the design and actual currents used for slowing Cs and Yb are given in table 5.2; the actual currents differ slightly from the design currents but have been optimised to give the highest MOT load for each species. The process used to find the optimum currents is detailed in Section 6.1 and the relevant results can be found in Chapters 6 and 7.

Before the Zeeman slower coils were installed over the Zeeman slower vacuum tube, the tube itself had a heater tape wrapped around it for use when the vacuum system was baked. This obviously remains in place in case vacuum ever needs to be broken and the tube baked again.

Coil	Cs currents (A)		Yb currents (A)	
	Design	Optimised	Design	Optimised
Solenoid	-18.85	-19.65	38.1	36.0
1	-1.25	-1.235	-4	-3.98
2	1.25	1.235	4	3.98
3	33.6	27.98	149	147.0
4	-26.9	-23.02	-116.5	-106.0

Table 5.2: The design and optimised Zeeman slower currents for Cs and Yb.

Parameter	Theory	Reality
v_0	One value	Maxwell-Boltzmann
v_f	Zero	MOT capture velocity
$B(z)$	Smooth profile	Discrete coil windings
	Discontinuity at ends	Smooth drop off
a	Continuous	Discrete kicks
Laser beam profile	Plane wave	Gaussian
MOT-ZS interaction	B-fields separate	B-fields merge
	Laser light separate	Beam affects MOT

Table 5.3: The differences between some parameters used in the idealised Zeeman slower design and in reality.

5.5 Numerical simulations

The real world differs from idealised theory in many subtle ways and each has to be taken into account when finalising the design of a Zeeman slower. Table 5.3 summarises the ways in which the idealised model differs in the real world as described above.

Therefore, before the Zeeman slower was wound numerical simulations were carried out to test whether the coils designed with the chosen parameters in table 5.1 would slow the Yb and Cs atoms to the required MOT capture velocities, taking into account the real world differences mentioned in table 5.3. These simulations were done by taking a sample of atoms with a given initial velocity distribution and stepping their positions forward in small time steps. The following differential equation gives the average velocity change of an atom taking into account some real-world effects:

$$\frac{\mathrm{d}\mathbf{v}(\mathbf{r})}{\mathrm{d}t} = \frac{a_{\max}\mathbf{k}(\mathbf{r})\frac{I(\mathbf{r})}{I_\mathrm{s}}}{1+\frac{I(\mathbf{r})}{I_\mathrm{s}}+\frac{4}{\Gamma^2}\left(\delta-\mathbf{k}(\mathbf{r}).\mathbf{v}(\mathbf{r})-\frac{m_\mathrm{J}g_\mathrm{J}\mu_\mathrm{B}B(z)}{\hbar}\right)^2}, \tag{5.9}$$

where $\mathbf{k}$ is the local wavevector for the Zeeman slower beam, which takes into account any focussing of the beam.

In the simulation, for each time step the number of absorption and spontaneous emission events is given by two Poisson distributions, which takes care of the random nature of the atom-photon interactions. The spontaneous emission events may not give a momentum kick in the same direction as the Zeeman slower beam and this is also accounted for in the simulations.

Once these factors have been taken into account, the simulation outputs a series of atom trajectories which can aid the design process by allowing various parameters to be adjusted. For example, typical trajectories for 10 Cs and 10 Yb atoms using the ideal design field (e.g., that seen in figure 5.7 for Cs and 5.6 for Yb) can be seen in figures 5.9 and 5.10. In this particular series of simulations the Zeeman slower beam power was varied between each run.

Figure 5.9(a) demonstrates the importance already mentioned of having the correct laser beam intensity at the end of the Zeeman slower where the atoms are released. In this figure for 10 Cs atoms the power in the beam was too low and so atoms are de-coupled from the Zeeman slower before the desired release point and so, as can be seen in figure 5.9(b), they have release velocities towards the higher end of the MOT capture velocity for Cs ($48\,\mathrm{m\,s^{-1}}$). This occurs because there are too few atom-photon absorption events to keep the atoms following the ideal slowing curve. If the intensity (or in other words, the power) is increased as in figure 5.9(c) then the atoms are slowed to approximately the design release velocity of $10\,\mathrm{m\,s^{-1}}$ or less. Figure 5.9(e) then shows how atoms can be turned back down the Zeeman slower if the intensity is too high.

Figure 5.10 show similar plots for Yb. Given the lower capture velocity for the 556 nm MOT the importance of simulating the Zeeman slower becomes apparent as being able to tailor the Zeeman slower magnetic field and beam properties to produce a beam of atoms with this release velocity before building the Zeeman slower is crucial. Again, going through figures 5.10(a), (c) and (e), the power in the Zeeman beam is increased to change the release velocity of the atoms.

Figure 5.10(e) is another good example of when the power in the Zeeman slower beam is not optimal. In this case the intensity at this critical point of the Zeeman slower is too high so the atoms absorb too many photons and so start to be accelerated in the opposite direction to their initial motion.

Figure 5.10(c) shows the optimum simulated power for the Yb Zeeman slower of 44 mW. This gives the highest number of atoms in the desired release velocity range of less than $5\,\mathrm{m\,s^{-1}}$ and all below $10\,\mathrm{m\,s^{-1}}$. However, some atoms are lost as they are turned back down the slower but these are acceptable losses for the advantage of having low positive release velocities for the majority of atoms.

The magnetic field profiles used in the simulations for both figures 5.9 and 5.10 are based on the contributions from the individual coils therefore they

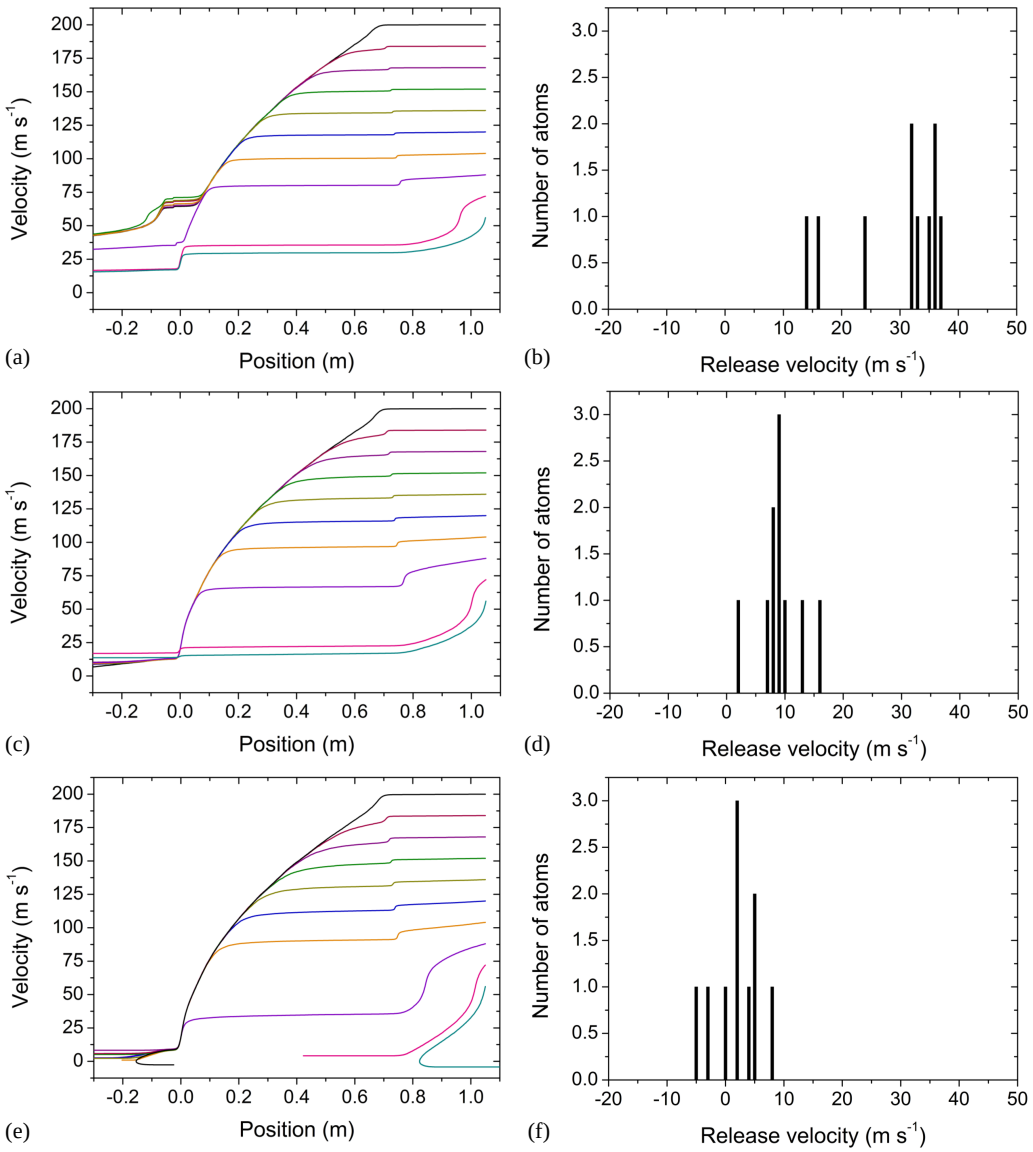

Figure 5.9: Examples of the output from the Zeeman slower simulator for Cs atoms. For each graph (a), (c) and (e) the trajectories of 10 atoms with various initial velocities are stepped through the Zeeman slower in discrete steps with a certain probability of absorbing a photon and being slowed each time. The three different examples are for Zeeman slower beam powers of (a) 4 mW, (b) 9.5 mW and (c) 18 mW. Graphs (b), (d) and (f) show the corresponding grouping of release velocities at the end of the Zeeman slower for each case. Atoms aren't slowed enough in (b) and are released from the Zeeman slower at a velocity greater than the capture velocity of the MOT. As the Zeeman slower beam power increases more atoms are pushed back along the tube, shown by some lines in (e) curving round and the negative release velocities in (f). (c) and (d) show the ideal case.

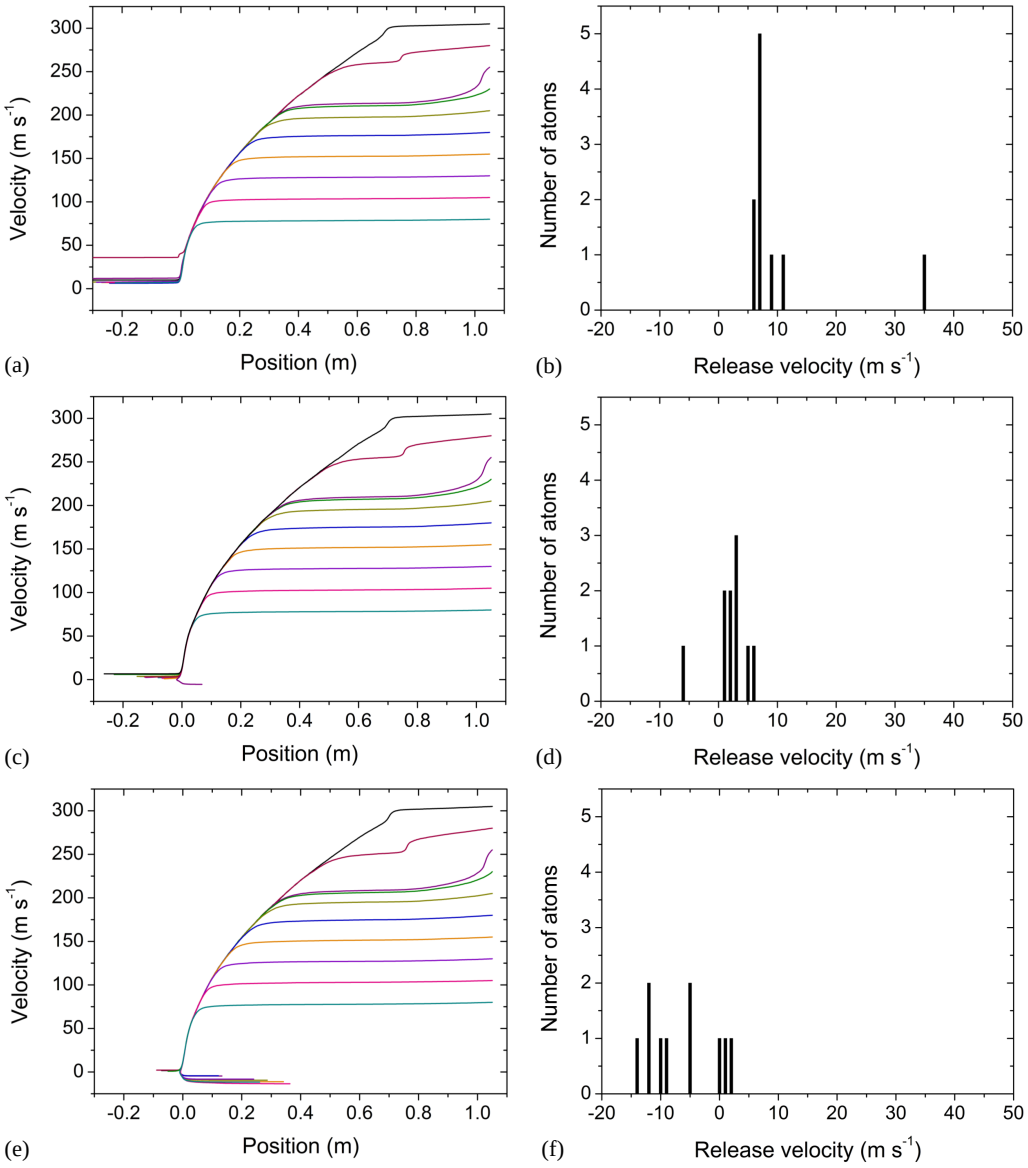

Figure 5.10: Examples of the output from the Zeeman slower simulator for Yb atoms. Again, the trajectories of 10 atoms with various initial velocities are stepped through the slowing process. Different Zeeman slower beam powers are shown; 35 mW for (a) and (b), 44 mW for (c) and (d) and 55 mW for (e) and (f). 35 mW is too low and does not slow the atoms sufficiently, whilst 55 mW turns most of the atoms around again and pushes them back down the Zeeman slower tube. 44 mW slows most atoms to below $5\,\mathrm{m\,s^{-1}}$, which is slow enough for the 556 nm MOT to capture them.

don't have the discontinuity of dropping to zero field at the start and end of the slower but are rounded instead. This throws up an interesting result that can be seen in the figures; some atoms are brought onto resonance with the Zeeman slower beam before the ideal start of the Zeeman slower at -0.1 m as the magnetic field magnitude starts to increase. This can particularly be seen in figures 5.9(a), (c) and (e) in the small kinks in the trajectories just before 0 m and in the red line of figures 5.10(a), (c) and (e).

Some more dramatic slowing occurs at earlier times (pink and cyan lines in figures 5.9(a), (c) and (e) and purple and green lines in figures 5.10(a), (c) and (e)). This is not due to the magnetic field profile at these points but is because the Doppler shift of these atoms is close to the detuning of the Zeeman slowing beam without the presence of a magnetic field. The Cs (Yb) detuning in the simulation is 58.7 MHz (609.2 MHz) which would match a velocity of $50\,\mathrm{m\,s^{-1}}$ ($243\,\mathrm{m\,s^{-1}}$). In reality the atoms will have a Maxwell-Boltzmann distribution coming out of the oven rather than the artificial spacing of the atoms in this simulation. Therefore, this extra slowing will have more of an effect on Yb as very few of the Cs atoms effusing from the oven will have a velocity as low as $50\,\mathrm{m\,s^{-1}}$ but the most likely velocity for Yb, v_g, is $254\,\mathrm{m\,s^{-1}}$.

Most simulations were carried out with more atoms with initial velocities given by the Maxwell-Boltzmann distribution for more accurate results. The evenly-spaced velocity distribution used here was chosen for clarity in explaining the figures.

Chapter 6

Results: Cs MOT

This chapter details the initial characterisation and experiments performed in the new vacuum chamber focussing on the realisation of a Cs MOT.

The Cs MOT was initially optimised using the Alvatec dispensers described in Section 3.2.2, however, these were then replaced with dispensers from SAES Getters. During this process the temperature gradients across the oven were re-assessed and we found that the coldest part of the oven had been running at roughly 20 °C colder than originally thought. This accounts for the fairly low atom numbers of high 10^6 to low 10^7 in some graphs.

After the dispensers had been changed, some parameters that had been previously optimised with the lower atom numbers were re-checked to make sure the optimum had not changed with an order of magnitude more atoms in the MOT. Therefore, some results presented in this chapter are from the first set of dispensers and some from the second, however, it will be made clear in the text which dispenser set was used.

Full control of atom number in the MOT can be achieved by varying the current across the dispensers (for either set) and atom numbers up to 4×10^9 have been observed, although the MOT is unstable at this value.

6.1 MOT in the new vacuum system

With the atomic beams characterised and the laser system tested, a Cs MOT was easily achieved in the new vacuum chamber. A process of optimisation was then carried out in order to get the largest number of trapped atoms.

6.1.1 Zeeman slower optimisation

It was immediately noticed that Cs atoms could be trapped with radically different Zeeman slower currents than those the slower was designed for,

and so finding the optimum Zeeman slower profile was expected to be fairly flexible and indeed this was what was seen - Cs atoms from the oven can be trapped in a MOT with only a small amount of slowing. This is not surprising as a Cs MOT can be loaded from background vapour, if inefficiently.

Polarisation of the Zeeman slower beam

The first parameter to be optimised was the angle of the quarter waveplate before the Zeeman slower. Changing this angle changes the handedness and ellipticity of the Zeeman slower beam and the maximum MOT load was expected to occur when the most atoms were slowed, corresponding to when the Zeeman slower beam is left hand circularly polarised. However, when initial measurements were taken the MOT was very unstable and an appreciable number of atoms could be trapped using what appeared to be linearly polarised light, figure 6.1(a). This suggested that the polarisation in the Zeeman slower fibre was not stable and was becoming elliptical at times. Therefore, before further optimisation took place it was necessary to stabilise the polarisation in the fibre. This was done using the method in [135] and as described in Section 4.3.4.

After this was complete, the quarter waveplate was again rotated and the atom number recorded as can be seen in figure 6.1(b). This time the results were more stable, with the largest MOT number occurring when the light was circularly polarised. The number of atoms in the MOT was calculated with equation (4.21). The waveplate was subsequently set to an angle of 235°.

These measurements were taken with the first set of dispensers and not repeated as the handedness of light required to slow the atoms would not change with atom flux.

Zeeman slower magnetic field profile

Figure 6.2 shows the process used to optimise the Zeeman slower profile. Each change made to a coil current impacts on all of the other coils and the overall shape of the Zeeman slower profile. It was decided that coil 3 (see the inset in figure 6.2 for coil designations) would be the 'control' coil and the other coils would be scanned for each change in this coil. Coil 3 was chosen as it mainly determines the maximum magnetic field amplitude the Zeeman slower reaches and so the release velocity of the Cs atoms. For each change in coil 3 current, the magnetic field profile was plotted in a LabVIEW program from the measurements taken in Section 5.4 to make sure that the field profile was still close to the ideal field. In reality, as expected, the currents to the solenoid and coils 1 and 2 did not change much for each iteration.

The results of the optimisation process for Cs (carried out with the first set

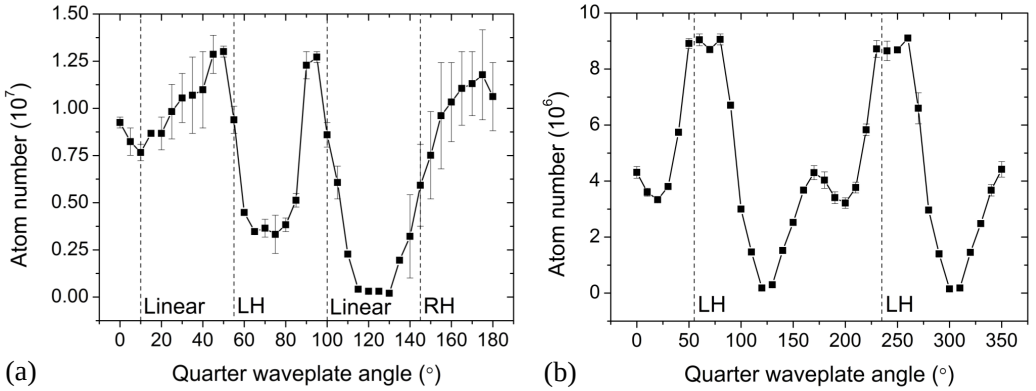

Figure 6.1: The steady state MOT atom number with quarter waveplate angle when the polarisation in the Zeeman slower fibre was (a) not stable and (b) stable. The handedness of the light (left hand circular, right hand circular and linear) is marked on with the dashed lines.

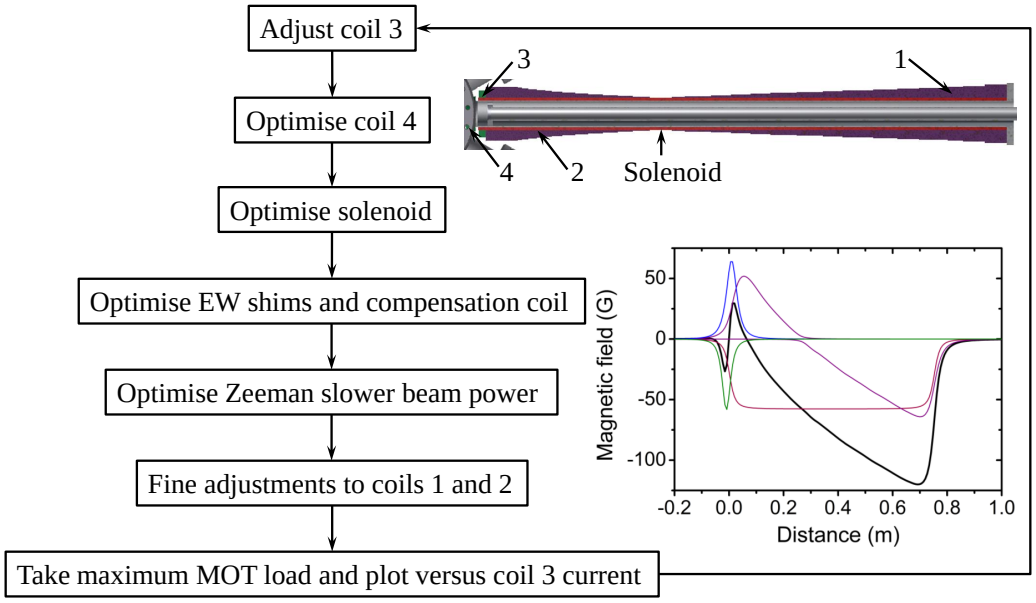

Figure 6.2: The iterative process used to optimise the Zeeman slower. Each change to a coil current has the ability to affect the optimal value for each of the others, so for each change in coil 3 the other coils had to be re-optimsed. The insets show the coil designations and the how the individual magnetic fields add to make the Zeeman slower magnetic field for Cs.

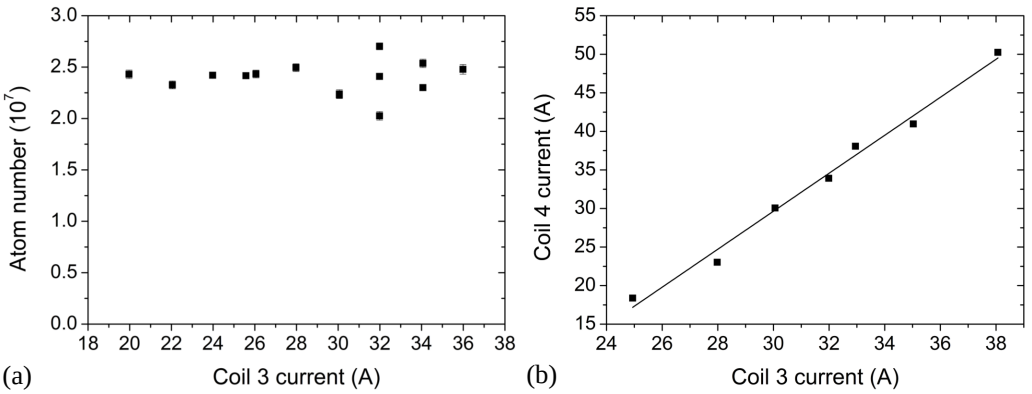

Figure 6.3: (a) There is no defined peak in atom number in the MOT as the current to coil 3 is varied. (b) The current in coil 4 increases as the current in coil 3 increases to keep the release velocity of the Zeeman slower at the optimum value.

of dispensers) can be seen in figure 6.3. As expected, there is no real peak in the data - the Zeeman slower works well over a range of coil currents. After changing to the second set of dispensers we wanted to check that the Zeeman slower currents were still at the optimum and the results can be seen in figure 6.4. Here we simply scanned the currents going to each coil in turn and recorded the current at which the MOT number was the largest. The final currents settled on are recorded in table 5.2, however all but the solenoid had not changed. It is thought that the solenoid needed to be slightly changed as the AOM frequency for the Zeeman slowing beam had slowly drifted over time so the solenoid was no longer exactly matched to the detuning of the light.

Changing the solenoid current, as in figure 6.4(d), is equivalent to changing the detuning of the Zeeman slower beam, but is experimentally easier to do as it does not require changing multiple AOM frequencies. Both the MOT and Zeeman slower beams are derived from the tapered amplifier and their frequencies changed by varying the frequency to the double-passed AOM 1 (going to the BoosTA) rather than either of the single-passed AOMs (AOMs 4 and 6) as this risks misaligning the fibres and so changing beam powers as well as detuning. Independent tuning of the Zeeman slower detuning is then best achieved by varying the solenoid current to match a set light frequency.

Zeeman slower beam powers

The Zeeman slower cooling and repump powers were optimised with both sets of dispensers, however, the same power was found to be needed for both, regardless of the increased atomic flux. Figure 6.5 shows the atom number in the MOT as the Zeeman slower powers are changed (using the data obtained

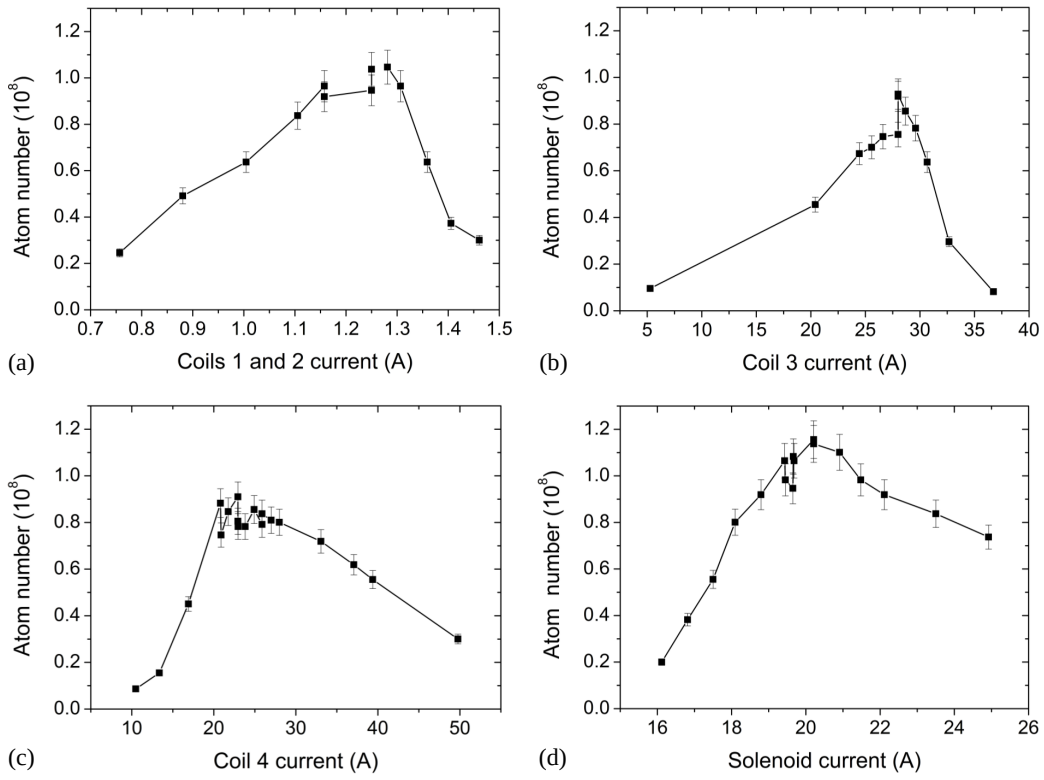

Figure 6.4: The current to (a) coils 1 and 2, (b) coil 3, (c) coil 4 and (d) the solenoid were varied to see the effect on the atom number in the MOT. This was done to check that the optimum had not changed for higher Cs flux from the oven with new dispensers in place. The lines joining the data points are just to guide the eye.

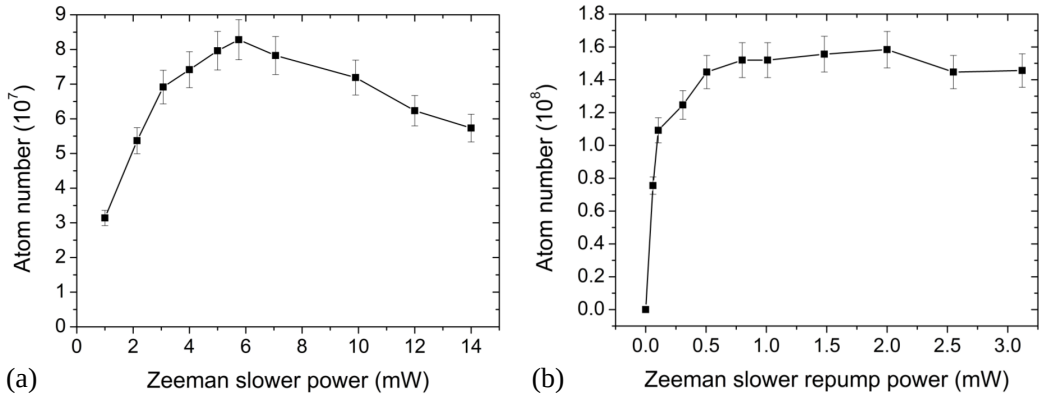

Figure 6.5: The optimised power for (a) Zeeman slower beam and (b) its associated repump. The lines between the data points are to guide the eye. These plots were taken with the new set of dispensers in place.

with the second set of dispensers as an example). A clear optimum of (6.0 ± 0.5) mW is seen in figure 6.5(a) for the cooling light (detuned from the $F = 4 \rightarrow F' = 5$ transition). This Zeeman slower beam power matches the design power found through the Zeeman slower simulations well. The optimum power of the three cases presented in Section 5.5 was 9.5 mW, however, the range over which the Zeeman slower was expected to work best by slowing the majority of atoms to under $10\,\mathrm{m\,s^{-1}}$ but without turning them back down the Zeeman slower was $4 < P_{\mathrm{ZS}} < 10$ mW. The experimentally found optimum of (6.0 ± 0.5) mW fit into this range well.

For the repump light (detuned from the $F = 3 \rightarrow F' = 4$ transition) the atom number plateaus in figure 6.5(b) for increased repump power. The repump power was set to (3.12 ± 0.01) mW.

It was observed during the optimisation process that the MOT could not be loaded without some repump light in the Zeeman slower beam, as evidenced by the sharp increase from zero atoms in figure 6.5(b). This is not surprising as there are multiple loss routes due to imperfect polarisation along the length of the Zeeman slower (as explained in Section 5.3.3). If no repump light were present, atoms would eventually all be lost into the dark $F = 3$ state.

It was also observed that if the MOT repump was blocked, but the Zeeman slower repump left on, a small MOT would still form even though the detuning for the Zeeman slower repump light is -50 MHz detuned from $F = 3 \rightarrow F' = 4$ rather than of the order of -5 MHz for the MOT repump.

6.1.2 MOT optimisation

After the Zeeman slower parameters were fixed, the MOT itself could be optimised. This included simple checks such as ensuring the quarter wave-

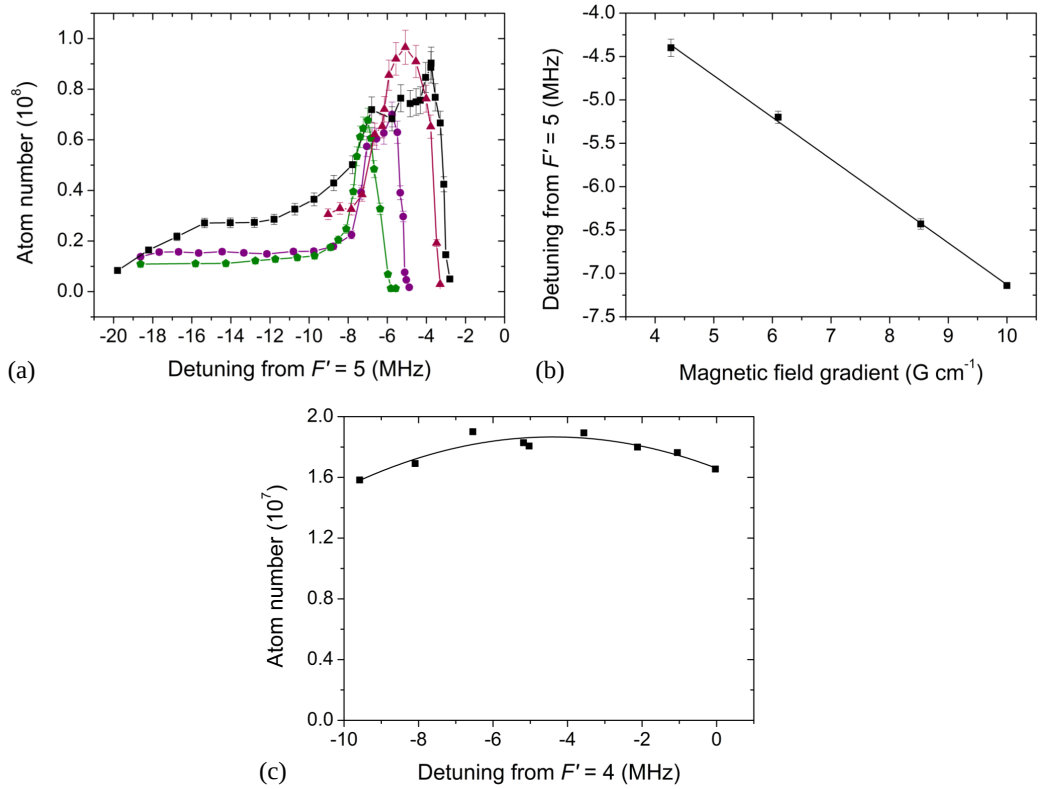

Figure 6.6: (a) The detuning of the MOT beams were varied for different magnetic field gradients of $4.27\,\mathrm{G\,cm^{-1}}$ (black), $6.10\,\mathrm{G\,cm^{-1}}$ (red), $8.53\,\mathrm{G\,cm^{-1}}$ (purple) and $10.0\,\mathrm{G\,cm^{-1}}$ (green). The dispensers currents were not exactly the same for each data run and so no conclusion can be drawn from the peak atom number for each gradient. (b) However, the optimum detuning becomes more red detuned as the magnetic field gradient increases. (c) The detuning of the repump beam does not have as defined a peak.

plates in the MOT beams were at the correct angle, as well as more involved measurements such as optimising beam powers and detuning.

Detuning and magnetic field gradient

The detuning of the MOT was varied for different magnetic field gradients using the new dispensers. Plots of the atom number versus detuning from the $F = 4 \rightarrow F' = 5$ transition can be seen in figure 6.6(a). There is a fairly sharp peak in the detuning, however, towards the red side there is a long tail where a smaller MOT is still loaded. As can be seen in figure 6.6(b), the detuning becomes more red detuned as the magnetic field gradient increases.

The results presented in figure 6.6(a) are a proof of principle that the Cs MOT is capable of being operated at a low magnetic field gradient, which may be necessary as a compromise when loading the dual species MOT with

Yb. The data runs in the figure were taken with slightly different dispenser currents, which accounts for the varying peak atom number, therefore no conclusion can be reached about the global optimum magnetic field gradient for loading Cs. However, the MOT at lower magnetic field gradients weren't as stable, with some flickering and motion of the cloud seen, therefore higher magnetic field gradients with larger detunings are where the Cs MOT will be operated in single species experiments.

All of the other optimisation processes detailed in this chapter were done with a MOT magnetic field gradient of $8.53\,\mathrm{G\,cm^{-1}}$ and from figure 6.6(a) it can be concluded that the optimum detuning for this gradient is -(5.6 ± 0.1) MHz from $F' = 5$. The detunings and their associated errors were found by fitting the peaks seen in figure 6.6(a) with Gaussian fits.

Figure 6.6(c) shows that the repump detuning does not have as defined a peak. The data shown in the plot is for a magnetic field gradient of $8.53\,\mathrm{G\,cm^{-1}}$. The repump detuning has been set to -(5.0 ± 0.5) MHz from $F' = 4$. The data for this plot was done with the original set of dispensers.

Full characterisation with regard to the magnetic field gradient was not done at this time as when the system is run as a dual species MOT a compromise situation will have to be found. This is because the two species require slightly different magnetic field gradients for the MOT; approximately 8-10 $\mathrm{G\,cm^{-1}}$ for Cs and 2-13 $\mathrm{G\,cm^{-1}}$ for Yb [120, 149, 152]. However, figure 6.6(a) does show that the Cs MOT is capable of being run at lower gradients that are more suitable for Yb.

Beam powers

The final set of parameters that were varied were the beam powers for both the cooling and repump light in the MOT beams. According to the process outlined in figure 6.2 the Zeeman slower cooling power was optimised at the same time as the Zeeman slower profile as they each have an effect on the other, with the final power curve plotted in figure 6.5(a).

Figure 6.7(a) shows the atom number as a function of the power in one MOT beam (therefore the total power the atoms see is 6 times this value). Past a certain value the number of atoms trapped reaches a rough plateau with no very significant increase in number. However, in general it is best to have as much power available in the MOT beams as possible so they were set to (29.9 ± 0.1) mW per beam.

Similarly the amount of MOT repump light was varied (figure 6.7(d)) and set to (13.5 ± 0.1) mW. This was a compromise to allow more repumping light in the Zeeman slowing beam. These plots were taken with the first set of dispensers; it was expected that the same behaviour would be seen with the higher atomic flux, therefore, the MOT beams are still set to (29.9 ± 0.1) mW per beam.

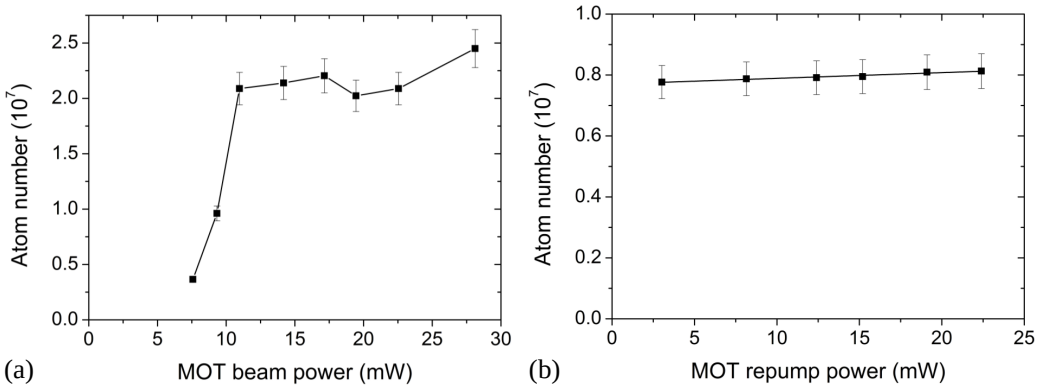

Figure 6.7: The optimised power (a) per MOT beam and (b) in total for the MOT repump.

6.2 Testing the Cs dispensers

During the first tests of the MOT with the original set of dispensers it was noticed that the MOT number, whilst steady over the course of a day, did decline over a period of several days. This was not surprising as the dispensers had only been run at 4 A for 6 hours at the start of the experiments on the MOT before the Cs oven was left to deplete over a week. This was done in order to get a feel for what combination of oven temperature and dispenser current would give a stable MOT number. The second set of dispensers contain less Cs and are not expected to last for a considerable length of time, however, similar control over the atom number is obtained.

To aid these investigations into control over the atom number the current to dispenser 1 was gradually increased and the MOT number monitored. The results for this study can be seen in figure 6.8 where the main figure is the MOT load over time and the inset shows how the atom number increases with dispenser current. Steps in the atom number can be seen as the dispenser current is turned up to 4 A and again when it goes to 4.5 A. Larger MOT loads could be obtained by using larger dispenser currents, however, this would result in the dispensers depleting faster.

It is interesting to note that the MOT load decreases almost immediately after the dispenser is turned off. This indicates that there is not a very large reservoir of Cs coating the walls of the oven under these conditions. This is not entirely surprising as the oven had been run for a number of weeks without the dispensers activated. Running in this way might be a good way to control the MOT load and not waste too much Cs at the same time as most of the Cs is instantly used in the atomic beam.

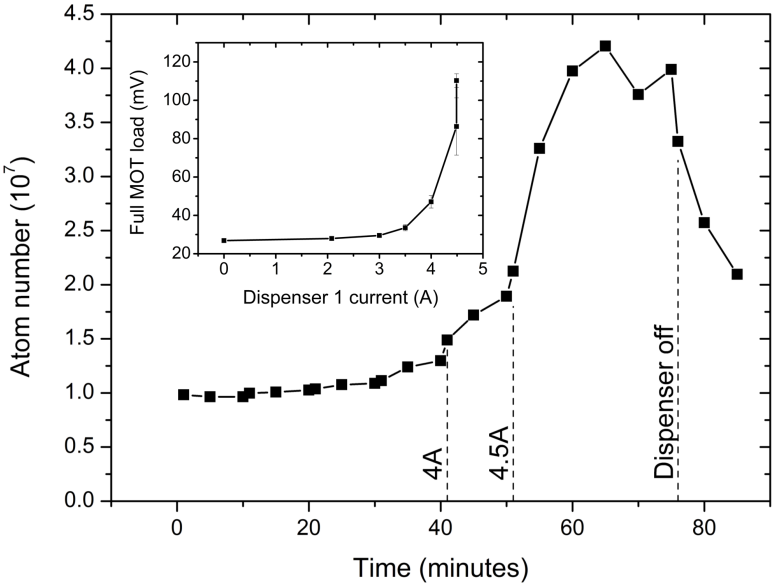

Figure 6.8: The atom number in the MOT increases with dispenser current almost immediately and decreases once the dispenser has been switched off. Inset: the atom number increases as the dispenser current is increased.

6.3 Loading rate

An important factor to measure with regard to the MOT is how fast it can be loaded from the Zeeman slower as this effects the repetition rate of the experiment. Therefore, once the MOT and Zeeman slower had been optimised with the second dispenser set a loading curve was recorded, figure 6.9.

The number of atoms in a continuously loaded MOT, N, is dependent on the capture rate from the Zeeman slower, R, and the loss rate from the MOT. This can be expressed as a differential equation,

$$\frac{\mathrm{d}N}{\mathrm{d}t} = R - \frac{N}{\gamma} - \frac{\beta N^2}{V}, \tag{6.1}$$

where γ is a single body loss coefficient (for example, from atom-light interactions) and β is a two-body loss coefficient from inelastic collisions between atoms in the MOT which depends on the density within the MOT (where V is the volume of trapped atoms). For low density samples, the two body loss can usually be ignored. Therefore, an exponential of the form,

$$N(t) = \frac{R}{\gamma}\left(1 - \exp\left(-\gamma \mathrm{t}\right)\right), \tag{6.2}$$

was fitted to the data. This gave a loading rate of $R = (4.046 \pm 0.009) \times 10^7\,\mathrm{s}^1$ and a loss rate of $\gamma = (0.5544 \pm 0.0013)\,\mathrm{s}^{-1}$.

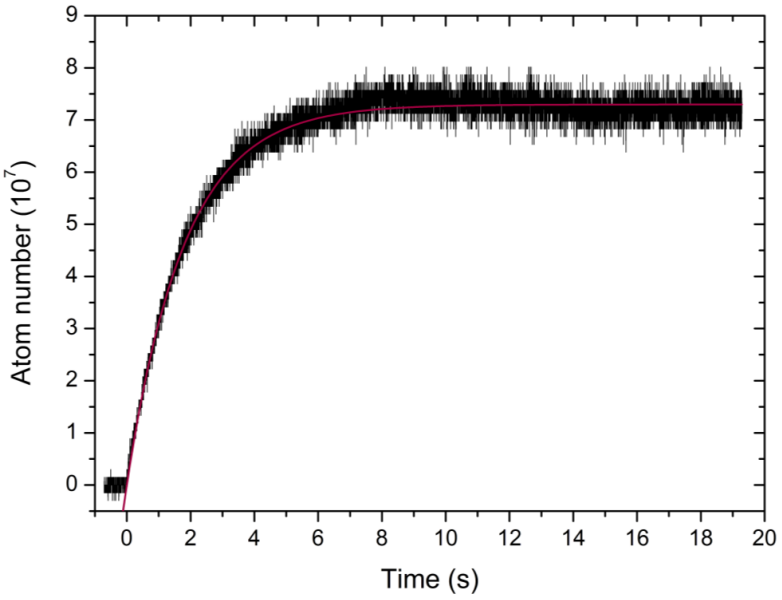

Figure 6.9: A typical MOT loading curve for Cs; the exponential fit (red line) gives a loading rate of $R = (4.046 \pm 0.009) \times 10^7\,\mathrm{s}^{-1}$.

6.4 Lifetime

If the MOT is no longer in an equilibrium, balancing a loading rate and a loss rate, then the atom number will drop according to a modified version of equation (6.1) where R is set to zero:

$$\frac{\mathrm{d}N}{\mathrm{d}t} = -\frac{N}{\gamma} - \frac{\beta N^2}{V}. \tag{6.3}$$

Now β becomes significant as it is no longer balanced by continuous loading into the MOT, therefore a solution of the form

$$N(t) = \frac{N_0\left(1 - \tanh\left(\frac{\gamma t}{2}\right)\right)}{1 + \tanh\left(\frac{\gamma t}{2}\right)\left[\frac{2N_0\beta}{\gamma} + 1\right]}, \tag{6.4}$$

can be fit to the lifetime curves seen in figure 6.10. Here the volume, V, has been arbitrarily set to 1 as we currently have no way of measuring the density of atoms within the MOT as absorption imaging has yet to be implemented.

Lifetime curves were taken under different conditions; with both the atomic beam and Zeeman slower beam blocked (figure 6.10(a)), just the atomic beam blocked (figure 6.10(b)) or just the Zeeman slower beam blocked (figure 6.10(c)). Each data set has also been plotted on a log scale, which can be seen in the figure insets. The log scale more clearly shows two regions

	γ (s^{-1})	β (s^{-1})
Atoms and beam blocked	0.01700 ± 0.00009	$(2.71 \pm 0.02) \times 10^{-10}$
Atoms blocked	0.01685 ± 0.00012	$(4.81 \pm 0.04) \times 10^{-10}$
Beam blocked	0.02346 ± 0.00011	$(2.59 \pm 0.03) \times 10^{-10}$

Table 6.1: The 'fast' and 'slow' loss rates within the Cs MOT for the three different conditions with combinations of the atomic and Zeeman slower beams blocked.

of decay where either the 'fast' decay due to two-body collisions occur (governed by β) or a 'slow' decay, primarily due to collisions between atoms in the MOT and background atoms within the vacuum chamber (governed by γ). These regions manifest in the data as straight lines with different gradients in the log plot.

Table 6.1 summarises the loss rates found from the fits for the three different cases. It can be seen that blocking the atoms decreases γ, which is expected as there will be fewer collisions from hot atoms bombarding the MOT. The lifetimes ($1/\gamma$) for each of the three cases are (58.9 ± 0.3) s, (59.3 ± 0.4) s and (42.6 ± 0.2) s respectively.

If the Zeeman slower beam is blocked then β decreases as the atom-light interactions will decrease. The best regime to work in is obviously the case where both the atoms and the Zeeman slower beam are blocked. However, depending on the loading sequence for a dual species MOT this may not be possible as the atomic beam will have to remain unblocked to load Yb.

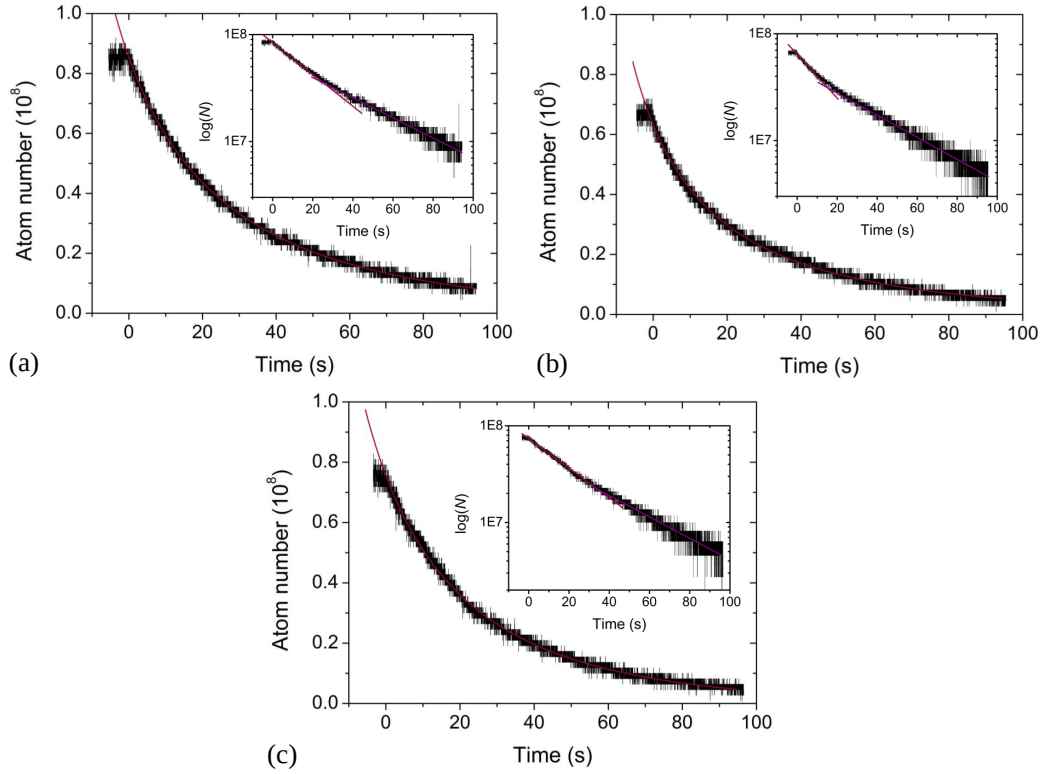

Figure 6.10: The Cs MOT lifetime with (a) both the atomic and Zeeman slower beams blocked, (b) just the atomic beam blocked and (c) just the Zeeman slower beam blocked. Each curve is fitted with equation (6.4) (see text). The insets show the data on a log plot where the two separate gradients of the 'fast' and 'slow' decay can be seen.

Chapter 7

Results: Yb MOT

This chapter details some initial characterisation and optimisation of the Yb MOT and Zeeman slower, starting with the process used to search for an Yb MOT on the narrow 556 nm transition.

7.1 The search for an Yb MOT

When a MOT is not immediately apparent on running a system for the first time there are many factors which can determine whether a MOT can form and each has to be considered carefully when the first attempt for a MOT is made. Some are obvious sanity checks, such as confirming that there are Yb atoms within the system, which is simply done by observing the fluorescence from the Zeeman slower beam (see figure 7.3(a)). Others require checking factors such as the MOT beam powers have sensible values and are well balanced between the six MOT beams, the Zeeman slower and MOT beams should have the right polarisations and detunings, the Zeeman slower should have the correct profile and the magnetic field centre should correspond with the centre of the laser beams. Therefore, if, as was the case, a MOT is not achieved straight away, each of these parameters have to be carefully set up and checked to trace the problem.

7.1.1 Nulling magnetic fields

All of the parameters above are easily checked apart from one; the most difficult parameter to quantify is the location of the magnetic field centre, as there are quite large residual fields and gradients due to the sharp drop off of the Zeeman slower magnetic field. This poses less of a problem for Cs than for Yb as the magnitude of the magnetic field at the end of the Zeeman slower is smaller and the MOT gradients typically used to trap Cs are larger than those used for Yb. As the MOT gradient is lower for Yb, any residual

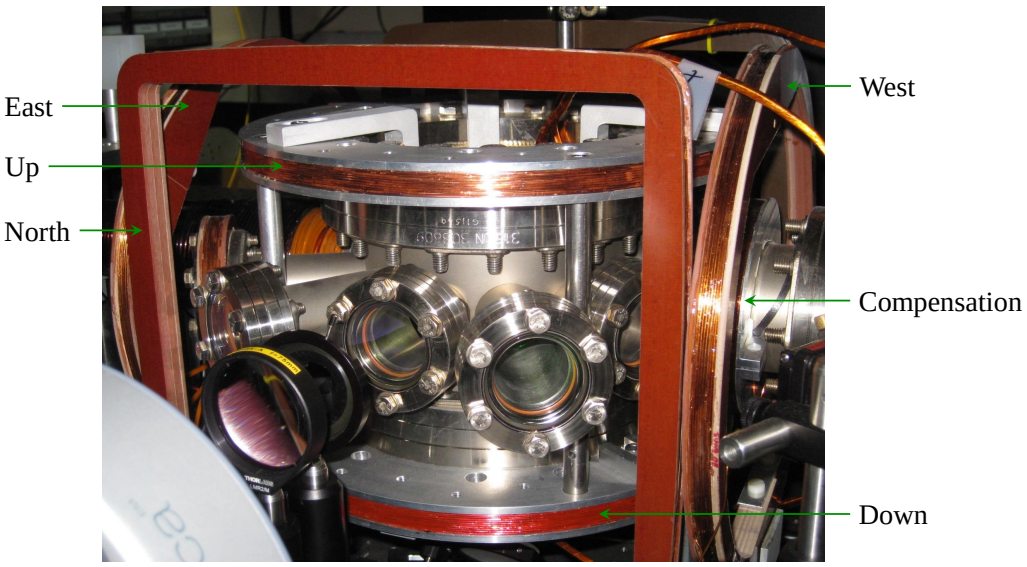

Figure 7.1: The shim coils around the science chamber. The square pair of coils are the North-South shims, with the North being in the foreground of the photograph. The circular coils perpendicular to these are the East-West shims. The Up-Down shim coil pair can be seen wound around the science chamber stand itself.

fields can easily push the magnetic field centre out of the overlap region of the MOT beams, resulting in no MOT formation.

The MOT magnetic field centre can be positioned using three pairs of shim coils wound around the outside of the science chamber. These are labelled North-South, East-West and Up-Down and it is the East-West (EW) shims that lie along the axis of the Zeeman slower. Therefore varying the current going to this pair of coils gives a varying bias field that can move the magnetic field centre further from or closer to the Zeeman slower. The current going to each shim pair is controlled using LabVIEW via an analogue output (as described in Section 4.6). A compensation coil is also wound on the science chamber flange directly opposite to the Zeeman slower which can cancel some of the gradients caused by the slower if necessary.

Initially no Yb atoms were captured in the MOT as there was no way of knowing exactly what magnetic field was at the centre of the science chamber. However, as we had already achieved a Cs MOT we could use its position to give information on the magnetic fields within the chamber when the Zeeman slower was switched to the currents required to slow Yb. This was done by loading a Cs MOT in the usual way with shim coil currents suitable for the Cs Zeeman slower magnetic field before switching the profile to the corresponding one for loading Yb. At first this resulted in the complete loss of the Cs atoms from the trap, indicating that the magnetic field from the slower was indeed not being correctly nulled. However, by looking at

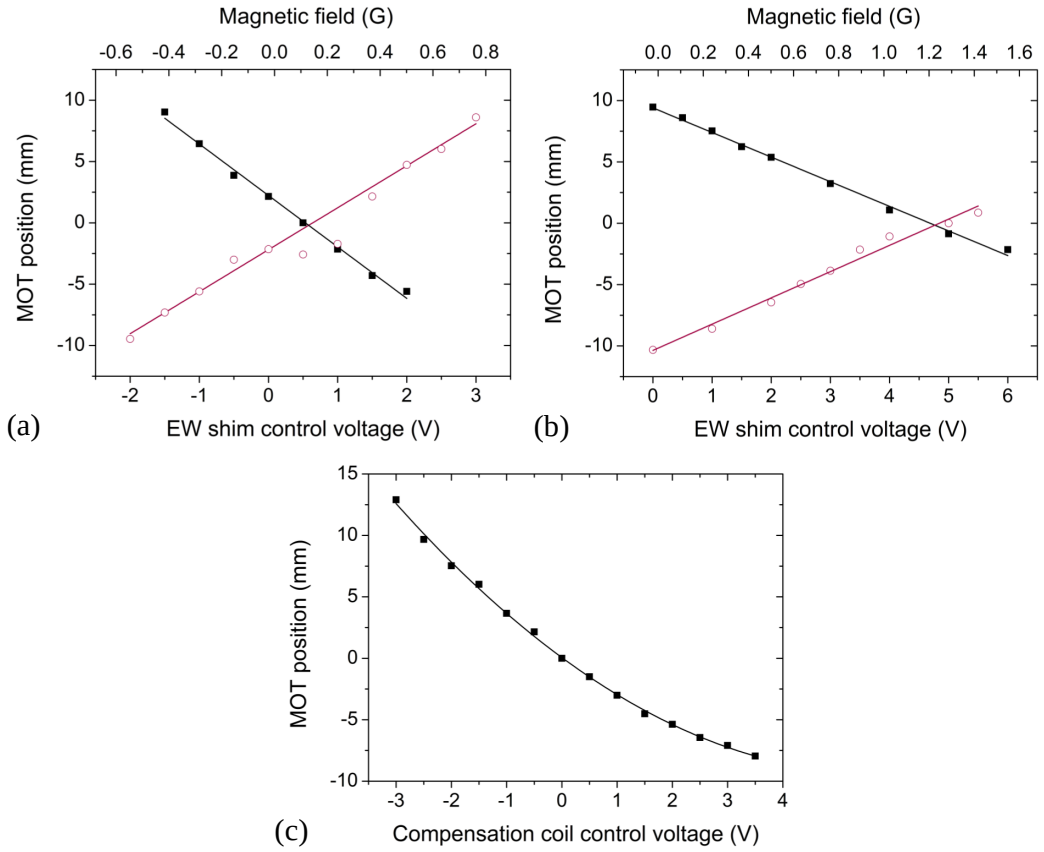

Figure 7.2: Position of the Cs MOT at various EW shim settings with (a) a $5\,\mathrm{G\,cm^{-1}}$ axial field gradient and the Zeeman slower set at the currents used to slow Cs and (b) a $10\,\mathrm{G\,cm^{-1}}$ axial field gradient and the Zeeman slower set at the currents used to slow Yb. The two colours are for different MOT magnetic field polarities. (c) Position of the Cs MOT at an axial field gradient of $5\,\mathrm{G\,cm^{-1}}$ when the compensation coil current was changed.

the direction in which the Cs atoms were being pushed when the magnetic field was switched, the shim coil currents could be gradually changed so that eventually the Cs atoms no longer changed position when switching between the two sets of Zeeman slower currents.

The results from this process can be seen in figure 7.2. In these plots the zero position corresponds to the position of the Cs MOT without the Zeeman slower magnetic field on and with the shim settings optimised to give a good molasses once the MOT magnetic field is turned off. A 'good' molasses is where the atoms are seen to expand fairly isotropically and are seen to linger in the MOT beams for a few seconds.

Figure 7.2(a) shows the position of the Cs MOT with a $5\,\mathrm{G\,cm^{-1}}$ axial field gradient with the Zeeman slower running at the Cs currents when the control voltage to the EW shims was varied. This was done for both polarities of the

MOT coils as it was uncertain at this point which polarity was required for the waveplate angle (and so polarisation handedness) that was set up for Yb (due to the positions of the waveplates it was easier to switch the polarity of the magnetic field than switch the waveplate angle per iteration of trying to trap Yb atoms in a MOT).

The same was done for the Zeeman slower running at the higher Yb currents but with an axial MOT field gradient of $10\,\mathrm{G\,cm^{-1}}$ (figure 7.2(b)). A higher MOT gradient was used to localise the Cs atoms more, so finding the cloud centre was easier.

Figure 7.2(c) shows the effect of the compensation coil on the position of the Cs MOT with an axial MOT gradient of $5\,\mathrm{G\,cm^{-1}}$. The compensation coil is not needed for a Cs MOT which is shown by the Cs MOT being at '0 m' for a compensation coil control voltage of 0 V. In fact, it is seen that the compensation coil is even unnecessary for an Yb MOT.

Using figure 7.2(b) and finding the crossing point of the two fitted lines gives the EW shim control voltage that corresponds to the MOT magnetic field being centred. This crossing also gives information about the residual field from the Zeeman slower at the MOT location; for figure 7.2(a) with the Zeeman slower currents for Cs the residual field is (0.13 ± 0.02) G. Conversely the residual field for the Yb Zeeman slower currents in figure 7.2(b) is (1.23 ± 0.02) G.

With this shim setting in place to cancel the residual field from the Zeeman slower Yb atoms were almost immediately captured in the MOT, see figure 7.3(b). The Zeeman slower currents were then optimised to give the maximum MOT load, however, for each current set the EW shim coils had to be used to bring the MOT back into the centre. The centre was marked as a set pixel position on a CCD camera centred on the MOT.

7.2 Optimising the Zeeman slower

Once the residual magnetic fields due to the Zeeman slower had been nulled in the MOT chamber, the number of atoms could be optimised. Initial optimisation was carried out using ^{174}Yb, although both ^{172}Yb and ^{176}Yb have also been trapped. Both fluorescence detection on a photodiode (Thorlabs, DET110) and fluorescence imaging on a CCD camera (Andor, Luca DL-658M-TIL) were set up. Fluorescence detection allowed the MOT loading rate and lifetimes to be measured directly on an oscilloscope, whereas the larger detection area of the CCD was useful for bringing the MOT back to the centre region when the Zeeman slower magnetic fields were changed. Both methods allow an approximate atom number to be calculated, although the absolute number cannot be known until absorption imaging is set up.

The following data presented in this chapter are given in terms of atom

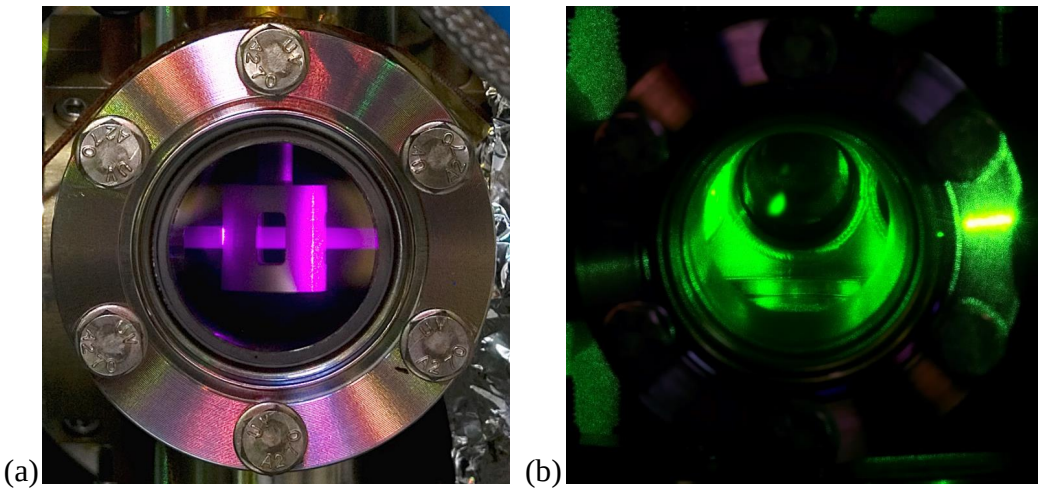

Figure 7.3: (a) Fluorescence from the Zeeman slower beam through the rotary shutter. (b) The Yb MOT on the 556 nm transition, loaded from the Zeeman slower working on the 399 nm transition.

number, however, this should be taken solely as a guide to the order of magnitude of the atoms present rather than the precise number. Accordingly, the CCD count data was converted into an approximate atom number using the following equation [53]:

$$N = \frac{8\pi N_{\mathrm{c}}(1 + 4(\frac{\delta}{\Gamma})^2 + \frac{I}{I_{\mathrm{s}}})}{\Gamma t_{\mathrm{exp}} \eta \Omega}, \tag{7.1}$$

where N_{c} is the integrated number of counts from the MOT on the CCD, t_{exp} is the exposure time (10 ms for all of the data presented here), Ω is the solid angle collected onto the CCD chip and η is the quantum efficiency of the detector (0.49 for the Andor Luca camera being used).

The photodiode voltage was used in a slight modification of equation (4.21) to find the approximate atom number:

$$N = \frac{V_{\mathrm{PD}}}{\mathcal{R}(\lambda) R} \frac{16L^2}{d^2} \frac{\lambda}{hc} \frac{2}{\Gamma} \frac{1 + 4(\frac{\delta}{\Gamma})^2 + \frac{I}{I_{\mathrm{s}}}}{\frac{I}{I_{\mathrm{s}}}}, \tag{7.2}$$

where V_{PD} is the photovoltage, R is the load resistance, $\mathcal{R}(\lambda)$ is the responsivity of the photodiode at the laser wavelength ($0.34\,\mathrm{A\,W^{-1}}$ for 556 nm), L is the atom-lens distance and d is the lens diameter.

For both of these methods one of the approximations used was that the detuning was -8.1 MHz, which cannot be accurately measured until beat measurements are taken, but this factor does not affect the order of magnitude of the atom number calculated as above. The other approximation was that the

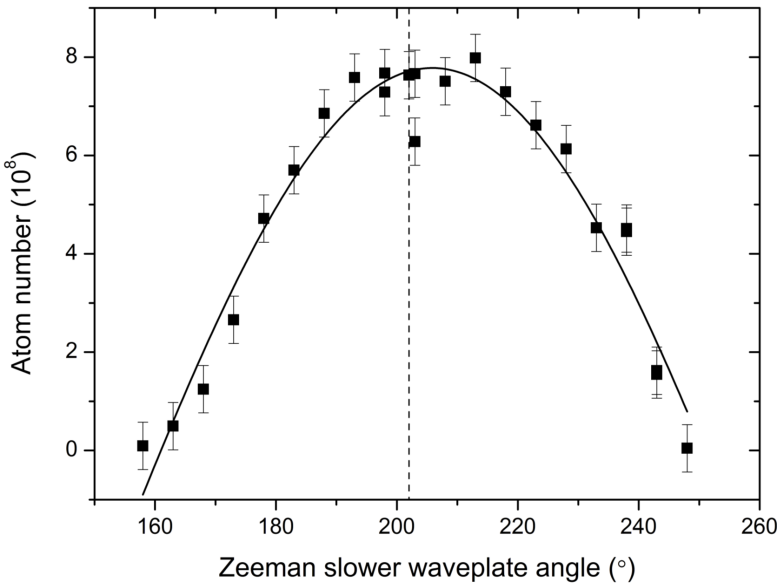

Figure 7.4: Fewer atoms are loaded into the MOT when the polarisation of the Zeeman slower beam is not perfectly circularly polarised. The dashed line indicates where the light should be circularly polarised according to the axis marked on the waveplate itself.

natural linewidth of $\Gamma = 2\pi \times 182.2\,\text{kHz}$ could be used. This is a more critical approximation, but this value gives an upper bound on the atom numbers presented here.

The first part of the slowing process to be optimised was the polarisation of the Zeeman slower beam and then the magnetic field profile.

7.2.1 Polarisation of the Zeeman slower beam

The Yb-Cs Zeeman slower was designed to work with left handed circularly polarised light. Figure 7.4 shows how the fluorescence (proportional to atom number) in the MOT starts to drop when the waveplate in the Zeeman slower beam (figure 4.13) is rotated and so the polarisation of the light moved away from pure circular polarisation. This is simply because, if the beam is thought of as a decomposition of both left handed and right handed circularly polarised light, there will be less light with the correct polarisation. The quarter waveplate was set to an angle of $(202 \pm 1)°$.

The atom number drops to zero at approximately 45° from the peak in figure 7.4, which would be when the light is linearly polarised. Therefore there will be half the power in the correct handedness of circularly polarised light which will result in most atoms being released from the Zeeman slower at higher velocities and so they will be unable to be captured by the MOT.

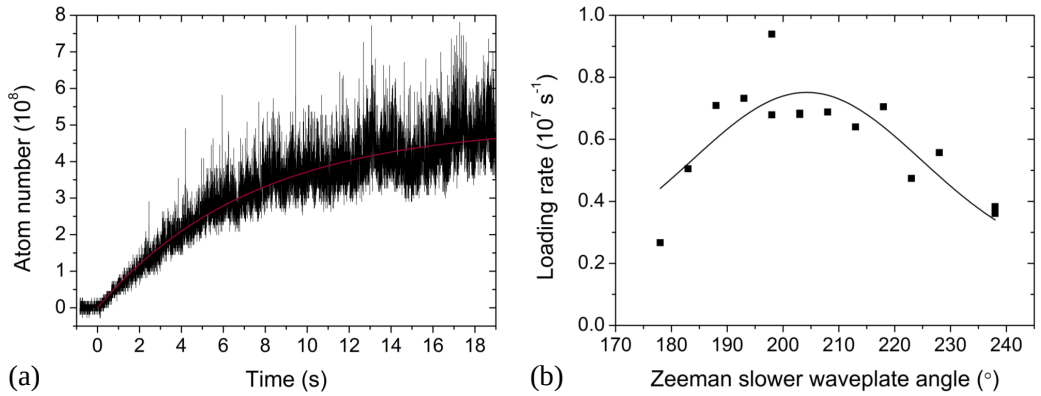

Figure 7.5: (a) An example loading curve for Yb. (b) The loading rate peaks at a waveplate angle of approximately 205°, which is also where the atom number in the MOT is at its largest.

Figure 7.7 corroborates this theory in that the atom number in the MOT falls to zero at half the maximum power.

Loading rate and polarisation

The loading rate for each waveplate angle was determined by fitting the individual loading curves with the same equation as for Cs in Section 6.3,

$$N(t) = \frac{R}{\gamma}\left(1 - \exp\left(-\gamma \mathrm{t}\right)\right),$$

where R is the loading rate and γ the decay rate.

An example of a typical loading curve can be seen in figure 7.5(a). The variation in the loading rate with quarter waveplate angle can be seen in figure 7.5(b). The loading rate does vary with polarisation of the Zeeman slowing beam, with a similar peak in the data at approximately the same waveplate angle of $(202 \pm 1)°$ as the atom number curve (figure 7.4).

7.2.2 Zeeman slower magnetic field profile

Once the polarisation of the Zeeman slowing beam was correct, the magnetic field profile of the Zeeman slower could be optimised. The method for optimising the Zeeman slower coil currents for Yb was to initially set the coils to their design currents and to scan each coil in turn about that value. This is a simpler process than that used for Cs as a global optimum might have existed for Cs depending on the number of atoms slowed to the MOT capture velocity, therefore necessitating the iterative process outlined in figure 6.2. On the other hand, the exit velocity of the Yb atoms from the Zeeman slower

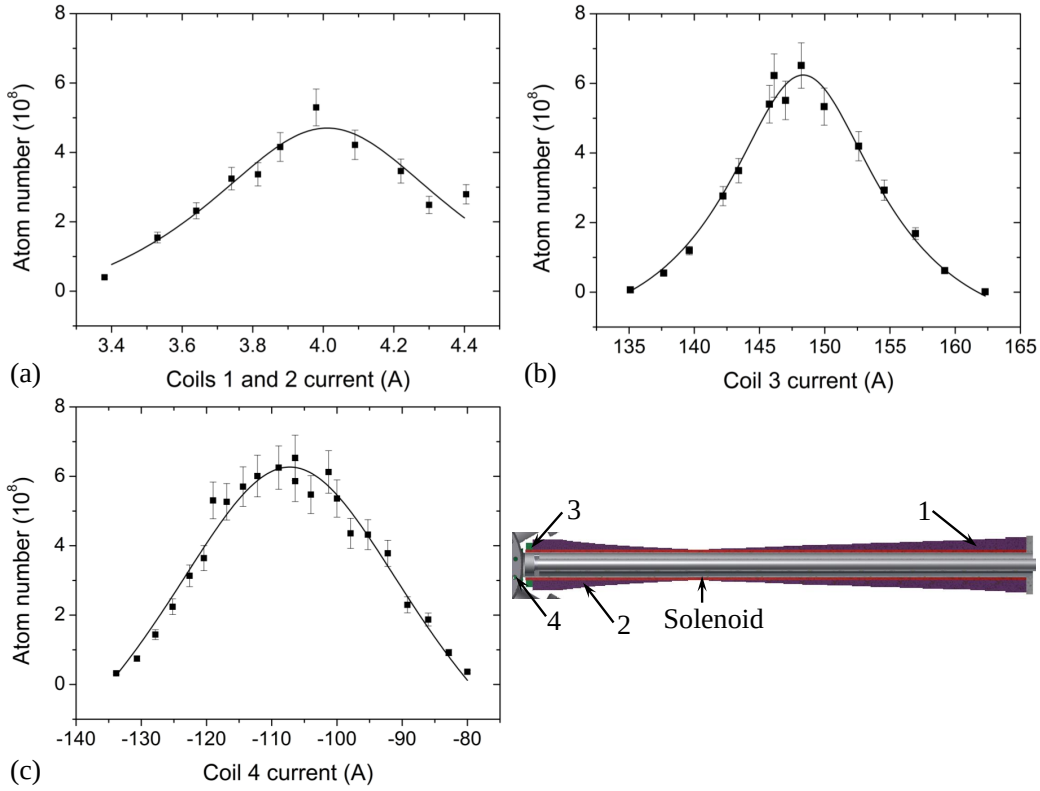

Figure 7.6: Counts from the MOT fluorescence on the CCD camera as the currents to (a) coils 1 and 2, (b) coil 3 and (c) coil 4 were varied. Clear peaks can be seen for all the coils. The inset is a reminder of the coil designations.

has a much smaller allowable range so the optimum settings must be close to the designed field profile, to give atoms with the correct velocities.

Increasing or decreasing the magnetic fields produced by each of the coils has an affect on the residual field within the science chamber. The position of the MOT at the start of the optimisation process was marked on the CCD image and the East-West shims used to bring the MOT back to that point each time. This would compensate for any bias created by the Zeeman slower fields. Throughout the optimisation process the axial field gradient for the MOT was kept at $3.66\,\mathrm{G\,cm^{-1}}$.

Figure 7.6 shows how the number of ^{174}Yb atoms in the MOT changed when the current to (and therefore magnetic fields produced by) coils 1 and 2, 3 and 4 were varied. Coils 1 and 2 give the main field profile along the length of the Zeeman slower. The field profile is given by the number of turns wound at each point along the slower, so increasing the current gives a steeper gradient along the slower. Looking at equation (5.4),

$$\begin{aligned} B(z) &= \frac{\hbar\Delta\omega}{\mu} \pm \frac{k\hbar v_0}{\mu}\sqrt{1-\frac{2\eta z}{L_0}} \\ &= B_0 \pm \Delta B\sqrt{1-\frac{z}{L}}, \end{aligned}$$

this equates to increasing ΔB or, specifically, increasing the initial velocity, v_0, that an atom can have before being slowed. Naïvely it might be expected that this would increase the number of atoms that can be loaded into the MOT, however, these faster atoms cannot be slowed to the capture velocity of the MOT within the length of the Zeeman slower, as this was designed for a certain initial velocity. Equation (5.5),

$$L = \frac{L_0}{2\eta} = \frac{v_0^2 m}{\eta\hbar k\Gamma},$$

shows that as the length of the Zeeman slower cannot be changed, as v_0 increases the efficiency η must decrease. This accounts for the fact that in figure 7.6(a) fewer atoms are loaded into the MOT when the current to coils 1 and 2 is increased above a certain point. If the current to these coils is decreased, this means that the velocity that an atom can have and still be captured by the Zeeman slower also decreases and so fewer atoms from the oven are slowed. A clear optimum current of (3.98 ± 0.02) A is shown, matching the design current of 4 A well.

Figure 7.6(b) shows how the atom number varies when the current to coil 3 is changed. As can be seen in figure 5.6, coil 3 provides the large field at the end of the Zeeman slower which directly affects the release velocity of the atoms (as discussed in Section 5.3.1). Therefore it is easy to see that changes to this coil will determine how many atoms are within the range that can be captured by the MOT. If the field is too high then atoms may be slowed too much and pushed back down the slower, or drop too far under gravity in the distance to the centre of the science chamber and therefore will not be captured by the MOT beams. If the field is too low then fewer atoms will be slowed to the required velocity and so the number in the MOT will decrease. Another clear optimum of (147.0 ± 0.2) A can be seen in the figure. The design current for this coil was 149 A.

Similarly, figure 7.6(c) shows how changing the field produced by coil 4 affects the MOT number. Coil 4 is used to give a sharp drop off in the magnetic field at the end of the Zeeman slower, however, increasing the current to this coil not only gives a sharper drop but also reduces the magnitude of the field at the end of the slower, in the same way as reducing the field produced by coil 3 would do. Therefore, as for coil 3, there is a well-defined optimum setting for coil 4 of -(106.0 ± 0.4) A. The design current was -116.5 A.

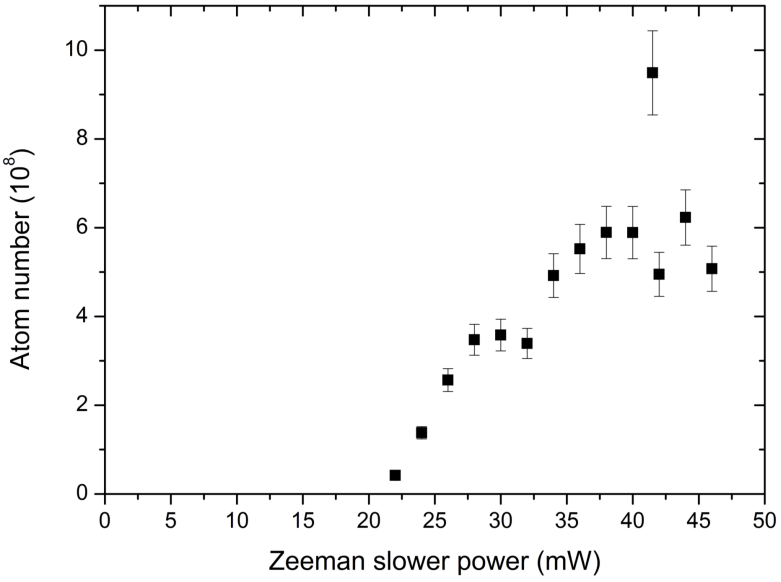

Figure 7.7: MOT counts as the power in the Zeeman slower beam is increased. A threshold power of approximately 20 mW is required to see enough atoms slowed to the correct velocity range to be captured in the MOT.

7.2.3 Power in the Zeeman slower beam

The power in the Zeeman slower beam was varied after the coil currents had been optimised to see if there was a defined peak as for Cs (figure 6.7(a)). The results for this can be seen in figure 7.7. From this figure it is unclear whether the atom number (or counts on the CCD camera) saturates at high powers or whether a peak might exist but there was not enough available power in the Zeeman slower beam to see the decrease in atom number.

From the Zeeman slower simulations in Section 5.5 the optimum power was expected to be approximately 44 mW with most atoms pushed back down the slower near 55 mW. There is not enough power available in the Zeeman slowing beam to see this downturn in atom number due to the power losses sustained through performing spatial filtering on the beam.

Figure 7.7 shows that a threshold of ~20 mW is required to see any atoms captured in the MOT. Below this threshold it is likely that the atoms were released too soon from the Zeeman slower and so all had velocities too high to be captured by the MOT even with sidebands frequency broadening the MOT beams. This is corroborated by the Zeeman slower simulations (figure 5.10) where atoms start to enter the $0 < v_\mathrm{f} < 10\,\mathrm{m\,s^{-1}}$ region required at 35 mW.

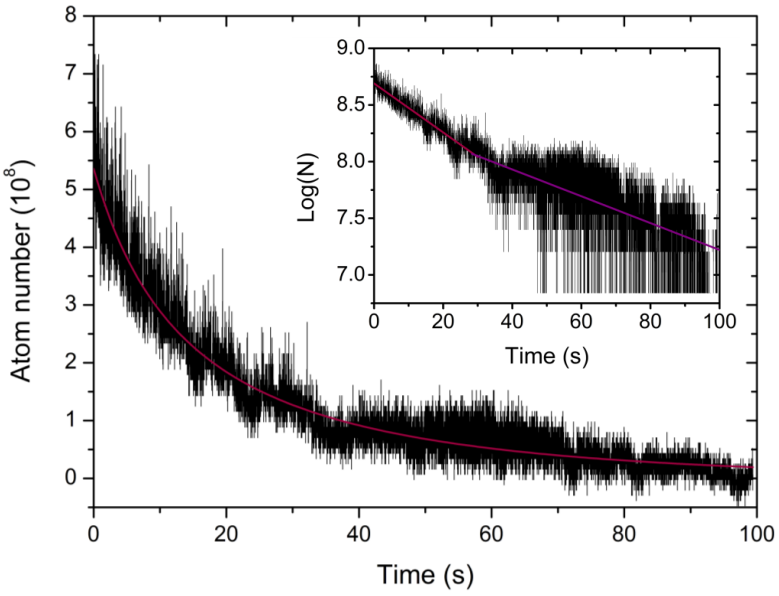

Figure 7.8: A typical lifetime curve for the Yb MOT. The inset shows the same data on a log scale showing the two regions of decay which give different gradients. The fluorescence signal from the MOT is quite small and so the signal to noise ratio is not ideal.

7.3 MOT lifetime

Lifetime measurements on the individual MOTs for Cs and Yb will influence the order in which the dual species MOT is loaded in future experiments, for example, if one species has a particularly long lifetime then it is more likely that we will load that species first, in order to still have a significant number of that atom left. A typical lifetime curve for Yb is shown in figure 7.8, where both the atomic and Zeeman slower beams have been blocked, to compare to figure 6.10(a) for Cs.

As for Cs, the Yb data was fitted with the following solution to equation (6.3),

$$N(t) = \frac{N_0\left(1 - \tanh\left(\frac{\gamma t}{2}\right)\right)}{1 + \tanh\left(\frac{\gamma t}{2}\right)\left[\frac{2N_0\beta}{\gamma} + 1\right]}.$$

The loss rates obtained from the fit are $\gamma = (0.0215 \pm 0.0005)\,\mathrm{s}^{-1}$ and $\beta = (1.02 \pm 0.02) \times 10^{-10}\,\mathrm{s}^{-1}$. Alternatively, the lifetime can be expressed as $1/\gamma = (46.5 \pm 0.2)\,\mathrm{s}$. The errors on these values are from the fit to the data (the red line in figure 7.8), however, as the data is quite noisy, the lifetimes obviously cannot be known to such precision, however, the lifetime appears to be similar to those obtained from the Cs data.

Again, as for Cs, a 'fast' and 'slow' lifetime can be seen by the different

gradients in the inset of figure 7.8, where the data has been plotted on a log scale. Comparing qualitatively with the curve in figure 6.10(a), the lifetime for Cs appears to be longer, however, this could be an artefact of the small fluorescence signal from the Yb MOT as the signal to noise ratio is fairly poor in this data (as shown most dramatically in the inset of the figure).

Chapter 8

Conclusions and Outlook

This thesis has described the design and construction of an apparatus to laser cool and trap Cs and Yb atoms. The later chapters have presented the optimisation and characterisation of the apparatus culminating in the observation of a dual species magneto-optical trap. In the following, a summary of the design and testing of the apparatus is given and an outlook to the future of the experiment is presented.

8.1 Realisation of the dual species MOT

A dual species MOT (figure 8.1(a)) was obtained by first loading the Cs and then the Yb. This is the first time both Yb and Cs have been trapped in the same chamber. The photograph shown is a composite image from a webcam as this was the only camera that could pick up the infra-red Cs MOT in a photograph as it has no IR filter on the detector.

The loading sequence from the LabVIEW control program used for this dual species MOT is shown in figure 8.1(b). For this proof of principle test the Cs was loaded first with an East-West shim coil control voltage of 1 V, before both the EW shim and Zeeman slower currents were switched to those optimised for Yb. Throughout the experiment, the MOT magnetic field gradient was kept at $3.66\,\mathrm{G\,cm^{-1}}$, which gave a smaller MOT for Cs but allowed Yb to be easily loaded.

Eventually it may be better to load the Yb first before loading the Cs, as this may allow the Cs to be loaded with a higher MOT magnetic field gradient; once the Yb MOT has been loaded it could be compressed to favour the Cs loading. However, this advantage would have to be balanced with the MOT lifetimes and whether a significant number of Yb atoms are still trapped in the MOT at the end of the Cs loading.

As can be seen in figure 8.1(a), the two MOTs are not yet spatially overlapped. This is because the radiation forces on the two MOTs are not quite

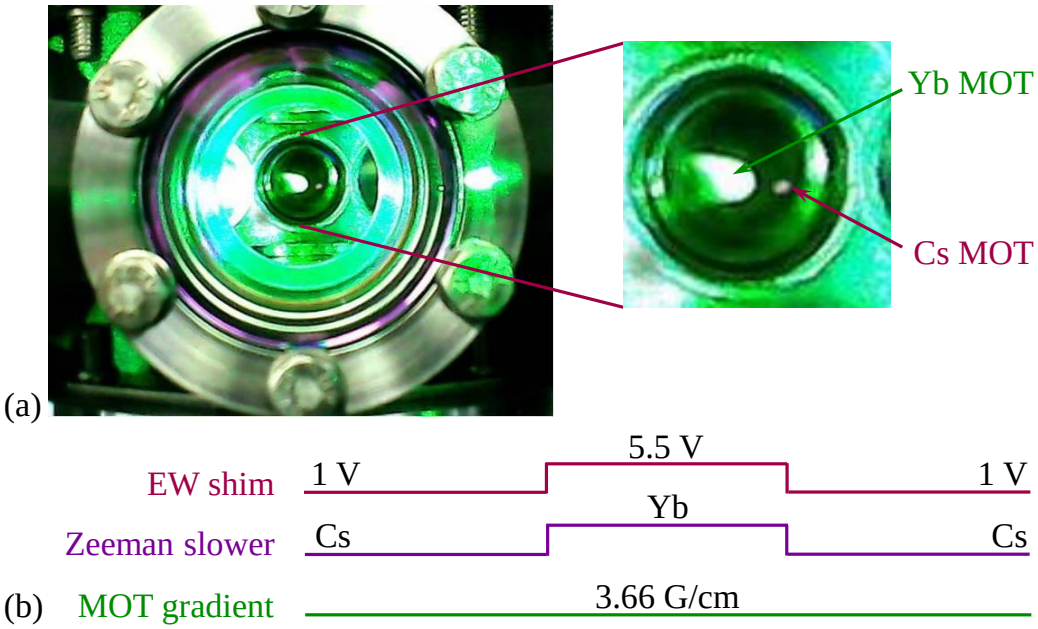

Figure 8.1: (a) The Yb and Cs MOTs in the same chamber. The slight offset of the Yb MOT is due to unequal radiation pressure from the MOT beams. This image is a composite of two images as the Cs MOT was washed out by the brighter Yb MOT. (b) The simple experimental sequence used to sequentially load the dual species MOT showing the East-West shim and Zeeman slower settings and the constant MOT gradient.

balanced due to the positions of the MOT fibres. As can be seen in figure 4.12, the two Cs fibres currently come in from the south side, whereas the Yb fibres come in either side of the Zeeman slower. Although each set of MOT beams are power balanced, losses through the viewports mean that the retro-reflected beams will have slightly less power. Therefore, to overlap the two MOTs one of the Cs MOT fibres will be moved to the north side of the table next to the combined MOT and imaging Yb fibre.

8.2 Summary

We have discussed the motivation for producing molecules with both an electric and magnetic dipole moment and how such molecules may be associated from ultracold mixtures of alkali metal atoms and alkaline earth-type atoms. In this regard, a mixture of Cs and Yb looks particularly promising for magnetoassociation on a Feshbach resonance, a potentially important step towards the creation of molecules in the ro-vibrational ground state.

In this work we have highlighted the design process behind creating an apparatus capable of laser cooling these two atomic species, specifically, the design, construction and testing of a dual species oven, Zeeman slower and magneto-optical trap. The oven was tested before the final connection was made to the rest of the vacuum system and it produces well collimated atomic beams of Cs and Yb. The Zeeman slower magnetic field profile was also measured before installation in the system and the measured field matched the ideal design field to within 1 % (1.5 %) for Yb (Cs). The new vacuum system was then constructed and baked out, a timelapse of which can be seen in [114].

The laser system for cooling Cs was planned and implemented, giving separately controlled Zeeman slower and MOT beams whose detuning can be individually controlled. The option for Degenerate Raman Sideband Cooling was also included if needed at a later date.

Two laser systems have been developed for cooling Yb in collaboration with Imperial College London; one at 556 nm for the MOT and the other at 399 nm for Zeeman slowing. At Durham a whole atomic beam machine was developed based upon the oven design used in the main apparatus to allow a dispersion signal to be created from a small fluorescence signal.

Finally, a fully optimised Cs MOT was achieved with $\sim 1 \times 10^8$ atoms (the atom number can be controlled with dispenser current) and an Yb MOT with the order of 10^8 atoms for several isotopes (^{172}Yb, ^{174}Yb and ^{176}Yb) loaded directly on the 556 nm transition was demonstrated - the first such in the UK. It was also shown that the two species could be loaded sequentially into their MOTs using the same magnetic field gradient. This paves the way for many further experiments exploring this novel mixture.

8.3 Outlook

The ultimate aim of this experiment is to create CsYb molecules in the ro-vibrational ground state. However, there are several essential steps that need to be completed before this can be achieved.

8.3.1 Characterisation of the dual species MOT

Now that both Cs and Yb have been loaded into a MOT the mixture can start to be characterised to enhance our knowledge of this system. The first step towards this goal is to implement absorption imaging so that temperature and atom number measurements can be made simultaneously in the MOT. This will allow us to fully characterise the Yb MOT with respect to the parameters of the sidebands applied to the cooling light. It is expected that the Yb can reach a Doppler temperature of the order of $4\,\mu$K in the 556 nm MOT, which should be of a similar order of magnitude to the expected temperature for a Cs MOT, which can access sub-Doppler cooling and has a theoretical recoil temperature of $0.2\,\mu$K.

As mentioned in Section 8.1, the two MOTs need to be overlapped spatially by adjusting the beam balancing of the individual MOT beams. Once this has been done complete characterisation of the dual species MOT can be carried out, specifically looking for interspecies losses (e.g., [153–155]).

8.3.2 Photoassociation in the dual species Yb-Cs MOT

Once the MOTs have been overlapped, photoassociation spectroscopy can be performed on the mixture to find the interspecies background scattering length. This factor is required to enable more accurate predictions of the locations and widths of the Feshbach resonances in this system. The measurement need only be done for one isotope of Yb as mass scaling can be used to calculate the scattering lengths for the other isotopes.

The photoassociation spectroscopy will be done below the $6\ ^2P_{1/2}$ limit of Cs, requiring a laser wavelength red-detuned from the 894.6 nm D_1 transition [53]. The photoassociation spectrum for Cs at this wavelength is already known [156] so the method can be tested against known lines and eventually any features due to Cs_2^* can be ruled out, leaving only peaks from Cs*Yb. Reference [156] discusses how those measurements were carried out by reducing the laser intensity as the laser frequency scan moved closer to the atomic resonance. The laser power used in their experiment was 450-900 mW, therefore a high power DBR laser has been purchased in order for the measurements on the Yb-Cs mixture to be carried out.

Distributed Bragg Reflector (DBR) lasers contain a gain medium surrounded

at each end by a distributed Bragg reflector as the end mirrors [157]. They allow single frequency operation at high power with the frequency tunable over a large range by a combination of temperature and current. This laser, in conjunction with an optical cavity, will be used to obtain the 1-photon photoassociation spectrum for Yb-Cs. This will be done by overlapping the 895 nm light with the dual species MOT and looking for atom loss at specific frequencies. The atom loss will occur for both species at a CsYb resonance. Therefore, if only the Yb atom number is monitored this automatically differentiates between Cs_2^* and Cs^*Yb features.

A fibre coupled EOM can then be added to the set up to stabilise the frequency of the first laser to a molecular resonance by locking a sideband to a stable optical cavity. A second laser (either another DBR or potentially an ECDL and a tapered amplifier) will form the second laser beam that will scan in frequency over the 2-photon photoassociation spectrum. The frequency difference will be measured using a beat frequency between the two lasers. This can be done as the wavelengths of the two photons will be approximately the same as the bound states being measured are very close to threshold.

The tell-tale sign of 2-photon photoassociation is a 'loss of loss' in the atom number in the MOT when the carrier frequency of the laser is set at a known resonance feature. The 1-photon photoassociation will be disrupted when the frequency of the second laser is such that it drives the transition between the electronically excited molecular state and a bound state in the ground molecular potential. The binding energies are then directly known from the frequency difference of the two laser beams. The last bound state can simply be found as the last frequency at which the 'loss of loss' occurs before the atomic D_1 transition in Cs.

8.3.3 Ultracold Yb and Cs in a dual species trap

Once the photoassociation measurements within the MOT are complete, the two species will be loaded into an optical dipole trap, either using a single wavelength of 1064 nm or with a bichromatic dipole trap using both 532 nm and 1064 nm. The bichromatic dipole trap would allow the trap depths to be equalised, as 1064 nm alone would create trap depths for Cs approximately 10× greater than that for Yb. There is a possibility that sympathetic cooling could occur between Yb and Cs so once in an optical dipole trap this can be investigated and used to verify the scattering lengths measured by the photoassociation spectroscopy.

The initial mixture that will be investigated is ^{174}Yb-Cs as this is the most abundant isotope of Yb. A logical first objective will be to condense both Cs and ^{174}Yb and investigate the miscibility of the BECs potentially whilst tuning the Cs intraspecies scattering length. Subsequently we should be

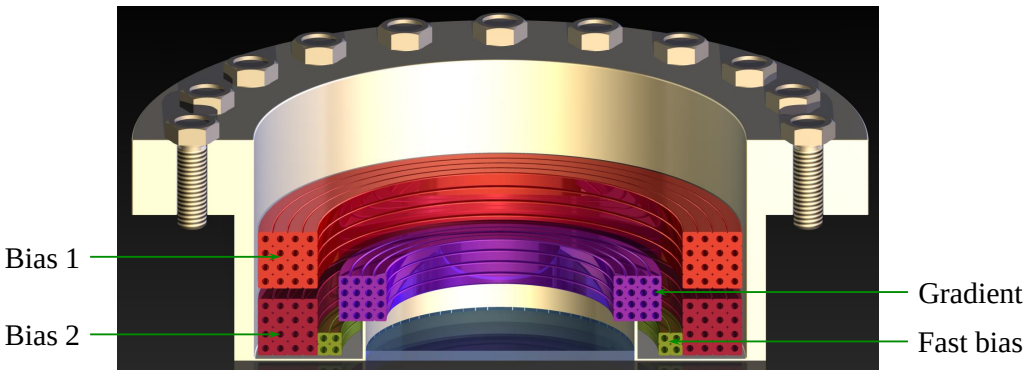

Figure 8.2: The coil set currently under development to produce large magnetic fields for searching for Feshbach resonances. The bulk of the bias field will be produced by the large coil pairs, Bias 1 and Bias 2, whilst finessing of the field will be achieved with the Fast bias pair. The gradient coils produce the magnetic field gradient required by the MOT. However, they could be controlled in such a way as to be able to switch to creating a bias field as well if required. Each coil is wound from hollow square wire to allow for water cooling.

able to replicate the condensation of all of the bosonic isotopes that are able to be condensed (^{168}Yb, ^{170}Yb, ^{174}Yb and ^{176}Yb [57, 59–61]) and to create degenerate Fermi gases with the fermionic isotopes (^{171}Yb and ^{173}Yb [60, 63]). Although, degenerate gases are not a necessary step towards ground state molecules of CsYb, they would just demonstrate a high level of control over the system.

8.3.4 Magnetoassociation of CsYb molecules

Once we have completed the interspecies background scattering length measurements, they can fed back into the scattering theory calculations to accurately predict the positions and widths of the Feshbach resonances. It will then be time to search for the presence of the resonances. This would be done by measuring atom loss from the optical dipole trap as a function of the applied magnetic field. However, this in itself is likely to throw up some technical challenges as the predicted Feshbach resonances for CsYb occur at very high magnetic fields and are relatively narrow [86]. Fields in excess of 1000 G will definitely be required and even up to 4000 G is a possibility. The lower part of this range will be accessible fairly easily, with similar magnetic fields of greater than 1000 G are routinely used in another lab in the research group [158]. However, as discussed in Section 2.2, the wider resonances will occur at larger fields as the resonance widths scale as B^2 meaning that access to higher fields is desirable.

Coil	Magnetic field ($\mathrm{G\,A^{-1}}$)
Fast bias	0.697
Bias 1	1.54
Bias 2	2.33
Gradient	1.087

Table 8.1: The magnetic fields produced by the coil pairs in bias configuration per amp of current applied.

The coil set currently under development consists of four pairs of coils which will sit in the re-entrant flanges on the main chamber, as can be seen in figure 8.2. Bias coils 1 and 2 provide the large magnitude bias fields, whereas the fast bias coil provides a very uniform bias field which can be used for fine tuning of the magnetic field and can be switched over faster time periods. The final coil pair provide the gradient field for the MOT. It is expected that we will be able to reach 2000 G with this coil set. Table 8.1 lists the magnetic field produced by each coil pair per amp of current applied to them. The large coils that will produce the bulk of the field (Biases 1 and 2) would need 649 A or 429 A respectively to get to 1000 G each, meaning that to obtain sub-mG stability for the Feshbach resonances the current will need to be stable to 6.49×10^{-1} mA or 4.29×10^{-1} mA. Accessing Feshbach resonances with smaller widths will therefore be very technically challenging.

If no resonances are found at lower magnetic fields due to the very small predicted widths other methods of creating higher magnetic fields may have to be investigated. These could include bitter electromagnets [159] or coils wound onto a more efficient heat-sink for operation at higher currents [160].

8.3.5 Other methods for creating molecules

However, if Feshbach resonances are still not found at reasonable magnetic fields, then magnetoassociation may not be a viable method to create CsYb molecules. Instead, there may be scope to use other methods for making molecules. These might include STIRAP directly on pairs on atoms in an optical lattice [161], using Yb Feshbach resonances in the triplet state [162] or direct photoassociation to create the loosely bound molecules before using STIRAP to transfer these molecules to the ro-vibrational ground state.

It is once in the ro-vibrational ground state that new areas of physics can start to be explored fully.

Appendix A

Rb-Cs mixture

During 2010-2011 I worked on the Rb-Cs mixture experiment in Durham. This is a similar, although more established, experiment to Yb-Cs. The experiment aims to combine Rb and Cs atoms to form ground state RbCs molecules. During my time working on the experiment we implemented a new laser locking scheme to enable work to start with ^{85}Rb, as previous to this results had only been obtained with ^{87}Rb. Initial results stemming from this work can be found in [85].

A.1 General outline of the RbCs experiment

A short outline of the RbCs experiment will be given here, but more detailed descriptions can be found in the five Ph.D. theses from this lab: [130, 163–166].

Rb and Cs are loaded from background pressure in a pyramid MOT chamber before being pushed through into a glass cell and reloaded into a second MOT stage. From here they are transferred to a magnetic trap where RF evaporation is carried out and the Rb sympathetically cools the Cs. They are then loaded into a crossed optical dipole trap at 1550 nm. Once at ultracold temperatures, experiments can be carried out; namely Feshbach spectroscopy leading to the formation of Feshbach molecules.

The laser frequencies needed for the various cooling and imaging stages are provided by AOMs in the same way as in the Yb-Cs experiment. The AOM frequencies are summarised in table A.1.

The Rb-Cs experiment has done extensive work with the ^{87}Rb-Cs mixture [130, 165, 166], but this mixture has a large interspecies scattering length which means that the collisional loss rate is quite high. This impacts on the number of Feshbach molecules that can be created [166]. Using ^{85}Rb-Cs is then desirable as the interspecies scattering length for this mixture is close to zero, which may allow a larger molecule production efficiency.

AOM	Destination	Frequency (MHz)	Δ (MHz)	Transition
1	Spectroscopy	2×125.58	0	$F = 3 \rightarrow F' = 4$
2	Imaging	2×124.68	-4.6	$F = 3 \rightarrow F' = 4$
3	Cooling	2×120.36	-10.8	$F = 3 \rightarrow F' = 4$
4	Optical pumping	-1×72.50	5.8	$F = 2 \rightarrow F' = 2$
5	Slave laser	2×117.57	-16.0	$F = 3 \rightarrow F' = 4$
6	Repump	1×79.99	-1.5	$F = 2 \rightarrow F' = 3$

Table A.1: The AOM frequencies for Rb. The slave laser provides the cooling light for the pyramid MOT.

A.2 Changing the laser locking scheme

The locking scheme for ^{87}Rb uses a combination of modulation transfer (MT) and frequency modulation (FM) locking for the cooling and repump light respectively [130], however, this is incompatible with ^{85}Rb due to the smaller excited state hyperfine splitting in ^{85}Rb. The locking for the cooling laser is unaffected by this change as in this scheme the laser frequency is set to an arbitrary detuning ($2 \times 125.58\,\text{MHz}$) from the $F = 3 \rightarrow F' = 4$ ($F = 2 \rightarrow F' = 3$) transition for ^{85}Rb (^{87}Rb) (see figures A.1(a) and (b) or (c)) and the imaging and cooling light is brought onto resonance with AOMs 2, 3 and 5.

However, the repump locking scheme is different in that the laser frequency is locked to the χ_{12} crossover feature in ^{87}Rb and the optical pumping and repump AOMs shift the frequency from there to the $F = 1 \rightarrow F' = 1$ and $F = 1 \rightarrow F' = 2$ transitions respectively. If the same locking scheme was used for ^{85}Rb the laser would be locked to the χ_{23} crossover but, because the $F' = 2$ and $F' = 3$ lines are split by 63 MHz (instead of the 157 MHz between the corresponding $F' = 1$ and $F' = 2$ lines in ^{87}Rb), the same AOMs would not then bring the optical pumping and repump light onto the correct frequencies.

Therefore, some other way of locking the repump laser needed to be found that would allow the laser to be locked to two separate places during the different stages of the experiment where repump or optical pumping is required.

A.2.1 DAVLL

Neither MT nor FM spectroscopy allow for the laser lock point to be changed by the frequencies required to swap between repump and optical pumping for ^{85}Rb as both of these methods produce error signals localised to the atomic transitions. Therefore a different method was required that gives a broader error signal covering the whole frequency range, in other words, an error signal produced from the Doppler background rather than the sub-Doppler

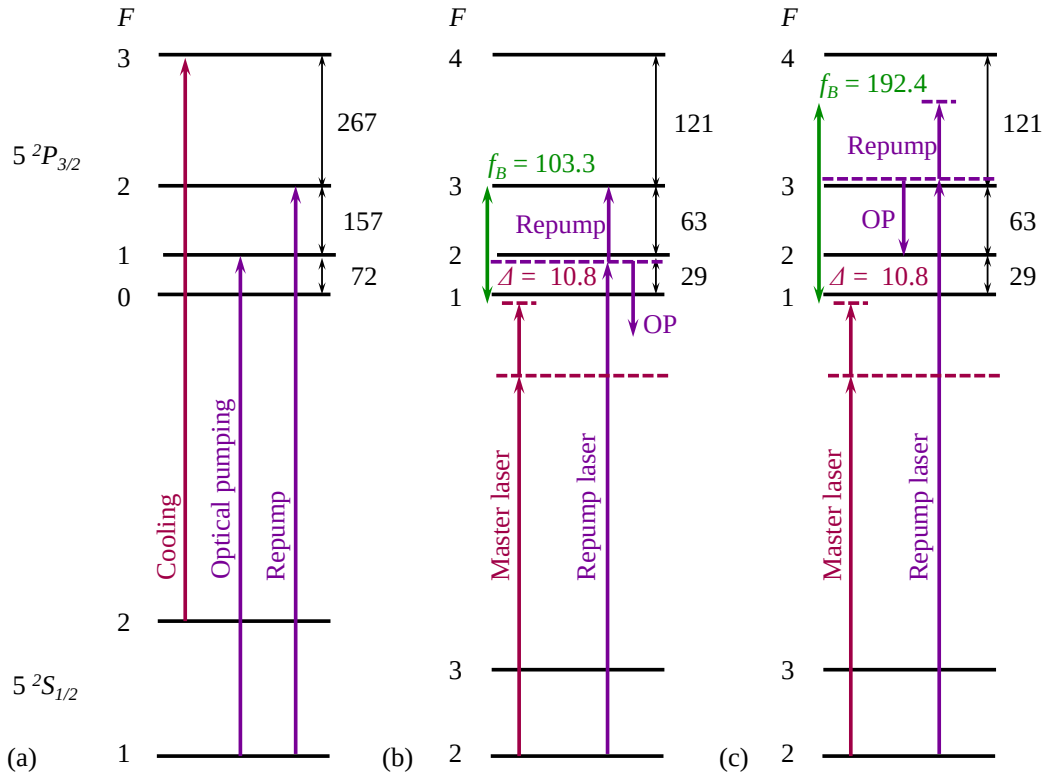

Figure A.1: (a) The energy level diagram with relevant cooling, repump and optical pumping transitions for ^{87}Rb. The cooling laser is locked to an arbitrary frequency away from the $F = 2 \rightarrow F' = 3$ transition, whilst the repump laser is locked to the χ_{12} crossover with two AOMs at approximately 80 MHz to bring repump and optical pumping onto resonance. Conversely, (b) and (c) show the energy level diagram for ^{85}Rb where it can be seen that due to the energy between the relevant levels differing from ^{87}Rb this is no longer an option. Instead the lock point is changed between stages with (b) showing the locking scheme for the repump experimental stage and (c) for the optical pumping stage. The beat frequency (green) for each case is checked by locking the master laser to the $F = 2 \rightarrow F' = 1$ transition. All frequencies are in MHz and the atomic properties were taken from [167].

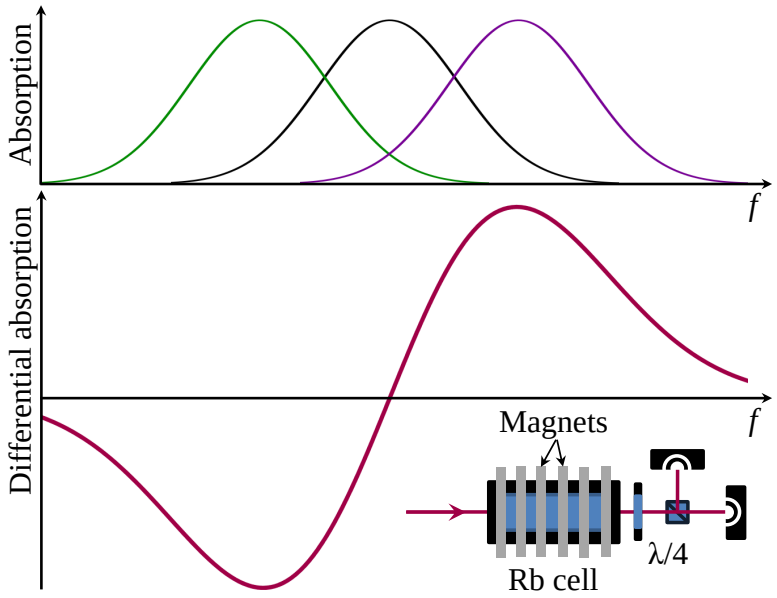

Figure A.2: Top panel: Depending on the handedness of the circularly polarised light relative to the applied magnetic field, the absorption peak is shifted higher or lower in frequency (green and purple traces) relative to the unperturbed peak (black). Bottom panel: A differencing photodiode can then be used to generate the locking signal (red). The optics required are shown in the inset.

peaks.

The method settled on was the Dichroic Atomic Vapour Laser Lock, or DAVLL [123–125]. In this method a Rb vapour cell is surrounded by permanent magnets (see inset in figure A.2) that act to split the Zeeman sublevels of the atoms. This means that when circularly polarised light is passed through the atomic vapour the centre frequency of the Doppler broadened absorption peak shifts up or down in frequency depending on the handedness of the polarisation, as illustrated by the green and purple absorption peaks in figure A.2. Therefore, if a linearly polarised beam (equivalent to equal amounts of right handed and left handed circularly polarised light) is passed through the cell before being decomposed by a polarising beam splitter on the other side, a differencing photodiode can be used to subtract the two absorption peaks giving an error signal to lock to, seen in the bottom plot of figure A.2. The gradient of the error signal can be increased by tuning the magnitude of the magnetic field.

The lock point can be changed by changing the set point voltage (achieved remotely from the LabVIEW program controlling the experiment) allowing the experiment to run smoothly whilst changing from repump to optical pumping light. The lock point can be monitored each morning before the

experiment is run by locking the master laser (normally used to produce the cooling light) to the $F = 2 \rightarrow F' = 1$ transition and beating the light from this with the repump light. For the repump (optical pumping) beam to be at the correct detuning the beat frequency should be 103.3 MHz (192.4 MHz) as illustrated in figures A.1(b) and (c). Light going to the MOT fibre can be used for this purpose as the repump and cooling light is already spatially overlapped at this point.

A.2.2 Laser frequency stability

There is one problem with using a method such as DAVLL and it comes from the very fact that the frequency range over which the laser can be locked is large - the error signal has a lower gradient to be able to span the whole Doppler broadened feature and this means that the locked laser frequency will not be as stable as other methods (such as MT or FM). DAVLL also depends heavily on the temperature of the atomic vapour as the depth of the Doppler feature changes with temperature. To investigate whether the required stability could be achieved some comparative studies were carried out comparing lasers locked with MT and DAVLL prior to installing DAVLL in the Rb-Cs experiment.

These investigations involved beating two lasers together that were locked by different methods (in this case the lasers were two 852 nm lasers instead of the 780 nm lasers that would be used for Rb, but the principle remains the same). The results of the investigation can be seen in figure A.3. In figure A.3(a) the two lasers were both locked with DAVLL, whilst in figure A.3(c) one laser was locked to an MT spectroscopy signal. Figures A.3(b) and (d) show the Allan deviation for the two beat measurements and from these it can be seen that the MT signal is much more stable as the Allan deviation approximately halves. (For a full explanation of Allan deviation, see Section 4.3.2 in the main body of this thesis).

However, it is only when compared to figure 4.8 in Chapter 4 which shows a later set of beat measurements with two lasers locked using FM and MT spectroscopy that it becomes apparent how unstable DAVLL is. The Allan deviation (figure 4.8(b)) for these beat measurements is an order of magnitude smaller than those shown in figure A.3.

Nevertheless, with DAVLL the laser frequency will drift by approximately 10 MHz over 6.5 hours, which is sufficient to carry out experiments with ^{85}Rb.

A.3 Sympathetic cooling of Cs by ^{85}Rb

Sympathetic cooling occurs when elastic collisions between atoms act to bring an atomic cloud into thermal equilibrium. The equilibrium temperature will

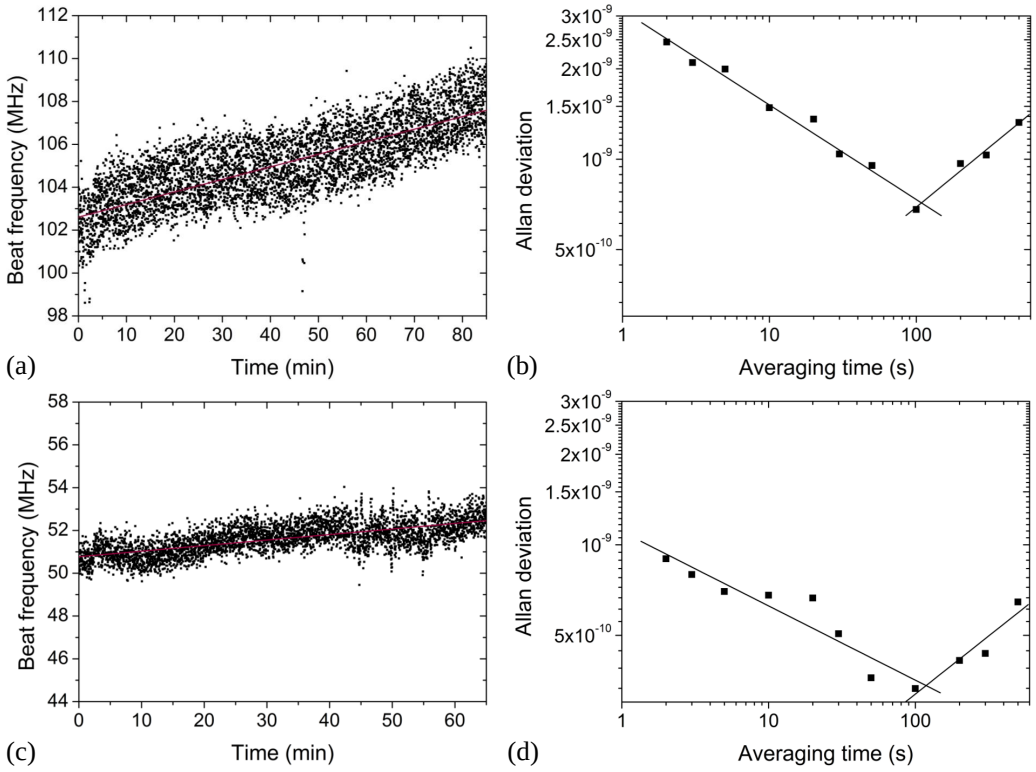

Figure A.3: The beat frequency (a) and Allan deviation (b) for two lasers both locked with DAVLL compared to the beat frequency (c) and Allan deviation (d) for one laser locked with MT spectroscopy and the other with DAVLL. It is immediately apparent from the beat data that locking just one of the lasers with MT reduces both the frequency drift and shot to shot noise.

be near that of the lower temperature species, the 'coolant'.

Once ^{85}Rb had been successfully trapped in the pyramid MOT and transferred to the second MOT, the RF evaporation was optimised for ^{85}Rb without Cs in the trap. After this the sympathetic cooling of Cs by ^{85}Rb could be investigated. This is done by plotting the phase space density [108],

$$\rho = n\lambda_{\mathrm{dB}}^3 = n\left(\frac{h}{\sqrt{2\pi M k_{\mathrm{B}} T}}\right)^3, \tag{A.1}$$

where n is the number density and λ_{dB} is the de Broglie wavelength, against the atom number. The phase space density allows both the number and temperature to be taken into account.

Figure A.4 shows the phase space density as a function of atom number in the magnetic trap for both ^{85}Rb (with Cs (red triangles) and without Cs (black squares) in the trap) and Cs when cooled by ^{87}Rb (purple circles) and ^{85}Rb (green pentagons). The decrease in phase space density of ^{85}Rb when Cs is

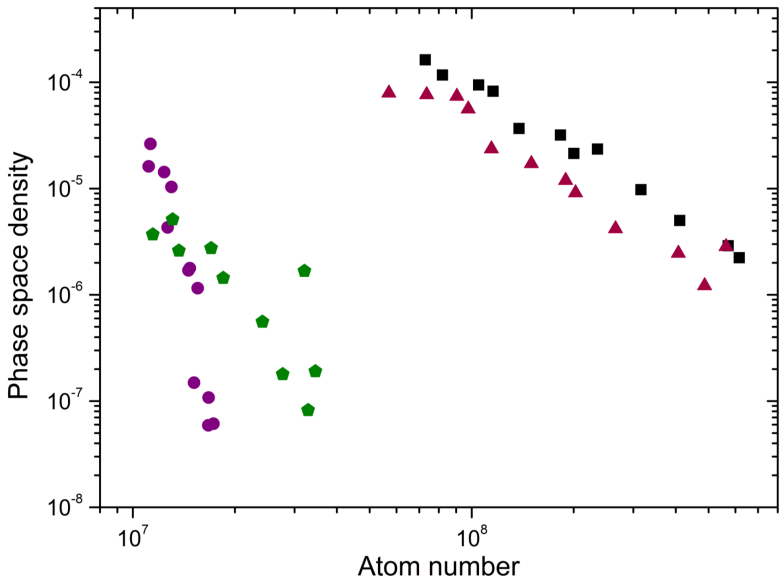

Figure A.4: The sympathetic cooling of Cs by ^{85}Rb; the phase space density of ^{85}Rb alone (black squares) is higher than when Cs is also present in the trap (red triangles). Cs is cooled more by ^{87}Rb (purple circles) than by ^{85}Rb (green pentagons). The ^{85}Rb was in the $|2,-2\rangle$ state whilst the Cs was in the $|3,-3\rangle$ state.

included shows that the ^{85}Rb has a higher temperature due to the additional heat load from the Cs.

It can also be seen that Cs is cooled to lower temperatures (higher phase space density for the same atom number) when ^{87}Rb is used as the coolant compared to ^{85}Rb. This is not unexpected as the ^{87}Rb-Cs interspecies scattering length is larger than that for ^{85}Rb-Cs, which is close to zero for s-wave collisions. Sympathetic cooling still occurs for ^{85}Rb-Cs as at the typical temperatures in the magnetic trap p-wave collisions can still occur.

For further results from the ^{85}Rb-Cs system, see [165, 166].

Appendix B

Dipole moment code

This is the code written in MATLAB for calculating the electric dipole moment according to equation (2.22) in Chapter 2. The code makes use of the already existing w3j code for calculating the Wigner 3-j coefficients developed by Jonathan Pritchard.

```
%%% Calculating the dipole moment matrix
d = 1/1e29;     % Permanent dipole moment [Cm]
(% 1.26/2.9979e29 for RbCs, d = 0.24/2.9979e29 for CsYb)
B = 1e-25;     % Rotational constant [J]
(% 3.3813e-25 for RbCs, B = 1.37241e-23 for CsYb)
delta = 0.01*(B/d);
Emax = 10*(B/d);
E = 0*(B/d):delta:Emax;     %Electric field [V/m]
lng2 = size(E);
lng2 = lng2(2);

%%% Constants
h = 6.626069e-34;
hbar = h/(2*pi);
c = 2.9979e8;
e = 1.60218e-19;
a0 = 0.529177e-10;

%%% J and mJ values to be evaluated
```

```
Jall = [5 5;5 4;5 3;5 2;5 1;5 0;4 4;4 3;4 2;4 1;4 0;3 3;3 2;3 1;3
0;2 2;2 1;2 0;1 1;1 0;0 0];

%%% Work out size of output matrix
lng = size(Jall);
lng = lng(1);

%%% Create and populate output matrix
HH2 = zeros(lng);
result = zeros(lng,(Emax-95*(B/d))/delta);
for i = 1:lng2
    for row=1:lng
        for col=1:lng
            J = Jall(row,1);
            mj = Jall(row,2);
            Jprime = Jall(col,1);
            mjprime = Jall(col,2);
            KroneckerDelta = 0;
            if( (J == Jprime) && (mj == mjprime) )
                KroneckerDelta = 1;
            end
% Selection rules:  DJ = 0, +/-1, Dmj = 0,+/-1, also puts 0 if J,
Jprime, mj, mjprime all 0
            if( ( (J-Jprime)==0 || (J-Jprime)==1 || (J-Jprime)==-1
) && ( (mj-mjprime)==0 || (mj-mjprime)==1 || (mj-mjprime)==-1 ) &&
(J  = 0 || Jprime  = 0 || mj  = 0 || mjprime  = 0) )
                HH2(row,col) = B*J*(J + 1)*KroneckerDelta -
                E(i)*d*sqrt((2*J + 1)*(2*Jprime + 1))*(-1)^mj*
                w3j(J,-mj,1,0,Jprime,mjprime)*w3j(J,0,1,0,Jprime,0);
            else
                HH2(row,col) = 0;
            end
        end
    end
```

```
    i;
    result(:,i) = sort(eig(HH2));     % result is in joules
end
plot(E,(result/h)*1e-9)
```

%%% Calculate the electric dipole moment from the Stark energies calculated

```
J0 = result(1,:);
dip = abs(gradient(J0,delta));
J10 = result(2,:);
J11 = result(3,:);
J20 = result(4,:);
J21 = result(5,:);
J22 = result(6,:);
```

%%% Getting the dipole moment in dimensionless units (i.e., divide by permanent dipole moment. Want E in units of B/d and d in units of d_{perm}

```
Eplot = E/(B/d);
dplot = dip/d;
Evar = rot90(Eplot);
dvar = rot90(dplot);
plot(Eplot,dplot)
J1var = [J10/(B); J11/(B)];
J2var = [J20/(B); J21/(B); J22/(B)];
```

Appendix C

Vacuum parts

For future reference, the following components were used to construct the main vacuum system for the Yb-Cs experiment. Viewports are not included in this list as details about them can be found in table 3.2. Some detailed engineering drawings for the custom parts can be found in Appendix B.

Vacuum part	Number	Company	Part number
DN40 feedthrough	1	MDC Vacuum	HV5-30C-4-C40
DN40 nipple	1	MDC Vacuum	CST40
Cs dispenser	3	Alvatec	AS-3-Cs-250-S
Yb ingots	3	Sigma-Aldrich	261300-5G
Barrel connector	4	LewVac	FHP-BECU-3IL-CON
Dual species oven	1	Imperial College London	Custom
Capillary holder	1	Imperial College London	Custom
Capillaries	55	Coopers Needleworks	304 SS, 0.58 mm ID, 0.89 mm OD
450 W nozzle heater	2	Watlow	MB1J2AN1-X56, MB1J1JN2-X66
600 W nozzle heater	2	Watlow	MB1J1JN4-X36
DN16 blank	1	MDC Vacuum	CFB34
DN40 blank	1	MDC Vacuum	CFB70
DN40 6-way cross	2	MDC Vacuum	CX6-40
Motorised feedthrough	1	MDC Vacuum	BRM-275-03
Atomic shutter	1	Durham University	Custom
Pumping station	2	VG Scienta	Custom
DN40 tee	3	MDC Vacuum	ET40
All metal valve	3	MDC Vacuum	MAV-150-T
Up-to-air valve	3	Swagelok	SS-4H-TW
NEG pump	2	SAES Getters	Capacitorr C400-2 DSK
$55\,\mathrm{l\,s^{-1}}$ ion pump	2	Agilent	VacIon 55
$40\,\mathrm{l\,s^{-1}}$ ion pump	1	Agilent (Varian)	VacIon 40
DN40 gate valve	1	MDC Vacuum	E-GV-1500M-11
Differential pumping tube	1	MDC Vacuum	Custom
DN40-DN16 reducer flange	1	MDC Vacuum	CFZ40-16
DN16 tube	1	MDC Vacuum	Custom length
DN16 bellows	1	MDC Vacuum	075-X
Science chamber	1	VG Scienta	Custom
Re-entrant viewports	2	AEA	Custom

Table C.1: A complete list of the parts used in the construction of the vacuum system, with company and part numbers for future reference.

Appendix D

Technical drawings

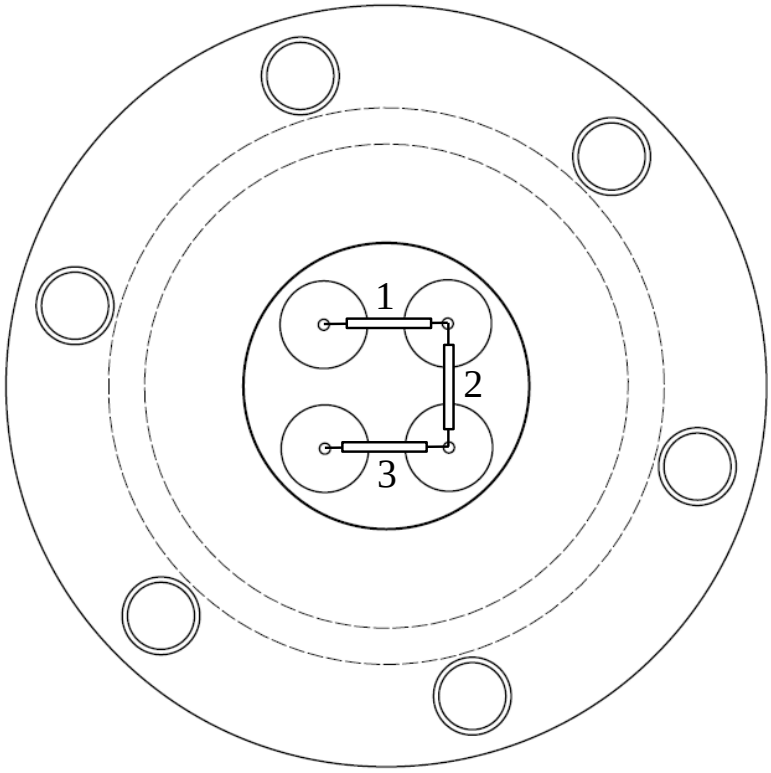

Figure D.1: The wiring diagram for the Cs dispensers with each dispenser labelled. This view is looking at the back of the flange.

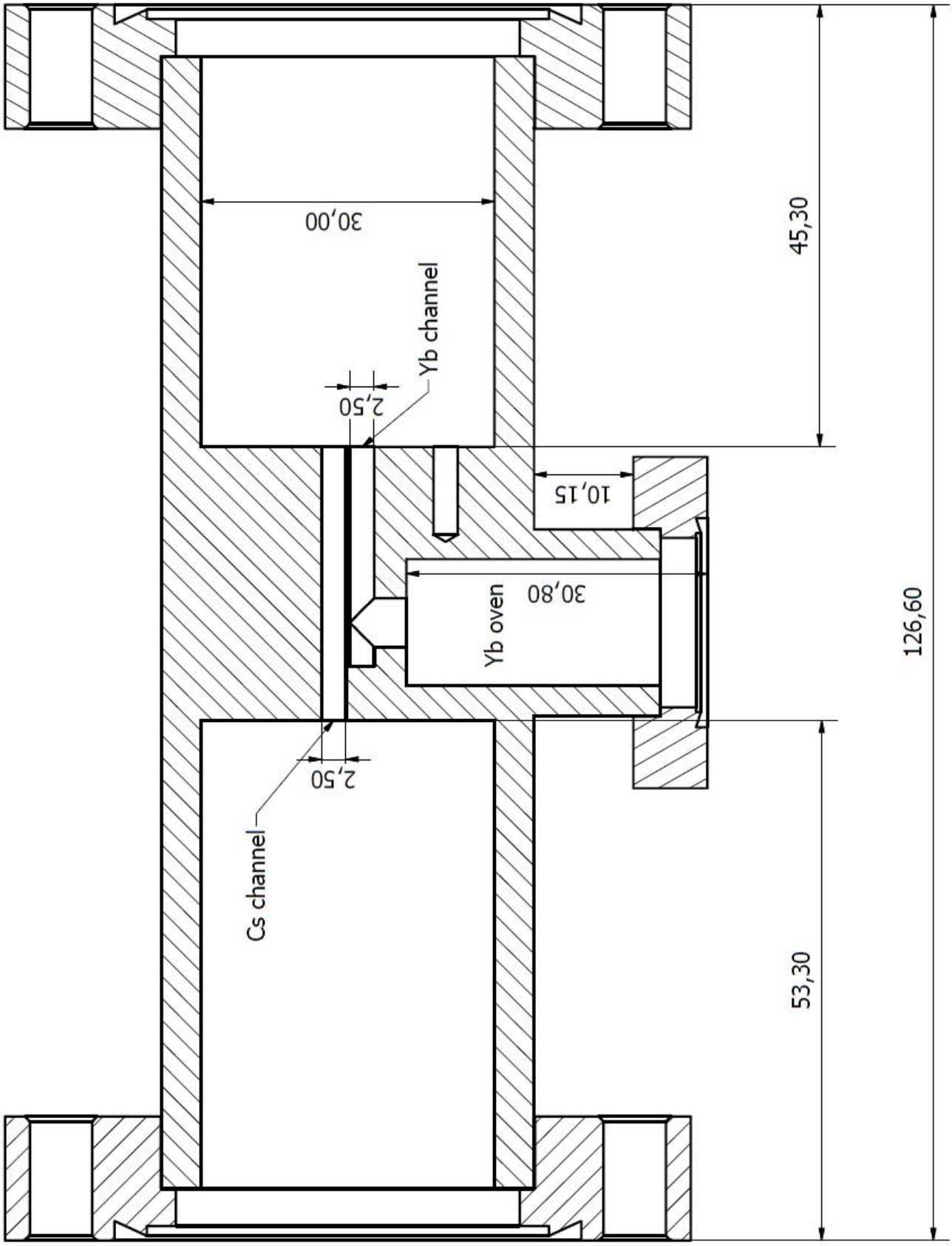

Figure D.2: The dual species oven.

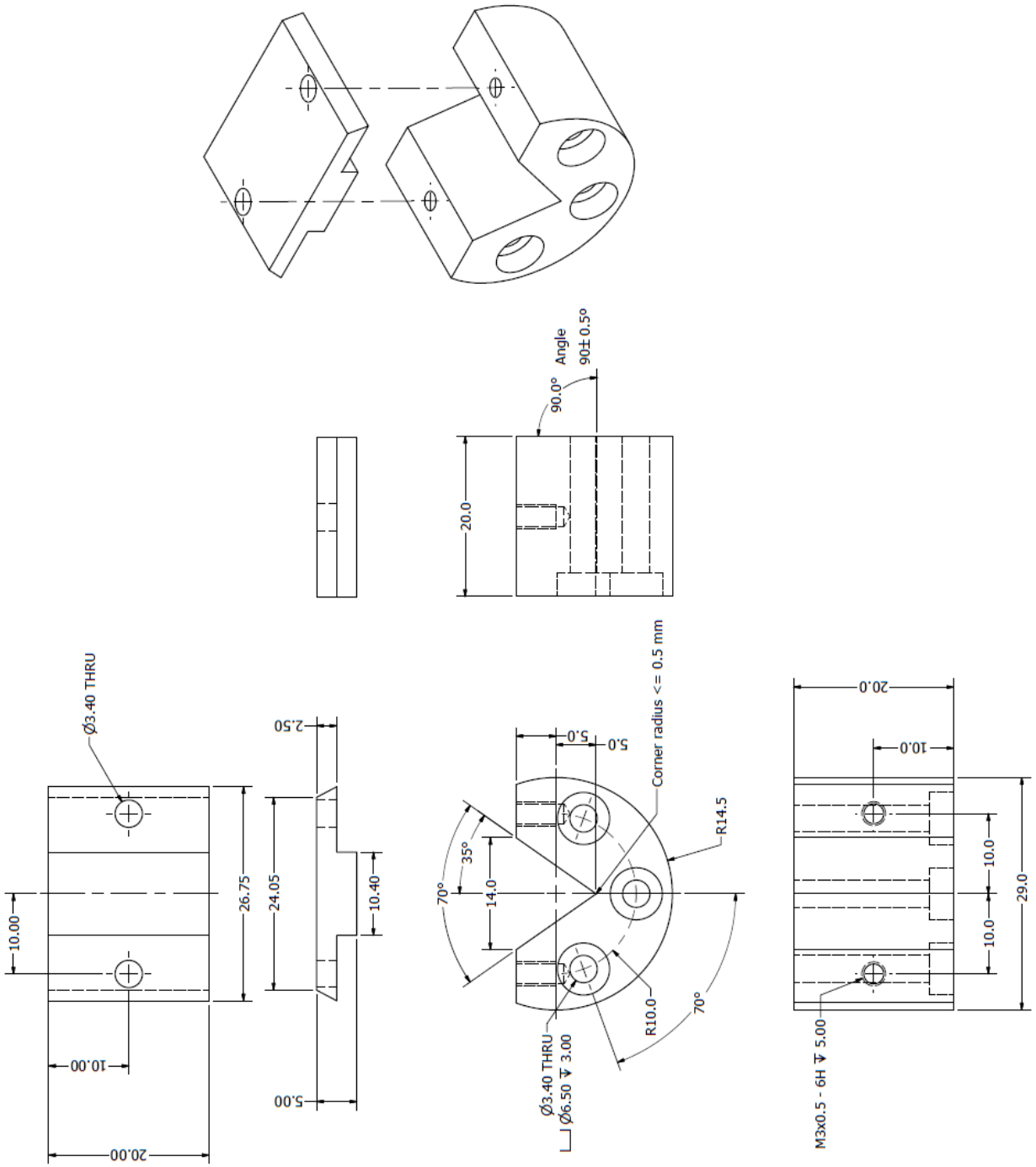

Figure D.3: Capillary holder for the dual species oven.

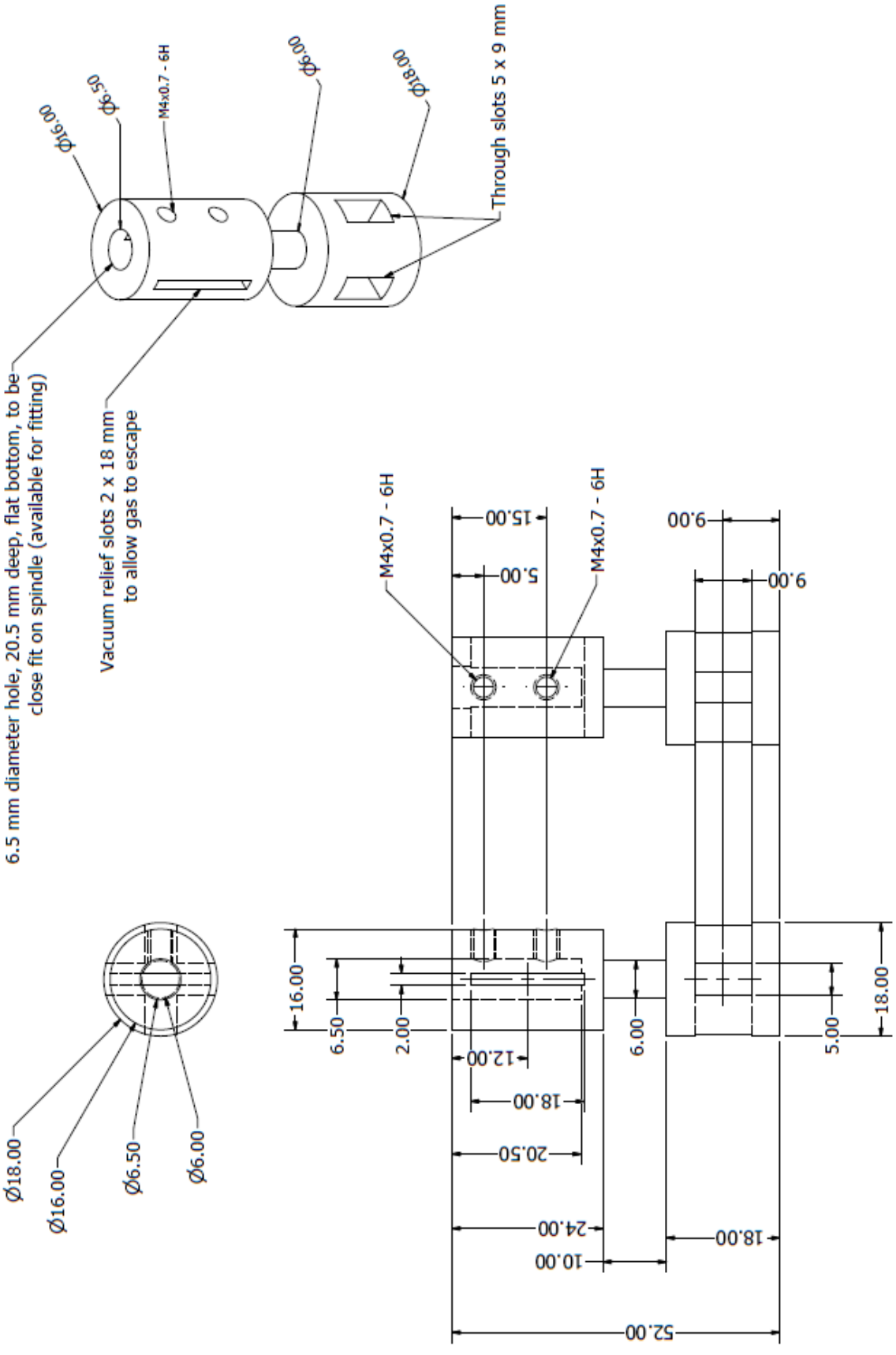

Figure D.4: The engineering drawing for the atomic rotary shutter.

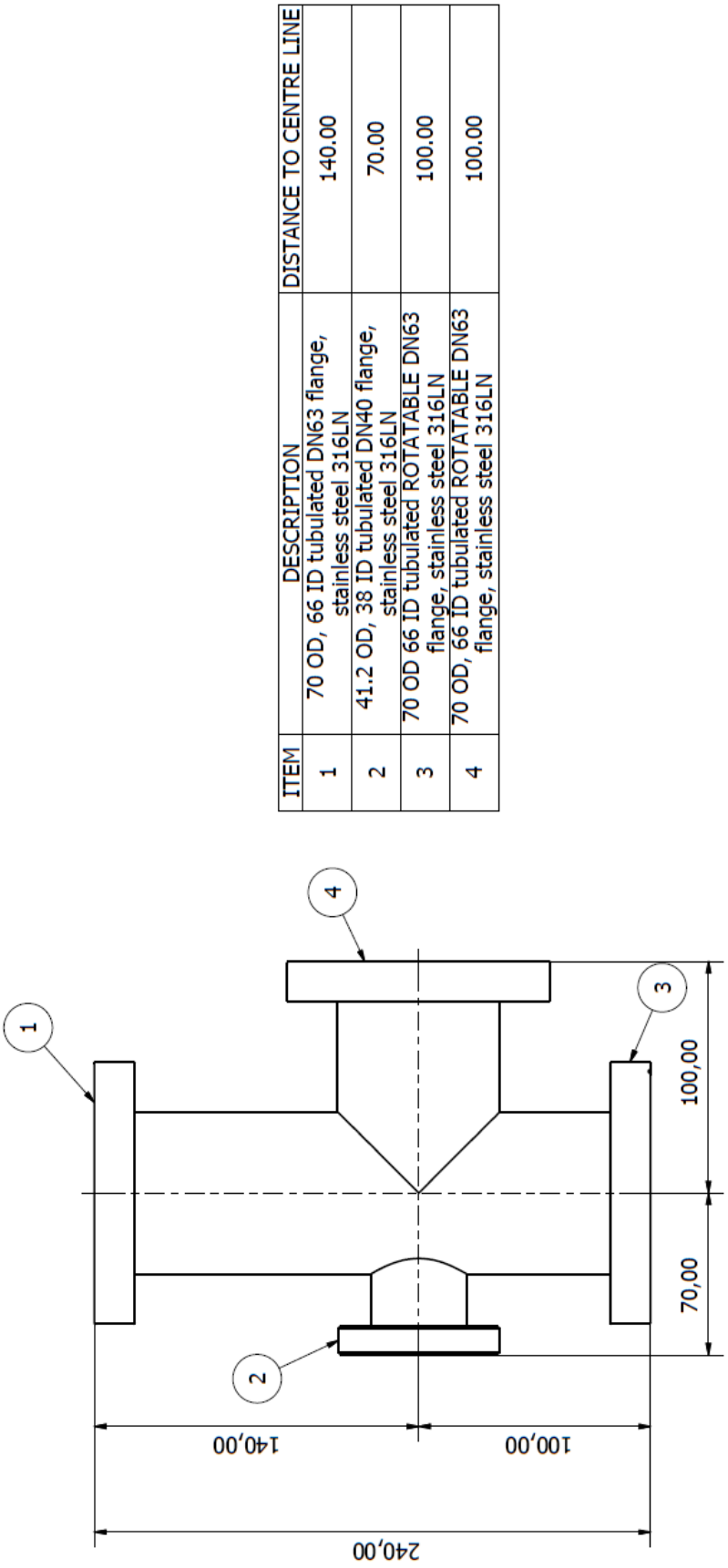

Figure D.5: The engineering drawing for the pumping station attached to each of the $55\,\mathrm{l\,s^{-1}}$ ion pumps.

ITEM	DESCRIPTION	DISTANCE TO CENTRE	QTY
A	156 OD, 150 ID chamber with two DN160 flanges. Height = 130. Ports every 30degrees. Stainless steel 316LN	N/A	1
B	38.1 OD, 34.9 ID tubulated DN40 flange, stainless steel 316LN	160	6
C	38.1 OD, 34.9 ID tubulated DN40 flange, stainless steel 316LN	120	4
D	19.1 OD, 16.7 ID tubulated DN16 flange, stainless steel 316LN	120	1
E	Conical tubulated DN63 flange, see sheet 2/2 for details, stainless steel 316LN	200	1

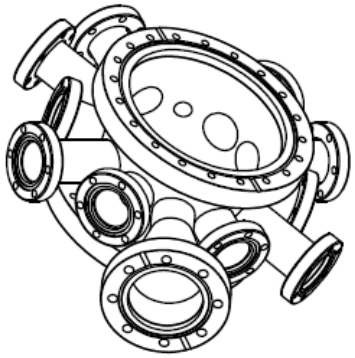

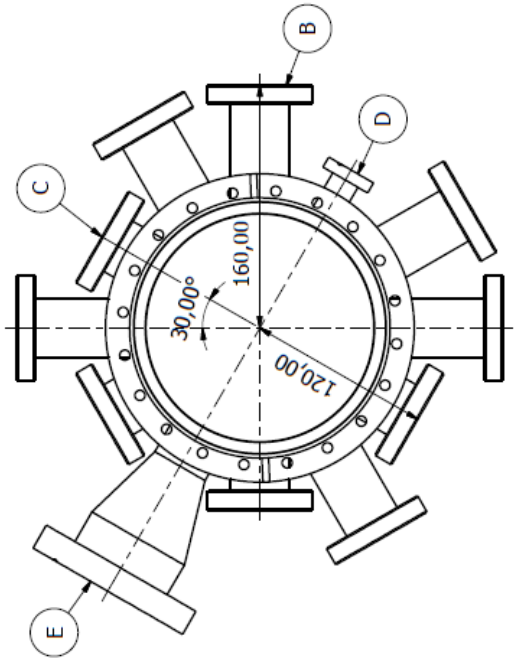

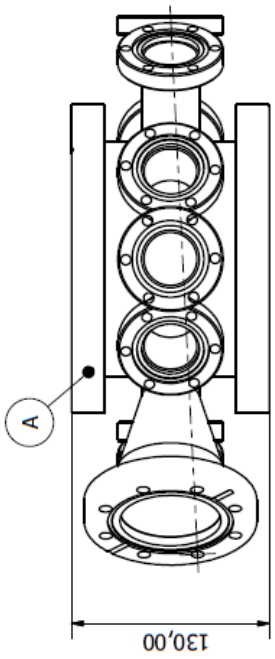

Figure D.6: The engineering drawing supplied to VG Scienta for the science chamber.

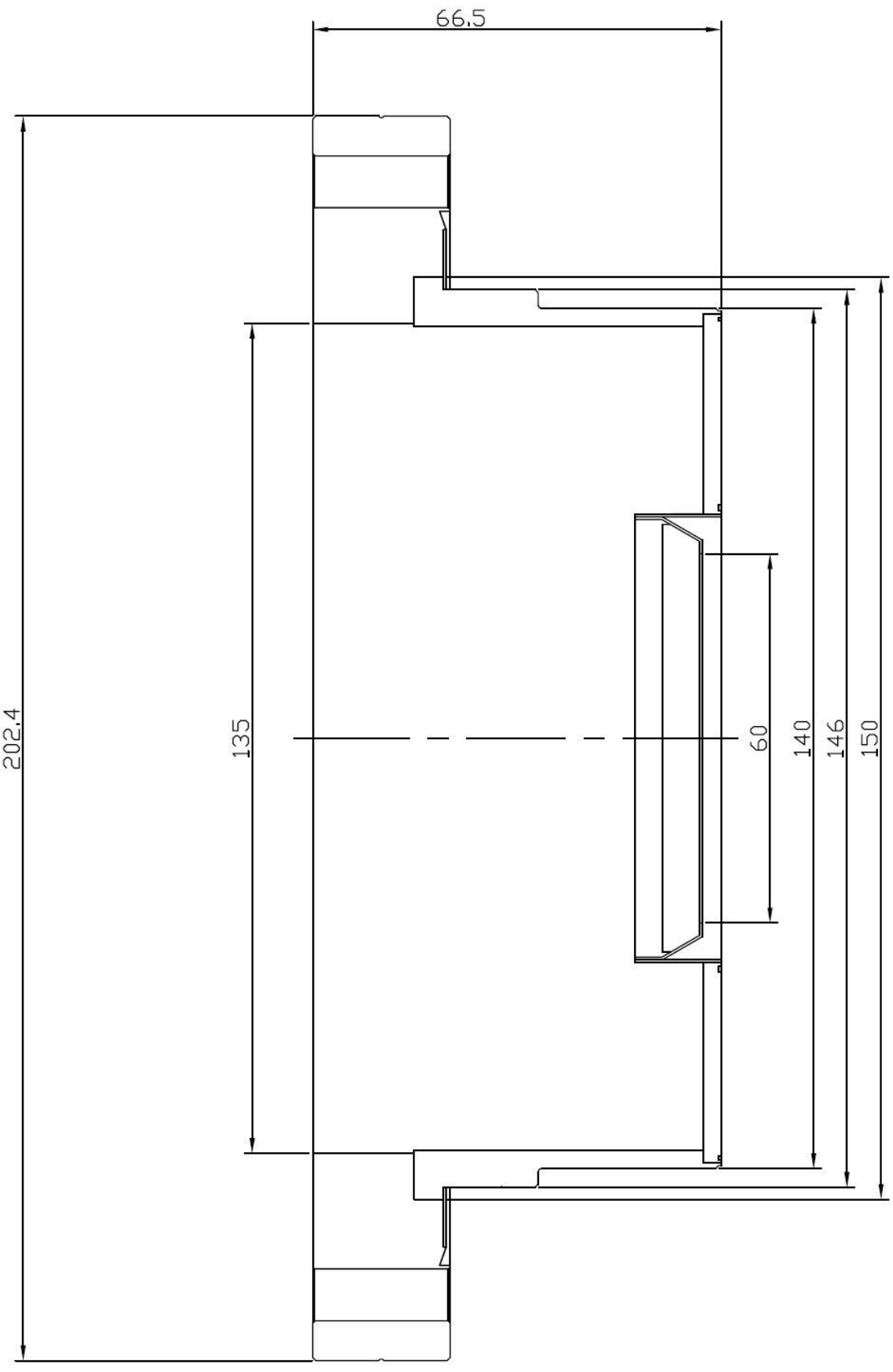

Figure D.7: The engineering drawing supplied by the UKAEA who made the viewports.

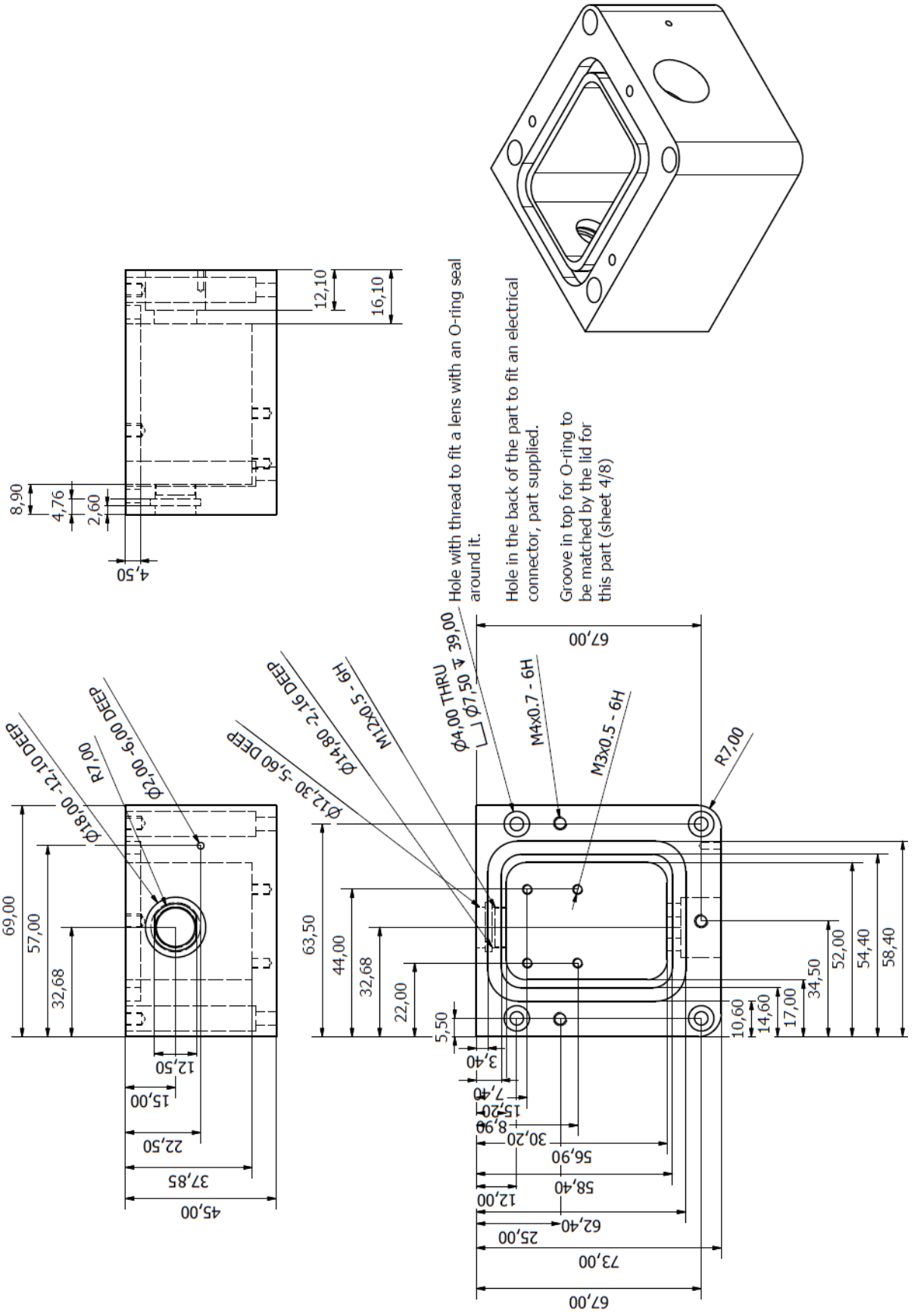

Figure D.8: The engineering drawing for the laser diode compartment for the 399 nm laser, capable of being hermetically sealed.

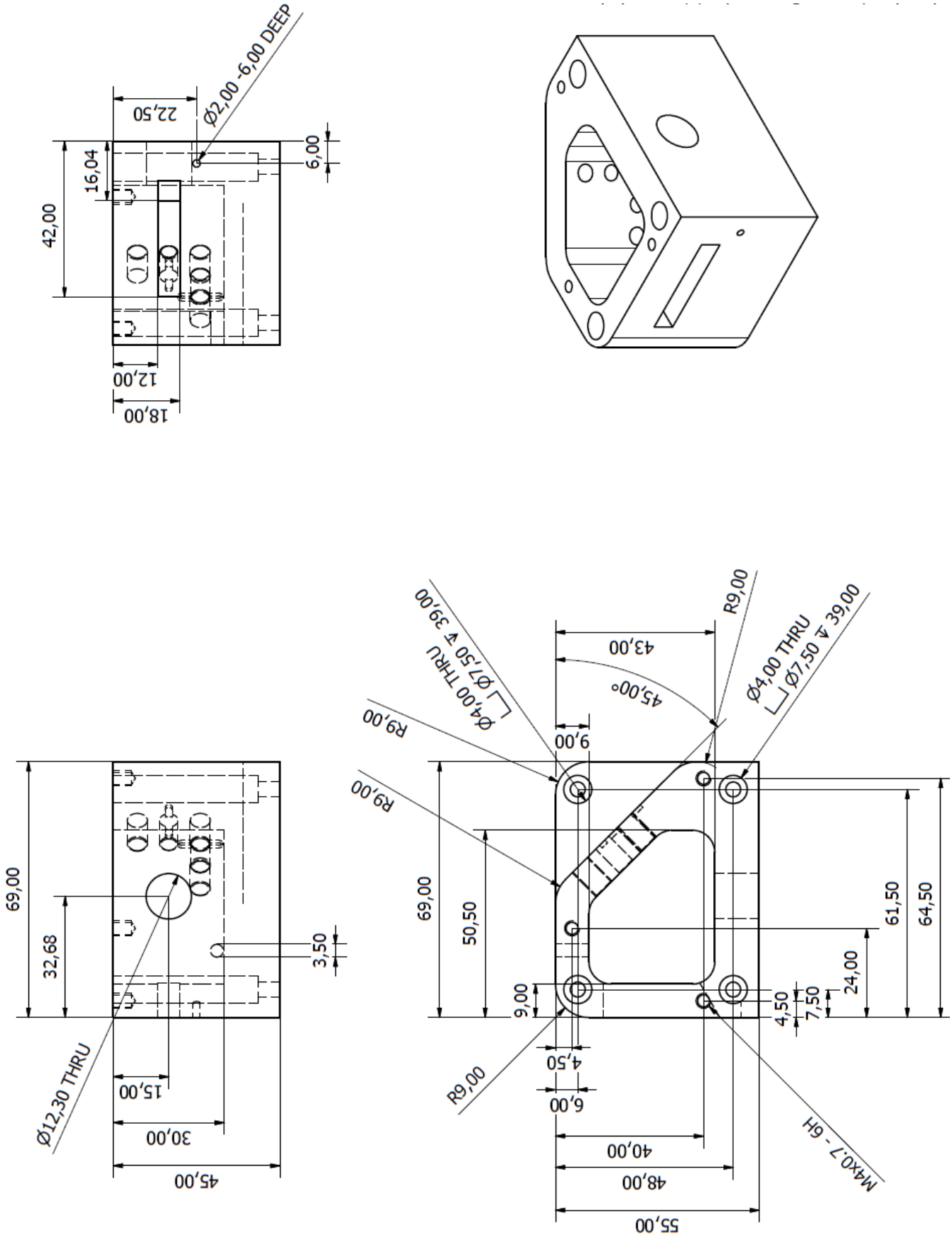

Figure D.9: The engineering drawing for the grating compartment for the 399 nm laser.

Appendix E

Vacuum cleaning procedure

It is important to clean vacuum components thoroughly before use to remove any contaminants. This can be achieved by completing the following process:

1. Place items to be cleaned in a container. Fill to just above the items with diluted Decon 90 (dilution details given on the bottle).
2. Place the container in a sonic bath filled with at least 1 inch of tap water for 1 hour (in 2 half hour sessions).
3. Cover a clear work bench with doubled over aluminium foil, making sure to touch the foil as little as possible (wear latex gloves).
4. Wearing latex gloves remove the items from the container once the sonic bath has finished. Place them on the foil.
5. Empty the container of Decon and rinse thoroughly with tap water.
6. Wearing a new pair of latex gloves replace the items in the container and fill to the same level with tap water.
7. Run the sonic bath for a further half hour.
8. As before, covering the worktop with a clean doubled over sheet of foil, remove the items from the container with a fresh pair of gloves.
9. Repeat steps 3-8 three times in total to make sure all of the Decon 90 has been removed.
10. After the third time, rinse the container thoroughly again and fill with methanol (wear goggles whilst handling the methanol). Make sure the level of methanol is higher than the items as some will evaporate during the sonic bath. With a fresh pair of gloves put the items into the container.

11. Run the sonic bath for another hour (again, broken into 2 half hour sessions so the level of methanol can be checked). Make sure the sonic bath is in a fume cupboard for this step.

12. As before, remove the items with a fresh pair of gloves and lay them on a clean sheet of foil.

13. Rinse and then fill the container with distilled water- enough to cover the items again.

14. Put the items back into the sonic bath for a further hour (again, two half hour sessions).

15. With a fresh pair of gloves lay the items on a clean sheet of foil and heat with an hot air gun to dry them thoroughly. Make sure every surface and notch is completely dry and hot to the touch.

16. Once cool, wrap the items in clean doubled over foil until they are needed.

It is important to make sure that fresh gloves are worn between each step so that no contaminants make their way back onto the components. Vacuum components should be handled as little as possible and never without powder-free latex gloves on.

If components have to be left whilst in the process of being cleaned, make sure that they are fully covered by the liquid at whatever stage they are at and that there are no air bubbles on any of the components; this is to ensure that the components do not go rusty. The container should then be covered with a sheet of foil so nothing can fall into the liquid.

Bibliography

[1] S. Chu, *Nobel Lecture: The manipulation of neutral particles*, Rev. Mod. Phys. **70**, 685 (1998).

[2] C. N. Cohen-Tannoudji, *Nobel Lecture: Manipulating atoms with photons*, Rev. Mod. Phys. **70**, 707 (1998).

[3] W. D. Phillips, *Nobel Lecture: Laser cooling and trapping of neutral atoms*, Rev. Mod. Phys. **70**, 721 (1998).

[4] W. Ketterle, *Nobel lecture: When atoms behave as waves: Bose-Einstein condensation and the atom laser*, Rev. Mod. Phys. **74**, 1131 (2002).

[5] E. A. Cornell and C. E. Wieman, *Nobel Lecture: Bose-Einstein condensation in a dilute gas, the first 70 years and some recent experiments*, Rev. Mod. Phys. **74**, 875 (2002).

[6] M. Weidemüller and C. Zimmermann, *Cold Atoms and Molecules*, 1 ed. (Wiley-VCH, Germany, 2009).

[7] E. R. Hudson, H. J. Lewandowski, B. C. Sawyer, and J. Ye, *Cold Molecule Spectroscopy for Constraining the Evolution of the Fine Structure Constant*, Phys. Rev. Lett. **96**, 143004 (2006).

[8] M. T. Murphy, V. V. Flambaum, S. Muller, and C. Henkel, *Strong Limit on a Variable Proton-to-Electron Mass Ratio from Molecules in the Distant Universe*, Science **320**, 1611 (2008).

[9] S. Truppe *et al.*, *A search for varying fundamental constants using hertz-level frequency measurements of cold CH molecules*, Nat Commun **4**, (2013).

[10] D. M. Kara *et al.*, *Measurement of the electron's electric dipole moment using YbF molecules: methods and data analysis*, New Journal of Physics **14**, 103051 (2012).

[11] M. T. Bell and T. P. Softley, *Ultracold molecules and ultracold chemistry*, Molecular Physics **107**, 99 (2009).

[12] L. D. Carr, D. DeMille, R. V. Krems, and J. Ye, *Cold and ultracold molecules: science, technology and applications*, New Journal of Physics **11**, 055049 (2009).

[13] L. Santos, G. V. Shlyapnikov, P. Zoller, and M. Lewenstein, *Bose-Einstein Condensation in Trapped Dipolar Gases*, Phys. Rev. Lett. **85**, 1791 (2000).

[14] T. Lahaye *et al.*, *Strong dipolar effects in a quantum ferrofluid*, Nature **448**, 672 (2007).

[15] T. Lahaye, C. Menotti, L. Santos, M. Lewenstein, and T. Pfau, *The physics of dipolar bosonic quantum gases*, Rep. Prog. Phys. **72**, 126401 (2009).

[16] A. Micheli, G. K. Brennen, and P. Zoller, *A toolbox for lattice-spin models with polar molecules*, Nat Phys **2**, 341 (2006).

[17] D. DeMille, *Quantum Computation with Trapped Polar Molecules*, Phys. Rev. Lett. **88**, 067901 (2002).

[18] J. J. Hudson, B. E. Sauer, M. R. Tarbutt, and E. A. Hinds, *Measurement of the Electron Electric Dipole Moment Using YbF Molecules*, Phys. Rev. Lett. **89**, 023003 (2002).

[19] M. Lu, N. Q. Burdick, S. H. Youn, and B. L. Lev, *Strongly Dipolar Bose-Einstein Condensate of Dysprosium*, Phys. Rev. Lett. **107**, 190401 (2011).

[20] A. Micheli, G. Pupillo, H. P. Büchler, and P. Zoller, *Cold polar molecules in two-dimensional traps: Tailoring interactions with external fields for novel quantum phases*, Phys. Rev. A **76**, 043604 (2007).

[21] G. K. Brennen, A. Micheli, and P. Zoller, *Designing spin-1 lattice models using polar molecules*, New Journal of Physics **9**, 138 (2007).

[22] E. S. Shuman, J. F. Barry, and D. DeMille, *Laser cooling of a diatomic molecule*, Nature **467**, 820 (2010).

[23] V. Zhelyazkova *et al.*, *Laser cooling and slowing of CaF molecules*, arXiv:1308.0421 [physics.atom-ph], 2013.

[24] M. Inguscio and L. Fallani, *Atomic Physics: Precise measurements and ultracold matter*, 1 ed. (Oxford University Press, UK, 2013).

[25] H. L. Bethlem, G. Berden, and G. Meijer, *Decelerating Neutral Dipolar Molecules*, Phys. Rev. Lett. **83**, 1558 (1999).

[26] S. Y. T. van de Meerakker, H. L. Bethlem, N. Vanhaecke, and G. Meijer, *Manipulation and Control of Molecular Beams*, Chemical Reviews **112**, 4828 (2012).

[27] E. Lavert-Ofir *et al.*, *A moving magnetic trap decelerator: a new source of cold atoms and molecules*, New Journal of Physics **13**, 103030 (2011).

[28] A. Trimeche, M. Bera, J.-P. Cromières, J. Robert, and N. Vanhaecke, *Trapping of a supersonic beam in a traveling magnetic wave*, The European Physical Journal D **65**, 263 (2011).

[29] D. Egorov *et al.*, *Buffer-gas cooling of NH via the beam loaded buffer-gas method*, The European Physical Journal D - Atomic, Molecular, Optical and Plasma Physics **31**, 307 (2004).

[30] N. E. Bulleid *et al.*, *Characterization of a cryogenic beam source for atoms and molecules*, Phys. Chem. Chem. Phys. **15**, 12299 (2013).

[31] W. G. Rellergert *et al.*, *Evidence for sympathetic vibrational cooling of translationally cold molecules*, Nature **495**, 490 (2013).

[32] S. Tokunaga *et al.*, *Prospects for sympathetic cooling of molecules in electrostatic, ac and microwave traps*, The European Physical Journal D **65**, 141 (2011).

[33] N. E. Bulleid *et al.*, *Traveling-wave deceleration of heavy polar molecules in low-field-seeking states*, Phys. Rev. A **86**, 021404 (2012).

[34] J. Ulmanis, J. Deiglmayr, M. Repp, R. Wester, and M. Weidemüller, *Ultracold Molecules Formed by Photoassociation: Heteronuclear Dimers, Inelastic Collisions, and Interactions with Ultrashort Laser Pulses*, Chemical Reviews **112**, 4890 (2012).

[35] K. M. Jones, E. Tiesinga, P. D. Lett, and P. S. Julienne, *Ultracold photoassociation spectroscopy: Long-range molecules and atomic scattering*, Rev. Mod. Phys. **78**, 483 (2006).

[36] C. Chin, R. Grimm, P. Julienne, and E. Tiesinga, *Feshbach resonances in ultracold gases*, Rev. Mod. Phys. **82**, 1225 (2010).

[37] K. Bergmann, H. Theuer, and B. W. Shore, *Coherent population transfer among quantum states of atoms and molecules*, Rev. Mod. Phys. **70**, 1003 (1998).

[38] A.-C. Voigt *et al.*, *Ultracold Heteronuclear Fermi-Fermi Molecules*, Phys. Rev. Lett. **102**, 020405 (2009).

[39] F. M. Spiegelhalder *et al.*, *All-optical production of a degenerate mixture of ^6Li and ^{40}K and creation of heteronuclear molecules*, Phys. Rev. A **81**, 043637 (2010).

[40] C.-H. Wu, J. W. Park, P. Ahmadi, S. Will, and M. W. Zwierlein, *Ultracold Fermionic Feshbach Molecules of* $^{23}Na^{40}K$, Phys. Rev. Lett. **109**, 085301 (2012).

[41] M.-S. Heo *et al.*, *Formation of ultracold fermionic NaLi Feshbach molecules*, Phys. Rev. A **86**, 021602 (2012).

[42] J. G. Danzl *et al.*, *Quantum Gas of Deeply Bound Ground State Molecules*, Science **321**, 1062 (2008).

[43] F. Lang, K. Winkler, C. Strauss, R. Grimm, and J. H. Denschlag, *Ultracold Triplet Molecules in the Rovibrational Ground State*, Phys. Rev. Lett. **101**, 133005 (2008).

[44] K.-K. Ni *et al.*, *A High Phase-Space-Density Gas of Polar Molecules*, Science **322**, 231 (2008).

[45] M. Debatin, *Creation of Ultracold RbCs Ground-State Molecules*, PhD thesis, University of Innsbruck, 2013.

[46] M. Repp *et al.*, *Observation of interspecies* ^{6}Li-^{133}Cs *Feshbach resonances*, Phys. Rev. A **87**, 010701 (2013).

[47] B. Pasquiou *et al.*, *Quantum degenerate mixtures of strontium and rubidium atoms*, Phys. Rev. A **88**, 023601 (2013).

[48] F. Munchow, C. Bruni, M. Madalinski, and A. Gorlitz, *Two-photon photoassociation spectroscopy of heteronuclear YbRb*, Phys. Chem. Chem. Phys. **13**, 18734 (2011).

[49] A. Khramov *et al.*, *Ultracold Heteronuclear Mixture of Ground and Excited State Atoms*, Phys. Rev. Lett. **112**, 033201 (2014).

[50] H. Hara, H. Konishi, S. Nakajima, Y. Takasu, and Y. Takahashi, *A Three-Dimensional Optical Lattice of Ytterbium and Lithium Atomic Gas Mixture*, Journal of the Physical Society of Japan **83**, 014003 (2014).

[51] W. Markowitz, R. G. Hall, L. Essen, and J. V. L. Parry, *Frequency of Cesium in Terms of Ephemeris Time*, Phys. Rev. Lett. **1**, 105 (1958).

[52] *Definition of the second*, www.bipm.org/en/si/si_brochure/chapter2/2-1/second.html.

[53] D. A. Steck, *Cesium D Line Data,* available online at `http://steck.us/alkalidata` (revision 2.1.4), 2010.

[54] T. Weber, J. Herbig, M. Mark, H.-C. Nägerl, and R. Grimm, *Bose-Einstein Condensation of Cesium*, Science **299**, 232 (2003).

[55] C.-L. Hung, X. Zhang, N. Gemelke, and C. Chin, *Accelerating evaporative cooling of atoms into Bose-Einstein condensation in optical traps*, Phys. Rev. A **78**, 011604 (2008).

[56] D. J. McCarron, H. W. Cho, D. L. Jenkin, M. P. Köppinger, and S. L. Cornish, *Dual-species Bose-Einstein condensate of* ^{87}Rb *and* ^{133}Cs, Phys. Rev. A **84**, 011603 (2011).

[57] Y. Takasu *et al.*, *Spin-Singlet Bose-Einstein Condensation of Two-Electron Atoms*, Phys. Rev. Lett. **91**, 040404 (2003).

[58] Y. Takasu, T. Fukuhara, M. Kitagawa, M. Kumakura, and Y. Takahashi, *Quantum-degenerate gases of Ytterbium atoms*, Laser Physics **16**, 713 (2006).

[59] T. Fukuhara, S. Sugawa, and Y. Takahashi, *Bose-Einstein condensation of an ytterbium isotope*, Phys. Rev. A **76**, 051604 (2007).

[60] T. Fukuhara, S. Sugawa, Y. Takasu, and Y. Takahashi, *All-optical formation of quantum degenerate mixtures*, Phys. Rev. A **79**, 021601(R) (2009).

[61] S. Sugawa, R. Yamazaki, S. Taie, and Y. Takahashi, *Bose-Einstein condensate in gases of rare atomic species*, Phys. Rev. A **84**, 011610(R) (2011).

[62] T. Fukuhara, Y. Takasu, M. Kumakara, and Y. Takahashi, *Degenerate Fermi Gases of Ytterbium*, Phys. Rev. Lett. **98**, 030401 (2007).

[63] S. Taie *et al.*, *Realization of a SU(2)×SU(6) System of Fermions in a Cold Atomic Gas*, Phys. Rev. Lett. **105**, 190401 (2010).

[64] M. Kitagawa *et al.*, *Two-color photoassociation spectroscopy of ytterbium atoms and the precise determinations of s-wave scattering lengths*, Phys. Rev. A **77**, 012719 (2008).

[65] *NIST Basic Atomic Spectroscopic Data*, available online at www.nist.gov/pml/data/handbook/index.cfm.

[66] R. Maruyama, *Optical trapping of Ytterbium atoms*, PhD thesis, University of Washington, USA, 2003.

[67] K. Honda *et al.*, *Magneto-optical trapping of Yb atoms and a limit on the branching ratio of the* $^1P_1$ *state*, Phys. Rev. A **59**, R934 (1999).

[68] K. Honda *et al.*, *Erratum: Magneto-optical trapping of Yb atoms and a limit on the branching ratio of the* $^1P_1$ *state [Phys. Rev. A,* ***59****, R934 (1999)]*, Phys. Rev. A **60**, 2603 (1999).

[69] C. J. Foot, *Atomic Physics (Oxford Master Series in Atomic, Optical and Laser Physics)*, 1 ed. (Oxford University Press, UK, 2005).

[70] D. Das, S. Barthwal, A. Banerjee, and V. Natarajan, *Absolute frequency measurements in Yb with 0.08 ppb uncertainty: Isotope shifts and hyperfine structure in the 399 nm* $^1S_0$ - $^1P_1$ *line*, Phys. Rev. A **72**, 032506 (2005).

[71] K. Pandey, A. K. Singh, P. V. K. Kumar, M. V. Suryanarayana, and V. Natarajan, *Isotope shifts and hyperfine structure in the 555.8-nm* $^1S_0$ *to* $^3P_1$ *line of Yb*, Phys. Rev. A **80**, 022518 (2009).

[72] M. J. Bijlsma, B. A. Heringa, and H. T. C. Stoof, *Phonon exchange in dilute Fermi-Bose mixtures: Tailoring the Fermi-Fermi interaction*, Phys. Rev. A **61**, 053601 (2000).

[73] M. Lewenstein, L. Santos, M. A. Baranov, and H. Fehrmann, *Atomic Bose-Fermi Mixtures in an Optical Lattice*, Phys. Rev. Lett. **92**, 050401 (2004).

[74] H. Feshbach, *Unified theory of nuclear reactions*, Annals of Physics **5**, 357 (1958).

[75] S. Inouye *et al.*, *Observation of Feshbach resonances in a Bose-Einstein condensate*, Nature **392**, 151 (1998).

[76] E. A. Donley, N. R. Claussen, S. T. Thompson, and C. E. Wieman, *Atom-molecule coherence in a Bose-Einstein condensate*, Nature **417**, 529 (2002).

[77] J. Herbig *et al.*, *Preparation of a Pure Molecular Quantum Gas*, Science **301**, 1510 (2003).

[78] S. Dürr, T. Volz, A. Marte, and G. Rempe, *Observation of Molecules Produced from a Bose-Einstein Condensate*, Phys. Rev. Lett. **92**, 020406 (2004).

[79] K. Xu *et al.*, *Formation of Quantum-Degenerate Sodium Molecules*, Phys. Rev. Lett. **91**, 210402 (2003).

[80] C. A. Regal, C. Ticknor, J. L. Bohn, and D. S. Jin, *Creation of ultracold molecules from a Fermi gas of atoms*, Nature **424**, 47 (2003).

[81] S. Jochim *et al.*, *Pure Gas of Optically Trapped Molecules Created from Fermionic Atoms*, Phys. Rev. Lett. **91**, 240402 (2003).

[82] C. Ospelkaus *et al.*, *Ultracold Heteronuclear Molecules in a 3D Optical Lattice*, Phys. Rev. Lett. **97**, 120402 (2006).

[83] S. B. Papp and C. E. Wieman, *Observation of Heteronuclear Feshbach Molecules from a $^{85}Rb^{87}Rb$ Gas*, Phys. Rev. Lett. **97**, 180404 (2006).

[84] C. Weber *et al.*, *Association of ultracold double-species bosonic molecules*, Phys. Rev. A **78**, 061601 (2008).

[85] H.-W. Cho *et al.*, *Feshbach spectroscopy of an ultracold mixture of ^{85}Rb and ^{133}Cs*, Phys. Rev. A **87**, 010703 (2013).

[86] D. A. Brue and J. M. Hutson, *Prospects of forming ultracold molecules in $^2\Sigma$ states by magnetoassociation of alkali-metal atoms with Yb*, Phys. Rev. A **87**, 052709 (2013).

[87] C. J. Joachain, *Quantum Collision Theory* (North-Holland, The Netherlands, 1987).

[88] J. M. Hutson, *KIPT conference talk: Molecules with electric and magnetic dipoles: magnetoassociation of alkali-metal with closed-shell atoms*, http://online.kitp.ucsb.edu/online/coldmoles_c13/hutson/, 2013.

[89] D. A. Brue and J. M. Hutson, *Magnetically Tunable Feshbach Resonances in Ultracold Li-Yb Mixtures*, Phys. Rev. Lett. **108**, 043201 (2012).

[90] J. Dalibard, *Collisional dynamics of ultra-cold atomic gases*, Proceedings of the International School of Physics Enrico Fermi, Varenna, Course CXL , 1 (1998).

[91] M. Berninger *et al.*, *Feshbach resonances, weakly bound molecular states, and coupled-channel potentials for cesium at high magnetic fields*, Phys. Rev. A **87**, 032517 (2013).

[92] E. Tiesinga, M. Anderlini, and E. Arimondo, *Determination of the scattering length of the a $^3\Sigma^+$ potential of ^{87}RbCs*, Phys. Rev. A **75**, 022707 (2007).

[93] R. Eisberg and R. Resnick, *Quantum Physics of Atoms, Molecules, Solids, Nuclei and Particles*, 2 ed. (John Wiley & Sons, 1985).

[94] P. G. Mickelson *et al.*, *Spectroscopic determination of the s-wave scattering lengths of ^{86}Sr and ^{88}Sr*, Phys. Rev. Lett. **95**, 223002 (2005).

[95] S. H. Autler and C. H. Townes, *Stark Effect in Rapidly Varying Fields*, Phys. Rev. **100**, 703 (1955).

[96] V. V. Flambaum, G. F. Gribakin, and C. Harabati, *Analytical calculation of cold-atom scattering*, Phys. Rev. A **59**, 1998 (1999).

[97] M. Borkowski *et al.*, *Scattering lengths in isotopologues of the RbYb system*, Phys. Rev. A **88**, 052708 (2013).

[98] R. J. LeRoy and R. B. Bernstein, *Dissociation Energy and Long-Range Potential of Diatomic Molecules from Vibrational Spacings of Higher Levels*, The Journal of Chemical Physics **52**, 3869 (1970).

[99] W. Stwalley, *Efficient conversion of ultracold Feshbach-resonance-related polar molecules into ultracold ground state ($X\,^1\Sigma^+ v = 0, J = 0$) molecules*, The European Physical Journal D - Atomic, Molecular, Optical and Plasma Physics **31**, 221 (2004).

[100] S. Kotochigova, P. S. Julienne, and E. Tiesinga, *Ab initio calculation of the KRb dipole moments*, Phys. Rev. A **68**, 022501 (2003).

[101] G. Herzberg, *Molecular Spectra and Molecular Structure I: Spectra of Diatomic Molecules*, 2 ed. (D. Van Nostrand Company, 1950).

[102] K.-K. Ni, *A Quantum Gas Of Polar Molecules*, PhD thesis, University of Colorado, USA, 2009.

[103] T. A. Delchar, *Vacuum Physics and Techniques*, 1 ed. (Chapman and Hall, UK, 1993).

[104] N. Ramsey, *Molecular beams* (Oxford science publications, 1986).

[105] G. Scoles, *Atomic and Molecular Beam Methods, Vol. 1* (Oxford University Press, UK, 1988).

[106] C. B. Alcock, V. P. Itkin, and H. M. K., *Vapor pressure equations for the metallic elements: 298-2500K*, Canadian Met **23**, 309 (1984).

[107] D. R. Lide, *CRC Handbook of Chemistry and Physics*, 87th ed. (CRC Press, USA, 2006).

[108] H. J. Metcalf and P. van der Straten, *Laser Cooling and Trapping*, 1 ed. (Springer, USA, 1999).

[109] J. C. Slater, *Atomic Radii in Crystals*, The Journal of Chemical Physics **41**, 3199 (1964).

[110] J. Millen, *A cold strontium Rydberg gas*, PhD thesis, Durham University, UK, 2011.

[111] A. H. Hansen *et al.*, *Production of quantum-degenerate mixtures of ytterbium and lithium with controllable interspecies overlap*, Phys. Rev. A **87**, 013615 (2013).

[112] I. Hughes and T. Hase, *Measurements and their Uncertainties: A Practical Guide to Modern Error Analysis*, 1 ed. (Oxford University Press, UK, 2010).

[113] J. H. Moore, C. C. Davis, and M. A. Coplan, *Building Scientific Apparatus*, 3rd ed. (Westview Press, USA, 2003).

[114] *Time lapse*, http://massey.dur.ac.uk/research/YbCs/YbCsgallery.html.

[115] J. Dalibard and C. Cohen-Tannoudji, *Laser cooling below the Doppler limit by polarization gradients: simple theoretical models*, J. Opt. Soc. Am. B **6**, 2023 (1989).

[116] P. D. Lett *et al.*, *Observation of Atoms Laser Cooled below the Doppler Limit*, Phys. Rev. Lett. **61**, 169 (1988).

[117] R. Maruyama *et al.*, *Investigation of sub-Doppler cooling in an ytterbium magneto-optical trap*, Phys. Rev. A **68**, 011403 (2003).

[118] A. J. Berglund, J. L. Hanssen, and J. J. McClelland, *Narrow-Line Magneto-Optical Cooling and Trapping of Strongly Magnetic Atoms*, Phys. Rev. Lett. **100**, 113002 (2008).

[119] D. Sukachev *et al.*, *Sub-doppler laser cooling of thulium atoms in a magneto-optical trap*, JETP Letters **92**, 703 (2010).

[120] T. Kuwamoto, K. Honda, Y. Takahashi, and T. Yabuzaki, *Magneto-optical trapping of Yb atoms using an intercombination transition*, Phys. Rev. A **60**, R745 (1999).

[121] V. Vuletić, C. Chin, A. J. Kerman, and S. Chu, *Degenerate Raman Sideband Cooling of Trapped Cesium Atoms at Very High Atomic Densities*, Phys. Rev. Lett. **81**, 5768 (1998).

[122] C. Wieman and T. W. Hänsch, *Doppler-Free Laser Polarization Spectroscopy*, Phys. Rev. Lett. **36**, 1170 (1976).

[123] K. L. Corwin, Z.-T. Lu, C. F. Hand, R. J. Epstein, and C. E. Wieman, *Frequency-Stabilized Diode Laser with the Zeeman Shift in an Atomic Vapor*, Appl. Opt. **37**, 3295 (1998).

[124] A. Millett-Sikking, I. G. Hughes, P. Tierney, and S. L. Cornish, *DAVLL lineshapes in atomic rubidium*, Journal of Physics B: Atomic, Molecular and Optical Physics **40**, 187 (2007).

[125] M. L. Harris, S. L. Cornish, A. Tripathi, and I. G. Hughes, *Optimization of sub-Doppler DAVLL on the rubidium D2 line*, Journal of Physics B: Atomic, Molecular and Optical Physics **41**, 085401 (2008).

[126] G. C. Bjorklund, M. D. Levenson, W. Lenth, and C. Ortiz, *Frequency Modulation (FM) Spectroscopy - Theory of Lineshapes and Signal-to-Noise Analysis*, Appl. Phys. B **31**, 145 (1983).

[127] J. H. Shirley, *Modulation transfer processes in optical heterodyne saturation spectroscopy*, Opt. Lett. **7**, 537 (1982).

[128] D. J. McCarron, S. A. King, and S. L. Cornish, *Modulation transfer spectroscopy in atomic rubidium*, Measurement Science and Technology **19**, 105601 (2008).

[129] D. A. Smith and I. G. Hughes, *The role of hyperfine pumping in multilevel systems exhibiting saturated absorption*, American Journal of Physics **72**, 631 (2004).

[130] D. J. McCarron, *A Quantum Degenerate Mixture of ^{87}Rb and ^{133}Cs*, PhD thesis, Durham University, UK, 2011.

[131] R. K. Raj, D. Bloch, J. J. Snyder, G. Camy, and M. Ducloy, *High-Frequency Optically Heterodyned Saturation Spectroscopy Via Resonant Degenerate Four-Wave Mixing*, Phys. Rev. Lett. **44**, 1251 (1980).

[132] D. Allan, *Statistics of atomic frequency standards*, Proceedings of the IEEE **54**, 221 (1966).

[133] N. M. Sampas, E. K. Gustafson, and R. L. Byer, *Long-term stability of two diode-laser-pumped nonplanar ring lasers independently stabilized to two Fabry–Perot interferometers*, Opt. Lett. **18**, 947 (1993).

[134] S. Händel, *Experiments on ultracold quantum gases of ^{85}Rb and ^{87}Rb*, PhD thesis, Durham University, UK, 2011.

[135] P. Arora, A. Agarwal, and A. S. Gupta, *Simple alignment technique for polarisation maintaining fibres*, Review of Scientific Instruments **82**, (2011).

[136] F. Baumer, *Isotope dependent interactions in a mixture of ultracold atoms*, PhD thesis, Heinrich-Heine-Universität Düsseldorf, Germany, 2010.

[137] M. Okano *et al.*, *Simultaneous magneto-optical trapping of lithium and ytterbium atoms towards production of ultracold polar molecules*, Applied Physics B **98**, 691 (2010).

[138] S. Tokunaga, *Production and Stark deceleration of lithium hydride molecules*, PhD thesis, Imperial College London, UK, 2009.

[139] S. Truppe, *New Physics with Cold Molecules: Precise Microwave Spectroscopy of CH and the Development of a Microwave Trap*, PhD thesis, Imperial College London, UK, 2014.

[140] C. G. Townsend *et al.*, *Phase-space density in the magneto-optical trap*, Phys. Rev. A **52**, 1423 (1995).

[141] T. P. Wiles, *Dynamics of bright solitary matter-waves*, PhD thesis, Durham University, UK, 2013.

[142] M. S. Safronova, B. Arora, and C. W. Clark, *Frequency-dependent polarizabilities of alkali-metal atoms from ultraviolet through infrared spectral regions*, Phys. Rev. A **73**, 022505 (2006).

[143] J. E. Sansonetti, *Wavelengths, transition probabilities and energy levels for the spectra of Cesium (Cs_I - Cs_{LV})*, J. Phys. Chem. Ref. Data **38**, 761 (2009).

[144] W. D. Phillips and H. Metcalf, *Laser Deceleration of an Atomic Beam*, Phys. Rev. Lett. **48**, 596 (1982).

[145] J. V. Prodan and W. D. Phillips, *Chirping the Light Fantastic - Recent NBS atom cooling experiments*, Progress in Quantum Electronics **8**, 231 (1984).

[146] E. Wille, *Preparation of an optically trapped Fermi-Fermi mixture of ^6Li and ^{40}K atoms and characterization of the interspecies interactions by Feshbach spectroscopy*, PhD thesis, Universität Innsbruck, Austria, 2009.

[147] M. Gustavsson, *A quantum gas with tunable interactions in an optical lattice*, PhD thesis, University of Innsbruck, Austria, 2008.

[148] M. Mudrich, *Interactions in an optically trapped mixture of ultracold lithium and cesium atoms: thermal, spin-exchange collisions and photoassociation*, PhD thesis, Ruperto-Carola University, Heidelberg, Germany, 2003.

[149] A. Yamaguchi, *Metastable State of Ultracold and Quantum Degenerate Ytterbium Atoms: High-Resolution Spectroscopy and Cold Collisions*, PhD thesis, University of Kyoto, Japan, 2007.

[150] S. C. Bell *et al.*, *A slow atom source using a collimated effusive oven and a single-layer variable pitch coil Zeeman slower*, Review of Scientific Instruments **81**, 013105 (2010).

[151] I. Hill *et al.*, *A simple, configurable, permanent magnet Zeeman Slower for Sr*, in *European Frequency and Time Forum (EFTF), 2012*, pp. 545–549, 2012.

[152] N. Nemitz, *Production and spectroscopy of ultracold YbRb* molecules*, PhD thesis, Heinrich-Heine-Universität Düsseldorf, Germany, 2008.

[153] H. C. Busch, M. K. Shaffer, E. M. Ahmed, and C. I. Sukenik, *Trap loss in a dual-species Rb-Ar* magneto-optical trap*, Phys. Rev. A **73**, 023406 (2006).

[154] A. Ridinger *et al.*, *Large atom number dual-species magneto-optical trap for fermionic* ^{6}Li *and* ^{40}K *atoms*, The European Physical Journal D **65**, 223 (2011).

[155] S. Dutta, A. Altaf, J. Lorenz, D. S. Elliott, and P. C. Yong, *Interspecies collision-induced losses in a dual species* ^{7}Li-^{85}Rb *magneto-optical trap*, arXiv:1306.5196 [physics.atom-ph], 2013.

[156] M. Pichler, H. Chen, and W. C. Stwalley, *Photoassociation spectroscopy of ultracold Cs below the* $6P_{1/2}$ *limit*, The Journal of Chemical Physics **121**, 1796 (2004).

[157] S. Wang, *Principles of distributed feedback and distributed Bragg-reflector lasers*, Quantum Electronics, IEEE Journal of **10**, 413 (1974).

[158] M. P. Köppinger *et al.*, *Production of optically trapped* $^{87}RbCs$ *Feshbach molecules*, Phys. Rev. A **89**, 033604 (2014).

[159] D. O. Sabulsky, C. V. Parker, N. D. Gemelke, and C. Chin, *Efficient continuous-duty Bitter-type electromagnets for cold atom experiments*, Review of Scientific Instruments **84**, (2013).

[160] G. Zürn, *Realization of an Optical Microtrap for a Highly Degenerate Fermi Gas*, Master's thesis, Max-Planck-Institute for Nuclear Physics, University of Heidelberg, Germany, 2009.

[161] S. Stellmer, B. Pasquiou, R. Grimm, and F. Schreck, *Creation of Ultracold* Sr_2 *Molecules in the Electronic Ground State*, Phys. Rev. Lett. **109**, 115302 (2012).

[162] S. Kato, S. Sugawa, K. Shibata, R. Yamamoto, and Y. Takahashi, *Control of Resonant Interaction between Electronic Ground and Excited States*, Phys. Rev. Lett. **110**, 173201 (2013).

[163] M. L. Harris, *Realisation of a Cold Mixture of Rubidium and Caesium*, PhD thesis, Durham University, UK, 2008.

[164] P. Tierney, *Magnetic Trapping of an Ultracold* ^{87}Rb-^{133}Cs *Atomic Mixture*, PhD thesis, Durham University, UK, 2009.

[165] D. L. Jenkin, *Feshbach spectroscopy of an ultracold Rb-Cs mixture*, PhD thesis, Durham University, UK, 2012.

[166] M. P. Köppinger, *Creation of ultracold RbCs molecules*, PhD thesis, Durham University, UK, 2014.

[167] D. A. Steck, *Rubidium 85 D Line Data,* available online at `http://steck.us/alkalidata` (revision 2.1.6), 2013.